DEVELOPMENT OF GRADIENT SMOOTHING OPERATIONS AND APPLICATION TO BIOLOGICAL SYSTEMS

LI QUAN BING ERIC

(B. Eng. (1ST Class Hons) NTU, Singapore)

A THESIS SUBMITTED

FOR THE DEGREE OF DOCTOR OF PHILOSOPHY

DEPARTMENT OF MECHANICAL ENGINEERING

NATIONAL UNIVERSITY OF SINGAPORE

2011

Acknowledgements

I would like to express deepest gratitude and appreciation to my two supervisors Associate Professors Tan Beng Chye Vincent and Professor Liu Gui Rong for their dedicated guidance, support and continuous encouragement during my PhD study. In my mind, these two supervisors influence me not only in my research but also in many aspects of my life.

I am also glad to extend my thanks to my friends and colleagues in the center of Advanced Computing and Engineering Science (ACES), Dr. Zhang Zhi Qian, Dr. Zhang Gui Yong, Mr. Chen Lei, Mr. Wang Sheng, Mr. Liu Jun and Mr. Jiang Yong for their kind support and valuable hints. The special thank will go to Dr. Xu Xiang Guo George. Without his endless assistance and supportive discussions in my research work, it is impossible to complete this thesis.

In addition, the sincere gratitude gives to my wife, Ms Luo Wen Tao, for her unwavering support and understanding during my research time.

Last but not least, the financial support from National University of Singapore (NUS) is highly appreciated throughout my study.

Table of Contents

Summary

This thesis focuses on the development of gradient smoothing operations in the weak and strong forms and the application of these methods to model biological systems. The work comprises three parts: the first is to apply edge-based smoothed finite element method (ES-FEM) in 2D and face-based smoothed finite element method (FS-FEM) in 3D based on the weak form in the thermal-mechanical models for the hyperthermia treatment of human breast, and to formulate the alpha finite element method (αFEM) based on the weak form to analyze phase changes in the liver cryosurgery and bioheat transfer in the human eye. The second part is to develop the gradient smoothing operation in the strong form to formulate a novel piecewise linear gradient smoothing method (PL-GSM) and alpha gradient smoothing method (αGSM) for fluid dynamics. The third part is to combine the gradient smoothing operation in the weak and strong form to develop the immersed gradient smoothing method (IGSM) to solve fluid-structure interaction (FSI) problem.

Traditional finite element method (FEM) has several limitations including ‘overly-stiff’ and rigid reliance on elements. Through gradient smoothing operations in the Galerkin weak form, the stiffness of FEM model can be reduced. The accuracy of numerical solutions can then be significantly improved. Numerical examples in biological systems such as liver cryosurgery, bioheat transfer in the human eye and hyperthermia treatment of the breast have strongly demonstrated that the results obtained from gradient smoothing operation in the Galerkin weak form are remarkably efficient, accurate and stable.

Enlightened by the attractive merits of gradient smoothing operation in the Galerkin weak from, the PL-GSM derived from the gradient smoothing operation to approximate the derivatives of any function applied directly to the strong form is proposed. The PL-GSM is a purely mathematical operation that adopts the piecewise linear smoothing function to approximate the gradient of unknown variables. The flexibility of the PL-GSM allows it to make use of existing meshes that have originally been created for finite difference or finite element methods. The PL-GSM solutions show perfect agreements with experimental and literature data in the fluid dynamics. Additionally, the alpha gradient smoothing method (αGSM) that combines piecewise constant and piecewise linear smoothing functions is proposed in this thesis. In the αGSM, the parameter α controls the contribution of piecewise constant and piecewise linear smoothing function.

The immersed gradient smoothing method (IGSM) couples the gradient smoothing operation in the weak and strong form to address fluid structure interaction problems. The algorithm of IGSM is similar to the immersed finite element method (IFEM). In the IGSM, a mixture of Lagrangian mesh for the solid domain and Eulerian mesh for the fluid domain is employed. However, the edge-based smoothed finite element method (ES-FEM) is used to discretize the solid structure in order to soften the finite element model in the solid domain. In the fluid domain, the piecewise linear gradient smoothing method (PL-GSM) is employed to solve the modified Navier –stokes equation, which reduces the computational cost of finite element method (FEM) without compromising

accuracy. Two numerical examples are presented to verify the application of IGSM. All the numerical solutions demonstrate that the IGSM is accurate, robust and efficient.

List of Figures

List of Tables

Chapter 1

Introduction

1.1 Gradient smoothing operation in the weak form

1.1.1 Background of weak form in the numerical technique

Analytical solutions are seldom obtained for partial differential equations governing a physical problem. Many numerical methods have been developed to obtain approximate solution such as Finite Element Methods (FEM), Finite Difference Methods (FDM), Finite Volume Methods (FVM), etc. All numerical methods are classified into two groups: direct approach and indirect approach. Weak form methods based on an alternative weak form system of equations are indirect approaches.

The vital idea of a weak form is to determine a global behavior of the entire system and then obtain a best possible solution to the problem that can strike a balance for the system in terms of the global behavior [1]. There are usually two ways to construct weak forms. One is the weighted residual methods, another is the energy principles. The Galerkin formulation can be derived from both methods. The weighted residual method is a more general and powerful mathematical tool that can be used for discretized system equations for many types of engineering problems. The minimum

energy potential principle is a convenient tool for deriving discrete system equations for FEM and also for many types of approximation methods.

The discretized equations derived based on the weak form are usually more stable and can provide more accurate results. This is because of the well-structured error control measures built into the weak formulation, which can produce a stable set of algebraic equation and preserves the symmetrical property for irregularly distributed nodes [1].

1.1.2 Introduction of Finite Element Method (FEM)

The traditional Finite Element Method (FEM) is founded on the variational or energy principles of virtual work, Hamilton's principle, the minimum total potential energy principle, and so on [1-2]. The FEM possesses many attractive features and is currently the most widely used and reliable numerical approach [2] with many commercial software packages available. In the FEM, the physical domain is denoted by an assemblage of subdivisions called elements. The governing partial differential equations (PDEs) called strong from that requires strong continuity on the field variables can be transformed into weak formulations. Once the weak form is formulated, the shape function is now created using polynomial functions. The stiffness and load vector can be computed when the strain field is calculated. After assembling the global matrices/vectors and imposing proper boundary conditions, the global equilibrium system of equations governing the problem domain can be established and solved.

Although the FEM has achieved remarkable progress in the development of numerical methods, there are some major issues related to the FEM. The first issue is the 'overly-stiff' phenomenon of a fully compatible FEM model of assumed displacement based on the Galerkin weak form [2], which can cause 'locking' behavior and poor accuracy in stress solution. In the FEM model, stresses are discontinuous and often less accurate. The second issue is that the FEM is limited by the rigid reliance on the elements. In large deformation problems, accuracy could be lost due to element distortion or even break down during the computation. The third issue is mesh generation. Engineers prefer using the triangular or tetrahedral elements because they can be generated automatically even for problems with complex geometry. However, triangular elements often give solutions of very poor accuracy.

1.1.3 Concept of gradient smoothing operation in the weak form

In order to overcome the shortcomings of overly stiff predictions and mesh dependency in FEM, many efforts have been made to address these issues, especially in the area of hybrid FEM formulation [3, 4]. In 2000, strain smoothing techniques applied in the FEM was proposed by the Chen et al. [5]to stabilize the solutions of nodal integrated meshfree methods and natural element method [6]. The essential idea of gradient smoothing operation in the weak form is to modify the compatible strain in the FEM model.

In the standard FEM model, strain energy is obtained based on the compatible strain using the strain-displacement relationship. The discrete system of equation is

established by the Galerkin weak form. However, the evaluation of strain energy is calculated by the modified strain in the gradient smoothing operations of weak form, and a proper energy weak form is used to construct the discretized model. The modified strain must be done properly to ensure stability and convergence.

The formulation of gradient smoothing operation in the weak form is quite similar to the FEM. First, the problem domain is discretized into elements. Triangular elements for 2D and tetrahedral elements for 3D are preferred. When triangular or tetrahedral elements are used, the process for meshing is the same as in the FEM. The smoothed strain is constructed via simple surface integration on the smoothing domain boundaries without any need for coordinate mapping. The smoothed Galerkin weak form is used to establish the discrete linear algebraic system equations instead of the Galerkin weak form. The treatment to impose boundary conditions is exactly the same as FEM.

The important outcome of gradient smoothing operation in the weak form is the creation of softer models than FEM models. It is noted that there is a number of gradient smoothing operations in the weak form due to the types of smoothing domains.

1.1.4 Features and properties of gradient smoothing operation in the weak form

In this thesis, three types of gradient smoothing operations are introduced. The first gradient smoothing operation in the weak form is the typical node-based finite

element method (NS-FEM) [7]. In the NS-FEM, the smoothing domain associated with the node is created by connecting sequentially the mid-edge-point to the central points surrounding elements sharing the node. It is found that when a reasonably fine mesh is used, the NS-FEM can produce upper bound solutions in strain energy for problems with homogeneous essential boundary conditions [7]. Using these bound properties of NS-FEM and FEM solutions, one can now effectively certify a numerical solution and conduct elegant adaptive analyses for solutions of desired accuracy [7]. Moreover, the NS-FEM is immune from volumetric locking and hence works well for nearly incompressible materials. However, the NS-FEM model is "overly-soft" leading to temporal instability which is observed as spurious non-zero energy modes in vibration analysis [7].

The second gradient smoothing method in the weak form is the alpha finite element method (αFEM) [8-10]. It is a fascinating and attractive idea to obtain exact solution in the energy norm using numerical method. The αFEM makes the best use of NS-FEM with upper bound property and FEM with lower bound property. The key point in the αFEM is to introduce an α coefficient to establish a continuous function of strain energy that includes the contributions from the FEM and NS-FEM. When $\alpha=0$, the αFEM is exactly the same as FEM, and the strain energy is underestimated. When $\alpha=1$, the αFEM becomes NS-FEM, and the strain energy is overestimated. Using meshes with the same aspect ratio, a unified approach has been proposed to obtain nearly exact solution in strain energy for any given linear elasticity problem. The formulation ensures varitaional consistency and compatibility of the displacement

field, so the αFEM is always spatially and temporally stable. The αFEM is very easy to implement and apply to practical problems of complicated geometry, because existing linear FEM code can largely be utilized.

The third gradient smoothing operation in the weak form is the edge-based smoothed finite element method (ES-FEM) [11, 12]for 2D and face-based finite element method (FS-FEM) [12, 13]for 3D. In the ES-FEM, strain smoothing domains and the integration are operated over the edge-based (2D) and face-based (3D) smoothing domains respectively. The smoothing domain of an edge is created by connecting the nodes at two ends of the edge to centroids of two adjacent elements that can be triangular, quadrilateral, and even *n*-sided polygonal elements. The ES-FEM and FS-FEM are found to have the following excellent properties: (1) a very close-to-exact stiffness: softer than the 'overly-stiff' FEM, but stiffer than the 'overly-soft' NS-FEM, (2) both spatial and temporal stability due to the absence of spurious non-zero-energy modes, (3) easy implementation without additional degrees of freedom, (4) improved accuracy compared to the FEM with the same set of nodes, (5) better computational efficiency.

1.2 Gradient smoothing operation in the strong form

1.2.1 Background of strong form in the numerical technique

Strong form equations are those given in the form of PDEs. In fluid mechanics, the velocity functions are required to have the second order consistency in the entire

problem which is the same as the order of the differentiations in PDEs. Such a requirement on consistency for the velocity functions is strong [1].

Obtaining the exact solution for such a strong form system equation is very hard in practical engineering problems. The finite difference method (FDM) which uses the finite differential representation (Taylor series) of a function in a local domain can be used to solve system equations of a strong form to obtain an approximate solution. In the FDM, the derivative is computed with an approximate difference formula derived from a Taylor series expansion, using single or multiple block structure mesh. The strong form equations are then discretized onto nodes of a set of structure mesh, which result in a system of algebraic equations with a banded matrix of coefficients. There are many numerical techniques available to obtain the solutions for a system of algebraic equations [14]. However, it is very difficult to discretize the boundary conditions with the FDM, especially in the case of arbitrary shaped domains [15]. Although the FDM may be applied to some slightly complicated geometry, issues related to the mapping from physical domain to computational domain complicate the process and usually requires additional and tedious mathematical transformations that can be more expensive than solving the problem itself in numerical implementation [16, 17].

In order to tackle the limitations of the FDM, some meshfree methods based on the strong form have been developed, such as smoothed particle hydrodynamics (SPH) [18, 19], meshfree collocation method [20] and the least squares radial point collocation method (LS-RPCM) [21]. The formulation of meshfree strong form

method is quite straightforward and computationally efficient. However, the solutions to such meshfree strong methods are often not very stable against the model setting and the node irregularity [22]. The accuracy of the result often is dependent on the treatment of boundary conditions, node distribution in the problem domain, and the selection of the nodes for the function approximation. Therefore, special techniques are needed to stabilize the solution [23].

1.2.2 Fundamental theories of gradient smoothing operations in the strong form

Inspired by the attractive features of gradient smoothing operations in the weak form, the gradient smoothing operations in strong form governing equations for fluid problems is proposed [24]. Unlike the Finite Volume Method (FVM) derived from physical conservation laws [25], this method based on gradient smoothing operation in the strong form works only when Partial Differential Equations (PDEs) are available. It is a completely mathematical operation to approximate the spatial derivatives in a weighted integral fashion regardless of its physical meaning. Once the derivatives are obtained, the procedure of gradient smoothing operation in the strong form is as easy as the traditional FDM.

Similar to the gradient smoothing operation in the weak form, triangular elements are primarily used because they can be generated very easily and efficiently. Both regular and irregular elements are used in the development of gradient smoothing operation in the strong form. The original elements created by triangulation are used as

background elements. All the unknown variables are stored at nodes and their derivatives at various locations are consistently and directly approximated with gradient smoothing operation using a set of properly defined gradient smoothing domains. All sorts of gradient smoothing domains are constructed based on these background cells [24].

Different smoothing functions (piecewise constant [24], piecewise linear [26] and alpha [27]) can be used. Obviously, the numerical treatment becomes more sophisticated if the smoothing function is more complicated. In the following section, illustration of these three smoothing function is given.

1.2.3 Brief of various gradient smoothing operations in the strong form

Based on different types of smoothing function, various gradient smoothing operations in the strong form have been formulated. Recently, Liu and Xu [24] have proposed piecewise constant gradient smoothing method (PC-GSM). In the PC-GSM, it adopts the piecewise constant gradient smoothing function to provide a way to approximate the spatial derivatives in a weighted integral fashion. The excellent scheme for the PC-GSM has been successfully formulated and applied for simulating compressible and incompressible flows; the numerical results have demonstrated that the proposed GSM is conservative, conformal, efficient, robust and accurate. The PC-GSM works very well with unstructured triangular mesh, and can be used effectively for adaptive analysis [28].

In order to enhance the accuracy of PC-GSM further, a novel piecewise linear gradient smoothing method (PL-GSM) based on the strong form formulation as an alternative to the generalized finite difference method for solving fluid problems is presented [26] in this thesis. Compared with PC-GSM, the PL-GSM adopts the linearly-weighted smoothing function in the gradient smoothing domain instead of piecewise constant smoothing function. In the PL-GSM， all the unknowns are also stored at nodes and their derivatives at various locations are consistently and directly approximated. Linearly-weighted gradient smoothing technique is utilized to construct first and second order derivative approximations by systematically computing weights for a set of nodal points surrounding an interest node. The flexibility of the PL-GSM allows it to make use of existing meshes that have originally been created for finite difference or finite element methods. The PL-GSM is an excellent alternative to the FVM for CFD problems

The alpha gradient smoothing method (αGSM) which combines the PC-GSM and PL-GSM is another novel formulation [27]. In the αGSM, the smoothing function still selects the linearly-weighted function. However, the contribution at node in the αGSM is $\alpha\frac{1}{V_i}$ ($\frac{1}{V_i}$ is the area of the smoothing domain) instead of zero in the PL-GSM. The α value controls the contribution of the PC-GSM and PL-GSM. If α=1, the formulation between the PC-GSM and the αGSM is identical. If α=0, the smoothing function is constant and the αGSM is the same as PL-GSM.

1.3 Gradient smoothing operations coupling with weak and strong form in Fluid-structure interaction problem

Fluid-structure interaction (FSI) problems have been a hot topic in the past few decades. In the past, research progress in the development of numerical methods for FSI problems has been achieved with the dramatic increase in computer power. Liu et al. [29-31]have applied the Arbitrary Lagrangian Eulerian (ALE) to simulate the complicated motion of fluid-structure interfaces. Among these numerical methods, the process for mesh updating or remeshing is a bottleneck due to high demands on computational cost.

In order to overcome the difficulties in re-meshing process for the moving boundary problems at every time step, many alternative methods have arisen to address this issue. Peskin [32-34] has proposed the immersed boundary (IB) method to analyze blood flow around heart valves. Mohd-Yusof [35] has introduced the hybrid Cartesian/immersed boundary (HCIB) method without coupling effects of fluids to solids. The IB method is an important turning point in the history of numerical methods for FSI problems, which removes the costly mesh updating algorithm and makes a great progress in the FSI solver. In the IB method, the Dirac delta function plays a prominent role to distribute the interaction force or velocity through interpolation. Eulerian meshes for fluids and Lagrangian meshes for solids are employed. The main advantage of IB method is its ability to track the interface of fluid and structure automatically. However, IB method is very difficult to use in the analysis of immersed flexible solids that may occupy volume within the fluid domain

under the assumption of immersed fiber-like elastic structure [36-38]. In addition, the IB is limited to regular boundaries due to the uniform fluid mesh [36-38]. Recently, the immersed finite element method (IFEM) [36-38] has been proposed to eliminate the shortcoming of the IB. The mathematical theory is basically based on the IB, but it absorbs some works on the extended immersed boundary method (EBIM) [39]. With the finite element formulation in both solid and fluid domains, the IFEM can be used to analyze the motion and large deformation of incompressible hyper-elastic material within an incompressible (or slightly compressible) fluid. Moreover, the proposed IFEM adopts the reproducing kernel function to improve the interfacial solutions.

Inspired by the attractive merits of IFEM and gradient smoothing operations in weak and strong form, a novel approach, the immersed gradient smoothing method (IGSM) is proposed [40]. The basic concept in the IGSM is quite similar to the IFEM [36-38]. Unlike the finite element method in the spatial approximation for solid, the edge-based smoothed finite element method (ES-FEM) [11, 12] is applied. For the ES-FEM, the smoothed Galerkin weak form [11, 12] that allows incompatible elements is used to derive the discretized system equations; numerical integration and gradient smoothing operation are applied based on the domains associated with the edges of the triangles.

In the IFEM, the incompressible viscous fluid is solved by the FEM. Various stable and powerful finite element procedures, such as Pressure-stabilized Petrov–Galerkin (PSPG) formulation [41, 42], streamline upwinding / Petrov-Galerkin (SUPG) formulation [43], Galerkin least-square (GLS) [44], bubble function [45], and

characteristic-based split (CBS) algorithm [2, 46] have been proposed to improve numerical stability. Generally, the FEM can lead to the higher accuracy with the same coarse mesh compared with the finite difference method (FDM) and finite volume method (FVM). However, the implementation of FEM is much more complicated than the FVM and FDM, and the computational time for the FEM is relatively costly. Although the FVM is the most popular numerical method in the computational fluid dynamics, it has some shortcomings, for example, false diffusion often occurs in the numerical solutions using FVM [47], and high order accuracy of solutions is very difficult to obtain [48]. In order to balance accuracy and computational cost, the piecewise linear gradient smoothing operation has been applied to strong form governing equations in the fluid dynamics [26]. Hence, the PL-GSM is employed to discretize the fluid domain because it can achieve second order accuracy in the spatial approximation and computational efficient [26].

1.4 Objectives and significance of the study

This thesis focuses on the development of gradient smoothing operations in the weak and strong form to overcome the shortcomings of the FEM, FVM and FDM, and combines the gradient smoothing operation in the weak and strong form to solve the Fluid-structure interaction problem. Some applications in the modeling of biological systems are presented. Major works reported in this thesis are as follow:

1. Application of alpha finite element method, edge-based smoothed finite element (ES-FEM) and face-based smoothed finite element method (FS-FEM) based on

the weak form to establish some biological models including the phase change in liver cryosurgery, bioheat transfer in the human eye and thermal-mechanical behavior of human breast in hyperthermia treatment.

2. Development of piecewise linear gradient smoothing method (PL-GSM) based on the strong form to solve fluid dynamics problem, and its application to study the shear stress in the Abdominal Aortic Aneurysm.
3. Development of alpha gradient smoothing method (αGSM) based on the strong form in the fluid dynamics and application this method to analyze the diseased artery of stenosis.
4. Coupling of the gradient smoothing operation in the weak and strong form to develop the Immersed gradient smoothing method (IGSM) for the analysis of Fluid-structure interaction (FSI) problems.

These works will be thoroughly discussed in the following chapters.

1.5 Organization of the thesis

The thesis consists of seven chapters and is summarized as follow:

In Chapter 1, the background of FEM, FDM and FVM are briefly presented. In addition, the basic concepts of gradient smoothing operations in the weak and strong forms and coupling with weak and strong forms in Fluid-structure interaction problem are presented.

In Chapter 2, the application of edge-based smoothed finite element method (ES-FEM) in 2D and face-based smoothed finite element method (FS-FEM) in 3D to

analyze thermal-mechanical behaviour in hyperthermia treatment of human breast is given.

In Chapter 3, the applications of the alpha finite element method (αFEM) to solve the phase change problems in the liver cryosurgery and bioheat transfer in the human eye are presented. In the liver cryosurgery simulation, a fixed grid method using the alpha finite element (αFEM) formulation is presented to simulate phase transformation and temperature field during the cryosurgery process. Other than that, computational modeling of the human eye using the αFEM to detect eye abnormalities and predict the temperature distribution in the hyperthermia treatments is also presented in this Chapter.

In Chapter 4, the theory of piecewise linear gradient smoothing method (PL-GSM) is presented in detail. The PL-GSM has been tested on the Possion Equation; the computational efficiency, accuracy, and stability have been compared with the piecewise constant gradient smoothing method (PC-GSM). Furthermore, the PL-GSM has been tested by some benchmark examples in the fluid dynamics. Finally, the PL-GSM is applied to study the wall shear stress in the Abdominal Aortic Aneurysm.

In Chapter 5, the alpha gradient smoothing method (GSM) is formulated. The main difference among the piecewise constant gradient smoothing method (PC-GSM), piecewise linear gradient smoothing method (PL-GSM) and αGSM is the selection of smoothing function. In the αGSM, the α value controls the contribution of PC-GSM and PL-GSM. The accuracy and computational time of αGSM, PC-GSM and PL-GSM have been compared by Possion Equation. In addition, the proposed αGSM

has been tested on one benchmark example. Finally, the αGSM has been applied to analyze the flow characteristic in diseased arteries.

In Chapter 6, the gradient smoothing operations in weak and strong form is combined to develop the immersed gradient smoothing method (IGSM) to solve the Fluid-structure interaction (FSI) problems. In the IGSM, the structural model is created by the ES-FEM; and PL-GSM is adopted to construct the fluid domain. Two numerical examples including a falling disk and aortic valve are solved to test the validity of the IGSM.

In Chapter 7, the conclusion and some recommendations for possible future research are presented.

Chapter 2

Edge-based Smoothed Finite Element Method for Thermal-mechanical Problem in the Hyperthermia Treatment of Breast

2.1 Introduction of hyperthermia treatment in the human breast

The modeling of heat transfer in the human body is very important for the hyperthermia treatment of tumors. The success of such treatment is strongly dependent on accurate prediction of the temperature distribution. Thus, understanding heat transfer in the human body is essential to improve such medical treatments. Currently, there are many models available to analyze the bioheat transfer in the living tissue [49]. However, almost all models are based on Pennes' bioheat equation. The main advantage for Pennes' model is that only one parameter (perfusion rate) is needed to simulate the blood flow in the tissue.

Recently, hyperthermia treatment has been demonstrated to be effective and has less side effects in some cancer treatment. Tang et al [50] has developed a numerical method to simulate the temperature distribution in a three-layered skin structure. These results are useful for skin and breast cancer treatment. He et al. [51] developed a two-dimensional finite element model to analyze the blood flow, temperature and oxygen transport in human breast tumor. The main objective of hyperthermia treatment

is to raise the surface temperature of the tumor to above 42^{o}C without damaging healthy tissue [52-54]. The main challenge of hyperthermia treatment is to minimize damage to surrounding tissue. During hyperthermia treatment, it is crucial to control the amount of energy in order to kill the tumor. Thus, it is very important to obtain the entire temperature distribution in the whole domain accurately. Although there are several analytical attempts that have been made to solve the Pennes' bioheat equation with very simple geometry [55], it is very hard to obtain the analytical solution for most of bioheat transfer problems. During the past several decades, there have been many numerical methods proposed to solve the bioheat transfer problems in living tissues. Finite difference method (FDM) [56-58] and finite element method (FEM) [59] are the well-known numerical methods for solving Pennes' bioheat problems. The FDM is very efficient, but applicable only for very simple geometry. Due to this reason, FEM has been proposed to solve to the mechanics problems since 1960's and has achieved remarkable progress [60-62]. The strength of FEM is that it can handle complicated geometries. However, there are some major issues related to the FEM, such as 'overly-stiff' phenomenon of a fully compatible FEM model and the rigid reliance on elements.

In recent years, various meshfree methods have been developed [1, 22, 63]. Compared with FEM, numerical treatments in meshfree methods are not confined by the elements/cells. Thus, meshfree methods can produce more accurate solution, are more flexible in implementation, have higher convergence rate, and are more effective. In this Chapter, the edge-based smoothing finite element (ES-FEM) [11] for 2D

problems with the strain smoothing performed over the edge-based smoothing domain, and the face-based smoothed finite element method (FS-FEM) [13]for 3D problems with the strain smoothing performed over the face-based smoothing domain are proposed to establish the thermo-mechanical model to analyze thermo-mechanical interaction when the human breast is undergoing hyperthermia treatment. Compared with the FEM models, the ES-FEM (or FS-FEM) often gives close-to-exact stiffness and the solutions are much more accurate and stable both spatially and temporally. In the ES-FEM, strain smoothing domains and the integration are operated over the edge-based (2D) and face-based (3D) smoothing domains respectively.

This Chapter is organized as follows: Section 2.2 shows a simple description of the Pennes' bioheat thermal model. Section 2.3 gives the detail formulation of ES-FEM and FS-FEM for 2D and 3D problems. Section 2.4 compares the numerical results in breast hyperthermia treatment between FEM and ES-FEM.

2.2 Briefing on Pennes' bioheat model

Heat transfer in living tissues involves two mechanisms: blood perfusion and metabolism [64]. Both these heat sources regulate temperature distribution in the human body. Many models have been developed to describe the thermal transport mechanism. The most popular and earliest model developed by Pennes has achieved remarkable progress in analyzing bioheat transfer in the human tissue. As suggested by Pennes, the thermal energy balance for perfused tissue can be written as [64]:

$$\rho c \frac{\partial T}{\partial t} = \nabla(k \nabla T) + Q_b + Q_r + Q_m \qquad 2.1$$

The tissue property of breast is listed in the Table 2.1. In the Pennes' model, the main assumption is that the net heat transfer rate between blood and tissue is proportional to the product of the volumetric perfusion rate and the difference between the arterial blood temperature and the local tissue temperature [64]. The blood acts as a locally distributed scalar source when positive, or sink when negative. Hence, the term Q_b can be expressed as

$$Q_b = c_b \omega_b (T_b - T) \tag{2.2}$$

It is also commonly assumed that the blood enters the tissue at a temperature T_b and immediately comes to the thermal equilibrium with the surrounding tissue. The convective term which could give directional property of blood heat source does not include in the Pennes' model.

Another assumption in the Pennes' model is that the arterial blood temperature T_b is kept unchanged through the tissue, and the tissue temperature is assumed to be the same as the vein temperature.

Substituting Eq. (2.2) into Eq. (2.1), the Pennes' bioheat equation can be written as

$$\rho c \frac{\partial T}{\partial t} = \nabla (k \nabla T) + \omega_b c_b (T_b - T) + Q_r + Q_m \tag{2.3}$$

The Dirichlet, Neumann and Robin boundary conditions on Γ_1, Γ_2, and Γ_3 can be described as follows:

$$T = T_\Gamma \qquad \Gamma_1 \qquad \text{Dirichlet boundary} \tag{2.4}$$

$$-n_1 k_1 \frac{\partial T}{\partial x} - n_2 k_2 \frac{\partial T}{\partial y} - n_3 k_3 \frac{\partial T}{\partial z} = q_\Gamma \qquad \Gamma_2 \qquad \text{Neumann boundary} \tag{2.5}$$

$$-n_1 k_1 \frac{\partial T}{\partial x} - n_2 k_2 \frac{\partial T}{\partial y} - n_3 k_3 \frac{\partial T}{\partial z} = h(T - T_a) \qquad \Gamma_3 \qquad \text{Robin boundary} \tag{2.6}$$

2.3 Formulation of the ES-FEM and FS-FEM

In this section, the formulations of ES-FEM for 2D and FS-FEM for 3D problems using triangular and tetrahedral elements are presented. Because the procedure of ES-FEM is similar to FEM, the formulation of FEM based on the standard Galerkin weak form [2] is firstly introduced.

2.3.1 Discretized System Equations

The weighted residual equation can be expressed by multiplying the governing equation (2.1) with a test function w in the entire domain.

$$\begin{aligned}\int_\Omega w\cdot\rho c T_t d\Omega = \int_\Omega w\cdot k\nabla^2 T d\Omega + \int_\Omega w\cdot\omega_b c_b(T_b - T)d\Omega \\ + \int_\Omega w\cdot Q_r d\Omega + \int_\Omega w\cdot Q_m d\Omega\end{aligned} \tag{2.7}$$

Using integration by parts:

$$\begin{aligned}&\rho c\int_\Omega w T_t d\Omega + k\int_\Omega \nabla w\cdot\nabla T d\Omega + \omega_b c_b\int_\Omega w T d\Omega = \\ &(\omega_b c_b T_b + Q_m + Q_r)\int_\Omega w d\Omega - \int_{\Gamma_2} w q_\Gamma \mathrm{d}\Gamma - \int_{\Gamma_3} w h(T - T_a)\mathrm{d}\Gamma\end{aligned} \tag{2.8}$$

The field temperature can be approximated in the following form;

$$T = \sum_{i=1}^{m} \mathbf{N}_i \mathbf{T}_i \tag{2.9}$$

where $\mathbf{N}_i$ is the shape function, and $\mathbf{T}_i$ is the unknown nodal temperature. In the Galerkin weak form, the weight function w is replaced by shape function $\mathbf{N}$, and the standard Galerkin weak form is expressed as:

$$\begin{aligned}&\rho c\int_\Omega \mathbf{N}\mathbf{T}_t d\Omega + k\int_\Omega \nabla\mathbf{N}\cdot\nabla\mathbf{T} d\Omega + \omega_b c_b\int_\Omega \mathbf{N}\cdot\mathbf{N}\mathbf{T} d\Omega = \\ &(\omega_b c_b T_b + Q_m + Q_r)\int_\Omega \mathbf{N} d\Omega - \int_{\Gamma_2} \mathbf{N} q_\Gamma \mathrm{d}\Gamma - h\int_{\Gamma_3} \mathbf{N}\cdot\mathbf{N}\mathbf{T} d\Gamma + h\int_{\Gamma_3} \mathbf{N} T_a \mathrm{d}\Gamma\end{aligned} \tag{2.10}$$

In the ES-FEM, the gradient component is replaced by the smoothed item by introducing the gradient smoothing technique. Therefore, the smoothed Galerkin weak form for Pennes' bioheat equation can be formulated [63].

$$\begin{aligned}&\rho c\int_{\Omega}\mathbf{N}\mathbf{T}_t d\Omega + k\int_{\Omega}\overline{\nabla\mathbf{N}}\cdot\overline{\nabla\mathbf{N}}\mathbf{T}d\Omega + \omega_b c_b\int_{\Omega}\mathbf{N}\cdot\mathbf{N}\mathbf{T}d\Omega = \\ &(\omega_b c_b T_b + Q_m + Q_r)\int_{\Omega}\mathbf{N}d\Omega - \int_{\Gamma_2}\mathbf{N}q_{\Gamma}\,\mathrm{d}\Gamma - h\int_{\Gamma_3}\mathbf{N}\cdot\mathbf{N}\mathbf{T}d\Gamma + h\int_{\Gamma_3}\mathbf{N}T_a d\Gamma\end{aligned} \tag{2.11}$$

The discretized system equation can be finally obtained and written in the following matrix form:

$$\left[\mathbf{M}\right]\left\{\dot{\mathbf{T}}\right\}^t + \left[\overline{\mathbf{K}} + \mathbf{C}\right]\left\{\mathbf{T}\right\}^t = \left\{\mathbf{F}\right\}^t \tag{2.12}$$

Therefore, the smoothed Galerkin weak form for Pennes' bioheat equation can be formulated.

$$\overline{\mathbf{K}} = k\int_{\Omega}\overline{\nabla\mathbf{N}}\cdot\overline{\nabla\mathbf{N}}d\Omega \quad \text{The stiffness matrix} \tag{2.13}$$

$$\mathbf{M} = \rho c\int_{\Omega}\mathbf{N}\cdot\mathbf{N}d\Omega \quad \text{The mass matrix} \tag{2.14}$$

$$\mathbf{C} = \omega_b c_b\int_{\Omega}\mathbf{N}\cdot\mathbf{N}\mathrm{d}\Omega + h\int_{\Gamma_3}\mathbf{N}\cdot\mathbf{N}\mathrm{d}\Gamma \quad \text{The equivalent damping matrix} \tag{2.15}$$

$$\mathbf{F} = (\omega_b c_b T_b + Q_m + Q_r)\int_{\Omega}\mathbf{N}d\Omega + h\int_{\Gamma_3}\mathbf{N}T_a\,\mathrm{d}\Gamma - \int_{\Gamma_2}\mathbf{N}q_{\Gamma}\,\mathrm{d}\Gamma \quad \text{The force matrix} \tag{2.16}$$

There are many techniques to solve the first-order time dependent problems, such as forward difference method, backward difference method, Crank-Nicholson method, etc. The following section is to develop finite element time stepping.

Discrete the temperature in time using standard finite element procedure:

$$\mathbf{T} = \sum\mathbf{N}_i(t)\mathbf{T}^i \tag{2.17}$$

The shape functions are given by:

$$\left.\begin{array}{l} N_n = 1-\xi \qquad N_{n+1} = \xi \\ \xi = \dfrac{t}{\Delta t} \end{array}\right\} \quad (0 \le \xi \le 1) \tag{2.18}$$

Take the derivative of shape function

$$\dot{N}_n = \frac{-1}{\Delta t} \qquad \dot{N}_{n+1} = \frac{1}{\Delta t} \tag{2.19}$$

Multiplying the governing Eq. (2.12) with a test function w gives

$$\int_0^1 w[\mathbf{M}(\dot{N}_n \mathbf{T}^n + \dot{N}_{n+1}\mathbf{T}^{n+1}) + \overline{\mathbf{K}}(N_n \mathbf{T}^n + N_{n+1}\mathbf{T}^{n+1}) - \mathbf{F}]d\varepsilon = 0 \tag{2.20}$$

Substituting Eq. (2.18) and (2.19) into equation Eq. (2.20) gives

$$(\overline{\mathbf{K}}\int_0^1 w\xi d\xi + \mathbf{M}\int_0^1 w\frac{d\xi}{\Delta t}d\xi)\mathbf{T}^{n+1} + (\overline{\mathbf{K}}\int_0^1 w(1-\xi)d\xi - \mathbf{M}\int_0^1 w\frac{d\xi}{\Delta t}d\xi)\mathbf{T}^n - \int_0^1 w\mathbf{F}d\xi = 0 \tag{2.21}$$

Eq. (2.21) is arranged to become

$$(\frac{\mathbf{M}}{\Delta t} + \overline{\mathbf{K}}\theta)\mathbf{T}^{n+1} = (\frac{\mathbf{M}}{\Delta t} - \overline{\mathbf{K}}(1-\theta))\mathbf{T}^n + \hat{\mathbf{F}} \tag{2.22}$$

where

$$\theta = \frac{\int_0^1 w\xi d\xi}{\int_0^1 w d\xi} \qquad \text{and} \qquad \hat{\mathbf{F}} = \frac{\int_0^1 w\mathbf{F}d\xi}{\int_0^1 w d\xi} \tag{2.23}$$

$$\hat{\mathbf{F}} = \theta\mathbf{F}^n + (1-\theta)\mathbf{F}^{n+1} \tag{2.24}$$

The value of θ is determined by the weight function w. Fig. 2.1 illustrates how θ changes with different weight functions.

From the whole procedure, it is very clear that the formulations of FEM and ES-FEM are almost the same. The main difference is the integration procedure to obtain the stiffness matrix of Eq. (2.13).

After obtaining the nodal temperature from solving Eq. (2.22), the thermal strain induced by the variation in temperature becomes the initial strain $\boldsymbol{\varepsilon}_0$:

$$\boldsymbol{\varepsilon}_0 = \{\alpha_x \Delta T \quad \alpha_x \Delta T \quad 0\} \qquad \text{2D problem} \qquad 2.25$$

$$\boldsymbol{\varepsilon}_0 = \{\alpha_x \Delta T \quad \alpha_y \Delta T \quad \alpha_z \Delta T \quad 0 \quad 0 \quad 0\}^{\mathrm{T}} \qquad \text{3D problem} \qquad 2.26$$

where α_i (i=x, y, z) is the thermal expansion coefficient in the ith direction. The relation between the thermal stress and strain can be expressed as

$$\bar{\boldsymbol{\sigma}} = \mathbf{D}(\bar{\boldsymbol{\varepsilon}} - \boldsymbol{\varepsilon}_0) \qquad 2.27$$

where $\bar{\boldsymbol{\sigma}}$ and $\bar{\boldsymbol{\varepsilon}}$ are smoothed stresses and strains, respectively, and $\mathbf{D}$ is the matrix of material constants for isotropic materials including only Poisson's ratio v and Young's modulus E:

$$\mathbf{D} = \frac{E}{1-v^2}\begin{bmatrix} 1 & v & 0 \\ v & 1 & 0 \\ 0 & 0 & \dfrac{1-v}{2} \end{bmatrix} \qquad \text{for 2D problem} \qquad 2.28$$

For 3D problem

$$\mathbf{D} = \frac{E}{2(1+v)(1-2v)}\begin{bmatrix} 2(1-v) & 2v & 2v & 0 & 0 & 0 \\ 2v & 2(1-v) & 2v & 0 & 0 & 0 \\ 2v & 2v & 2(1-v) & 0 & 0 & 0 \\ 0 & 0 & 0 & 1-2v & 0 & 0 \\ 0 & 0 & 0 & 0 & 1-2v & 0 \\ 0 & 0 & 0 & 0 & 0 & 1-2v \end{bmatrix} \qquad 2.29$$

In the standard weak formulation, the potential (strain) energy of the thermo-mechanical model is expressed in the following form:

$$\Pi(\mathbf{u}) = \frac{1}{2}\int_{\Omega} \boldsymbol{\varepsilon}^{\mathrm{T}}\mathbf{D}\boldsymbol{\varepsilon}\,\mathrm{d}\Omega - \int_{\Omega} \boldsymbol{\varepsilon}^{\mathrm{T}}\mathbf{D}\boldsymbol{\varepsilon}_0\,\mathrm{d}\Omega \tag{2.30}$$

where the strains are the compatible strains obtained using the (linear) kinematics relation of the strains and the displacements. The variational form is given by:

$$\delta\Pi(\mathbf{u}) = \int_{\Omega} (\delta\boldsymbol{\varepsilon})^{\mathrm{T}}\mathbf{D}\boldsymbol{\varepsilon}\,\mathrm{d}\Omega - \int_{\Omega} (\delta\boldsymbol{\varepsilon})^{\mathrm{T}}\mathbf{D}\boldsymbol{\varepsilon}_0\,\mathrm{d}\Omega - \int_{\Gamma_t} (\delta\mathbf{u})^{\mathrm{T}} t_{\Gamma}\,\mathrm{d}\Gamma = 0 \tag{2.31}$$

In the formulation, the compatible strain $\boldsymbol{\varepsilon}$ in Eq. (2.31) is replaced by the smoothed strain $\bar{\boldsymbol{\varepsilon}}$ that satisfies the generalized (smoothed) Galerkin weak form derived from the Hellinger-Reissner's two-field variational principle. The smoothed Galerkin weak form for our thermomechanical problems can be formulated as:

$$\delta\Pi(\mathbf{u}) = \int_{\Omega} (\delta\bar{\boldsymbol{\varepsilon}})^{\mathrm{T}}\mathbf{D}\bar{\boldsymbol{\varepsilon}}\,\mathrm{d}\Omega - \int_{\Omega} (\delta\bar{\boldsymbol{\varepsilon}})^{\mathrm{T}}\mathbf{D}\boldsymbol{\varepsilon}_0\,\mathrm{d}\Omega - \int_{\Gamma_t} (\delta\mathbf{u})^{\mathrm{T}} t_{\Gamma}\,\mathrm{d}\Gamma = 0 \tag{2.32}$$

The above discretized system equations for thermomechanical problems can be expressed in the following matrix form.

$$[\bar{\mathbf{K}}^{u}]\{\mathbf{d}\} = \{\bar{\mathbf{F}}\} \tag{2.33}$$

where

$$\bar{\mathbf{K}}^{u}_{IJ} = \int_{\Omega} \bar{\mathbf{B}}_I^{\mathrm{T}}\mathbf{D}\bar{\mathbf{B}}_J\,\mathrm{d}\Omega \tag{2.34}$$

$$\bar{\mathbf{F}}_I = \int_{\Gamma_t} \boldsymbol{\Phi}_I^{\mathrm{T}} t_{\Gamma}\,\mathrm{d}\Gamma + \int_{\Omega} \bar{\mathbf{B}}_I^{\mathrm{T}}\mathbf{D}\boldsymbol{\varepsilon}_0\,\mathrm{d}\Omega \tag{2.35}$$

in which $\bar{\mathbf{B}}$ is the smoothed strain matrix obtained through the gradient smoothing operation, and the superscript *u* represents the stiffness matrix associated with the displacement field of a given discretization. To obtain the smoothed stiffness matrix of thermo-mechanical system, the edge integration scheme with edge-based gradient smoothing technique will be used to perform the domain integration, which will be discussed in the following Section. The next section will illustrate how to perform the

integration process based on the smoothing domains associated with the edges of the triangles in 2D or surfaces of tetrahedrons in 3D.

2.3.2 Numerical integration with edge-based gradient smoothing operation

This section formulates the gradient smoothing domains of ES-FEM for 2D and 3D problems using triangular elements and tetrahedral elements, respectively. The formulation is almost the same for any other 2D and 3D *n*-side polygonal elements as long as the simple point interpolation method is used to create the shape functions [22]. In the numerical integration of ES-FEM for 2D problems, a mesh of 3-node triangles is generated first, which can be done easily and automatically using any mesh generator. Afterwards, the problem domain Ω is further divided into N smoothing domains associated with edges of the triangles such that $\Omega_1 \cup \Omega_2 \cup \ldots \Omega_N = \Omega$ and $\Omega_i \cap \Omega_j = \emptyset$, $i \neq j$, where N is the number of total edges of triangles. As shown in Figure 2.2(a), the smoothing domain Ω_k for edge k is created by connecting sequentially the end-points of edge k to the centroids of the neighbor triangles. Extending the smoothing domain Ω_k in 3D problems, the domain discretization is the same as that of standard FEM using tetrahedral elements and the smoothing domain is associated with the faces of tetrahedrons. As shown in Fig. 2.2(b), the smoothing domain Ω_k for face k is created using the neighboring tetrahedral elements by connecting the vertices of the triangle (face k) to the centroids of two adjacent elements.

The boundary of the smoothing domain Ω_k of edge k (or face k) is labeled as Γ_k and the union of all Ω_k forms the global domain Ω exactly. To perform the numerical integration based on the smoothing domains, Eq. (2.13) can be further rewritten as:

$$\overline{\mathbf{K}} = \sum_{k=1}^{N} \overline{\mathbf{K}}^{(k)} \tag{2.36}$$

in which

$$\overline{\mathbf{K}}^{(k)} = k \int_{\Omega_k} \overline{\mathbf{B}}^{\mathrm{T}} \overline{\mathbf{B}} \mathrm{d}\Omega \tag{2.37}$$

The generalized gradient smoothing technique that works also for discontinuous field functions [65] is now applied over the smoothing domain to obtain the smoothed nodal gradient for the node of interest $\mathbf{x}_k$

$$\overline{g}_i(\mathbf{x}_k) = \int_{\Omega_k} g_i(\mathbf{x}) \overline{W}(\mathbf{x} - \mathbf{x}_k) \mathrm{d}\Omega \tag{2.38}$$

where g_i is the derivative of the field function (temperature) with respect to x_i, and W is a smoothing function. For simplicity, a piecewise constant function is used.

$$\overline{\mathrm{W}}(\mathbf{x} - \mathbf{x}_k) = \begin{cases} 1/V_k & \mathbf{x} \in \Omega_k \\ 0 & \mathbf{x} \notin \Omega_k \end{cases} \tag{2.39}$$

where $V_k = \int_{\Omega_k} \mathrm{d}\Omega$ is the area of smoothing domain for edge k in 2D problems. When it comes to 3D problems, the V_k is the volume of smoothing domain for face k.

The temperature gradient for node k and for any point in the smoothing domain is obtained as follows even for discontinuous functions of temperature [65]:

$$\overline{g}_i(\mathbf{x}_k) = \frac{1}{V_k} \int_{\Gamma_k} T n_i \mathrm{d}\Gamma \tag{2.40}$$

which is constant in the smoothing domain Ω_k. Using FEM shape functions to construct the field function for temperature, the smoothed gradient for node k can be written in the following matrix form

$$\overline{\mathbf{g}}(\mathbf{x}_k) = \sum_{I \in D_k} \overline{\mathbf{B}}_I^{\Omega_k} \mathbf{T}_I \tag{2.41}$$

where D_k is the set of all the nodes used in the interpolation for the field function on Ω_k.

$$\bar{\mathbf{g}}^{\mathrm{T}} = \{\bar{g}_1 \quad \bar{g}_2\} \tag{2.42}$$

$$\left[\bar{\mathbf{B}}_I^{\Omega_k}\right]^T = \left[\bar{b}_{I1} \quad \bar{b}_{I2}\right] \tag{2.43}$$

$$\bar{b}_{Ip} = \frac{1}{A_k}\int_{\Gamma_k} \mathbf{N}_I(\mathbf{x}) n_p(\mathbf{x}) \mathrm{d}\Gamma \qquad (p=1, 2) \tag{2.44}$$

For three dimensional spaces, the corresponding forms are given by

$$\bar{\mathbf{g}}^{\mathrm{T}} = \{\bar{g}_1 \quad \bar{g}_2 \quad \bar{g}_3\} \tag{2.45}$$

$$\left[\bar{\mathbf{B}}_I^{\Omega_k}\right]^T = [\ \bar{b}_{I1} \quad \bar{b}_{I2} \quad \bar{b}_{I3}] \tag{2.46}$$

$$\bar{b}_{Ip} = \frac{1}{V_k}\int_{\Gamma_k} \mathbf{N}_I(\mathbf{x}) n_p(\mathbf{x}) \mathrm{d}\Gamma \qquad (p=1, 2, 3) \tag{2.47}$$

where $\mathbf{N}_I(\mathbf{x})$ is the shape function for node *I*.

Using Gauss integration along each segment (or each surface triangle for 3D) of boundary Γ_k of the smoothing domain Ω_k, the above equations can be rewritten in the following summation form as

$$\bar{b}_{ip} = \frac{1}{A_k}\sum_{q=1}^{N_s}\left[\sum_{r=1}^{N_g} w_r \mathbf{N}_i(\mathbf{x}_{qr}) n_p(\mathbf{x}_q)\right] \tag{2.48}$$

where N_s is the number of segments (or each surface triangle for 3D) of the boundary Γ_k, N_g is the number of Gauss points distributed in each segment(or each surface triangle), and w_r is the corresponding weight for the Gauss point. The smoothed stiffness matrix shown in Eq. (2.13) can be calculated as:

$$\bar{\mathbf{K}}^{(k)} = k\int_{\Omega} \bar{\mathbf{B}}^{\mathrm{T}}\bar{\mathbf{B}}\mathrm{d}\Omega = k\bar{\mathbf{B}}^{\mathrm{T}}\bar{\mathbf{B}}A_k \tag{2.49}$$

It can be easily seen from Eq. (2.49) that the resultant linear system is symmetric and banded (due to the compact supports of FEM shape functions), which implies that the system equations can be solved efficiently.

2.4 Numerical example

Breast cancer is one of the most prevalent types of cancer. Computer modeling has become a powerful tool to analyze bioheat transfer in the breast tumor treatment [66-68]. The low-risk of breast cancer can be treated by applying heat therapy on the targeted tumor to cure the cancer. Hyperthermia is often used in clinical applications in breast tumor control by artificially raising the tissue temperature to gain therapeutic benefits. In the hyperthermia treatment, the heat source is localized to the targeted area to elevate the temperature to cause the death of cancerous cell [69]. The heat source can be microwave, radiofrequency and ultrasound. In order to simplify the problem, the detail of heat source is ignored. Thus, the knowledge of the temperature distribution and heat transport rates is important in hyperthermia treatments. The goal of this study is to evaluate the potential to apply the ES-FEM and FS-FEM to become a viable method for breast cancer treatment. Two examples including 2D and 3D for breast hyperthermia treatment are presented in this section. In the simulation, we investigate the temperature distribution first, and the consequent effect of thermal stress.

2.4.1 Hyperthermia treatment in 2D breast tumor

The 2D breast model is shown in Fig. 2.3. The internal heat source is uniformly distributed at a small tumor with r=6mm (center of tumor：$x = -0.0138m,\ y = 0.0071m$). The initial condition is $T(x, y, 0) = 37^{\circ}$ and the boundary condition can be described as:

(1) Along the boundary Γ_1 as shown in Fig. 2.3, assuming there is no heat flux in and out:

$$k\frac{\partial T}{\partial n}=0 \tag{2.50}$$

(2) Along the boundary Γ_{23} as shown in Fig. 2.3:

$$-k\frac{\partial T}{\partial n}=h(T-T_f) \quad \text{where } T_f=25^{\circ}\text{C},\ h=10\ \text{W/m}^2,\ k=0.5\ \text{W/(m}^{\circ}C) \tag{2.51}$$

where h is the convetion coefficient, T_f is the temperature of cooling mdium.

2.4.1.1 Stability analysis with different time integration

Stability is an important attribute in the numerical analysis. In the section 2.3, a clear explanation for different time integration in bioheat transfer is given. The value of θ acts as a knob which controls the method of time stepping algorithm. The external of heat source Q_r is expressed as follows:

$$Q_r=\begin{cases}\left(2\times10^5\right)t & 0\le t\le 5s\\ 1\times10^6 & t>5s\end{cases} \tag{2.52}$$

In general, the method to check stability is to consider the test problem in the complex domain.

$$\dot{x}=\eta x \qquad \eta=a+bi; \tag{2.53}$$

The exact solution is

$$x(t)=\exp(\eta t)=\exp(at)\left[\cos(bt)+i\sin(bt)\right] \tag{2.54}$$

In the forward difference method ($\theta=0$)

$$x_{i+1}=x_i+p\eta x_i \qquad \Rightarrow \qquad \rho^{i+1}=(1+p\eta)\rho^i \qquad \rho=1+p\eta \tag{2.55}$$

The solution is stable if the complex modulus of ρ is less or equal than 1

$$\left|1+p\eta\right|\le 1 \tag{2.56}$$

The region of absolute stability in the forward difference method is the shaded area as shown in Fig. 2.4(a). Thus, the forward difference method is conditionally stable [70],which implies that numerical results diverge for a certain time step for both FEM and ES-FEM model.

In the backward difference method ($\theta=1$)

$$x_{i+1}=x_i+p\eta x_{i+1} \qquad \Rightarrow \qquad \rho^{i+1}=\left(1-p\eta\right)^{-1}\rho^i \qquad \rho=\frac{1}{1-p\eta} \tag{2.57}$$

The solution is stable if the complex modulus of ρ is large or equal than 1.

$$\left|1-p\eta\right|\ge 1 \tag{2.58}$$

Thus, at the entire left part of the $p\eta$ plane, the solution for backward difference is unconditionally stable as shown in Fig. 2.4(b). This conclusion is still applicable to ES-FEM formulation. As outlined in Fig. 2.5(a), it is obviously found that the temperature at the center of heat source obtained from ES-FEM formulation is still stable even for very large time step t=10s.

In the central difference method ($\theta=\frac{1}{2}$)

$$x_{i+1}=x_i+\frac{p\eta}{2}\left(x_{i+1}+x_i\right) \qquad \rho^{i+1}=\rho^i+\frac{p\eta}{2}\left(\rho^i+\rho^{i+1}\right) \qquad \Rightarrow \rho=\frac{1+\frac{1}{2}p\eta}{1-\frac{1}{2}p\eta} \tag{2.59}$$

Let $\rho=a+bi \qquad a\le 0$

$$\frac{\left(1+\frac{1}{2}a\right)^2+b^2}{\left(1-\frac{1}{2}a\right)^2+b^2}\le 1 \quad \Rightarrow \quad \left|\frac{1+\frac{1}{2}\left(a+bi\right)}{1-\frac{1}{2}\left(a+bi\right)}\right|\le 1 \quad \Rightarrow \quad \rho\le 1 \tag{2.60}$$

Thus, the central difference is absolutely stable in the entire of left plan as shown in Figure 2.4(c). It is noted that the backward and forward difference methods provide only a first order accuracy [70]. Although the center difference method ($\theta = \frac{1}{2}$) has second order accuracy, it exhibits some oscillation for certain time steps in the FEM formulation [70]. This phenomenon is still observed in the ES-FEM formulation. As shown in Fig. 2. 5(b), the temperature at the center of heat source obtained from ES-FEM begins to oscillate using time step t=0.5s although the numerical results converge.

In order to obtain stable and accurate results, the backward difference is adopted to discretize the Eq. (2.12) in both FEM and ES-FEM (or FS-FEM).

2.4.1.2 Temperature distribution

The temperature distribution at the whole domain at $t = 10s$ is computed and plotted in Fig. 2.6 using the ES-FEM, FEM model and the reference result. The external heat source is expressed as follows:

$$Q_r = \begin{cases} \left(1.667 \times 10^5\right) t & 0 \le t \le 3s \\ 5 \times 10^5 & t > 3s \end{cases} \qquad 2.61$$

It is observed that ES-FEM gives more accurate results than those of FEM using the same 3-node triangular mesh and linear shape functions at the heating source location. It is also found that the tissue temperature around the heating source is well below 37°, which has a great benefit in hyperthermia treatment because the temperature of health tissue is below the safe threshold. This is one of the most attractive features why internal heating is frequently used to thermally kill tumors in the deep tissue, although it

may cause some mechanical injuries [69]. As shown in Fig. 2.6, the highest temperature always occurs at the heating source in ES-FEM, FEM and reference solutions. Thus, it is necessary to investigate the maximum temperature variation with the time at the heating source.

The maximum temperature history at the center of heating source using ES-FEM and FEM is depicted in Fig. 2.7 together with the reference results. It is observed that the solution from ES-FEM is much closer to the reference results compared with FEM model. More than two degree error in the FEM model is observed, which may cause the operation unsuccessfully in the treatment. On the other hand, the computational cost for reference model is quite high. Thus, ES-FEM model provides a much better way in the simulation in terms of accuracy and computational cost. This again demonstrates the ES-FEM is much more accurate than the FEM due to the 'soften' property.

Figure 2.8 presents the temperature distribution along circumference of the tumor in counterclockwise direction starting from the left horizontal using FEM, ES-FEM with 133 nodes, together with the reference using 3546 nodes. It is easily found that the solution obtained from ES-FEM agrees very well the reference one compared with the FEM model. However, there is a large deviation between the FEM and reference. This validates our two-dimensional ES-FEM model for heat transfer problems again.

2.4.1.3 Thermal deformation

After the temperature field is obtained, the stress resulted from the thermal expansion can be obtained based on Eq. (2.25). It is noted the there is zero displacement along

$y = 0$. The ES-FEM is then used again to compute the deformational of breast due to the thermal loads. The modeling of mechanical stress due to external heat source is useful to develop the biological technology in the design of hyperthermia equipment. Figure 2.9, 2.10 and 2.11 show the normal stress in x and y direction, and the shear stress at the center of heating source obtained from both ES-FEM and FEM, together with the reference one obtained using irregularly distributed 3546 nodes respectively. It can be observed that the present results from ES-FEM are in a better agreement with the reference solution compared to those of the FEM when the same mesh is used. This shows the effectiveness of the ES-FEM formulation for this 2D thermo-elastic problem.

2.4.2 Hyperthermia treatment in 3D breast tumor

The simulation of 3D model is much more important to obtain an accurate description of temperature for the hyperthermia treatment of female breast model. This section presents a 3D model of hyperthermia treatment in female breast to improve the 2D model mentioned in the previous section using ES-FEM and FEM respectively. It is expected that 3D model will provide more accurate prediction in temperature distribution. The geometry of 3D breast model is shown in Fig. 2.12. The center of heat source is $x = -0.0138m,\ y = 0.0071m,\ z = 0m$, and the radius of heat source is 6 mm. The type of heat source is expressed as follows:

$$Q_r = \begin{cases} \left(3.6\times10^5\right)t & 0 \le t \le 5s \\ 1.8\times10^6 & t > 5s \end{cases} \qquad 2.62$$

2.4.2.1 Effect of boundary condition

The boundary condition is essential to predict the temperature distribution accurately. Different boundary condition can yield completely different results. Because the bottom surface (boundary Γ_1) of breast as shown in Fig. 2.12(a) is very difficult to define the exact boundary condition in real clinical application, in the following section, we discuss the effect for two different boundary conditions.

Case 1: $k\dfrac{\partial T}{\partial n}=0$ Case 2: $T=37^{o}\mathrm{c}$

As the maximum temperature at the center of heating source is very crucial for successful hyperthermia treatment, the maximum temperature variation with time for two different boundary conditions is presented in Fig. 2.13. As shown in Fig. 2.13, it is found that the maximum temperature (reference results) is quite close with each other for both cases, which implies maximum temperature does not vary significantly with change of boundary condition. This is very important because doctor can operate on the patient without concerning too much incorrect result due to the boundary condition. Further, the solution obtained from FS-FEM using a coarse mesh agrees very well the reference solution compared with FEM using the same mesh. This numerical example validates that FS-FEM provides a soft effect to the model and can give more accurate solutions compared with FEM.

Figure 2.14 shows the temperature contours using FS-FEM, FEM with 457 nodes and the reference solution with 14916 nodes at time $t=10s$ for case 1. It is observed that the temperature distribution at the breast outer surface obtained using both

FS-FEM and FEM are very close to the reference. It is also found the temperature at the breast surface is well below 37^{o}C which guarantee the tissue under the safety temperature. More importantly, the temperature contour around the tumor region obtained from the FS-FEM are in a better agreement with the reference ones, compared with that of the FEM using the same coarse mesh.

2.4.2.2 Thermal-elastic deformation

Thermal-elastic interaction in the 3D breast hyperthermia treatment is investigated using the FEM and FS-FEM. In the mechanical model, the bottom surface has zero displacement. Since the maximum temperature occurs at the center of heat source, it is necessary to investigate the mechanical stress at that point. Fig 2.15, 2.16 and 2.17 present the normal stress in the x, y and z directions with the time at the center of heating source using FEM and FS-FEM together with reference results using very fine mesh (case 1). It is found that the solutions of FS-FEM are closer with the reference than those of FEM. This attributes to the "softening" effect of FS-FEM model induced by the gradient smoothing technique. This findings show again that FS-FEM works well even in the 3D mechanical model compared with FEM.

2.4.2.3 Computational efficiency

A comparison study on computational efficiency is now performed on the same Dell PC of Inter® Pentium (R) CPU 2.80GHz, 2.00GB of RAM using models of same DOFs. The 3D breast model of hyperthermia treatment is tested in this section. The total

computational time to complete the solution of reference, FEM and FS-FEM model is listed in Table 2.2.

It is found that total time to obtain the solution in the reference model is 116878 seconds. This is not acceptable in clinical application in order to control the heat source and optimize the damage of tumor in a short time. Although the solution can be quickly obtained for coarse mesh (457 nodes) using finite element method, there is a big discrepancy in the solutions between the reference and coarse mesh (457 nodes) as shown in section 2.4.2. In the operation, even one degree error can affect the treatment. The traditional finite element method fails to predict accurate results especially in the high gradient regions using the tetrahedral element. This is due to the property of 'overly-stiff' FEM. Although the time to complete the FS-FEM model is slightly higher than FEM using the same degree of freedom (457 nodes) as shown in the Table 2.2, the solution obtained from FS-FEM model is much more accurate than FEM. The extra CPU time for FS-FEM model is to construct the smoothing domain. Therefore, the FS-FEM model using coarse mesh is a good candidate replacing the FEM to achieve much more accurate results in a short time, which can reduce the cost of operation and enhance the efficiency of treatment.

2.5 Remarks

In this Chapter, the edge-based smoothed finite element (ES-FEM) in 2D and face-based smoothed finite element (FS-FEM) in 3D are formulated to simulate hyperthermia treatment in the breast model. The discretized system equations are

formulated using the smoothed Galerkin weak form. The numerical integration is performed based on the smoothing domains associated with the edge of the triangles in 2D and face of the tetrahedrons in 3D. Examples of 2D and 3D complex thermoelastic problems are analyzed to examine the accuracy, stability and efficiency of ES-FEM and FS-FEM. The following remarks can be drawn as follows:

1) The stiffness of the discretized model in ES-FEM and FS-FEM is reduced compared to the FEM.

2) The ES-FEM using the triangular elements in 2D and FS-FEM using tetrahedral elements in 3D are quite stable and accurate. Compared with FEM, there are no additional parameters in ES-FEM and FS-FEM. Hence, this method can be implemented in a straightforward way.

3) Different boundary condition defined in section 2.4 for 3D breast hyperthermia treatment does not affect the maximum temperature too much.

4) The degree of freedom for both standard FEM and ES-FEM are exactly the same using the same linear mesh, thus the computational cost for both ES-FEM and the FEM models are of the same order.

5) The ES-FEM is triangular elements in two-dimensional and tetrahedral elements in three-dimensional problem, and hence is particularly suitable to simulate complicated geometry such as human breast. However, the FEM does not like such elements and often gives poor solution of accuracy, especially at high temperature gradient region. In the hyperthermia treatment,

the temperature changes very fast at the tumor region. Thus, the results obtained from FEM using triangular element are poor due to its ‘overly-stiff’ behavior.

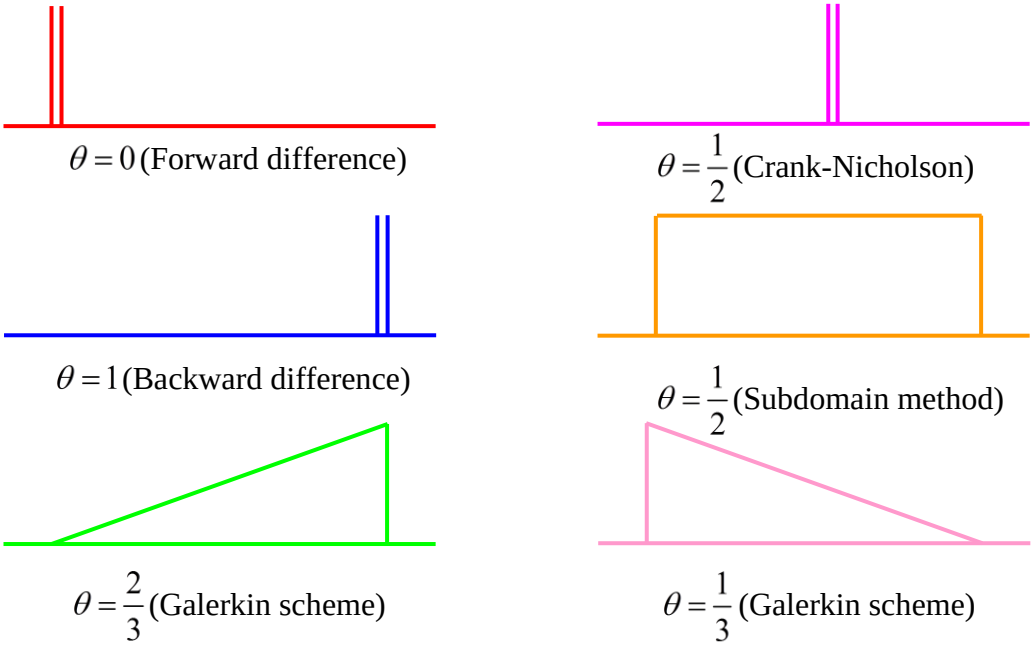

Figure 2.1: Shape and weighting functions [70]

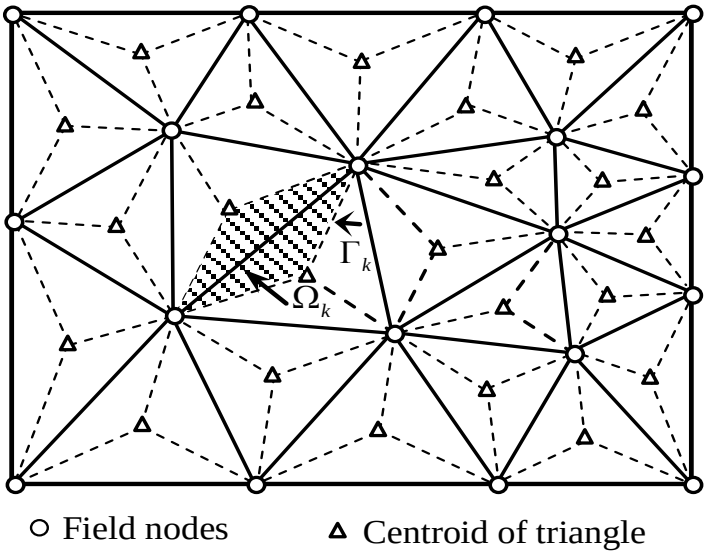

(a) Edge-based smoothing domains in 2D problem for gradient smoothing and integration are created by sequentially connecting the centroids of the adjacent triangles with the end-points of the edge.

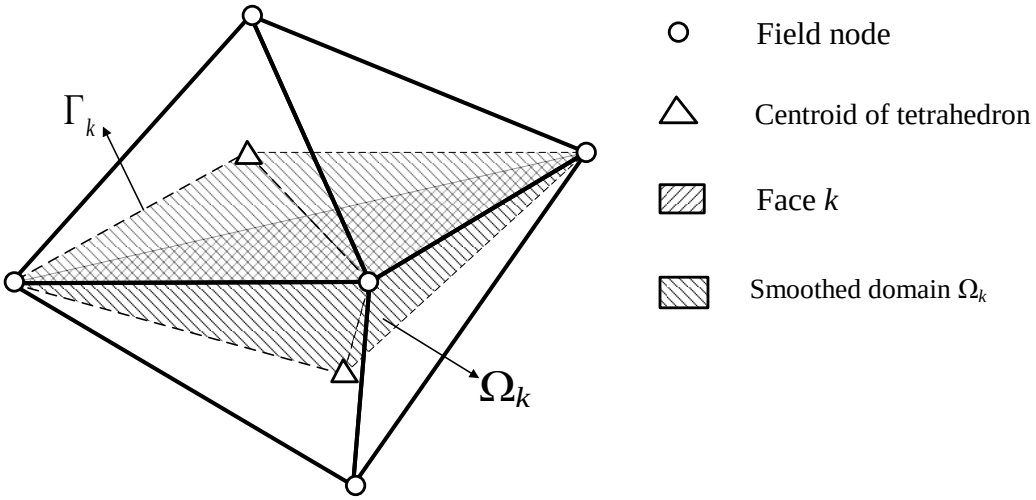

(b) For 3D problems, the smoothing domain is created using the neighbor tetrahedral elements by connecting vertexes of the triangle (face k) to the centroids of two adjacent elements.

Figure 2.2: Illustration of construction of smoothing domain for 2D and 3D problems

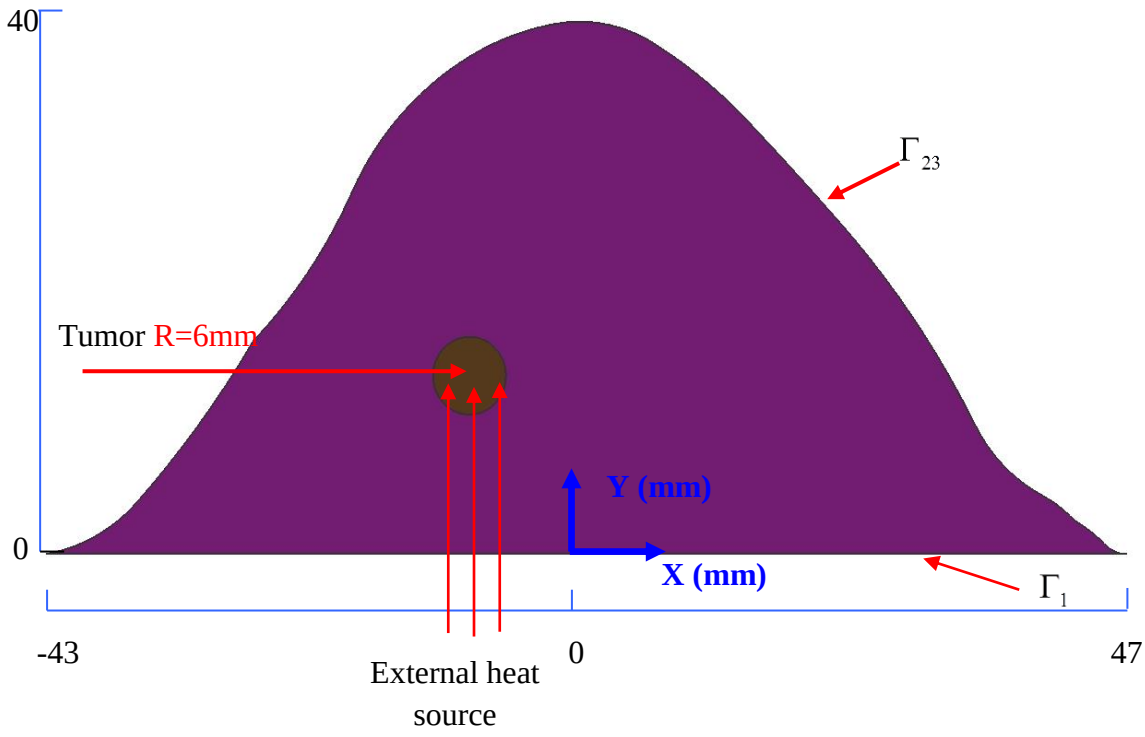

Figure 2.3: Location of heat source uniformly distributed in a small tumor of r=6mm

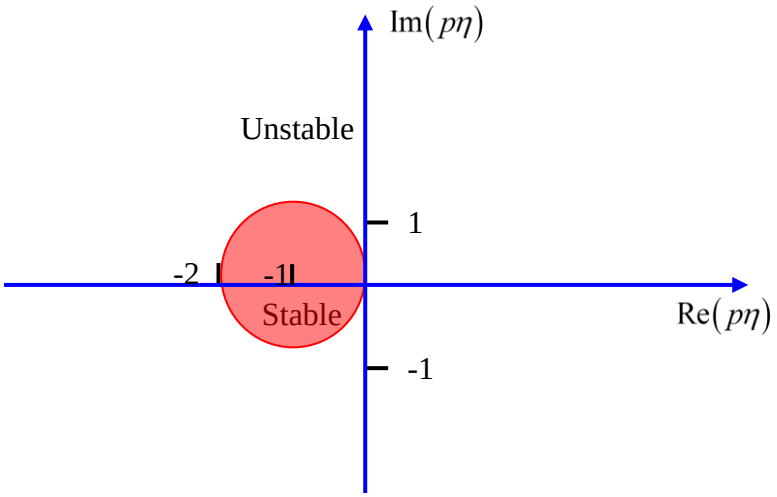

(a) Forward difference scheme

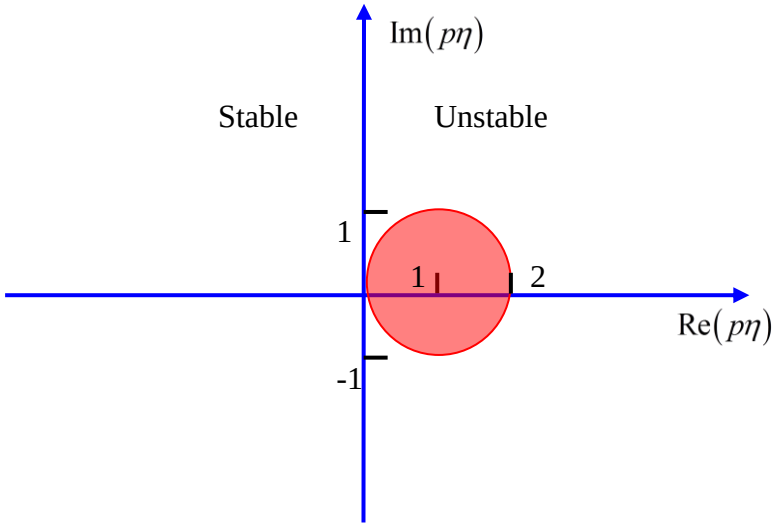

(b) Backward difference scheme

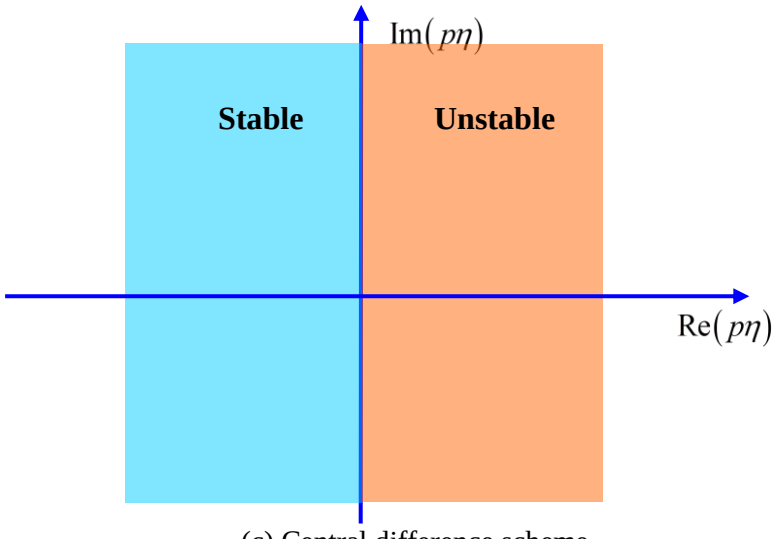

(c) Central difference scheme

Figure 2.4: Stability analysis of with different time integration

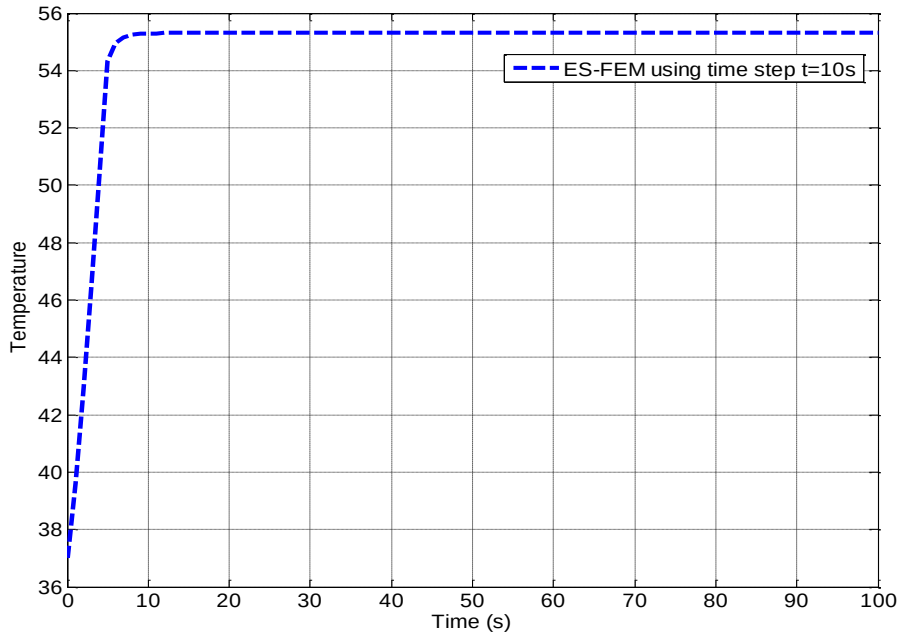

(a) Temperature variation with time at the cente of heat source using backward difference scheme in ES-FEM

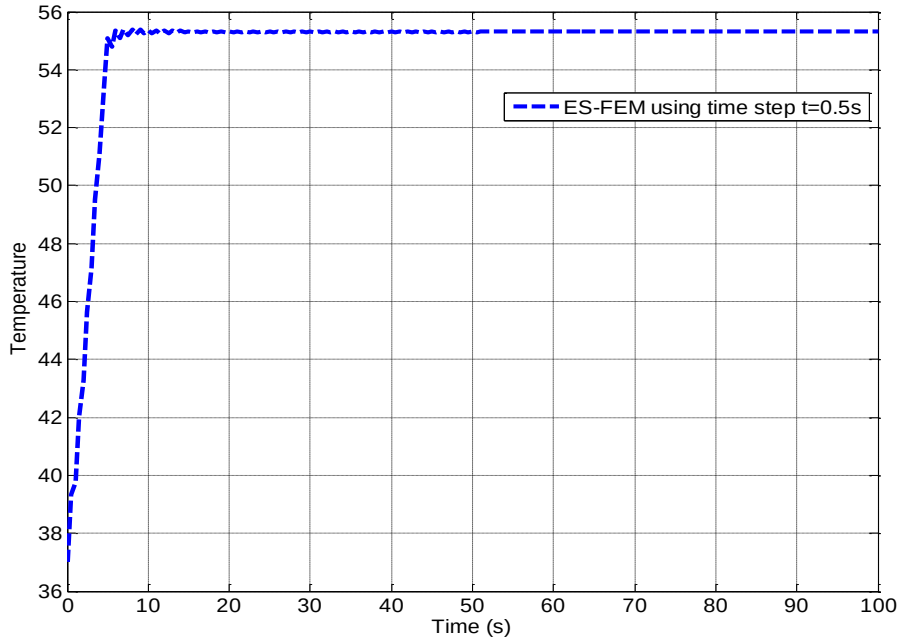

(b) Temperature variation with time at the cente of heat source using central difference scheme in ES-FEM

Figure 2.5: Analysis of ES-FEM stability in backward and central difference scheme

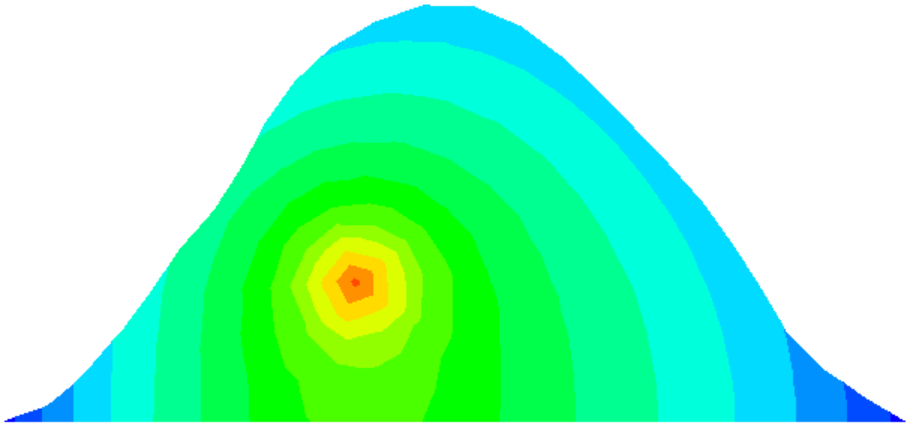

Temperature contour for ES-FEM using 288 nodes

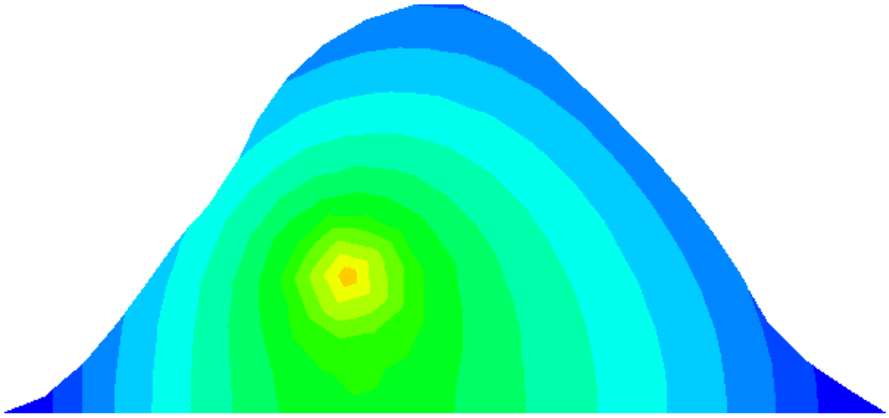

Temperature contour for FEM using 288 nodes

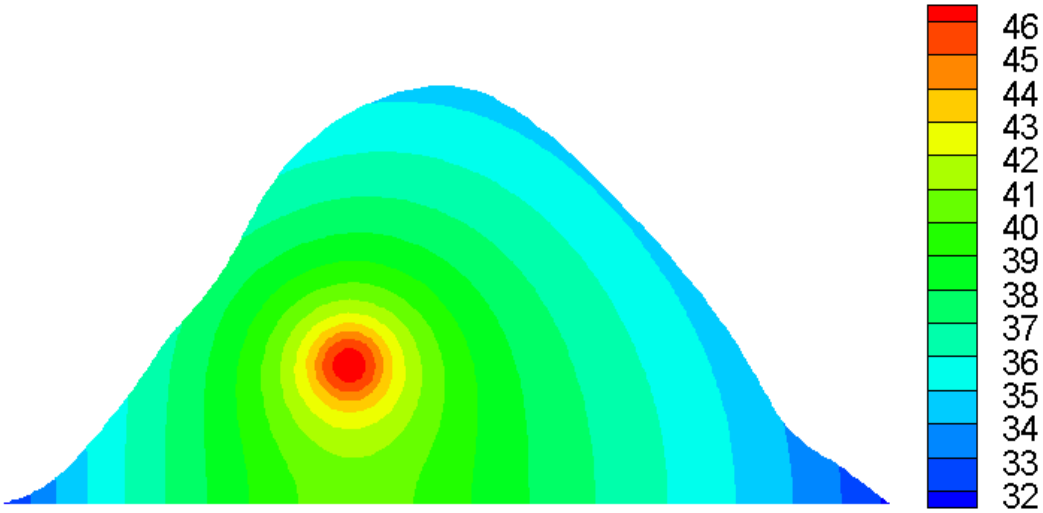

Temperature contour for reference results using 3546 nodes

Figure 2.6: Transient temperature distribution at t=10s

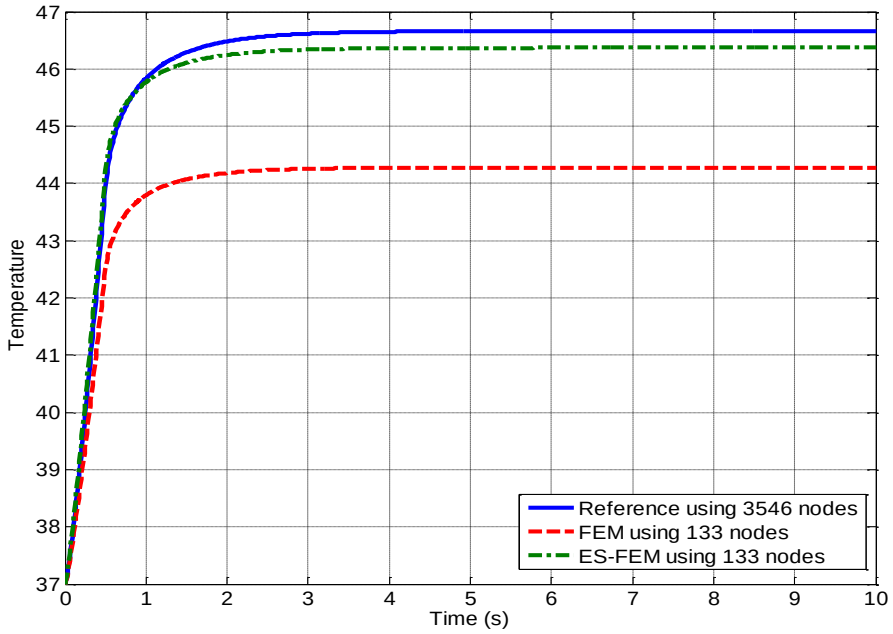

Figure 2.7: Maximum temperature variation with time (step time t=0.01s)

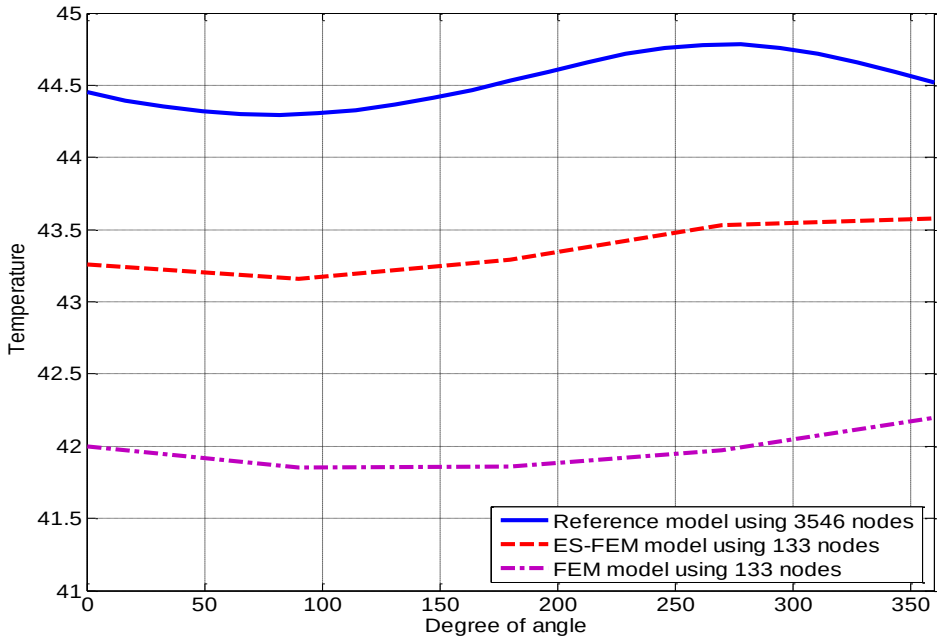

Figure 2.8: Comparison of temperature distribution along the circumference of tumor

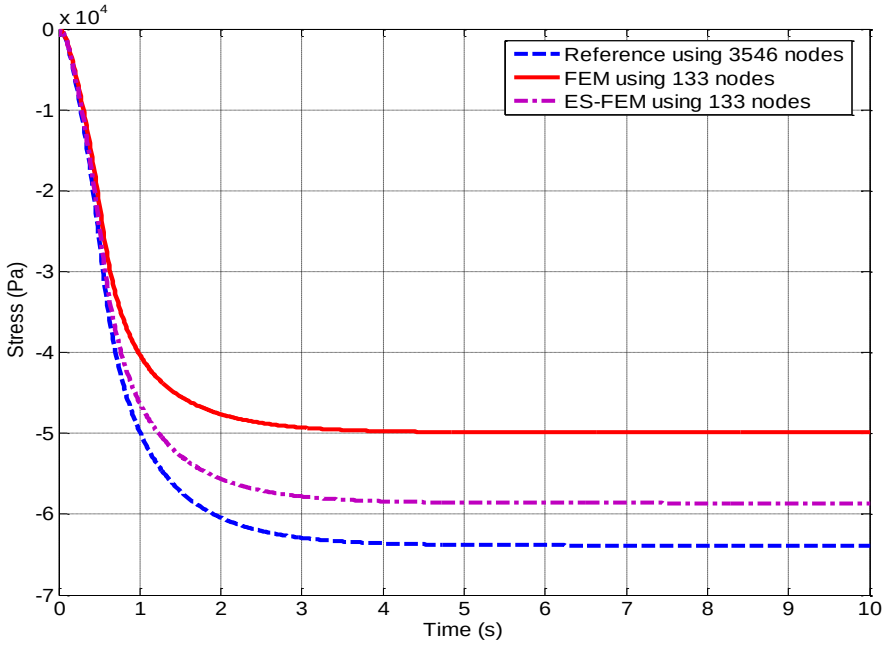

Figure 2.9: Normal stress (σ_{xx}) variation with time at the center of heat source (step time t=0.01s)

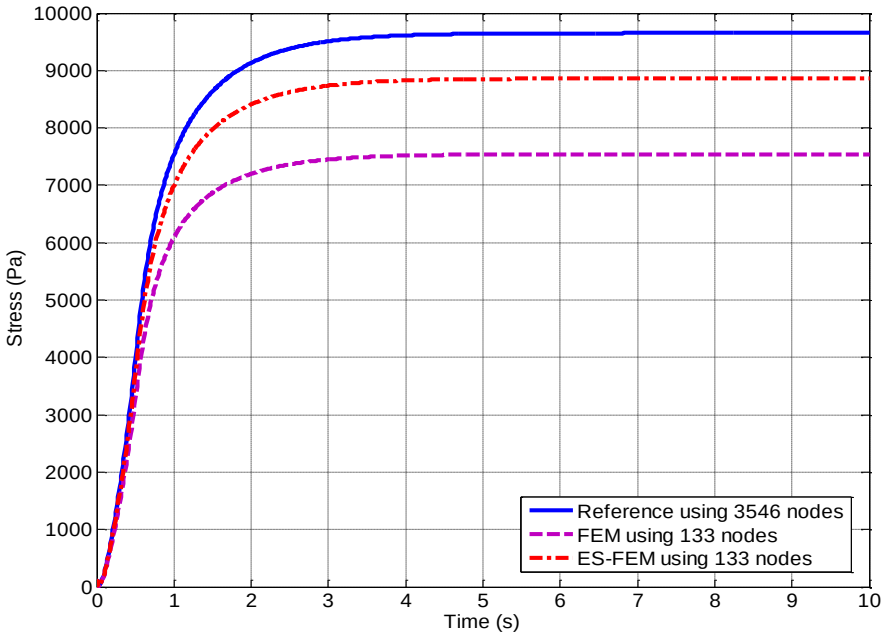

Figure 2.10: Normal stress (σ_{yy}) variation with time at the center of heat source (step time t=0.01s)

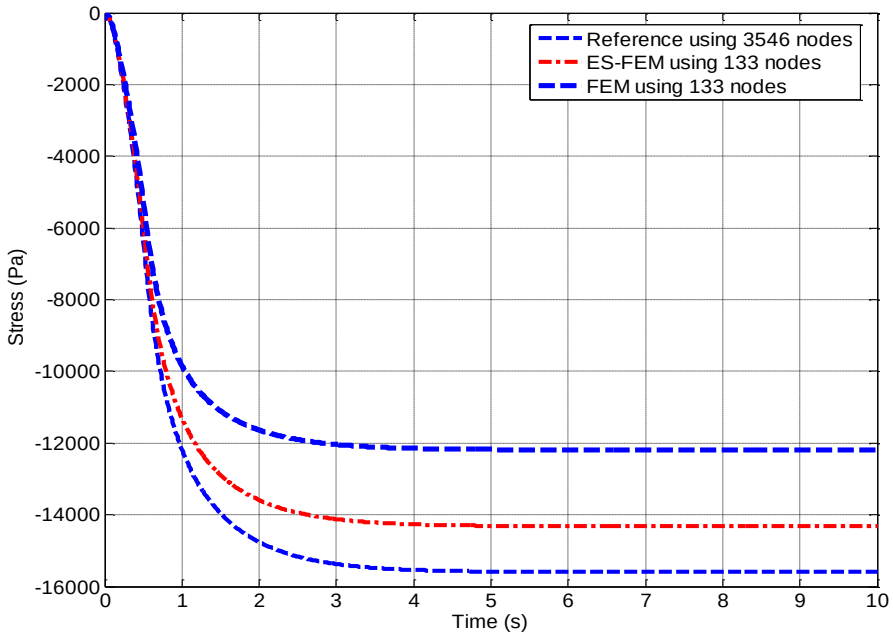

Figure 2.11: Shear stress (τ_{xy}) variation with time at the center of heat source (step time t=0.01s)

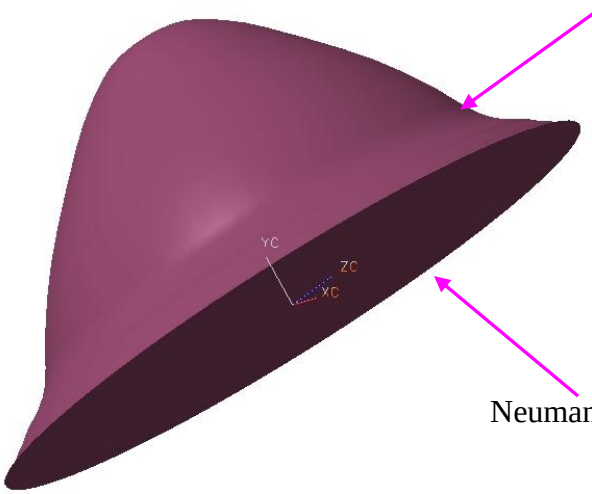

Boundary Γ_1, $k\dfrac{\partial T}{\partial n}=0$

Boundary Γ_{23},

a) Geometry of 3D breast model

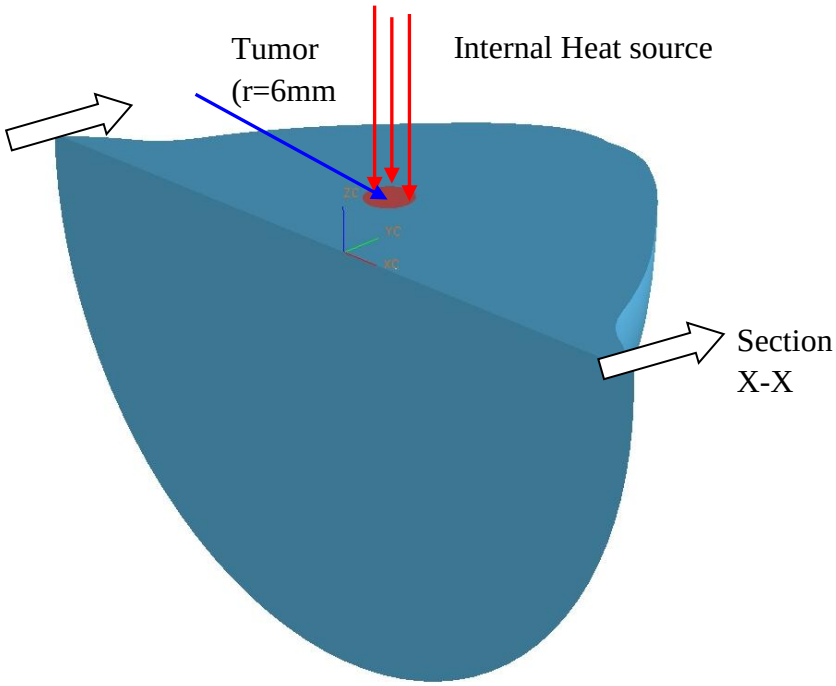

b) Location of heat source uniformly distributed in a small tumor of $r=6mm$

Center of heat source ($x=-13.8mm, y=7.1mm, z=0$)

Figure 2.12: Computational domain of 3D model

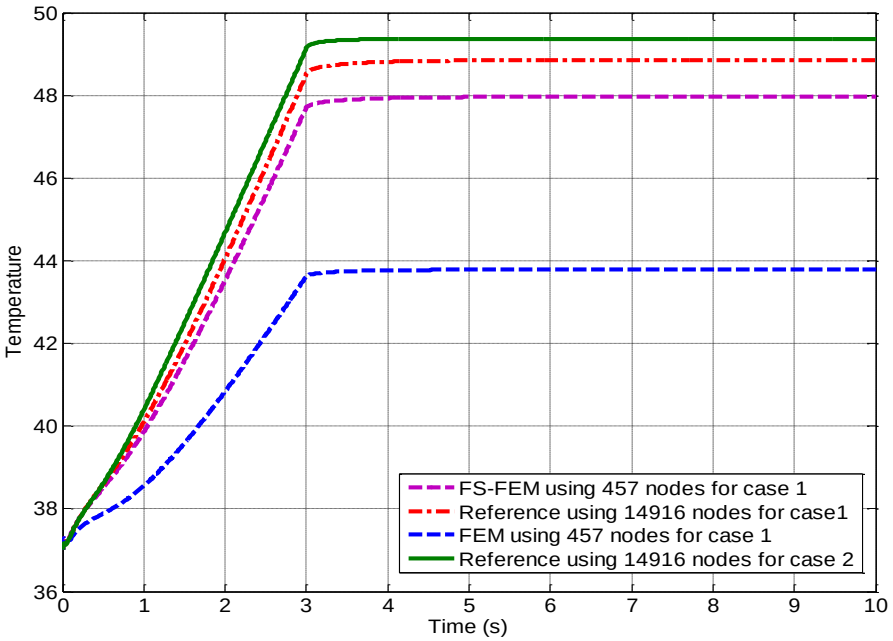

Figure 2.13: Maximum temperature variation with time (step time t=0.01s)

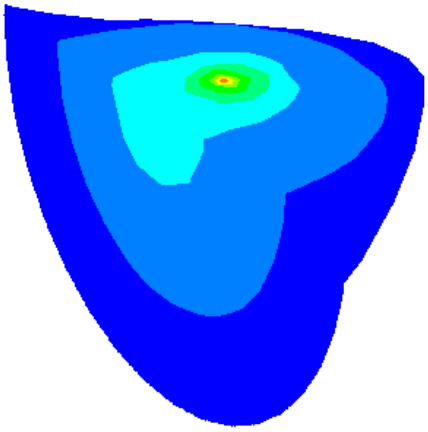

Temperature contour for section X-X using FS-FEM with 457 nodes

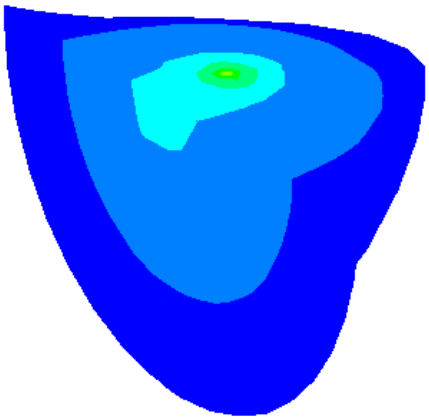

Temperature contour for section X-X using FEM with 457 nodes

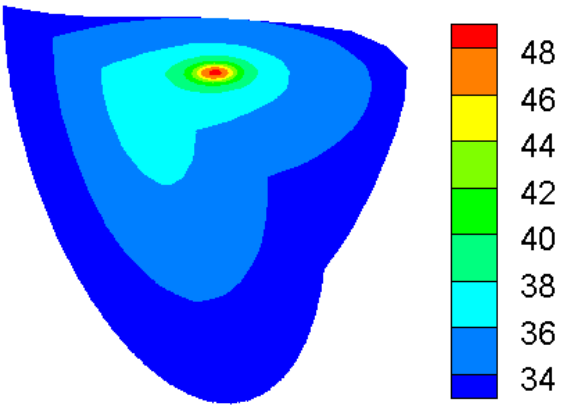

Temperature contour for section X-X using FEM with 14916 nodes

Figure 2.14: Transient temperature distribution at t=10s for case1

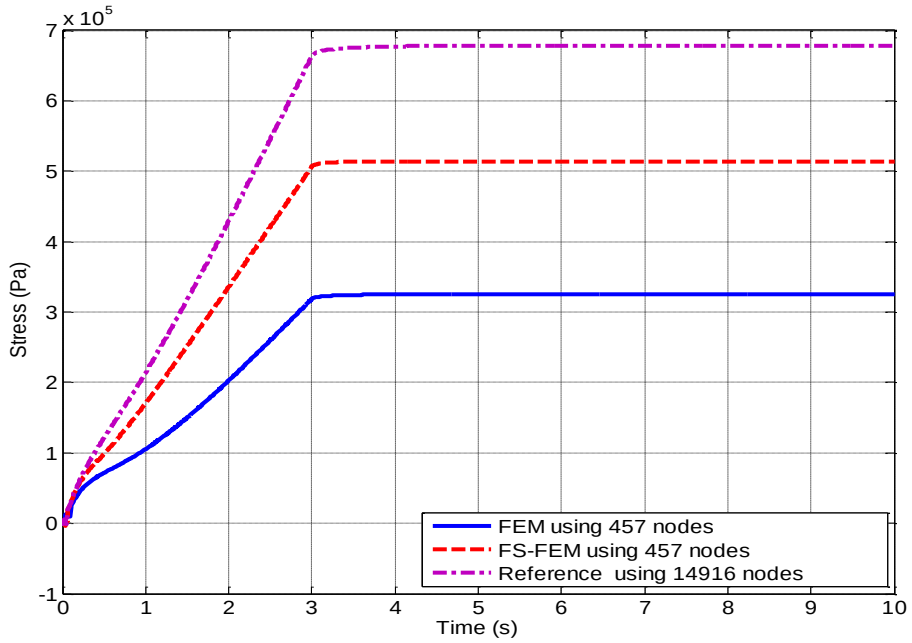

Figure 2.15: Normal stress (σ_{xx}) variation with time (step time t=0.01s)

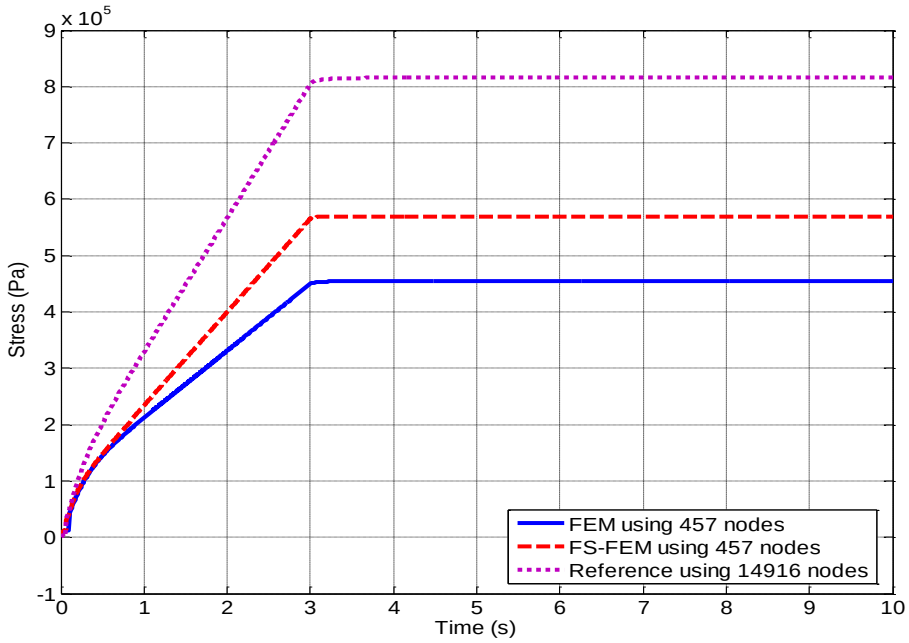

Figure 2.16: Normal stress (σ_{yy}) variation with time at the center of heat source (step time t=0.01s)

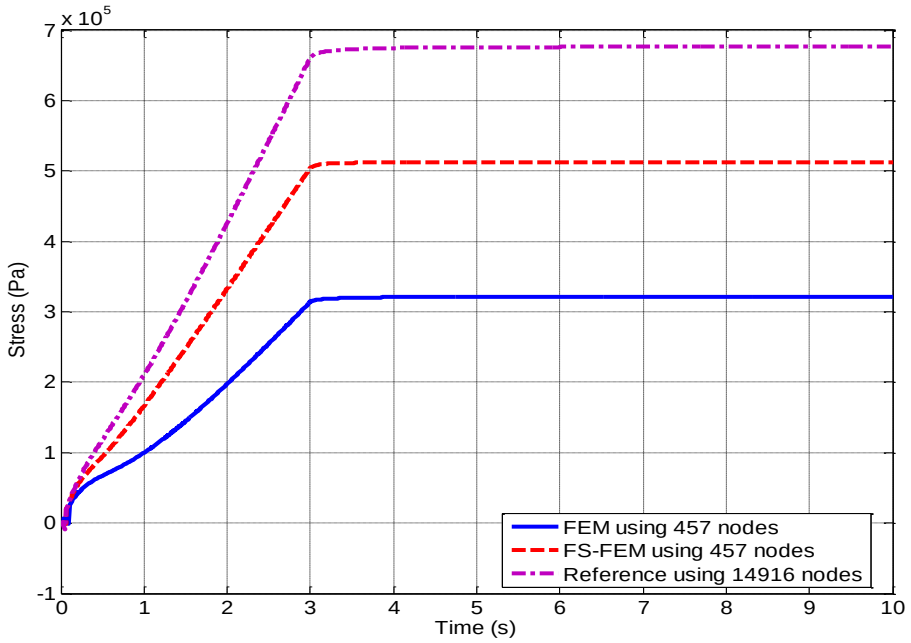

Figure 2.17: Normal stress (σ_{zz}) variation with time at the center of heat source (step time t=0.01s)

Table 2.1: Tissue property

c	Specific heat of tissue 4200 J/kg $^{\circ}C$	k	Thermal conductivity of tissue $k = 0.5$ W/(m$^{\circ}C$)
ρ	Density of Tissue 1000 kg/m^3	ω_b	Blood perfusion rate 0.5 kg/m^3
c_b	Specific heat of blood 4200 J/kg $^{\circ}C$	Q_m	Metabolism 450 W/m^3
T_b	Body core temperature 37°	T	Tissue temperature
T_a	known ambient temperature 25$^{\circ}C$	h	Ambient heat transfer coefficient 10W/m^2
α	thermal expansion 6×10^{-6}/°C	υ	Poisson's ratio 0.3
E	Elastic modulus 10 GPa	Q_r	External heat source (W/m^3)

Table 2.2**:** Comparison of the CPU time (s)

model	Degree of	Total time to complete
Reference	14916	116878s
FEM	457	476s
FS-FEM	457	587s

Chapter 3

Alpha Finite Element Method for Phase Change Problem in Liver Cryosurgery and Bioheat Transfer in the Human Eye

3.1 Alpha finite element method (αFEM) in liver cryosurgery

3.1.1 Introduction of liver cryosurgery

Traditional treatments for cancer include radiation therapy, chemotherapy and surgical removal [71]. However, the side effects of these treatments may seriously weaken the patient. Currently, cryosurgery is extensively used in tumor treatments. The main advantages of cryosurgery over traditional surgery are that there is minimal invasion, little pain, minimal scarring, and low cost. In cryosurgery, the continuous tip of a probe directly contacts with the target tumor tissue to introduce extremely low temperature resulting damage to the tumor cells. At present, the use of liquid nitrogen is the most popular method of freezing lesions. The two mechanisms of injury induced in the targeted tissue in cryosurgery are: the immediate effect related to cooling rate and solidification also known as vascular injury [72]. When the temperature falls into the freezing range, ice crystals form in the extra-cellular spaces. Extracellular crystallization cell destruction occurs when the temperature drops to the range of -4^{o}C and -21^{o}C [71]. As freeing continues, the ice crystals grow resulting loss of liquid water,

which causes cell shrinkage and membrane damage. These deleterious effects of cell dehydration are not always lethal to tumor cells [72]. When the cooling rate is very high, extracellular ice crystallization has no time to form. In that case, it is the intracellular ice that destroys the membrane and organelles [73-77].Vascular injury is also key to destroy tumor cells because vasculature is essential for tumor growth [71, 74].

The important feature of cryosurgery is that a phase change process occurs in the treatment. The direction of ice growth, temperature distribution, and irregular shape of frozen region are challenge in cryosurgical simulation [78]. In particular, there is a big difference in freezing of ideal materials having fixed freezing points and biological tissues. Phase change for biological material occurs over a temperature range between $-1^{o}C$ and $-8^{o}C$, and lower limit due to the complex condition and inhomogeneity of tissues [78-81].

In cryosurgery, a number of numerical models to solve phase change problems of biological tissue have been proposed. Generally, existing numerical methods for phase change can be categorized into two groups: one is front tracking method; another is fixed grid method [82-89]. For the front tracking technique, the liquid and solid domains are two separate domains where latent heat is treated as a moving boundary condition. By the application of energy balance, the velocity and position of the interface can be determined [90]. This requires deforming or altering grids, transformation or co-ordinates introduction of special algorithms near the phase change interface or choosing the space step or the time step so that the interface coincides with the grids points [90]. The advantage of front tracking methods is capable to provide

accurate prediction of the location of solid-liquid interface, but computer coding can be complicated. More importantly, front tracking methods are not suitable for material with a finite freezing range [89]. Due to this reason, fixed grid method has become the most powerful method in simulation of phase change problem. In the fixed grid method, the solid and liquid parts are treated as one single domain where the position of interface needs to be specified. The fixed grid method not only has ease implementation, but also can handle complex multi-dimensional problem and finite freezing material. However, oscillations may occur in the fixed grid method due to the discontinuity in effective heat capacity [83, 89]. Another disadvantage of the fixed grid method is that isothermal phase change is difficult to handle because the effective heat capacity becomes infinite at the freezing point [83]. In order to overcome this problem, a narrow temperature range is assumed in the simulation.

In the fixed grid method, there are several procedures to solve phase change problems such as finite difference method (FDM) and finite element method (FEM) depending on the discretization process. The main drawback for FDM is the difficulty in handling complex geometries. Due to this reason, FEM has gradually replaced FDM to solve heat transfer problems. However, FEM has some inherent drawbacks due to its strong reliance on the element mesh. In order to overcome the shortcomings of FEM, meshfree methods have been developed to circumvent some of the problems and have achieved remarkable progress [91-93].

It is a fascinating idea to obtain exact solution in the energy norm using numerical method. For this purpose, a novel alpha finite element method (αFEM) using triangular elements in 2D and tetrahedral elements in 3D has been developed [8]. The

αFEM makes the best use of NS-FEM with upper bound property and FEM with lower bound property. The key point in the αFEM is to introduce an α value to establish a continuous function of strain energy that includes the contributions from the FEM and NS-FEM. When $\alpha=0$, the αFEM is exactly the same as FEM, and the strain energy is underestimated. When $\alpha=1$, the αFEM becomes NS-FEM, and the strain energy is overestimated. The αFEM is variation consistence. However, the use of quadrilateral elements cannot provide the exact solution in certain norms.

Although different α value can achieve different solutions in the αFEM, the αFEM is always stable and converges for any α value. This ensures that no matter what the α value is, the result is still reliable. At this moment, how to "tune" the α value in the αFEM is still an open question. Our earlier works [8] have found for many cases that an $\alpha \in [0.4,0.6]$ usually achieves much better results compared with the standard FEM using the same number of nodes. Although this is not very precise, it is very simple to use. In this Chapter, the alpha value is simply fixed at 0.5.

3.1.2 Fundamental of alpha finite element method (αFEM) in phase change problem

3.1.2.1 Model of cryosurgery

Many bioheat transfer models have been developed to simulate the cryosurgery process in liver treatment [94]. In this Chapter, the Pennes bioheat transfer model is still used [64] because this model is only one variable (temperature) involved in the simulation.

$$\rho c \frac{\partial T}{\partial t} = k\nabla^2 T + \omega c_b (T_{bl} - T) + Q_m + Q \qquad 3.1$$

where ρ is density of liver; k is the thermal conductivity; ω is blood perfusion rate; c is the specific heat capacity of liver; c_b is the specific heat capacity of blood; T_{bl} is the blood temperature; Q_m is the volumetric heat source associated with the metabolism; Q is the external volumetric heat source. In cryosurgery, an extremely low temperature is used to destroy malignant tissues. There are several assumptions made in the simulation of phase changes in cryosurgery.

1. Latent heat is constant.
2. The thermal properties vary at the point of complete phase change from liquid to solid.
3. The density is constant at the solid and liquid region.
4. At the interface, only heat conduction is involved in the heat transfer.
5. Blood flow rate is constant when the temperature is above the lower phase transition temperature
6. The metabolism is zero when the temperature is at the freezing range.
7. Liquid fraction is taken to be a function of temperature only.

3.1.2.2 Mathematical formulation of phase change problem

A bounded region is divided into three regions, liquid part Ω_1, solid region Ω_3, and mushy part Ω_2 as shown in Fig. 3.1.

Bioheat transfer in the solid is governed by:

$$\rho c_s \frac{\partial T}{\partial t} = \nabla \bullet (K_s \nabla T_s) + \omega_s \rho c_s (T_{bl} - T) + Q_m + Q \tag{3.2}$$

Bioheat transfer in the liquid is governed by:

$$\rho c_l \frac{\partial T}{\partial t} = \nabla \bullet (K_l \nabla T_l) + \omega_l \rho c_l (T_{bl} - T) + Q_m + Q \tag{3.3}$$

Heat balance at the solid / liquid interface is governed by:

$$k_s (\frac{\partial T_s}{\partial n}) - k_l (\frac{\partial T_l}{\partial n}) = (\rho_l h_l - \rho_s h_s) v_x - \rho_l h_l v_l \tag{3.4}$$

where h_s, h_l are the enthalpies per unit mass of solid and liquid, v_x, v_l are the velocity of the interface and liquid at the interface.

Conservation of mass at the interface gives

$$(\rho_l - \rho_s) v_x = \rho_l v_l \tag{3.5}$$

$$v_l = -\frac{\rho_s - \rho_l}{\rho_l} v_x \tag{3.6}$$

Substituting Eq. (3.6) into Eq. (3.4) gives

$$k_s \frac{\partial T_s}{\partial n} - k_l \frac{\partial T_l}{\partial n} = \rho_s L v_x \tag{3.7}$$

In this thesis, the density is constant in the whole domain, thus the bioheat transfer at the interface is:

$$k_s (\frac{\partial T_s}{\partial n}) - k_l (\frac{\partial T_l}{\partial n}) = \rho L \frac{\partial s}{\partial t} \tag{3.8}$$

$$T_1 = T_2 = T_f \qquad \text{for } t > 0 \text{ and } x = s(t) \tag{3.9}$$

where n is the unit normal on the phase interface (pointing into the liquid), s is the velocity of the interface and L is the latent heat per unit mass of solid. For a number of

simple geometry and conditions, analytical and approximate solutions to the Stefan problem are available [95].

3.1.2.3 The Enthalpy method

The essence of the enthalpy method is that the latent heat effect is incorporated into the heat capacity which is dependent on the temperature. Thus, a new parameter *H* (enthalpy) is introduced. The enthalpy is defined as the sum of latent and sensible heat effect.

For isothermal freezing, the enthalpy *H* is defined as:

$$\begin{aligned} H(T) &= \int \rho c_s(T)dT && (T < T_f) \\ H(T) &= \int \rho c_s(T)dT + \rho L + \int \rho c_f(T)dT && (T \geq T_f) \end{aligned} \tag{3.10}$$

In the biological material, there is no single freezing temperature. Thus, a mushy zone exists between the solid and liquid part.

$$\begin{aligned} H(T) &= \int \rho c_s(T)dT && (T < T_s) \\ H(T) &= \int \rho c_s(T)dT + \rho L + \int \rho c_f(T)dT + \int \rho c_l(T)dT && (T_s \leq T \leq T_l) \\ H(T) &= \int \rho c_s(T)dT + \rho L + \int \rho c_l(T)dT && (T > T_l) \end{aligned} \tag{3.11}$$

where T_s is the solidus temperature, T_l is the liquidus temperature. With the above definition, the bioheat equation in Eq. (3.1) can be rewritten in terms of enthalpy:

$$\frac{\partial H}{\partial t} = k\nabla^2 T + \omega\rho c_b(T_{bl} - T) + Q_m + Q \tag{3.12}$$

where *H* is the enthalpy. Assuming a linear release of latent heat over the mushy region, the variation of *H (T)* with temperature is shown in Fig. 3.2:

Taking the derivative of *H*,

$$\frac{\partial H}{\partial t} = \frac{\partial H}{\partial T}\frac{\partial T}{\partial t} \tag{3.13}$$

The effective heat capacity is expressed as:

$$c_{eff} = \frac{dH}{dT} \tag{3.14}$$

Thus, Eq. (3.1) becomes

$$\rho c_{eff}\frac{\partial T}{\partial t} = k\nabla^2 T + \omega\rho c_b(T_{bl} - T) + Q_m + Q \tag{3.15}$$

The effective heat capacity, blood perfusion, metabolic heat generation and thermal conductivity for different phase region are:

$$\begin{aligned} c_{eff} &= \rho c_s && (T < T_s) \\ c_{eff} &= \rho c_f + \frac{Q}{T_l - T_s} && (T_s \le T \le T_l) \\ c_{eff} &= \rho c_s && (T > T_l) \end{aligned} \tag{3.16}$$

$$\begin{aligned} \omega &= 0 && (T < T_s) \\ \omega &= 0 && (T_s \le T \le T_l) \\ \omega &= \omega_b && (T > T_l) \end{aligned} \tag{3.17}$$

$$\begin{aligned} Q_m &= 0 && (T < T_s) \\ Q_m &= 0 && (T_s \le T \le T_l) \\ Q_m &= Q_u && (T > T_l) \end{aligned} \tag{3.18}$$

$$\begin{aligned} k &= k_s && (T < T_s) \\ k &= \frac{(k_l + k_s)}{2} && (T_s \le T \le T_l) \\ k &= k_l && (T > T_l) \end{aligned} \tag{3.19}$$

3.1.2.4 Finite element formulation for phase change problem

The discrete equations of the FEM can be obtained by multiplying the governing Eq. (3.1) with a test function w in the entire domain [2].

$$\int_\Omega w\cdot\rho c_{eff}T_t d\Omega=\int_\Omega w\cdot k\nabla^2 T d\Omega+\int_\Omega w\cdot\omega_b c_b(T_b-T)d\Omega+\int_\Omega w\cdot Q_m d\Omega+\int_\Omega w\cdot Q d\Omega \tag{3.20}$$

Using integration by parts:

$$\rho c_{eff}\int_\Omega wT_t d\Omega+k\int_\Omega \nabla w\cdot\nabla T d\Omega+\omega_b c_b\int_\Omega wT d\Omega=(\omega_b c_b T_b+Q_m+Q)\int_\Omega w d\Omega-\int_{\Gamma_2} wq_\Gamma \mathrm{d}\Gamma-\int_{\Gamma_3} wh(T-T_a)\mathrm{d}\Gamma \tag{3.21}$$

In the FEM, the temperature is expressed as the following trial and test function:

$$T=\sum_{i=1}^{m}\mathbf{N}_i\mathbf{T}_i \tag{3.22}$$

where $\mathbf{N}_i$ is the shape function, and $\mathbf{T}_i$ is the unknown nodal temperature. In the Galerkin weak form, the weight function w is replaced by shape function $\mathbf{N}$, and the standard Galerkin weak form is expressed as:

$$\rho c_{eff}\int_\Omega \mathbf{N}\mathbf{T}_t d\Omega+k\int_\Omega \nabla\mathbf{N}\cdot\nabla\mathbf{T}d\Omega+\omega_b c_b\int_\Omega \mathbf{N}\cdot\mathbf{N}\mathbf{T}d\Omega=(\omega_b c_b T_b+Q_m+Q)\int_\Omega \mathbf{N}d\Omega-\int_{\Gamma_2}\mathbf{N}q_\Gamma \mathrm{d}\Gamma-h\int_{\Gamma_3}\mathbf{N}\cdot\mathbf{N}\mathbf{T}d\Gamma+h\int_{\Gamma_3}\mathbf{N}T_a\,\mathrm{d}\Gamma \tag{3.23}$$

The discretized system equation can be finally obtained and written in the following matrix form:

$$[\mathbf{M}]\{\dot{\mathbf{T}}\}^t+[\mathbf{K}+\mathbf{C}]\{\mathbf{T}\}^t=\{\mathbf{F}\}^t \tag{3.24}$$

Therefore, the smoothed Galerkin weak form for Pennes' bioheat equation can be formulated.

$$\mathbf{K}=k\int_\Omega\nabla\mathbf{N}\cdot\nabla\mathbf{N}d\Omega \quad \text{The stiffness matrix} \tag{3.25}$$

$$\mathbf{M}=\rho c_{eff}\int_\Omega\mathbf{N}\cdot\mathbf{N}d\Omega \quad \text{The mass matrix} \tag{3.26}$$

$$\mathbf{C}=\omega_b c_b\int_\Omega\mathbf{N}\cdot\mathbf{N}\mathrm{d}\Omega+h\int_{\Gamma_3}\mathbf{N}\cdot\mathbf{N}\mathrm{d}\Gamma \quad \text{The equivalent damping matrix} \tag{3.27}$$

$$\mathbf{F}=(\omega_b c_b T_b+Q_m+Q)\int_\Omega\mathbf{N}d\Omega+h\int_{\Gamma_3}\mathbf{N}T_a\,\mathrm{d}\Gamma-\int_{\Gamma_2}\mathbf{N}q_\Gamma\mathrm{d}\Gamma \quad \text{The force matrix} \tag{3.28}$$

Eq. (3.24) is numerically solved via αFEM. The numerical algorithm of αFEM is presented in the following section.

3.1.2.5 Briefing on the node-based finite element method (NS-FEM)

In this section, a brief of the formulation of NS-FEM is presented. In the NS-FEM, the domain discretization is the same as the standard FEM. However, the integration of stiffness matrix for NS-FEM in Eq. (3.25) is based on node instead of element, and the strain smoothing technique is applied. It has been found that the NS-FEM works well for polygonal elements [24]. Because of its upper bound properties [7], and the ease of generating triangular (2D) and tetrahedron (3D) elements for complicated domains, it is used in this work for formulating our αFEM for cryosurgery in the liver and bioheat transfer in the human eye. In the numerical integrations of NS-FEM, a mesh of 3-node triangles for 2D is firstly generated. This can be performed easily by using any mesh generator well-developed for FEM. Based on the triangular mesh, the problem domain Ω is further divided into N smoothing domains associated with nodes of the triangles such that $\Omega_1 \cup \Omega_2 \cup \ldots \Omega_N = \Omega$ and $\Omega_i \cap \Omega_j = \emptyset$, $i \neq j$, where N is the total number of nodes. As shown in Fig. 3.3(a), the smoothing domain Ω_k for node k is created by connecting sequentially the mid-edge-point to the centroids of the surrounding triangles of the node of interest. The boundary of the smoothing domain Ω_k is labeled Γ_k and the union of all Ω_k forms exactly the global domain Ω. For 3D problems as shown in Fig. 3.3(b), the domain discretization is the same as that of standard FEM using tetrahedral elements, and the smoothing domains for node k inside cell I are formed by connecting

sequentially the mid-edge-points, the centroids of the surface triangles, and the centroids of the cell I.

Using the node-based smoothing operation, the temperature gradient is assumed to be the smoothed strain for node *k* defined by:

$$\bar{\boldsymbol{\varepsilon}}_k = \int_{\Omega^{(k)}} \boldsymbol{\varepsilon}(\mathbf{x}) W(\mathbf{x}) d\Omega = \int_{\Omega^{(k)}} \nabla_s \mathbf{T}(\mathbf{x}) W(\mathbf{x}) d\Omega \tag{3.29}$$

where $W(\mathbf{x})$ is a given smoothing function that satisfies at least the partition of unity property.

$$\int_{\Omega^{(k)}} W(\mathbf{x}) d\Omega = 1 \tag{3.30}$$

Using the following constant smoothing function:

$$W_k(\mathbf{x}) = \begin{cases} \dfrac{1}{S^{(k)}} & x \in \Omega^{(k)} \\ 1 & x \notin \Omega^{(k)} \end{cases} \tag{3.31}$$

where $S^{(k)}$ is the area of cell expressed as:

$$S^{(k)} = \int_{\Omega^{(k)}} d\Omega = \frac{1}{3} \sum_{i=1}^{N_e^{(k)}} S_e^{(i)} \tag{3.32}$$

where N_e is the number of elements around the node *k*, and $S_e^{(i)}$ is the area of the *i*th element around the node *k*.

$$\bar{\boldsymbol{\varepsilon}}_k = \sum_{I \in N_n^{(k)}} \bar{\mathbf{B}}_I(\mathbf{x}_k) \mathbf{T}_I \tag{3.33}$$

where $N_n^{(k)}$ is the number of nodes in the influence domain of node *k*. When linear shape functions are used, it is the number of nodes that is directly connected to node *k* in the triangular mesh. $\bar{\mathbf{B}}_i(\mathbf{x}_k)$ is termed as the smoothed strain matrix on the cell:

$$\bar{\mathbf{B}}_I(\mathbf{x}_k) = \frac{1}{S^{(k)}} \sum_{i=1}^{N_e^{(k)}} \frac{1}{3} S_e^{(i)} \mathbf{B}_i \tag{3.34}$$

The entries $\mathbf{B}_i$ are constant due to the linear shape function used. The assembly of stiffness matrix is similar to procedure in the FEM. The entries in sub-matrices of the stiffness matrix K in Eq. (3.25) are then expressed as:

$$\overline{\mathbf{K}} = \sum_{k=1}^{N} \overline{\mathbf{K}}^{(k)} \tag{3.35}$$

where the $\overline{\mathbf{K}}^{(k)}$ is the smoothed stiffness matrix associated with the node *k*. It can be calculated from:

$$\overline{\mathbf{K}}^{(k)} = \int_{\Omega_k} \overline{\mathbf{B}}^{\mathrm{T}} k \overline{\mathbf{B}} \mathrm{d}\Omega = \overline{\mathbf{B}}^{\mathrm{T}} k \overline{\mathbf{B}}_I^{\Omega_k} S_k \tag{3.36}$$

It can be easily seen from Eq. (3.36) that the resultant linear system is symmetric and banded (due to the compact supports of FEM shape functions), which implies that the discretized system equations can be solved efficiently.

3.1.2.6 The formulation of alpha finite element method

The αFEM is a combination of NS-FEM and FEM determined by a scaling function $\alpha \in [0,1]$. The entries in the sub-matrices of the system stiffness matrix $K_{\alpha FEM}$ will be the assembly of the entries of those from both the NS-FEM and the FEM. In 2D NS-FEM, the area S_e of each triangular element is divided into four parts with a scale factor α as shown in Fig. 3.4(a): three quadrilaterals scaled by (1 − α) at three corners with equal area of $\frac{1}{3}\alpha V_e$, and the remaining Y-shaped part in the middle of the element of area (1-α)V_e. The NS-FEM is used to calculate three quadrilaterals, and the FEM is used to calculate the remaining part (Y shape area). The entries in sub-matrices of the system stiffness matrix KαFEM will be the assembly of the entries

of those from both the NS-FEM and the FEM. The procedure for assembling the stiffness K is as follow:

$$\mathbf{K}_{\mathrm{IJ}}^{\alpha\mathrm{FEM}} = \sum_{l=1}^{N_n} \mathbf{K}_{\mathrm{IJ(l)}}^{\mathrm{NS\text{-}FEM}} + \sum_{k=1}^{N_n} \mathbf{K}_{\mathrm{IJ(k)}}^{\mathrm{FEM}} \tag{3.37}$$

where N_e is the total number of total elements in the entire problem domain:

$$\mathbf{K}_{\mathrm{IJ(k)}}^{\mathrm{FEM}} = \int_{\Omega_e^{(\alpha)}} \mathbf{B}_{\mathrm{I}}^{\mathrm{T}} k \mathbf{B}_{\mathrm{J}} d\Omega \tag{3.38}$$

$$\mathbf{K}_{\mathrm{IJ(l)}}^{\mathrm{NS\text{-}FEM}} = \int_{\Omega^{(k,\alpha)}} \left(\overline{\mathbf{B}}_I^{(\alpha)}(\mathbf{x}_k) \right)^T k \left(\overline{\mathbf{B}}_J^{(\alpha)}(\mathbf{x}_k) \right) d\Omega \tag{3.39}$$

In which $\Omega_e^{(k,\alpha)}$ is the area associated the node *k* and bounded by the boundary $\Gamma^{(k,\alpha)}$ as shown in Fig. 3.5. $\Omega_e^{(\alpha)}$ is the Y shape of area. The smoothed strain $\overline{\mathbf{B}}^{(\alpha)}(\mathbf{x}_k)$ for $\Omega_e^{(k,\alpha)}$ is determined by:

$$\overline{\mathbf{B}}_I^{(\alpha)}(\mathbf{x}_k) = \frac{1}{S^{(k,\alpha)}} \sum_{i=1}^{N_e^{(k)}} \frac{1}{3}(1-\alpha^2) S_e^{(i)} \mathbf{B}_i = \frac{1}{S^{(k,\alpha)}} \sum_{i=1}^{N_e^{(k)}} \frac{1}{3} S_e^{(i)} \mathbf{B}_i = \overline{\mathbf{B}}_I(\mathbf{x}_k) \tag{3.40}$$

The smoothed strain matrix is expressed as:

$$S^{(l,\alpha)} = \int_{\Omega^{(k,\alpha)}} d\Omega = \sum_{i=1}^{N_e^{(k)}} \frac{1}{3}(1-\alpha^2) S_e^{(i)} = (1-\alpha^2) S^{(k)} \tag{3.41}$$

Thus, the stiffness for NS-FEM is expressed as:

$$\mathbf{K}_{IJ(k)}^{NS-FEM} = (1-\alpha^2) \overline{\mathbf{B}}_I^T k \overline{\mathbf{B}}_J^T S^{(k)} \tag{3.42}$$

Which implies that in the coding of αFEM, we can use the original NS-FEM to calculate the stiffness matrix and then multiply $(1-\alpha^2)$.

From the formulation of αFEM, it is seen that αFEM using a scale factor α that controls the contribution of NS-FEM and FEM. When α varies from 0 to 1, the solution of αFEM is continuous combination of the FEM and NS-FEM solutions. Further, it is observed that the stiffness matrix of the αFEM has the same unknowns of only the temperature, the same bandwidth and sparsity as that of the standard FEM,

and hence the same computational complexity. The 3D αFEM as shown in Fig. 3.4(b) can be formulated in the similar way.

3.1.2.7 Assembly of mass matrix

The major challenge in the fixed grid method of phase change problem is to determine the mass matrix. Based on the expression of mass matrix ($\mathbf{M} = \rho c_{eff} \int_{\Omega} \mathbf{N} \cdot \mathbf{N} d\Omega$), it is seen that the latent heat effect is incorporated into the mass matrix. If the shape functions used to describe stiffness over the element are the same as the mass distribution, then the corresponding mass matrix is regarded as the consistent mass matrix. In the lumped mass matrix, it is assumed that the mass is only concentrated on the node. A lot of researchers have discussed the relative merits of consistent lumped and lumped mass matrix [2, 96]. The expressions of consistent and lumped mass matrix are listed as follow:

$$\mathbf{M}_{consist} = \frac{\rho c_{eff} A}{3} \begin{bmatrix} \frac{1}{2} & \frac{1}{4} & \frac{1}{4} \\ \frac{1}{4} & \frac{1}{2} & \frac{1}{4} \\ \frac{1}{4} & \frac{1}{4} & \frac{1}{2} \end{bmatrix} \quad \mathbf{M}_{lump} = \frac{\rho c_{eff} A}{3} \begin{bmatrix} 1 & 0 & 0 \\ 0 & 1 & 0 \\ 0 & 0 & 1 \end{bmatrix} \tag{3.43}$$

A is the area of the triangular element. Many authors claim that the lumped mass matrix is a good way to simulate the phase change problem even for a constant specific heat capacity in terms of better stability, accuracy and convergence [97, 98]. In an addition, the use of a lumped mass matrix can reduce computational cost significantly. Thus, the lumped mass matrix is preferred in the simulation.

It is easy to integrate the mass matrix in complete liquid, solid or mushy regions because they have a constant specific heat value. The simple approximation of specific heat in an element is based on the average temperature. However, this method is only valid for alloys with very large finite freezing range [87]. There are some difficulties in determining the mass matrix for the elements that contain two or three phases. In this case, the effective heat capacity is not a continuous function as shown in Figure 3.2. The effective heat capacity may be missed if the average temperature is not in the range of the mushy region. On the other hand, the effective heat capacity is overestimated if the average temperature is in the mushy region. A very popular smoothing method is to split the moving front into a phase transformation region of width 2ε by incorporating the latent heat effect into a equivalent heat capacity over the range 2ε [87]. The numerical is sensitive to range ε . If the element is not dense or the time step is large, the temperature may skip the phase change interval. Additionally, the latent heat of the associated volume may be entirely missed if the interface jumps across one nodal point in less than one time step [87]. In order to tackle this problem, many researchers have proposed the ways to handle the discontinuity of effective heat capacity. Del Giudice [99] suggested the orientated direction *s* of the temperature gradient:

$$c_{eff} = \frac{\left(\frac{\partial H}{\partial s}\right)}{\left(\frac{\partial T}{\partial s}\right)} = \frac{\left[\left(\frac{\partial H}{\partial x}\right)l_{sx} + \left(\frac{\partial H}{\partial y}\right)l_{sy}\right]}{\left(\frac{\partial T}{\partial s}\right)},\ l_{sx} = \frac{\left(\frac{\partial T}{\partial x}\right)}{\left(\frac{\partial x}{\partial s}\right)},\ l_{sy} = \frac{\left(\frac{\partial T}{\partial y}\right)}{\left(\frac{\partial y}{\partial s}\right)} \qquad 3.44$$

And $\frac{\partial T}{\partial s}$ is defined:

$$\frac{\partial T}{\partial s} = \left(\frac{\partial T}{\partial x}\right)^2 + \left(\frac{\partial T}{\partial y}\right)^2 \tag{3.45}$$

Thus, the effective heat capacity is:

$$c_{eff} = \frac{\left[\frac{\partial H}{\partial x}\frac{\partial T}{\partial x} + \frac{\partial H}{\partial y}\frac{\partial T}{\partial y}\right]}{\left[\left(\frac{\partial T}{\partial x}\right)^2 + \left(\frac{\partial T}{\partial y}\right)^2\right]} \tag{3.46}$$

Lemmon [99] developed a new method to handle the effective heat capacity:

$$c_{eff} = \left\{\frac{\left[\left(\frac{\partial H}{\partial x}\right)^2 + \left(\frac{\partial H}{\partial y}\right)^2\right]}{\left[\left(\frac{\partial T}{\partial x}\right)^2 + \left(\frac{\partial T}{\partial y}\right)^2\right]}\right\}^{\frac{1}{2}} \tag{3.47}$$

Although the above two methods are good approximations in evaluating the effective heat capacity, an additional variable (enthalpy) is introduced to increase the computational complexity. Further, the temperature gradient at each step must be evaluated in both methods. Here, a simple and accurate method so called 'nodal assembly' of mass matrix to handle the effective heat capacity is presented. In the FEM, the assembly of mass matrix is based on element. The assembly of mass matrix based on the node guarantees that the phase change does not omitted. The principle of nodal assembly is the same as the node-based smoothed finite element (NS-FEM) as shown in Fig. 3.5. If one or two node's temperature is in the mushy range, it is not necessary to calculate the average temperature. It implies the pre-process to judge the element in phase range can be ignored. For numerical integration, the problem domain Ω is partitioned into N integration domains Ω_k (k=1, 2… N) with one for each node based on the background triangular mesh. The integration domain Ω_k for node k is created by connecting sequentially the mid-edge-points to the centroids of the surrounding triangles of node k. According to the node's temperature, we assign a

specific effective heat capacity to a node and multiply the mass matrix. It is noted there is no smoothed technique involved in the assembly of mass matrix. If the effective heat capacity is continuous function or constant value, the nodal assembly is the same as element assembly. A more accurate method is to find the interface using interpolation at each time step, which needs a lot of computational time and is very difficult to apply in the computer code. Thus, the nodal assembly of mass matrix not only keeps the main feature of fixed grid method, but also can capture the latent heat effect.

3.1.2.8 The time discretization

Although there are many time-stepping algorithms available, in this thesis only one-step methods and two-steps methods are discussed. The stability and convergence are two important factors in evaluating time stepping schemes. The family of one-step methods is characterized as follows:

$$\frac{\mathbf{M}(\mathbf{T}_{n+1}-\mathbf{T}_n)}{\Delta t}+(\overline{\mathbf{K}}+\mathbf{C})(\theta\mathbf{T}_{n+1}+(1-\theta)\mathbf{T}_n)=\mathbf{F} \qquad 0\le\theta\le 1 \tag{3.48}$$

The above time discretization is referred to as the θ method. In the θ method, θ is a parameter that determines the time stepping technique. When $\theta = 0, \frac{1}{2}, 1$, the time stepping scheme becomes Euler-forward, Crank-Nicolson, and backward respectively. If $\theta > \frac{1}{2}$, the numerical results are unconditional stable for non-linear and linear problems. In the θ method, only the Crank-Nicolson scheme is second order accurate in the time step size, and the rest are all first order accurate. However, the θ method presents oscillation in the temperature field although the numerical results converge.

The main reason is the discontinuity of effective heat capacity which results in oscillation in the neighborhood of the freezing front. Thus, two-steps methods are preferred in the time discretization for phase change problems. The first two-time-level scheme was the Lees three-level technique [100]:

$$(\overline{\mathbf{K}}^n + \mathbf{C}^n)\left[\frac{\mathbf{T}_{n+1} + \mathbf{T}_n + \mathbf{T}_{n-1}}{3}\right] + \mathbf{M}^n\left[\frac{\mathbf{T}_{n+1} - \mathbf{T}_{n-1}}{2\Delta t}\right] = \mathbf{F}^n \tag{3.49}$$

$$\mathbf{T}_{n+1} = \left[\frac{\overline{\mathbf{K}}^n + \mathbf{C}^n}{3} + \frac{\mathbf{M}^n}{2\Delta t}\right]^{-1}\left[-\frac{\overline{\mathbf{K}}^n + \mathbf{C}^n}{3}\mathbf{T}_n - \frac{\overline{\mathbf{K}}^n + \mathbf{C}^n}{3}\mathbf{T}_{n-1} + \frac{\mathbf{M}^n}{2\Delta t}\mathbf{T}_{n-1} + \mathbf{F}^n\right] \tag{3.50}$$

Lees three-level method is stable, but the solution exhibited strong oscillatory behavior. This is because T defined in Eq. (3.50) is based on the average $\mathbf{T} = \frac{\mathbf{T}_{n+1} + \mathbf{T}_n + \mathbf{T}_{n-1}}{3}$.

The most general two-steps time discretization is [100]:

$$\mathbf{M}\frac{(\mathbf{T}_{n+1} - \mathbf{T}_n)}{\Delta t} + (\overline{\mathbf{K}} + \mathbf{C})((\frac{1}{2} + a)\mathbf{T}_{n+1} + (\frac{1}{2} - 2a)\mathbf{T}_n + a\mathbf{T}_{n-1}) = \mathbf{F} \tag{3.51}$$

$$\mathbf{T}_{n+1} = \left[\mathbf{M} + \Delta t \times (\frac{1}{2} + a)(\overline{\mathbf{K}} + \mathbf{C})\right]^{-1}\begin{bmatrix}\mathbf{F} \times \Delta t - (\Delta t \times (\frac{1}{2} - 2a)(\overline{\mathbf{K}} + \mathbf{C}) - \mathbf{M})\mathbf{T}_n \\ -\Delta t \times a \times (\overline{\mathbf{K}} + \mathbf{C})\mathbf{T}_{n-1}\end{bmatrix} \tag{3.52}$$

Many researchers have found $a = \frac{1}{4}$ works very perfectly in pure solidification simulations [100]. The results were found stable and very accurate, and the thermal properties should be evaluated at the time step t^n[101]. Therefore, in this thesis, we use Eq. (3.52) with $a = \frac{1}{4}$ to discretize the time.

3.1.3 Numerical example

3.1.3.1 Case 1: Single probe

The test problem considered is the freezing of a liver tumor. For small tumors with regular shape, a single probe is sufficient to freeze the tumor. For simplicity, the tumor is modeled as a sphere of 8mm in diameter. The probe of 2 mm diameter is targeted at the center of the tumor. A schematic of the 2D geometry for the liver tumor cryosurgery is depicted in Fig. 3.6. The temperature at the outer boundary of the liver is kept constant at T=37^{o}C. The initial temperature in the tissue is set at 37^{o}C.

The thermal property is listed in Table 3.1. Because the property of the tumor is not available, it is taken to be the same as normal tissue in the simulation. The internal working process of the probe is very complicated, and it is assumed that the probe works as a heat sink. The cooling rate is 2.4×10^{-7} W/m^{3}s for 5 seconds. After 5 seconds, the heat sink is maintained at 1.2×10^{-8} W/m^{3}. Two sets of different meshes, coarse mesh with 291 nodes and fine mesh with 12876 nodes are shown in Fig. 3.7. The reference model using 12876 nodes are sufficient to capture the physics of the problem, because the same numerical results are obtained using more dense nodes (19872 nodes). This implies that numerical results have already converged using 12876 nodes. In order to prevent the recurrence of cancer, the standard cryosurgical technique must freeze 10mm beyond the tumor [71]. Thus, the mesh is dense in the region surrounding the tumor in the coarse mesh.

It has been well known that the final temperature is a key factor contributing to freezing injury during cryosurgery [71, 79-81]. The destructive effects in cryosurgery can be classified as two types: one is immediate and another is delayed. The delayed effect is due to the restriction of blood flow. However, the vascular stasis should be taken over a few days. In this thesis, only the immediate effect (direct cell injury) is investigated. For direct cell injury, extracellular and intracellular ice crystallizations are serious effects to cell viability. In particular, intracellular ice crystallization is lethal to cells. A cell is collapsed due to the excessive stress resulting from volumetric expansion of water.

The temperature profiles at time t=600s for the αFEM model, together with linear FEM and reference solutions are shown in Fig. 3.8. It can be found that, the numerical solutions obtained using the present αFEM are in very good agreement with those of the reference ones compared with FEM. This validates our two-dimensional αFEM model for phase change problem in the bioheat transfer process. At the region surrounding the tumor, the temperature changes very fast and phase change occurs. However, the FEM model using triangular element gives very poor results in this region. This is due to the "overly-stiff" phenomenon of a fully-compatible FEM model of assumed temperature based on the Galerkin weak form. As expected, the tissue temperature far away from the tumor is almost unchanged compared the region near the probe. In cryosurgery, minimizing the damage to healthy tissue is crucial to determine a successful treatment. From Fig. 3.8, it is found that the healthy region of the liver tissue is not affected by the cooling too

much. On the other hand, the temperature along the periphery of the tumor is about -90^{o}C much lower than the critical temperature (-40^{o}C) to kill the tumor.

Because the temperature at the center of the tumor is the lowest, it is necessary to investigate the temperature variation with the time at this point as shown in Fig. 3.9. It is found that there are severe oscillations for FEM model using coarse mesh. The oscillation is due to discontinuity in the effective heat capacity and thermal properties. Additionally, the temperature variation with time predicated by FEM is much larger than the reference solution. However, the αFEM model can avoid the oscillation in the simulation as shown in Fig. 3.9. Moreover, the numerical results from αFEM is closer to the reference compared with the FEM. This phenomenon is due to the use of a combination of FEM and NS-FEM which gives the model close to exact stiffness. The novel formulation of αFEM has overcome the 'overly-stiff' of FEM and 'overly-soft' NS-FEM, thus it can provide much more accurate results compared with the standard FEM.

Figure 3.10 presents the size and location of ice ball generated by the freezing of probe at t=600s. The isothermal surface T=-1^{o}C separates the ice ball and unfrozen tissue. During the freezing process, the ice ball is developed by the probe. Based on the size and location of ice ball obtained from numerical simulation, the clinician can have a good understanding of freezing necrosis for a specific probe. Therefore, the clinician can select the correct probe parameters to achieve a desirable lesion size [71, 79-81]. As shown in Fig. 3.10, the ice ball for the FEM, αFEM and reference is presented. The ice ball domains predicted by the FEM, αFEM and reference are listed as follow:

$$-39mm \le x \le 0mm,\ 35mm \le y \le 75mm \quad \text{(FEM model)}$$
$$-40mm \le x \le 2mm,\ 35mm \le y \le 76mm \quad (\alpha\text{FEM model})$$
$$-42mm \le x \le 3mm,\ 32.5mm \le y \le 78mm \quad \text{(reference model)}$$

It is easily noticed that the domain of ice ball developed by the FEM model is much smaller than that of the reference model, however, the αFEM model can predict more closely the region compared with the FEM. In Fig. 3.10, it is found that the whole region developed by the ice ball exceeds the region of the tumor. The location and size of ice ball in medical treatment are very important to control the freezing to maximize damage to the tumor cell. These information can minimize the damage to healthy liver tissues to avoid an irreversible injury to the neighboring liver tissue due to the over freezing.

The mushy zone (determined by the isothermal T=-8^{o}C and T=-1^{o}C) predicted by the αFEM , FEM and reference is also depicted in Fig. 3.10. As shown in Figure 3.10, the mushy zone is marked in green. It is obviously found that the location and size of the mushy region is developed by αFEM which matches very well with the reference model compared with the FEM. The information of the mushy zone is beneficial for cryosurgeons to plan a specific extent and size of the freezing lesion [79].

The destructive mechanisms occurring after the phase transition is also lethal to tumor cells in the solid state [72]. The mechanical stress is caused due to the temperature gradient during the cooling. Many experiments have shown that the stress due to the constrained contraction of the frozen tissues can easily exceed the yield strength of the frozen tissues, which results in plastic fracture or deformation [72]. As

shown in Figure 3.11, the temperature gradients for the FEM, αFEM and reference model are presented. It is found that the maximum temperature gradient occurs at the edge of probe. This is because the edge of probe is the boundary of heat sink. It is also expected the temperature gradient at the region far away from the probe is quite small, which preserve the property of healthy tissues. From Fig. 3.11, it can be observed again that the computed results obtained using the αFEM are more accurate than that obtained from the linear FEM, and closer to the reference, especially in the high temperature gradient region. It is well known that triangular elements are not suitable for FEM without additional treatment in some cases such high gradient problem due to the 'overly-stiff' property. Such an "overly-stiff" behavior is responsible for the inaccuracy in temperature gradient solutions for triangular mesh. However, the αFEM works very well in triangular elements even in coarse mesh in the numerical simulation. More importantly, the triangular element is very easily generated in any mesh generator. In an addition, the tissue in the human body is quite complicated, thus, the triangular element is a good candidate.

3.1.3.2 Case 2: Multiple probes

It is very difficult to control the freezing process for large tumors and irregular shape tumors with a single probe. Large tumors with irregular shape are extremely tough to destroy due to difficult optimization of cooling rate and location of probes. The use of multiple probes facilitates the overlapping of the required frozen areas in the treatment of large tumors, and provides a method of destroying the tissue to the desired

size and shape in complex tumor ablation [79]. Therefore, it is obvious that the use of multiple probes can shorten the time of treatment. However, the use of multiple probes may limit the applicability of the thermocouple to measure the tissue temperature, which creates some difficulty in monitoring the freezing effect. Thus, numerical simulation provides an effective tool to track the tissue temperature responses and significantly improve the treatment. In an addition, the treatment parameters can be optimized through numerical simulations before the tumor operation [79].

Two examples of regular tumor with 12mm diameter and irregular tumor as shown in Fig. 3.12 are presented in this section. Three identical probes with 2mm diameter are targeted at the tumor. In order to compare the numerical results of FEM and αFEM, four sets of mesh for regular and irregular shape tumors are shown in Figure 3.13 and 3.14 respectively. The cooling rates for regular and irregular shape tumor are 1.4×10^{-7} W/m^{3}s and 1.44×10^{-7} W/m^{3}s respectively for 5 seconds. After 5 seconds, the heat sink is constant at 7×10^{-7} W/m^3 and 7.2×10^{-7} W/m^3 for regular and irregular tumors respectively. Fig. 3.15 present the temperature contours at the time t=600s for regular shape of tumor. From Fig. 3.15, it can be clearly found that, compared with the numerical solution obtained from standard FEM using the same triangular mesh; the present αFEM solution in temperature is much closer to the reference result. The temperature profile predicted by the FEM has a large deviation from the reference model. It is obviously shown that the temperature surrounding the probe is much lower than the region far away from the probe in Figure 3.15. This is one of attractive feature of cryosurgery that the healthy region of the tissue is not damaged.

In section 3.1.3.1, it is mentioned that the final temperature is a dominating factor affecting the destructive mechanism. The following Fig. 3.16, 3,17 and 3.18 check the numerical accuracy by plotting the time history of temperature at sample points A, B, C (center of each probe) in the regular shape tumor (shown in Fig. 3.13), for present αFEM and FEM using the same mesh as well as the reference solution with 12974 nodes. It can be clearly seen that the computed temperatures of A, B, and C obtained from αFEM are closer to the reference results than those of linear FEM using the same linear mesh. The αFEM model so-constructed possesses 'close to exact' stiffness, and hence can produce more accurate results

Figure 3.19 describes the temperature contours at the time t=600s for irregular shape tumor. In Fig. 3.19, once again, it is clearly found that, the FEM results of temperature are much larger than the reference solutions at the tumor domain, while the αFEM solutions are in good agreement with the reference solutions. For irregular shape tumor, the temperature far away from the probe also almost keeps unchanged, compared with temperature at the domain surrounding the tumor. However, the temperature is more difficult to control in the irregular shape tumor. Thus, accurate prediction of temperature distribution, precise treatment planning and optimization of cryosurgery process are very important.

Figure 3.20, 3.21 and 3.22 compare the temperature variation with time at sample points D, E, F (center of each probe) in the irregular shape tumor (shown in Figure 2.14) for αFEM and FEM using 322 nodes as well as the reference solution using 11978

nodes. As expected, the numerical results from αFEM is closer to the reference model compared with FEM model.

In the treatment planning stage, the reference results using very fine mesh for both regular and irregular shape tumors took around 25 hours for Dell PC with Inter® Pentium (R) CPU 2.80GHz, 2.00GB of RAM . It is well known that accurate temperature prediction is crucial in the treatment planning process. Although the computation cost is lower for FEM model with coarse mesh (about 2 hours for 322 nodes), solutions obtained from FEM has a large deviation from the reference. For αFEM, the most important factor consuming CPU time is the low sparsity in the stiffness matrix due to more local nodes used in computing the smoothed strain fields. Based on the analysis of section 3.3, it is noted that the αFEM and FEM have the same complexity, the computational time for αFEM using coarse mesh (322 nodes) is about 2.3 hours. Thus, the αFEM is a good way to simulate the phase problem in cryosurgery to reduce the computational time without losing accuracy.

The αFEM is found to be superior to the FEM in terms of computational efficiency, accuracy, stability. This is because αFEM has overcome the drawback of NS-FEM with 'overly-soft' property and FEM with 'overly-stiff' property. More importantly, the αFEM model possesses a "close-to-exact" stiffness and can produce exact solutions, in contrast to the "overly-stiff" FEM model that produces lower bound solutions, and NS-FEM that produces upper bound lower property[7].

3.2 Alpha finite element (αFEM) for bioheat transfer in the human eye

3.2.1 Mathematical model for human eye

In this section, the αFEM is formulated to investigate bioheat transfer in the human eye such as temperature distribution in the steady state, hyperthermia treatment and sensitivity analysis. In order to compare the results of previous work done by others, the unit for temperature in this section 3.2 is used Kevin instead of Degree. Figure 3.23 shows the eye anatomy. The anterior portion of the eye contains the cornea, anterior chamber and iris. The posterior portion contains the lens, vitreous and sclera. A, B, C, D, and E are points on the corneal surface, anterior of lens, anterior of vitreous, posterior of vitreous and the sclera.

The Pennes bioheat equation [20] is used to analyze heat transfer in the human eye. Since only a small part in the human eye is responsible for blood perfusion and metabolic heat generation, these two terms can be neglected. Thus, the final governing equation for steady state condition can be written as follow:

$$k\nabla^2 T + Q = 0 \tag{3.53}$$

where K is the thermal conductivity of tissue of human eye, T is the temperature of tissue of human eye, and Q is external heat source.

The first boundary condition can be defined as follow:

At the sclera,

$$-k\frac{\partial T}{\partial n} = h_{bl}(T - T_{bl}) \tag{3.54}$$

Here, *n* is the outward normal direction on the surface boundary, h_{bl} is the coefficient of ambient convection, and T_{bl} is the blood temperature.

The second boundary condition is at the cornea, where heat is lost to the ambient environment

$$-k\frac{\partial T}{\partial n} = h_{amb}(T - T_{amb}) + \sigma\varepsilon(T^4 - T_{amb}^4) + E \tag{3.55}$$

The three terms on the RHS of the equation denote heat loss due to convection, radiation and tear evaporation. T_{amb} , σ , ε , and E represent the ambient temperature, the Stefan Boltzmann constant(5.67×10^{-8} $Wm^{-2}K^{-4}$), Emissivity (0.975) and Evaporation rate. The properties of each part of the eye are listed in Table 3.2 [102]:

3.2.2 Formulation of the αFEM

In this section, we first present the formulation of the FEM based on the standard Galerkin weak form [2]. The weighted residual equation can be obtained by multiplying Eq. (3.53) with a test function *w* over the entire domain.

$$\int_\Omega (wk\nabla^2 T + wQ)d\Omega = 0 \tag{3.56}$$

Using integration by parts:

$$\begin{aligned} k\int_\Omega \nabla w\cdot\nabla T d\Omega = {} & Q\int_\Omega w d\Omega - \int_{\Gamma_2} w h_{bl}(T - T_{bl})\mathrm{d}\Gamma - \\ & \int_{\Gamma_3} w((h_{amb}(T - T_{amb}) + \sigma\varepsilon(T^4 - T_{amb}^4) + E)\mathrm{d}\Gamma \end{aligned} \tag{3.57}$$

The field temperature can be approximated in the following form；

$$T = \sum_{i=1}^{m} \mathbf{N}_i \mathbf{T}_i \tag{3.58}$$

where $\mathbf{N}_i$ is the shape function, $\mathbf{T}_i$ is the unknown nodal temperature. In the Galerkin weak form, the weight function w is replaced by the shape function $\mathbf{N}$.

So the standard Galerkin weak form is expressed as:

$$k\int_{\Omega}\nabla\mathbf{N}\cdot\nabla\mathbf{T}d\Omega+h_{bl}\int_{\Gamma_2}\mathbf{N}\cdot\mathbf{N}\mathbf{T}\,\mathrm{d}\Gamma+h_{amb}\int_{\Gamma_3}\mathbf{N}\cdot\mathbf{N}\mathbf{T}\,\mathrm{d}\Gamma=Q\int_{\Omega}\mathbf{N}d\Omega+\int_{\Gamma_2}\mathbf{N}h_{bl}T_{bl}\,\mathrm{d}\Gamma-\int_{\Gamma_3}\mathbf{N}(-T_{amb}+\sigma\varepsilon(T^4-T_{amb}^4)+E)\mathrm{d}\Gamma \tag{3.59}$$

The discretized system equation can be finally obtained and written in the following matrix form:

$$[\mathbf{K}+\mathbf{M}]\{\mathbf{T}\}=\{\mathbf{F}\} \tag{3.60}$$

where the stiffness, force and mass matrices are given by:

$$\mathbf{K}=k\int_{\Omega}\nabla\mathbf{N}\bullet\nabla\mathbf{N}d\Omega \tag{3.61}$$

$$\mathbf{F}=Q\int_{\Omega}\mathbf{N}d\Omega+\int_{\Gamma_2}\mathbf{N}h_{bl}T_{bl}\,\mathrm{d}\Gamma+\int_{\Gamma_3}\mathbf{N}(T_{amb}+T_{amb}^4-E)\mathrm{d}\Gamma-\int_{\Gamma_3}\mathbf{N}\sigma\varepsilon T^4\,\mathrm{d}\Gamma \tag{3.62}$$

$$\mathbf{M}=h_{bl}\int_{\Gamma_2}\mathbf{N}\cdot\mathbf{N}\mathbf{T}\,\mathrm{d}\Gamma+h_{amb}\int_{\Gamma_3}\mathbf{N}\cdot\mathbf{N}\mathbf{T}\,\mathrm{d}\Gamma \tag{3.63}$$

It is noted that the presence of the non linear term in the force matrix can be dealt with by using an iterative scheme in the solution.

In the αFEM, the formulation process for the mass and force matrix is the same as the standard FEM procedure. The stiffness in the Eq. (3.61) can be formulated in the process of αFEM mentioned in the section 3.1.2.6.

3.2.3 Numerical results for 2D problem

In considering hyperthermia treatment of the eye tumor, it is important to calculate the temperature distribution in the eye under steady state condition. Figure 3.24 shows

the thermal patterns of the eye model using FEM with 151 nodes, αFEM with 151 nodes, and FEM with 11113 nodes as reference. It is observed that numerical results obtained from FEM and αFEM using coarse mesh are in good agreement with the reference results. The parameters for steady sate condition are illustrated in Table 3.3:

The temperatures along the papillary axis at different locations (A, B, C, D, and E as shown in Fig. 3.23) are presented in Fig. 3.25. The lowest temperature occurs at the corneal surface. This is due to large heat loss to the ambient environment. It is also observed that temperature increases along the papillary axis.

3.2.3.1 Case study 1: Hyperthermia model

Cancer cells in the eyes can develop into tumors. These cells are often found in the eyeball, the eyelids and the orbit. There are largely two types of tumors, known as retinoblastoma and melanoma, within the eyes that can badly affect vision. In serious cases, eye tumors can spread to other parts of the human body. Thus, it is very important to detect eye tumors and give proper treatment at an early stage. There are many ways to treat eye tumors. Hyperthermia treatment is often found to be powerful and effective.

The main concern in hyperthermia treatment is to preserve vision and eye structure. The size and location of the tumor is a key point to determine this risk. The main challenges in hyperthermia models for the human eye are the change in blood flow rate and thermal properties. These make it difficult to predict heat transfer in the tissue. Heating for hyperthermia can be through microwave heating, ultrasound heating,

electrode heating, or thermal dose [103]. Any form of external heating or internal heating can be adopted in hyperthermia treatment depending on the heating source. A typical medical application in hyperthermia is cancer treatment by selectively attacking deep-seated tumors with high temperature [104]. The main feature of hyperthermia treatment in the human eye is to increase the tumor temperature up to 315K-319K without major effect on the surrounding tissue. It is noted that the ambient temperature is kept 273K in the hyperthermia treatment simulation. As shown in Figure 3.26, the external heat source is distributed in a small circle with radius $r=0.36mm$, and the power of the heat source is $Q_{rm}=3.5\times10^{7}w/m^{3}$.

3.2.3.1.1 Convergence study

In order to illustrate the novel property of αFEM , a convergence study is conducted by employing three models with 174, 1215 and 2315 uniformly distributed nodes as shown in Fig 3.26. The equivalent strain energy norm for heat transfer problems [2] is defined as:

$$U_T = \int_\Omega \bar{\mathbf{g}}^T \mathbf{k} \bar{\mathbf{g}} \, d\Omega \qquad 3.64$$

where, in our current case, $\bar{\mathbf{g}}$ is the smoothed temperature gradient.

The αFEM makes the good use of lower bound solution of FEM and upper bound solution of NS-FEM, thus the exact solution in equivalent strain energy exactly falls in the range of the αFEM with an $\alpha \in [0,1]$. This implies that the exact solution in equivalent strain energy can be obtained using the αFEM using triangular elements with $\alpha \in [0,1]$. The important property is proven by Liu [8].

When $\alpha = 0$, the αFEM is exactly the same as the FEM with lower bound property. When $\alpha = 1$, the αFEM becomes the NS-FEM with upper bound property. If α changes from 0 to 1, the solutions of the αFEM are continuous functions of α from the solution of the NS-FEM and that of the standard FEM.

The exact equivalent strain energy of the test problem is 2.274×10^5 $Jm^{-3}K$ using FEM with 12827 nodes. As shown in Fig. 3.27, the equivalent strain energy increases with increase of α for three different set of meshes. When $\alpha \in [0.4, 0.6]$, the energy curves for three sets of mesh intercept the exact equivalent strain energy, which strongly demonstrates the novel property of αFEM capable of providing the exact energy norm. The corresponding temperature solution of the αFEM using $\alpha = 0.5$ with the nearly exact energy is also much better than those of either the standard FEM or the NS-FEM [8].

3.2.3.1.2 Temperature distribution

The temperature at different locations is plotted in Fig. 3.28 to show the results of αFEM, FEM using a coarse mesh and the reference mesh respectively. It is observed that αFEM gives more accurate results than FEM using the same 3-node triangular mesh and linear shape functions. This validates that αFEM can provide more accurate results. It is also found that the tissue temperature around the heating source is around $310K$, which is desirable in hyperthermia treatment because it is below the critical threshold. This is one of the most attractive features of internal heating and it is frequently used to thermally kill tumors in deep tissues, although it

may cause some mechanical injuries [56]. As shown in Fig. 3.28, the highest temperature always occurs at the heating source in the αFEM model, FEM model and reference model. Thus, it is necessary to investigate the temperature at the heating source.

Figure 3.29 describes the temperature distribution along the circumference of the heat source in counterclockwise direction starting from the left horizontal. It is observed that the temperature obtained from αFEM is closer with the reference solution compared with FEM.

Figure 3.30 shows the maximum temperature at the heating source. Again, the αFEM result is in good agreement with the reference solution. On the other hand, the FEM result deviates significantly from the reference result. The predicated maximum temperature of αFEM is about 1.5K away from the reference solution. That of the FEM is, however, about 3.2K, when the same mesh is used. We know that even one degree difference can make a significant difference in the treatments. Therefore, the improvement of αFEM on the solution accuracy is very important. Such an improvement is achieved by a 'close to exact stiffness' property of the αFEM [8].

3.2.4 Numerical results for 3D analysis

3.2.4.1 Sensitivity analysis

A similar analysis for the 2D eye model has been done by [102, 105] to study various factors determining the temperature distribution within the eye. In this section, we extend the 2D model to a 3D model as shown in Fig. 3.31 to identify the key factors

affecting the temperature distribution in the human eye and provide some possibilities to identify the sickness. It is noted that all other parameters are kept at steady state condition when changing the control parameters. Results at five sample points (the intersection of the anterior corneal surface with the axis of symmetry), B (anterior of lens), C (anterior of vitreous)， D (posterior of vitreous), E (sclera) are chosen to carry out the sensitivity analysis.

Firstly, the results of temperature contours for the 3D model under steady state condition using the FEM, and the αFEM with the same mesh of 620 nodes are plotted in Fig. 3.32. The reference solution obtained using a very fine FEM model with 17386 nodes is also computed and plotted in Fig. 3.32. As shown in Fig. 3.32, the temperature distribution patterns for both FEM and αFEM match the reference results very well under steady state conditions. It is also found that the temperature contour for the 3D model is quite similar to the 2D model under steady state conditions. The temperature increases from the ocular surface to the sclera along the papillary axis as shown in Figure 3.33. The difference between the 2D and 3D model is that the temperature along the papillary axis in the 3D model is slightly higher than the 2D model. This is due to the extra dimension for heat transfer.

In the following investigations, the fine mesh of 17386 nodes is used.

3.2.4.1.1 Effects of evaporation rate

The cornea surface contains a three-layered structure: a thin mucoid layer, a thick aqueous layer and an extremely thin oily layer. The function of the oily layer is to

retard evaporation from the eye. Five sets of data are used in this investigation. All the test data are between the maximum and minimum values recorded in experiments. Results in Table 3.4 have showed that evaporation rate is an important factor influencing the temperature distribution. From 30 Wm^{-2} to 230 Wm^{-2}, the temperature dropped by almost 2K at the corneal surface. The moisture level in the eyes is balanced by tear loss and tears production. Excessive or insufficient evaporation rate will break the balance. When this balance is broken, dry spots form on the surface of the eyes and cause irritation. Through the measurement of ocular temperature, the doctor can check for the symptoms and signs of chronic dry eye.

3.2.4.1.2 Effects of ambient convection coefficient

In this section, the effect of ambient convection coefficient is analyzed. As mentioned in section 3.2.1, there is heat exchange between the eye and the enviorment. The results in Table 3.5 have shown that with increase in the ambient convection coefficient, the temperature in the human eye decreases. The temperature at the corneal surface is the most sensitive to the variation of the ambient convection coefficient. However, the temperature for the inner part of human eye is not affected too much even when the ambient convection coefficient increases to the maximum value.

3.2.4.1.3 Effects of ambient temperature

At the corneal surface, there is heat loss due to convection and radiation. This is strongly related with the ambient temperature. The ambient temperature is also one of factors to affect the amount of tears in the eyes. The best way to relieve the symptoms

of dry eye is to maintain the eyes moist. In this section, five ambient temperatures listed in Table 3.6 are chosen to investigate the effect of the ambient temperature. It is observed that there is a significant change at the corneal surface temperature. However, there is only slight change in the retinal temperature with change in the ambient temperature.

3.2.4.1.4 Effect of blood temperature

At the unexposed eye, there is a heat exchange between the blood and the retina. Five values, 308, 309, 310, 311 and 312K, are employed to discuss the effect of blood temperature. It is noted that blood temperatures of 308, 310 and 312K are undesirable for the human eye. The objective of presenting this is to provide the possibility detecting sickness based on the ocular temperature [21]. For example, the measurement of ocular temperature can provide a quick way to check fever. Based on the ocular temperature, the doctor can have a better understanding of patient's condition and prescribe a more effective treatment. From Table 3.7, it is shown that the blood temperature is a dominant factor in the temperature distribution in the human eye compared with the blood convection coefficient. The temperature dropped by more than 3K when the blood temperature varied from 308 K to 312K. It is no wonder that the blood temperature plays an important role to regulate the human body's temperature. Changes in blood temperature affect the temperature distribution throughout the eye significantly.

3.2.4.1.5 Effect of blood convection coefficient

The blood convection coefficient is determined by the blood flow in the human eye. The values of 50, 70, 90, 110 and 120 $Wm^{-2}K^{-1}$ are employed to assess the importance of the blood convection coefficient. From Table 3.8, it is found that the temperature variation at each location is minimally affected. The temperature difference between the maximum blood convection coefficient and the minimum blood convection coefficient is less than 0.5K.

From the above analysis, it is found that evaporation, ambient temperature and blood temperature are the most important factors dominating the temperature distribution in the human eye. These 3D results are the same as finding in 2D reported by Scott and Ooi [21, 28].

3.2.4.2 Case study 2: Hyperthermia model

In this section, the 3D human eye of hyperthermia treatment is investigated. A 3D model is important to predict the temperature distribution accurately in the hyperthermia model. In the 3D model, the heating source is distributed in a small sphere with radius $r = 0.6mm$ as shown in Fig. 3.34. The power of heat source is $Q_{rm} = 4 \times 10^7 w/m^3$.

The problem domain is firstly discretized with 1292 regularly distributed nodes, based on which the 4-node tetrahedrons are constructed as shown in Fig 3.34. For comparison, FEM solutions are also computed using the same tetrahedral mesh. The

reference solutions are obtained using FEM with a refined mesh of 17867 regular nodes.

The computed temperature patterns of the whole domain using αFEM are plotted in Fig. 3.35, together with linear FEM and reference solutions. As outlined in Figure 3.35，it can be found that the temperature contours at the corneal surface obtained from the αFEM model are in very good agreement with those of the reference ones compared with the FEM model. It is also observed that the lowest temperature always occurs at the corneal surface where there is a large heat transfer between the eye and the cooling ambient. Fig. 3.36 presents the temperature contour for section X-X obtained from FEM, αFEM and reference model. It is found that the temperature distribution at the heat source obtained from FEM has a large deviation from the reference model, while the αFEM still provides more close results to the reference compared with FEM at the heating source using the same mesh. This validates our three-dimensional αFEM model for bioheat transfer problems. As shown in Figure 3.36, the location of peak temperature is the heating source position. The raised temperature will kill the tumor without damaging the healthy tissue. Thus, the accurate prediction of temperature at the heating source is crucial to a successful treatment.

Figure 3.37 presents the peak temperature at the heating source. It is shown that the αFEM results agree well with the reference solutions, and are more accurate than those obtained from linear FEM using the same mesh. The difference of predicated maximum temperature between the αFEM and the reference solution is about 1.4K. That of the FEM is, however, about 3.1K with the same mesh. It is noted that the

present αFEM formulation is derived from the smoothed Galerkin weak form and standard Galerkin weak form. The αFEM model so constructed behaves "softer" compared with the FEM model, has "close to exact" stiffness feature and hence produces much more accurate results.

3.3 Remarks

In this work, two biological models using αFEM are established: one is phase change in the liver cryosurgery; another is bioheat transfer in the human eye. From the numerical results, the following remarks can be derived as:

1. Through numerical investigation, it is found that the αFEM achieves very accurate results compared to the FEM with the same number of degree of freedom. This is because that the αFEM can be made with a good combination of lower bound property for FEM and upper bound property for NS-FEM. Furthermore, the αFEM is not only spatially stable, but also temporally stable.
2. The αFEM uses triangular elements in two-dimensional and tetrahedral elements in three-dimensional problems, and hence is particularly good for very complicated in geometry. However, the triangular and tetrahedral elements are not suitable for standard finite element method in certain cases without additional treatment such as high temperature gradient.
3. In the αFEM model, no additional parameters or degrees of freedoms are needed; the system matrices have the same dimension with the FEM model of same mesh. Thus, the same computational complexity is expected for both

FEM and αFEM.

4. Based on the sensitivity analysis in the human eye, it has been found that blood temperature, ambient temperature and evaporation rate are the most important factors affecting the corneal surface temperature.
5. Last but not least, the measurement of ocular surface temperature of the human eye can provide a fast and safe way to detect fever and dry eyes, which can help doctors improve the diagnosis and treatment.

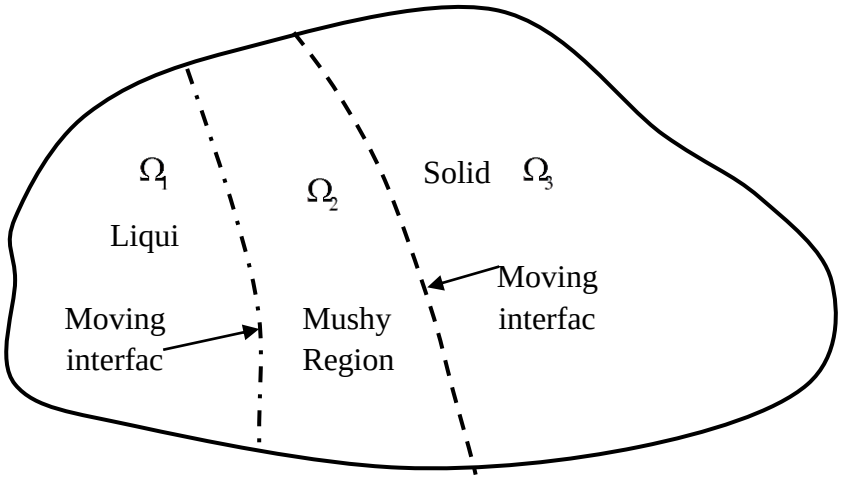

Figure 3.1: Domain of phase change

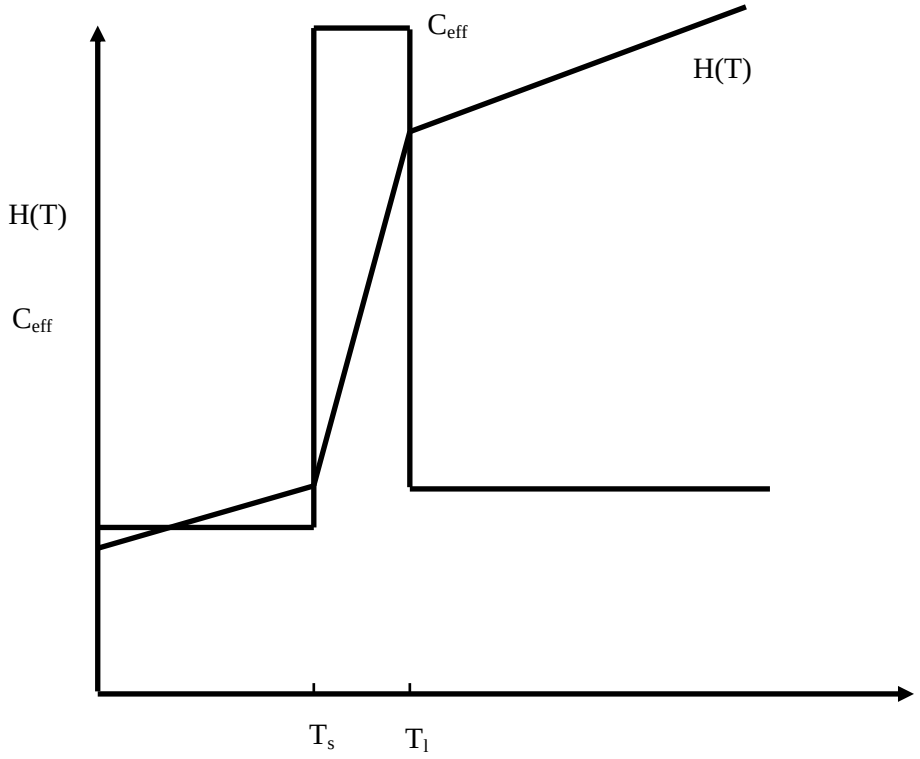

Figure 3.2: Plot of enthalpy, effective heat capacity against Temperature

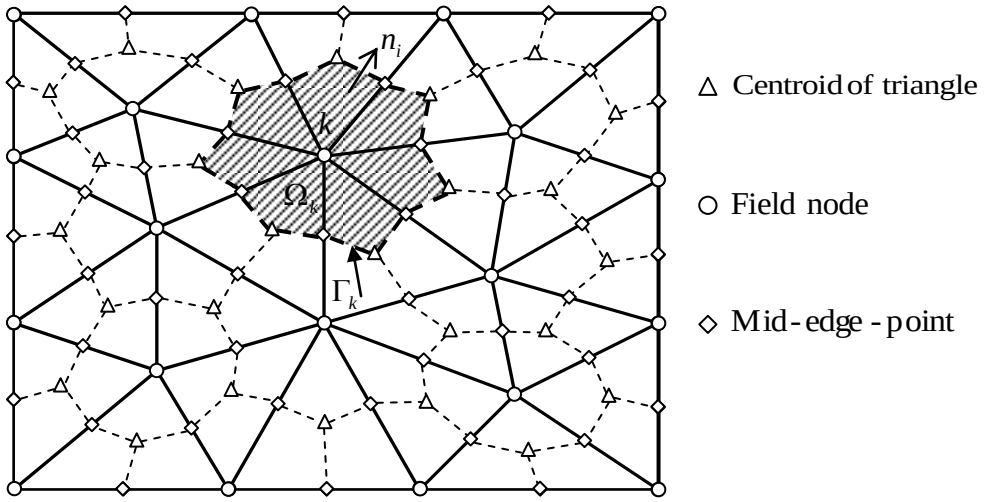

(a) background triangular cells and nodal smoothing domains for node *k* in 2D

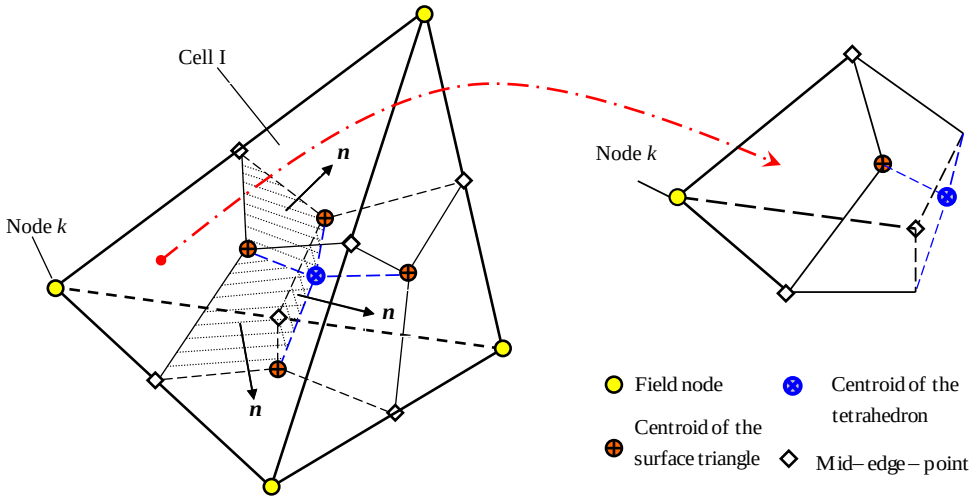

(b) background tetrahedral cells and nodal smoothing domains for node *k* in 3D

Figure 3.3: Illustration of smoothing domain in the NS-FEM

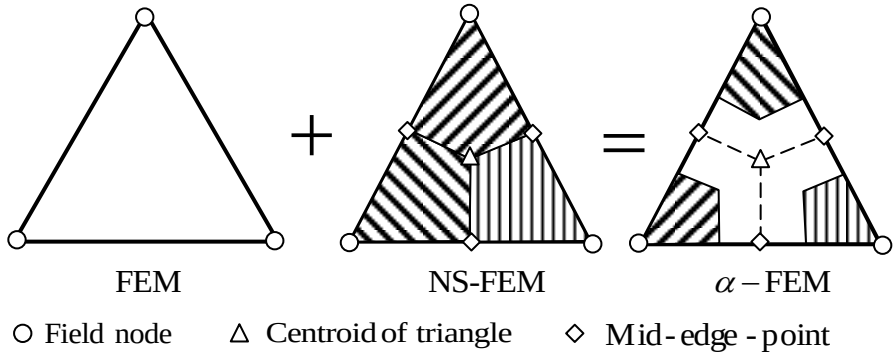

(a) Combination of triangular element of FEM and NS-FEM in 2D

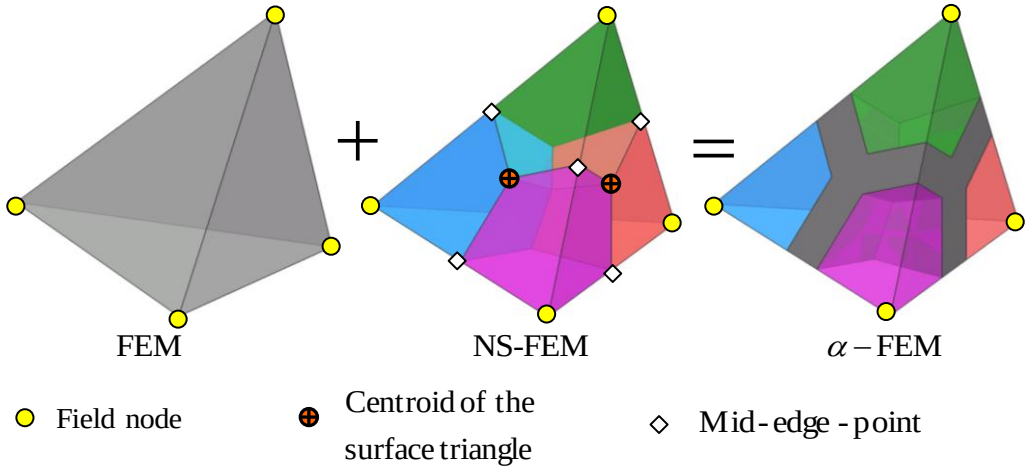

(b) Combination of tetrahedral element of FEM and NS-FEM in 3D

Figure 3.4: Illustration of smoothing domain in the αFEM

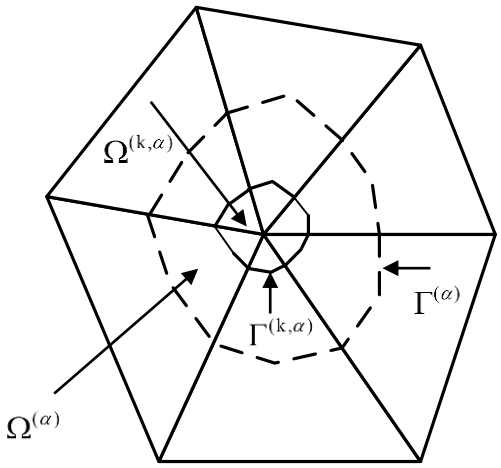

Figure 3.5: Cell associated with nodes for triangular elements in the αFEM

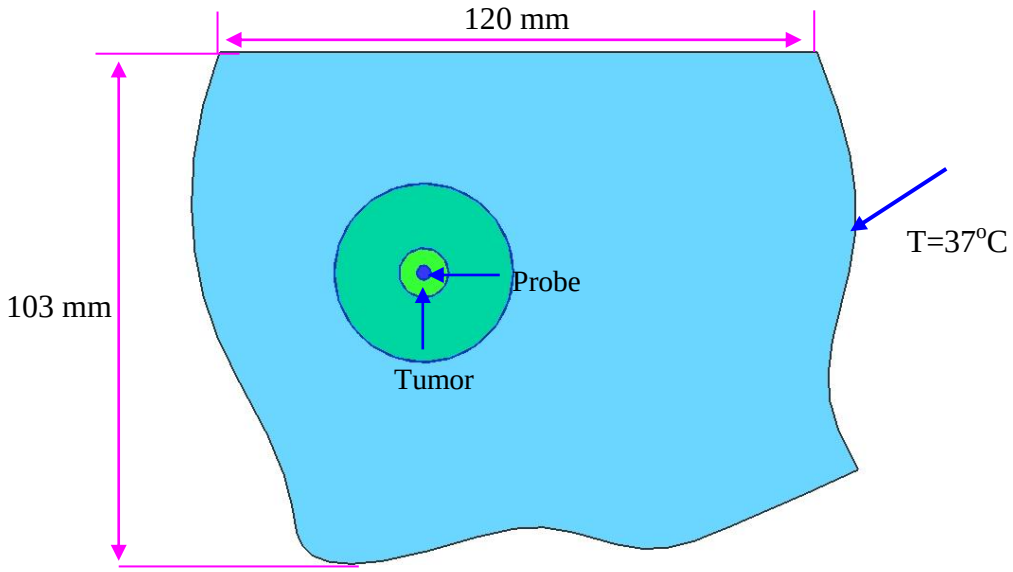

Figure 3.6: Geometry of investigated domain [106]

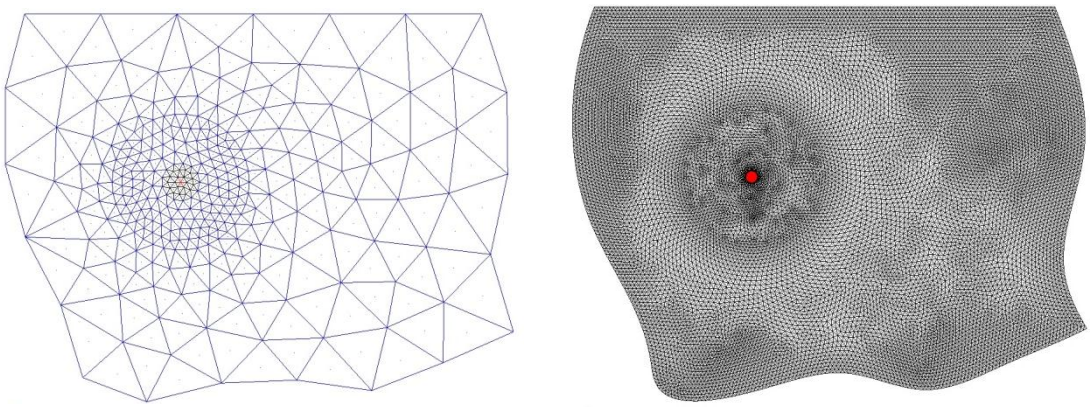

Mesh a: 291 nodes Reference mesh: 12876 nodes

Figure 3.7: Mesh for liver

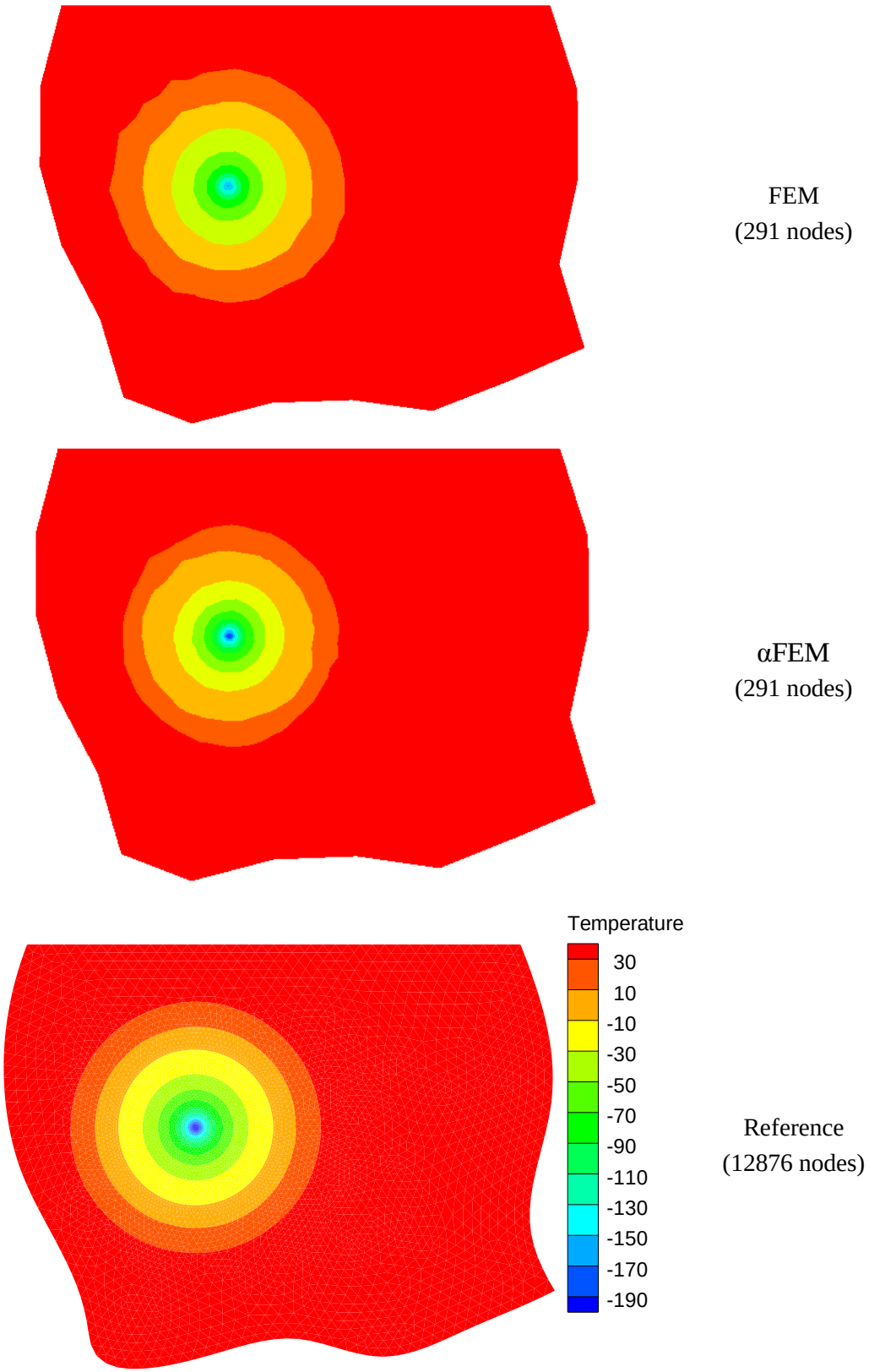

Figure 3.8: Comparison for temperature contour at t=600s

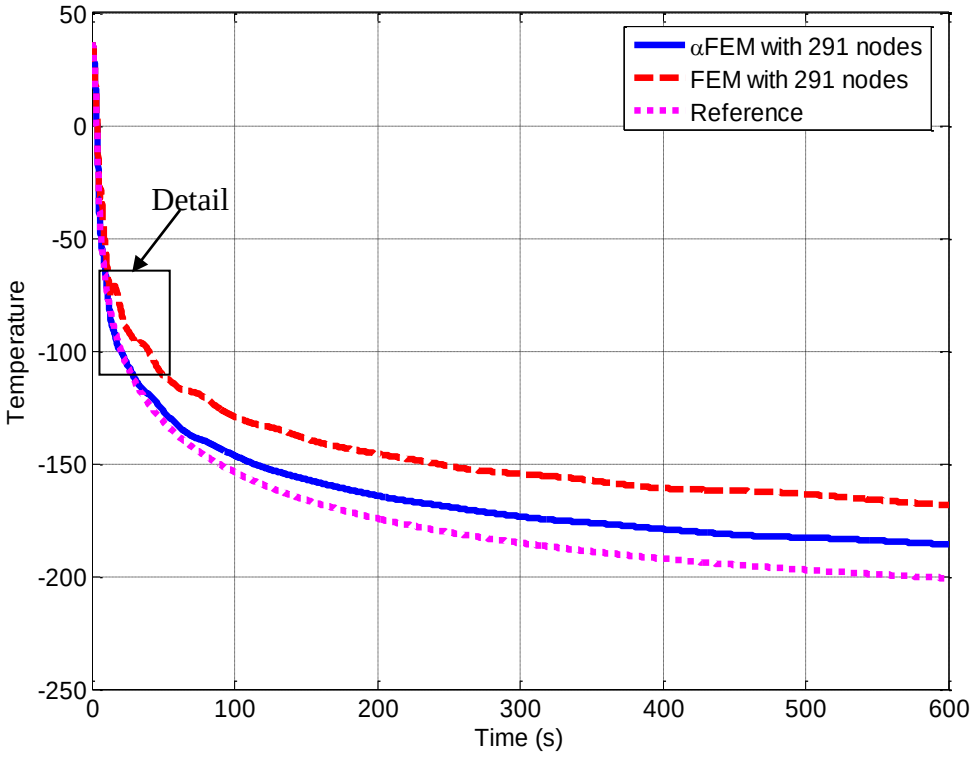

(a) Full scale distribution

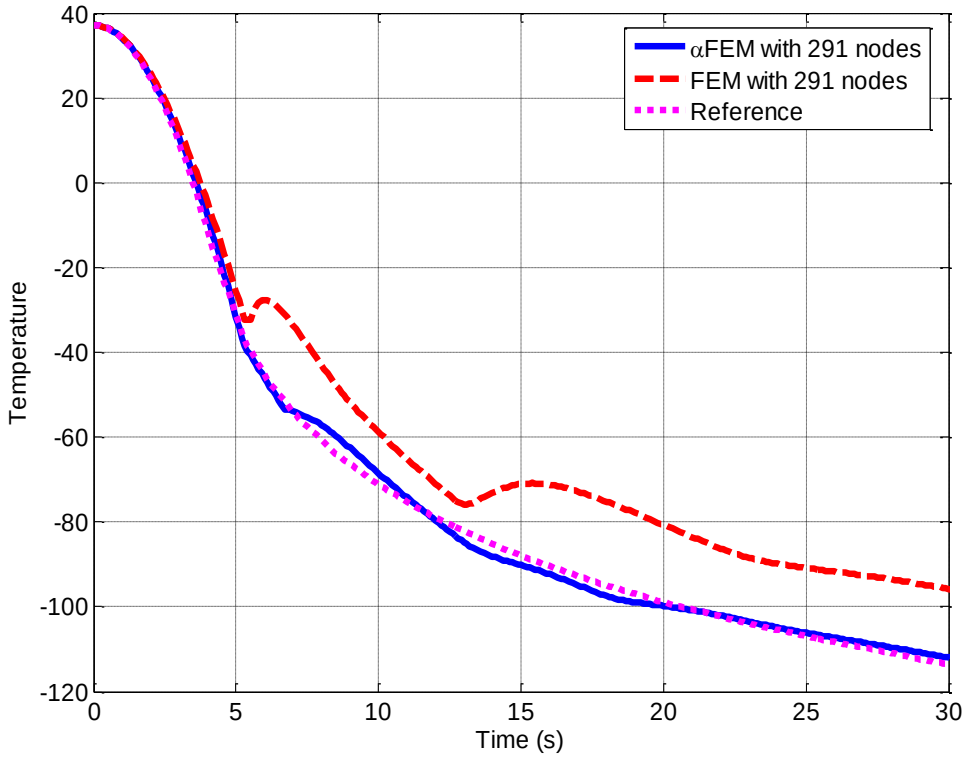

(b) Zoomed-in distribution

Figure 3.9: Temperature variation with time at the center of tumor

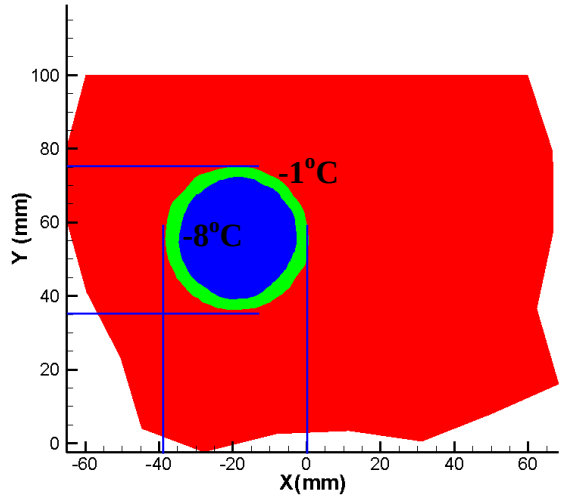

FEM model using 291 nodes

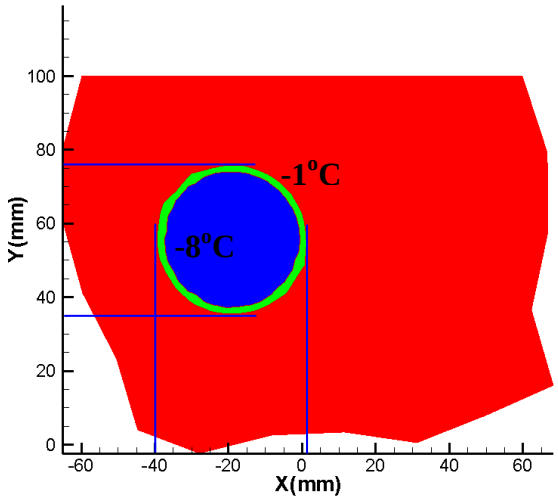

αFEM model using 291 nodes

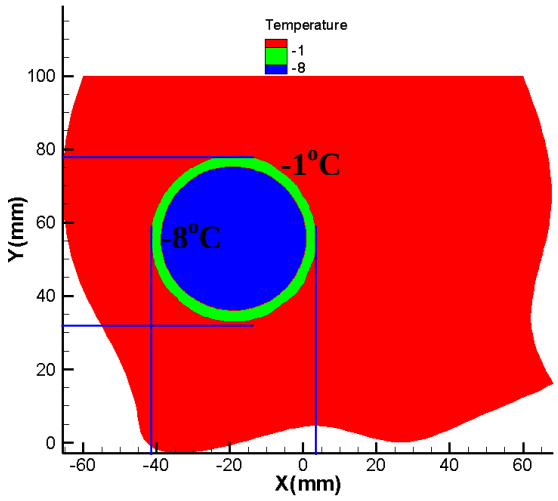

Reference model

Figure 3.10: Size and location of ice ball

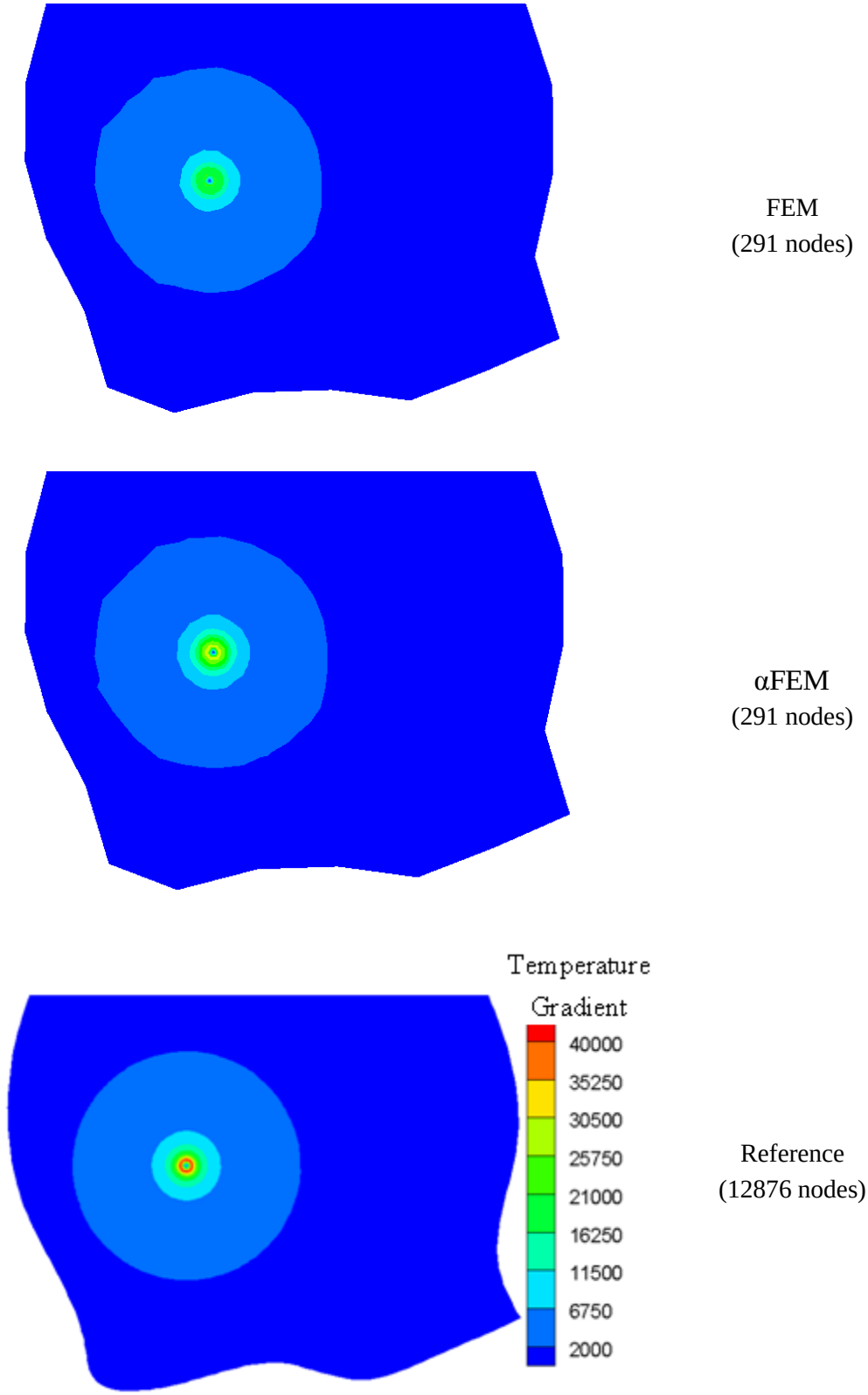

Figure 3.11: Comparison for temperature gradient

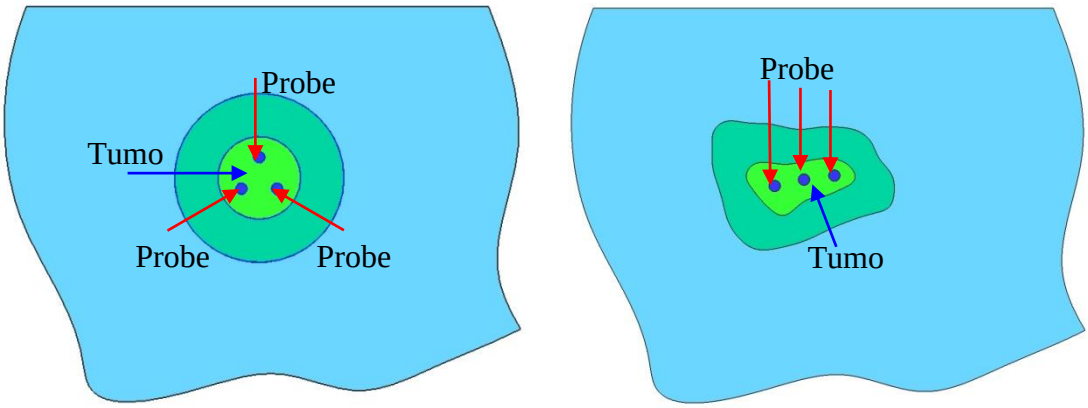

Regular shape with three probes Irregular shape with three probes

Figure 3.12: Geometry of liver

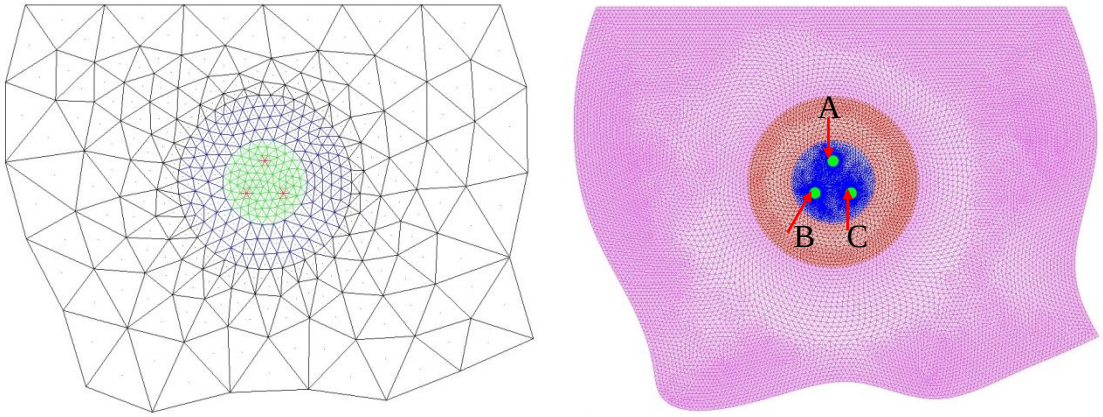

Coarse mesh information for regular shape Fine mesh information for regular shape

Figure 3.13: Mesh information for regular shape of tumor

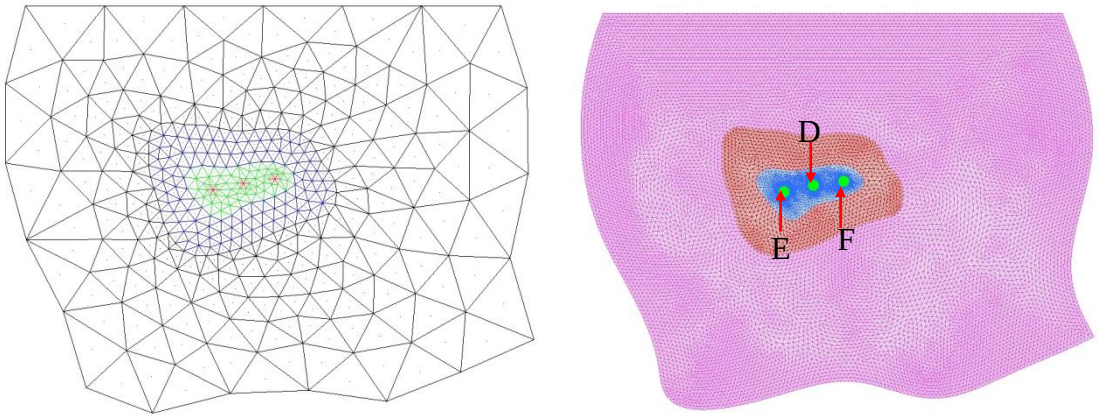

Coarse mesh information for irregular shape Fine mesh information for irregular shape

Figure 3.14: Mesh information for irregular shape of tumor

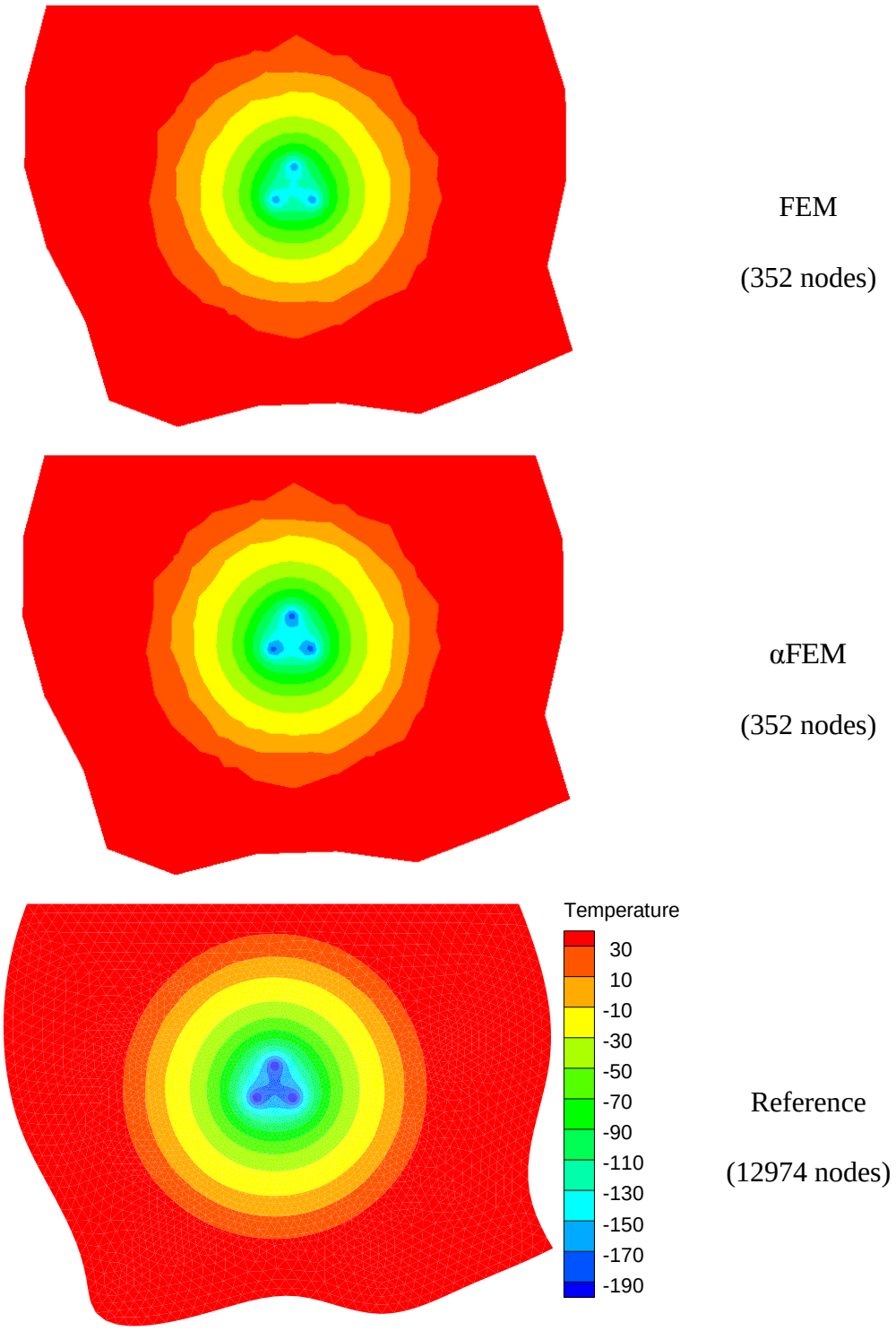

Figure 3.15: Comparison of temperature contour at time t=600s

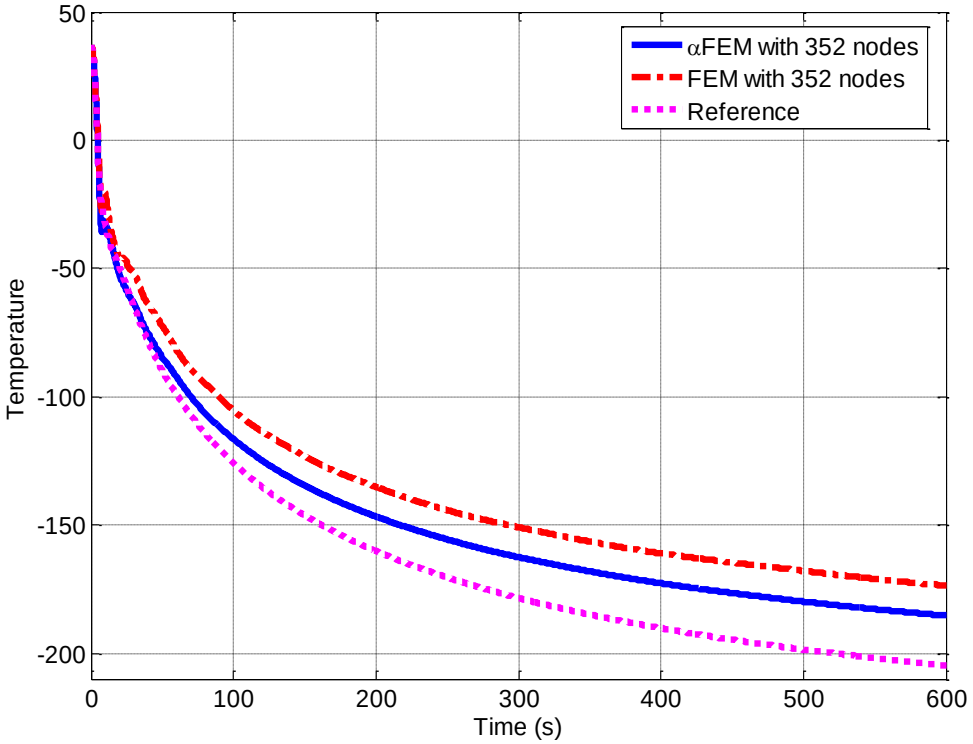

Figure 3.16: Point A temperature with time for regular shape tumor

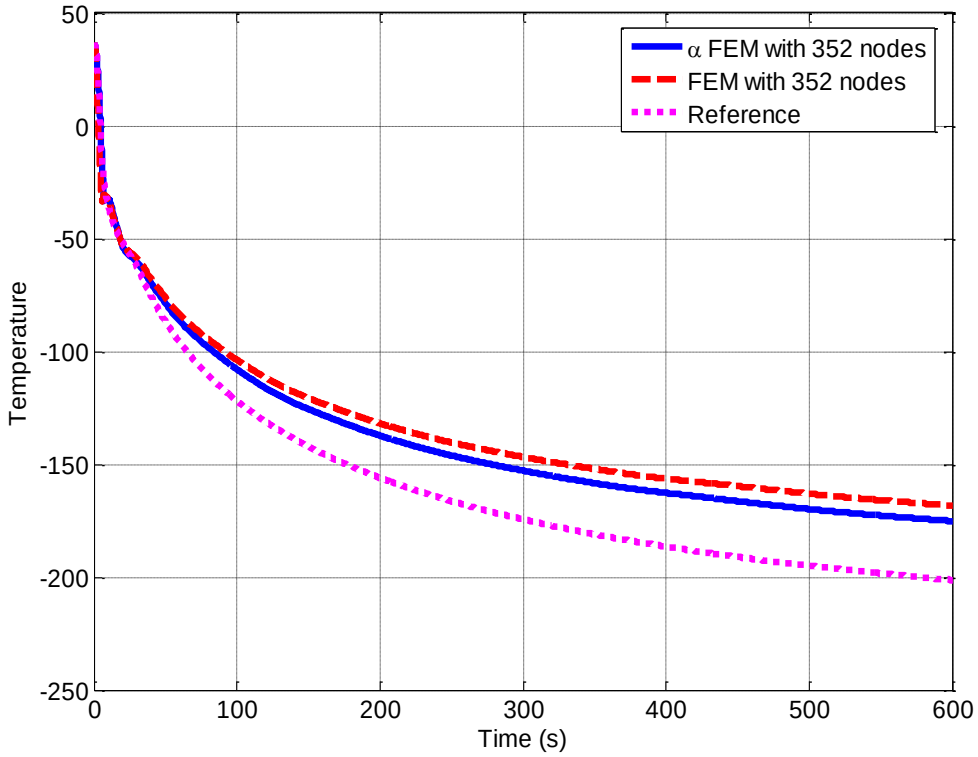

Figure 3.17: Point B temperature with time for regular shape tumor

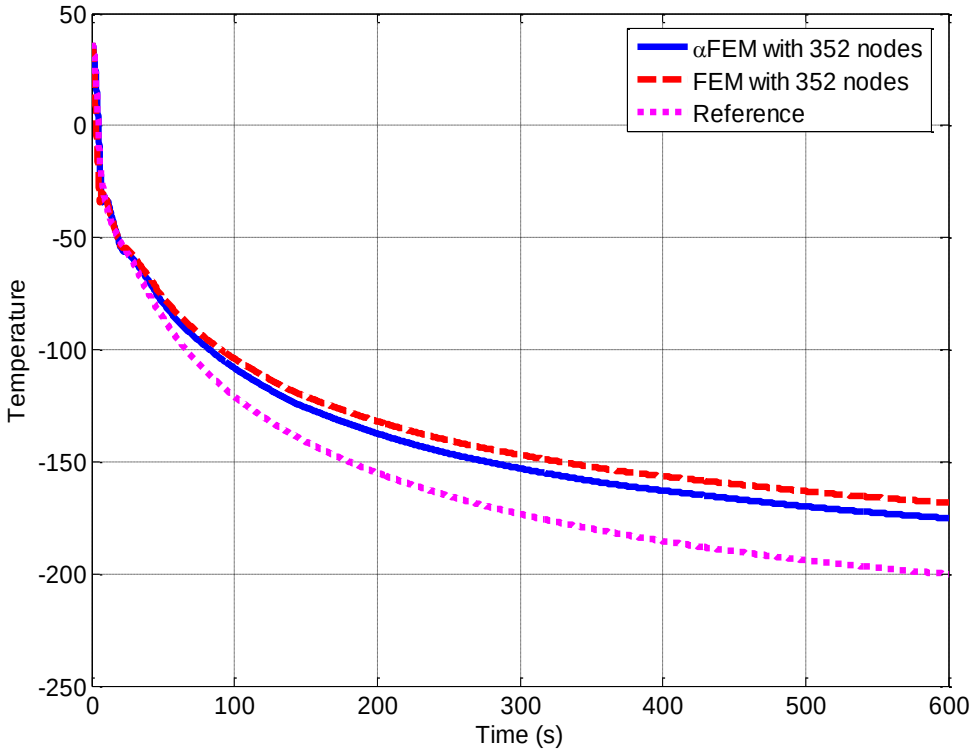

Figure 3.18: Point C temperature with time for regular shape tumor

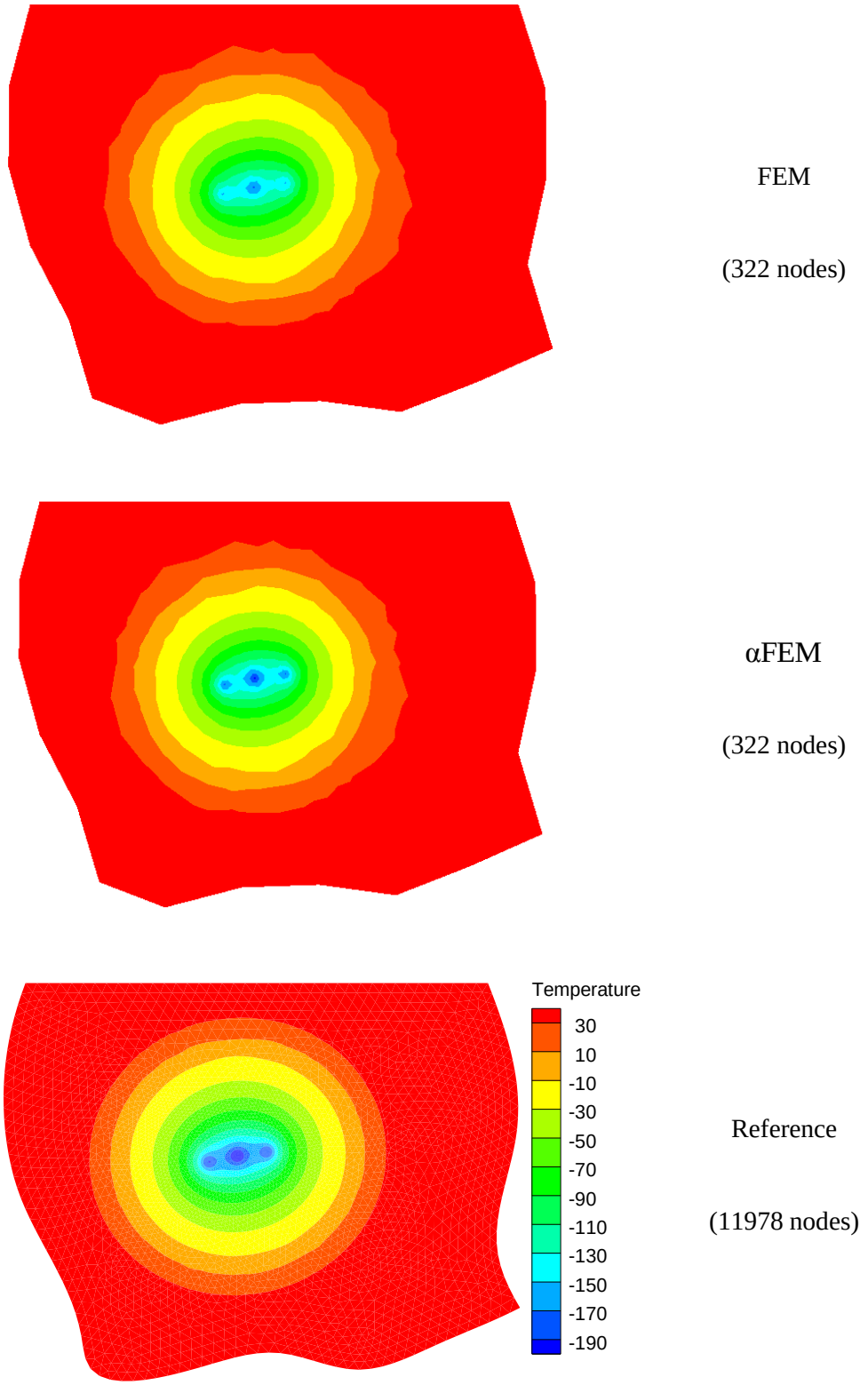

Figure 3.19: Comparison of temperature contour at time t=600s

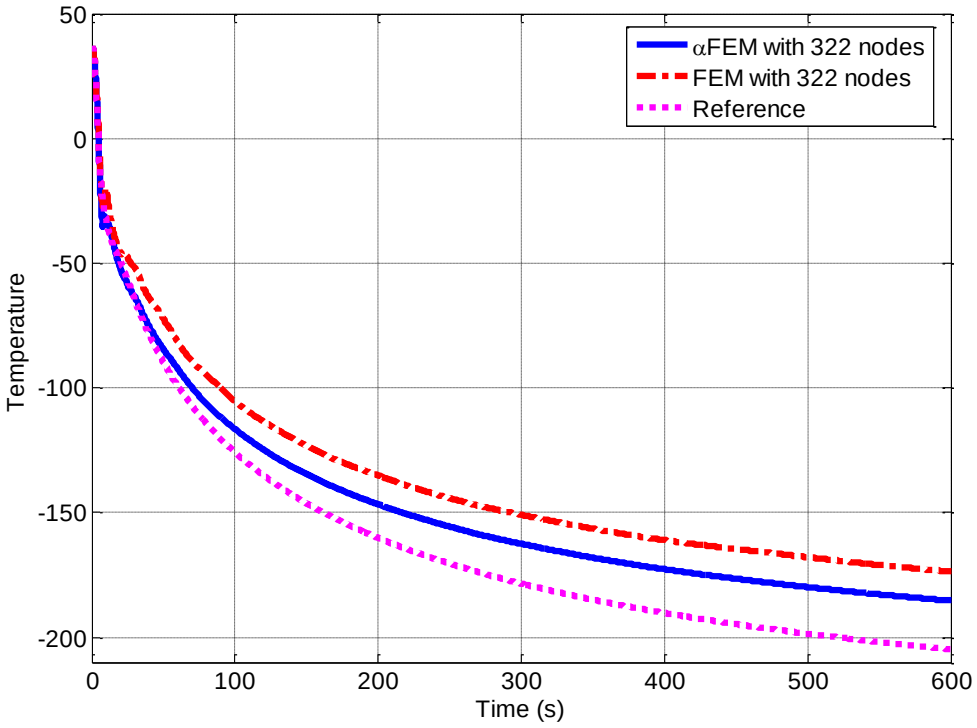

Figure 3.20: Point D temperature with time for irregular shape tumor

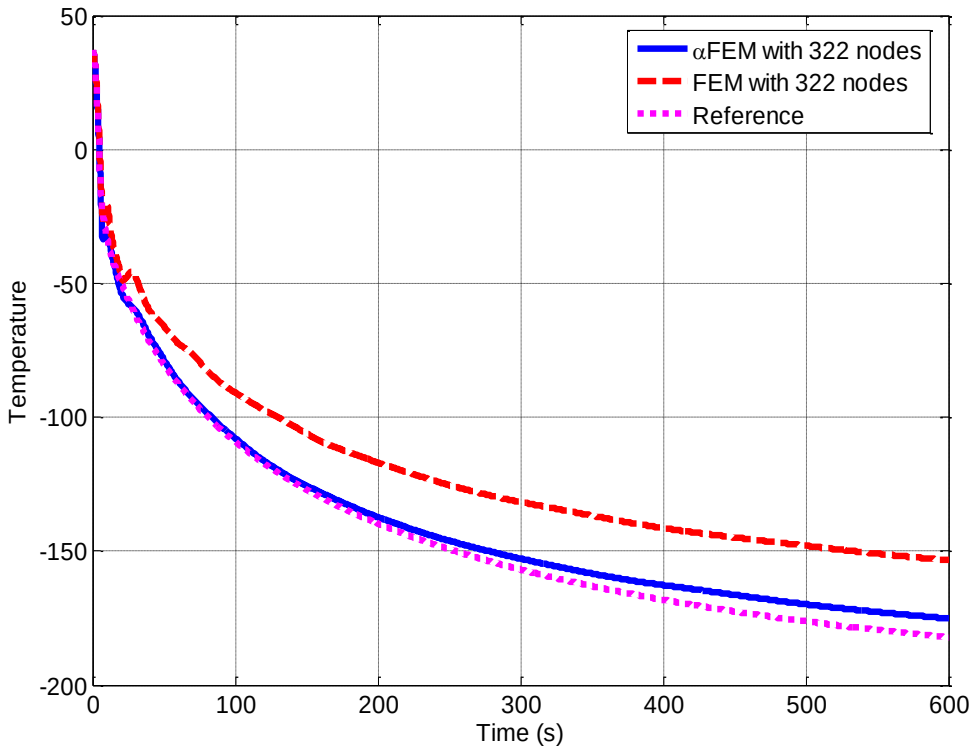

Figure 3.21: Point E temperature with time for irregular shape tumor

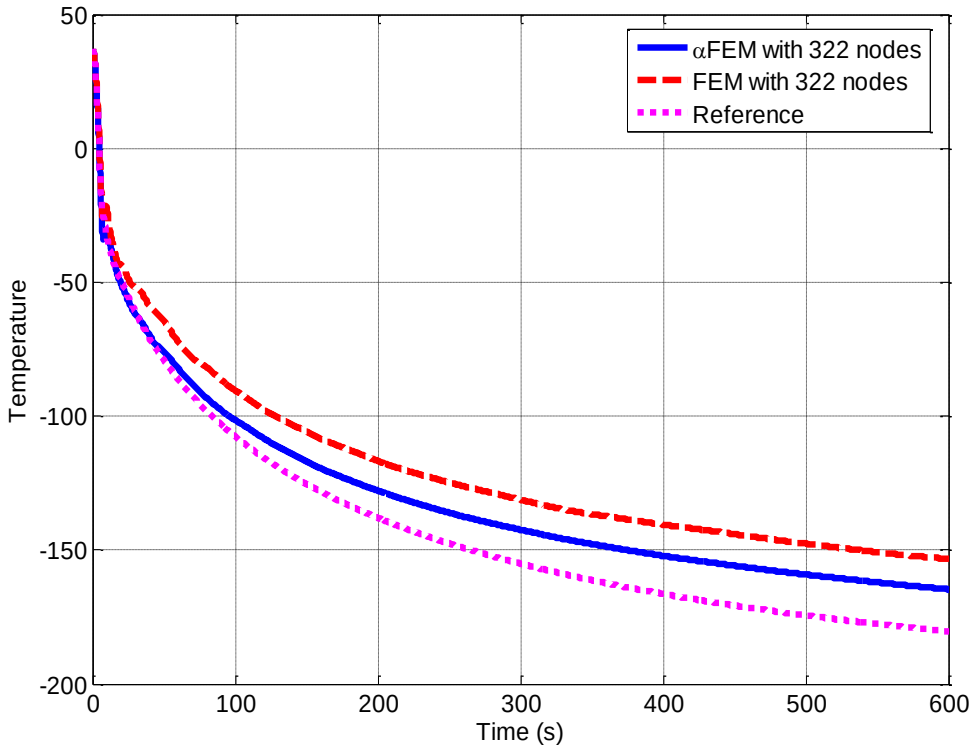

Figure 3.22: Point F temperature with time for irregular shape tumor

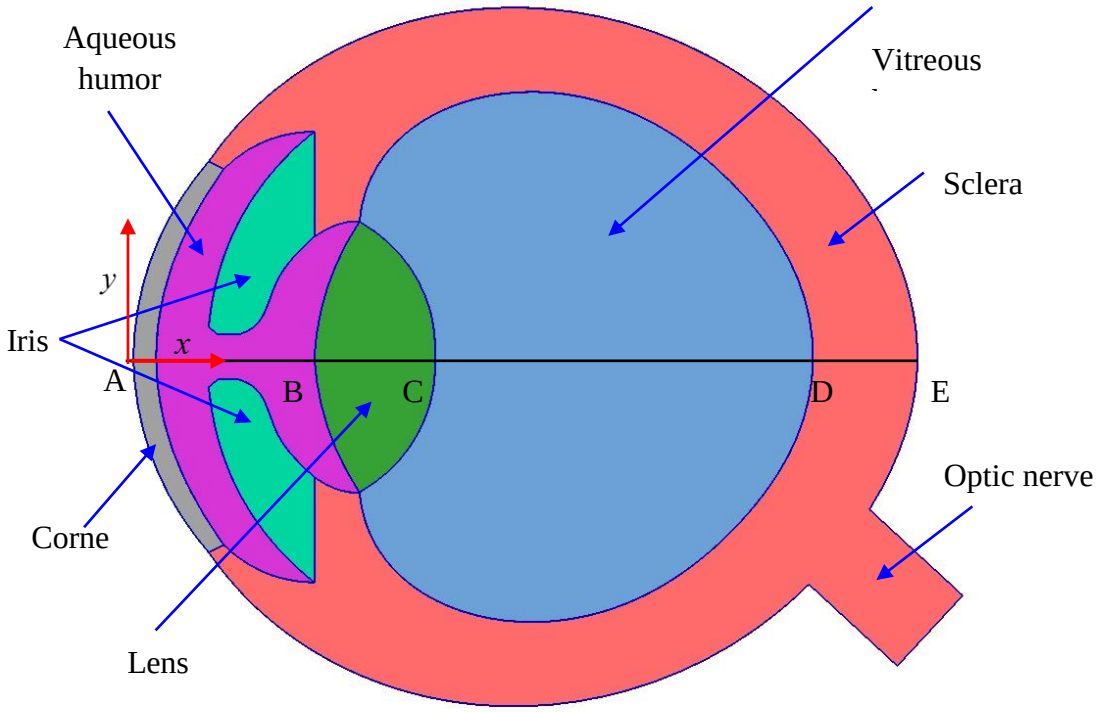

Figure 3.23: Anatomy of 2D model of eye

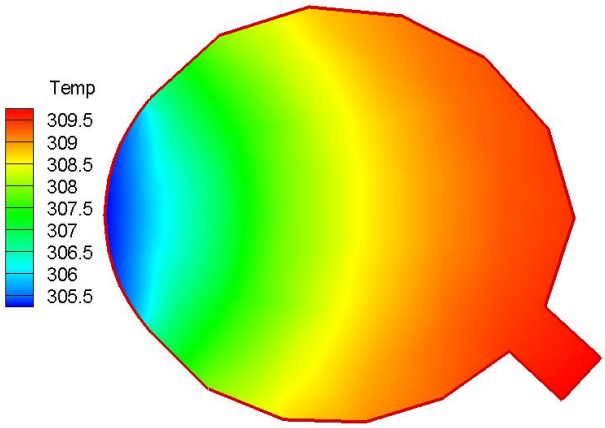

(a) Temperature contour for alpha FEM using 151 nodes

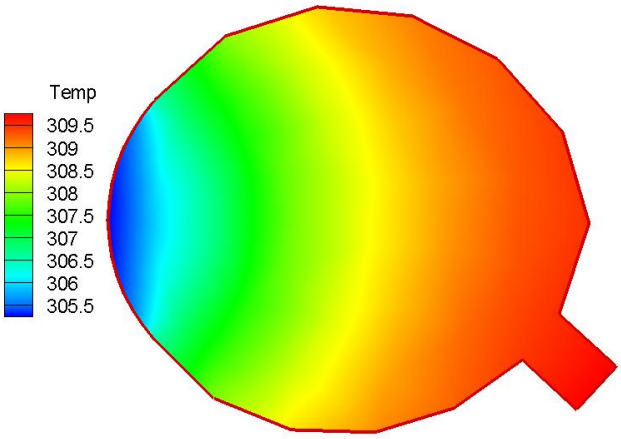

(b) Temperature contour for FEM using 151 nodes

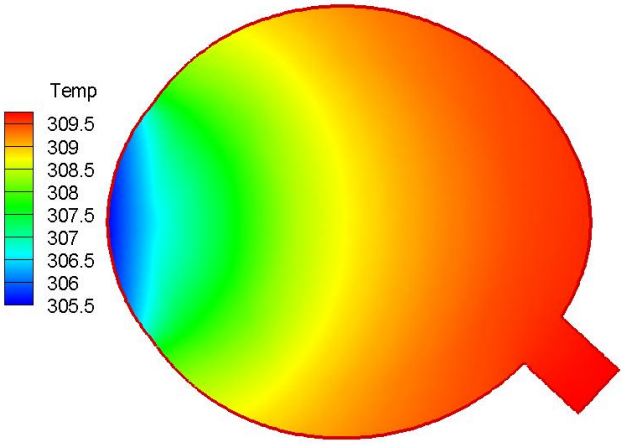

(c) Temperature contour for reference using 11113 nodes

Figure 3.24: Temperature contour of 2D eye model under steady condition

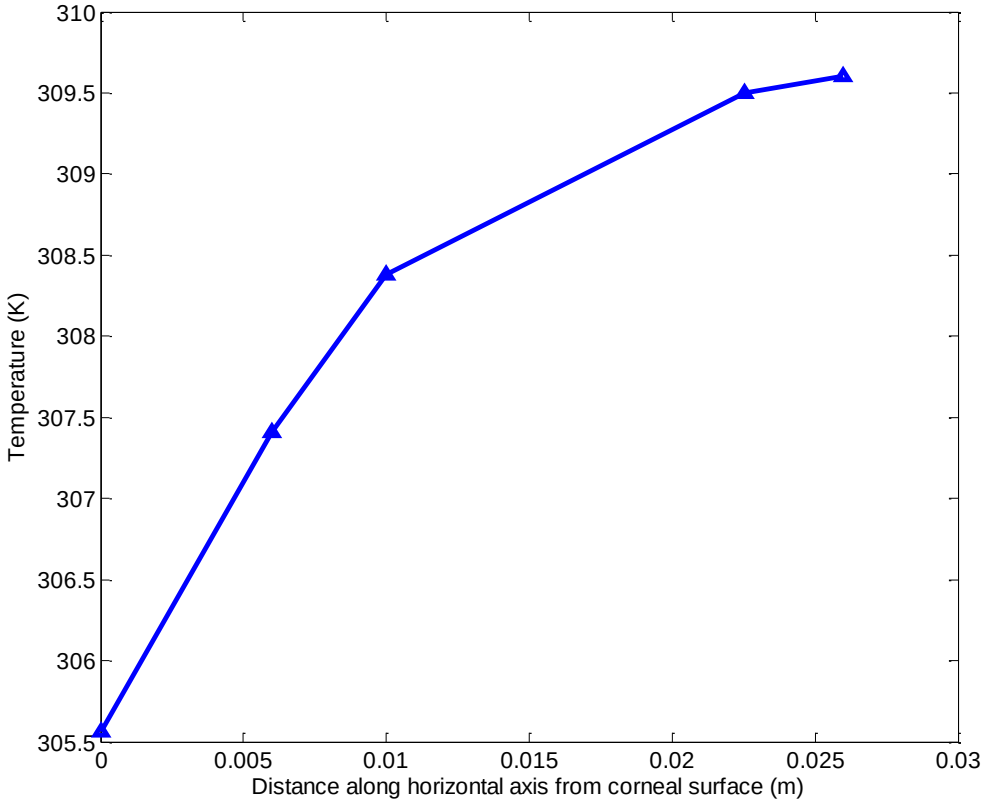

Figure 3.25: Temperature along horizontal axis from corneal surface

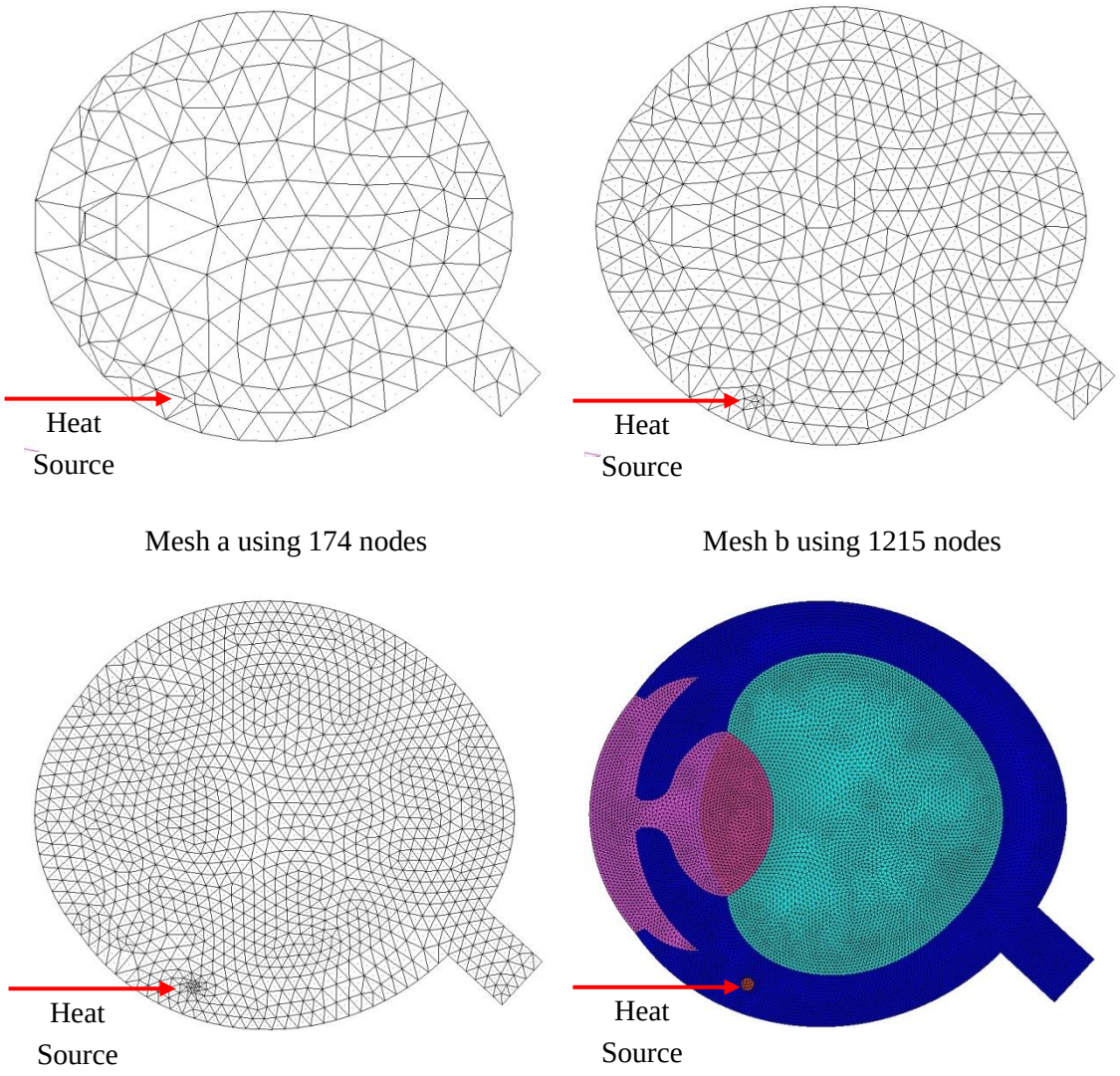

Mesh a using 174 nodes

Mesh b using 1215 nodes

Mesh c using 2315 nodes

Mesh d using 12827 nodes

Figure 3.26**:** Four sets of different mesh with heat source distributed in a small circle

Center of heat source : x=8.6mm, y=-9.3mm

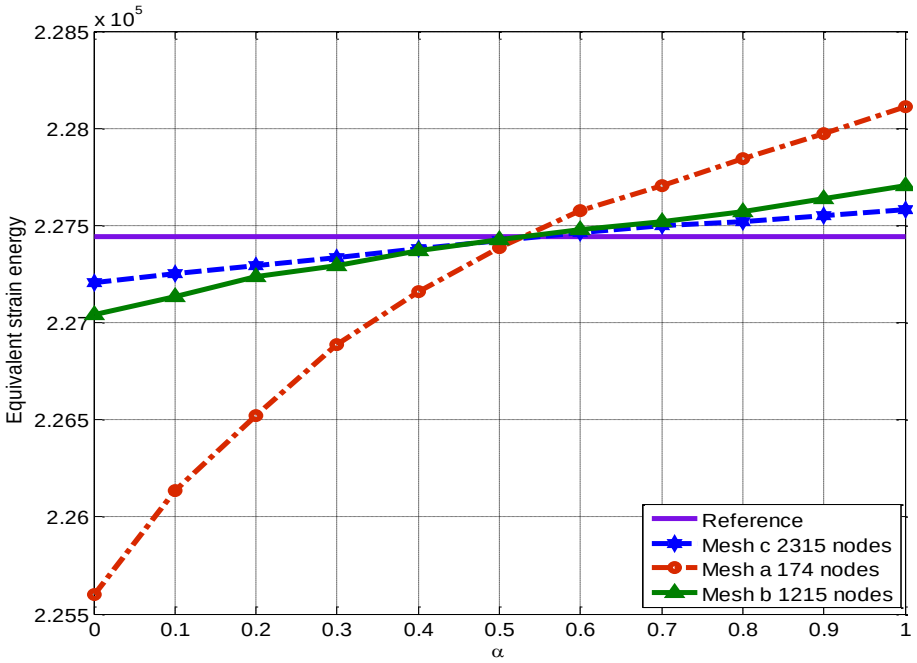

Figure 3.27: Equivalent strain energy

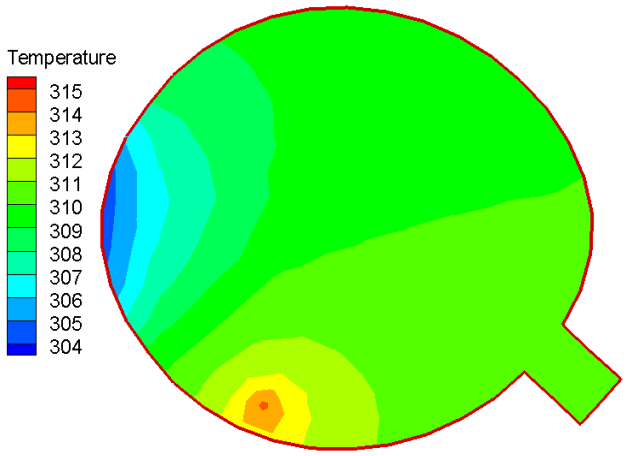

(a) Temperature contour for alpha FEM using 174 nodes $(\alpha = 0.5)$

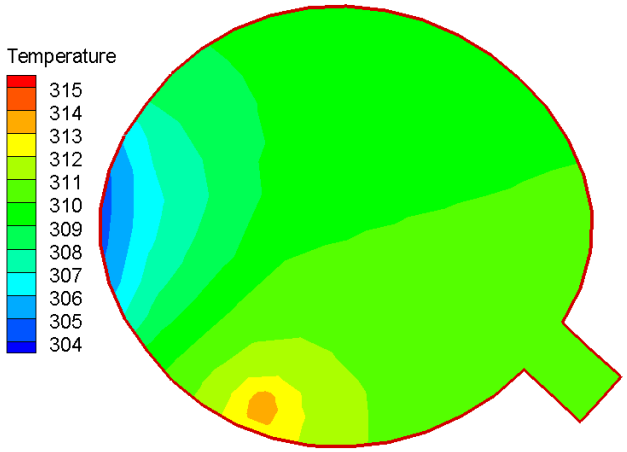

(b) Temperature contour for FEM using 174 nodes

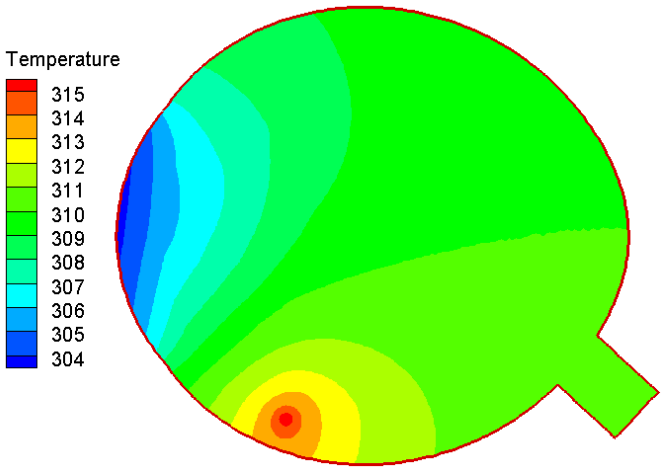

(c) Temperature contour for reference using 12827 nodes

Figure 3.28: Temperature contour of 2D eye model under hyperthermia treatment

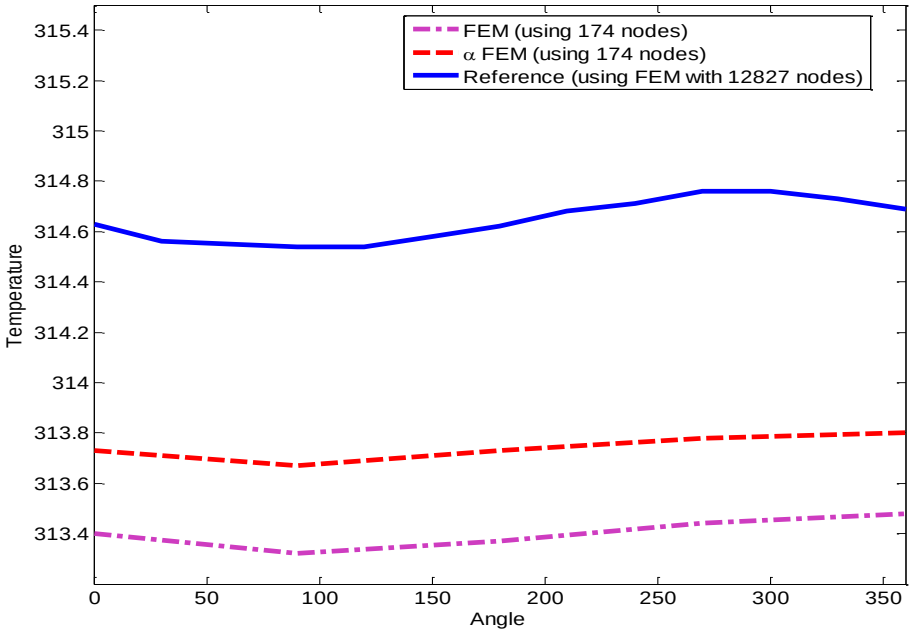

Figure 3.29: Temperature distribution at the heating source

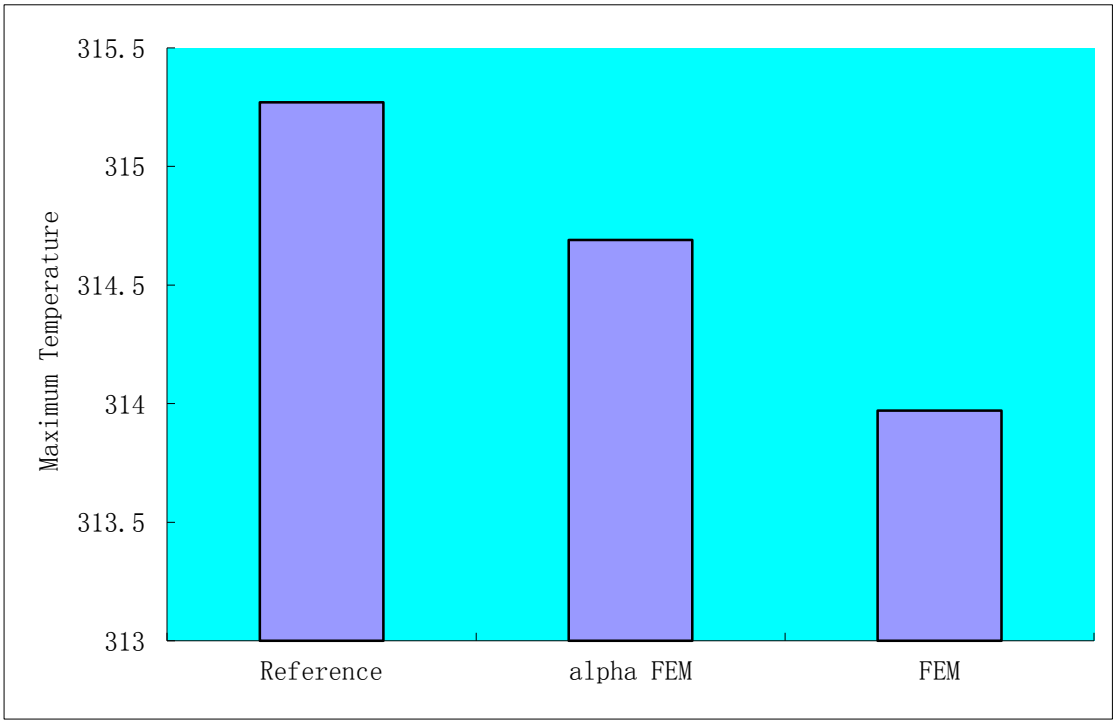

Figure 3.30: Comparison for maximum temperature at the heating source

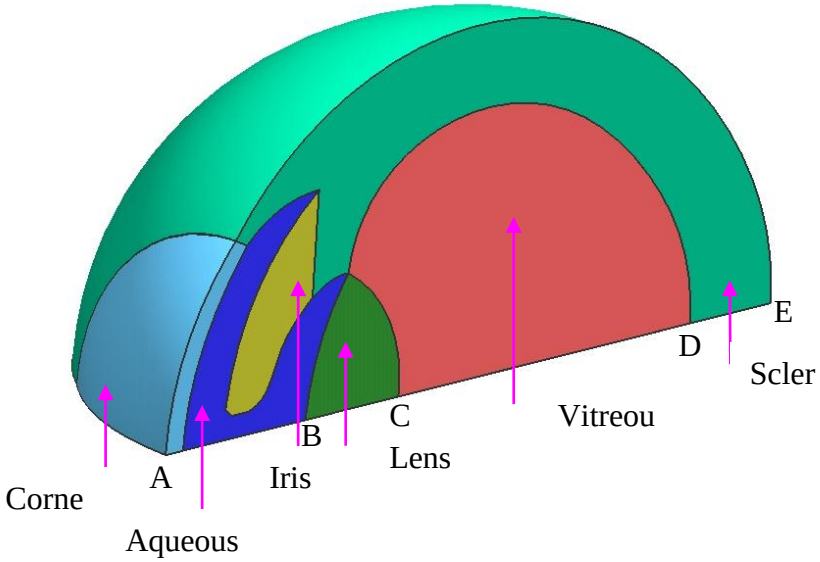

Figure 3.31: 3D quarter model of human eye

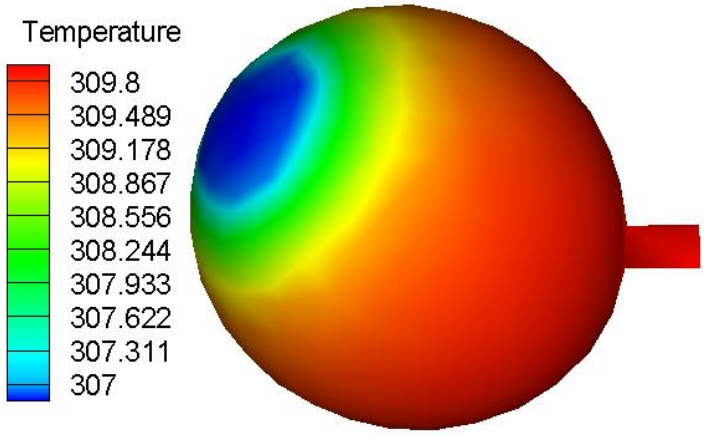

Temperature contour for α FEM using 620 nodes

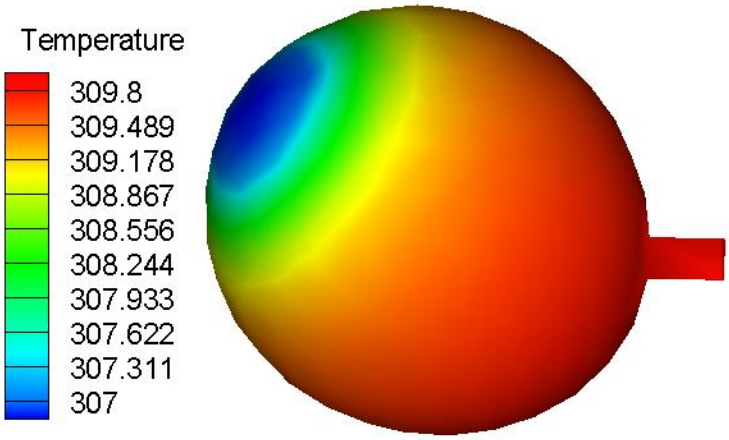

Temperature contour for FEM using 620 nodes

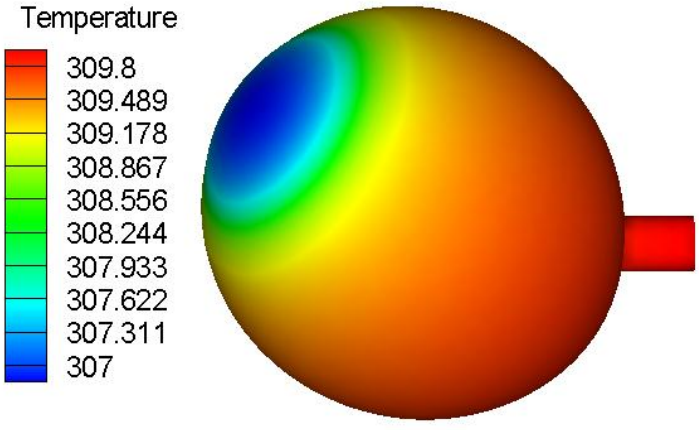

Temperature contour for reference using 17386 nodes

Figure 3.32: Temperature contour of 3D eye model under steady condition

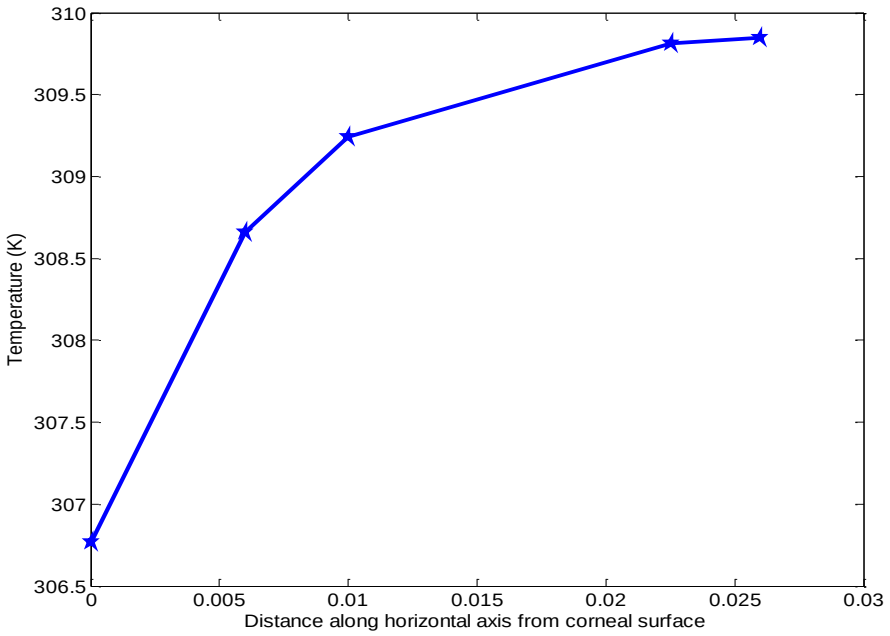

Figure 3.33: Temperature along horizontal axis from corneal surface

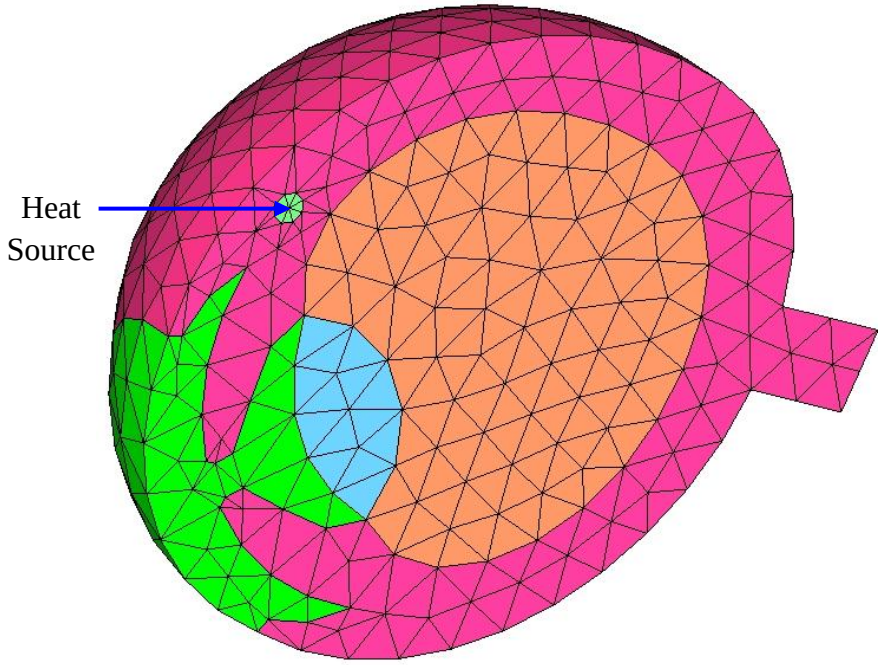

a) Coarse mesh with 1292 nodes for section X-X

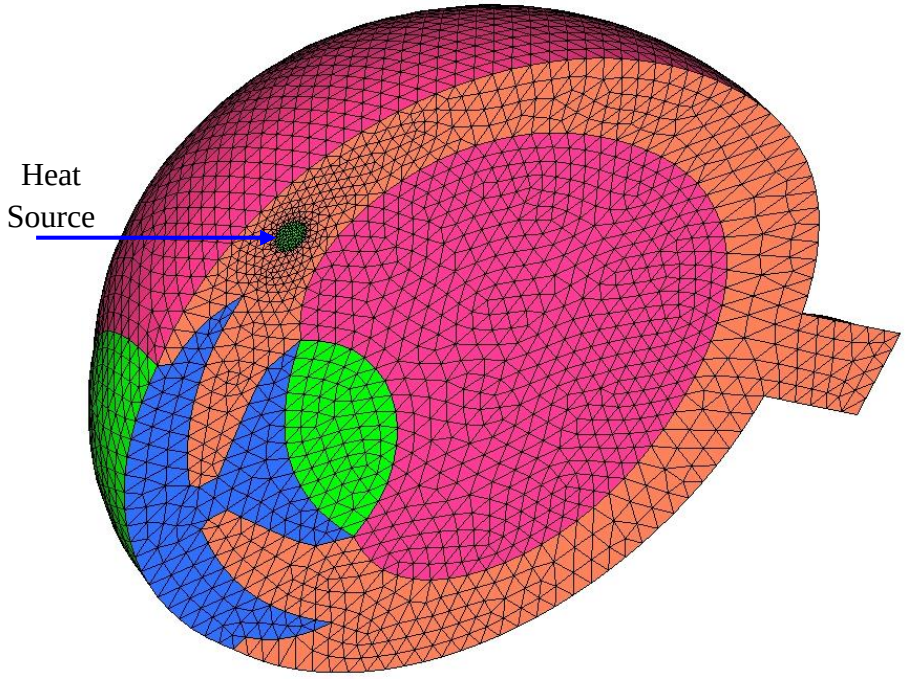

b) Very fine mesh with 17867 nodes for section X-X

Figure 3.34: Two sets of different mesh with heat source distributed in a small sphere

Center of heat source : $x = 8.10mm,\ y = 8.86mm,\ z = 0mm$

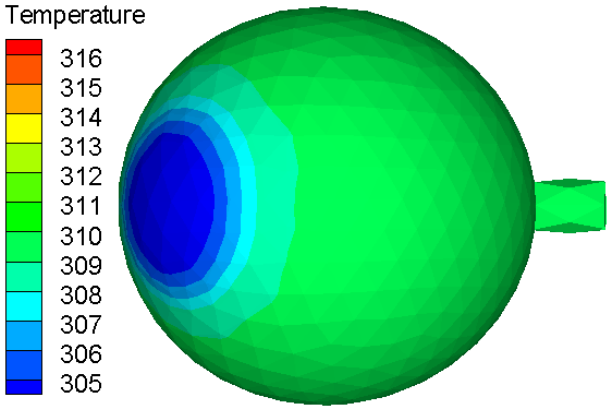

(a) Temperature contour for αFEM using 1292 nodes

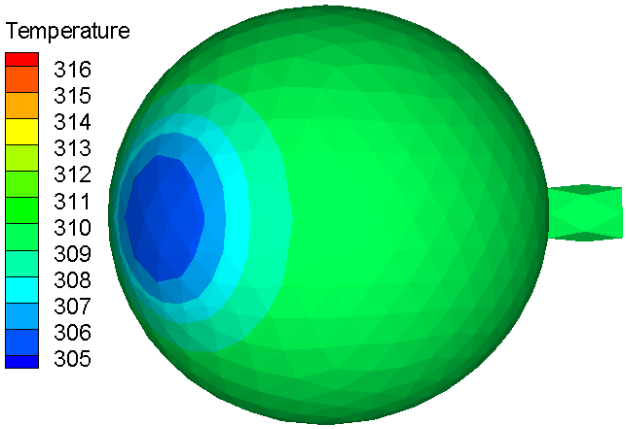

(b) Temperature contour for FEM using 1292 nodes

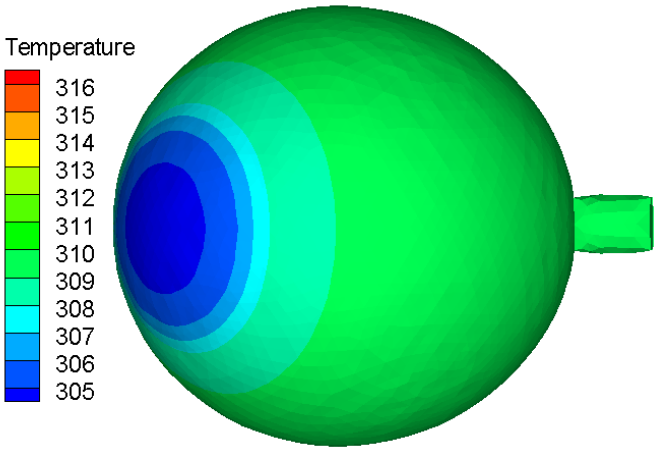

(c) Temperature contour for reference using 17867 nodes

Figure 3.35: Temperature contour of 3D eye model under hyperthermia treatment

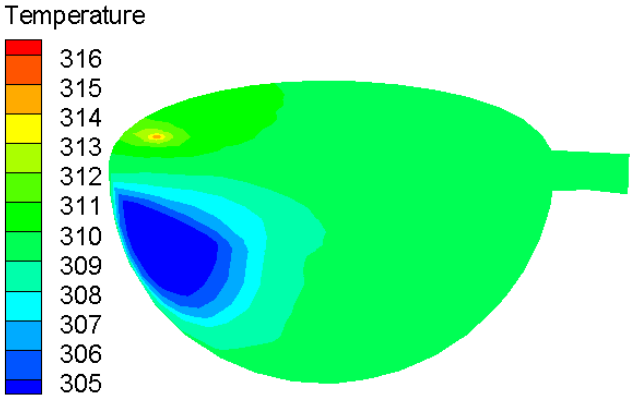

(a) Temperature contour for αFEM using 1292 nodes

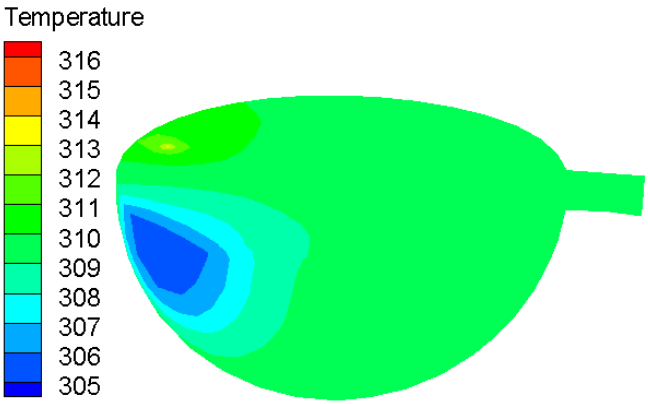

(b) Temperature contour for FEM using 1292 nodes

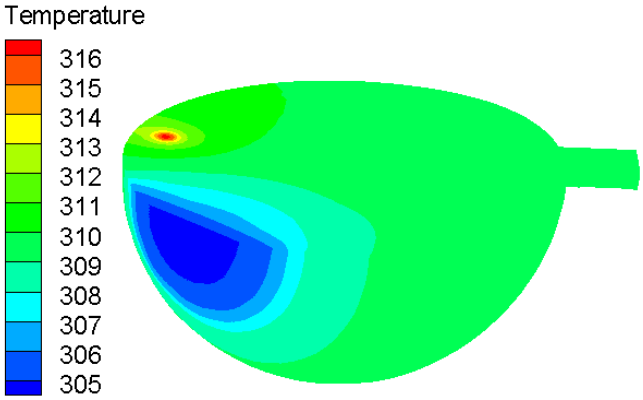

(c) Temperature contour for reference using 17867 nodes

Figure 3.36: Temperature contour of 3D eye model for section X-X

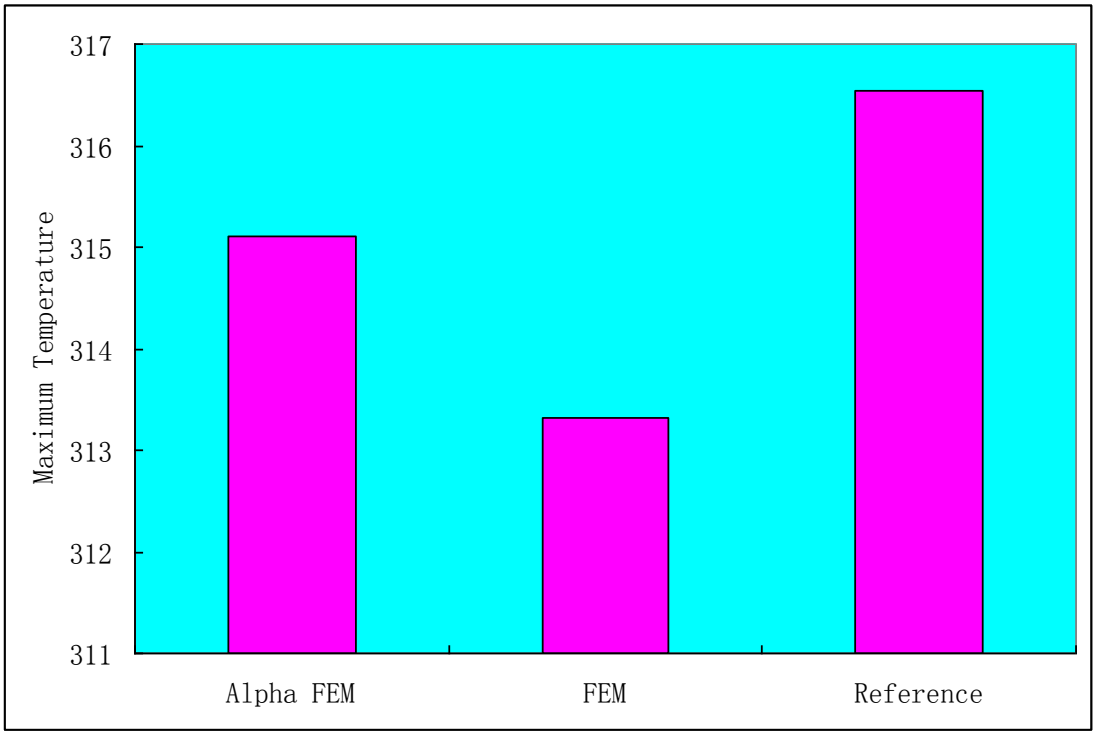

Figure 3.37: Comparison for maximum temperature at the heating source

Table 3.1: Thermal properties of liver tissues [80]

	Unit	Value
Thermal conductivity of the	W/m^oC	0.5
Thermal conductivity of the frozen	W/m^oC	2
Heat capacity of the unfrozen tissue	$J/m^3{}^oC$	3.6×10^3
Heat capacity of frozen tissue	$J/m^3{}^oC$	1.8×10^3
Latent heat	KJ/kg	4200
Lower phase-transition temperature	^oC	-8
upper phase-transition temperature	^oC	-1
Metabolic rate of the liver	W/m^3	4200
Body core temperature	^oC	37
Density of unfrozen tissue	Kg/m^3	1000
Density of frozen tissue	Kg/m^3	1000
Density of blood	Kg/m^3	1000

Table 3.2: Properties of the human eye

	Thermal conductivity ($Wm^{-1}K^{-1}$)	Specific heat	Density (kgm^{-3})
Cornea	0.58	4178	1050
Aqueous	0.58	3997	996
Iris	1.0042	3180	1100
Lens	0.40	3000	1050
Vitreous body	0.603	4178	1000
Sclera	1.0042	3180	1100

Table 3.3: Parameters under steady state condition

h_{amb}	Ambient convection coefficient	10 $Wm^{-2}K^{-1}$
h_{bl}	Blood convection coefficient	65 $Wm^{-2}K^{-1}$
T_{amb}	Ambient temperature	293 K
E	Evaporation rate	40 Wm^{-2}
T_{bl}	Blood temperature	310 K

Table 3.4: Effect of evaporation rate

E ($W\ m^{-2}$)	Temperature distribution (K)				
	A	B	C	D	E
30	306.87	308.71	309.27	309.82	309.86
80	306.35	308.49	309.15	309.79	309.83
130	305.84	308.28	309.03	309.76	309.81
180	305.32	308.06	308.94	309.73	309.78
230	304.80	307.85	308.79	309.70	309.76

Table 3.5: Effect of ambient convection coefficient

H ($Wm^{-2}K^{-1}$)	Temperature distribution (K)				
	A	B	C	D	E
15	306.67	308.37	309.08	309.77	309.82
30	304.30	307.61	308.65	309.66	309.73
50	302.50	306.82	308.20	309.55	309.64
80	300.59	305.95	307.70	309.43	309.54
100	299.65	305.50	307.44	309.36	309.49

Table 3.6: Effect of ambient temperature

T (K)	Temperature distribution (K)				
	A	B	C	D	E
273	303.66	307.38	308.52	309.63	309.71
278	304.42	307.69	308.70	309.68	309.74
283	305.19	308.01	308.88	309.72	309.78
303	308.40	309.34	309.63	309.91	309.93
308	309.25	309.69	309.82	309.96	309.97

Table 3.7: Effect of blood temperature

T (K)	Temperature distribution (K)				
	A	B	C	D	E
308	305.10	306.80	307.32	307.83	307.86
309	305.94	307.73	308.28	308.82	308.86
310	306.77	308.66	309.25	309.81	309.85
311	307.60	309.59	310.26	310.80	310.84
312	308.43	310.52	311.17	311.80	311.83

Table 3.8: Effect of blood convection coefficient

H ($Wm^{-2}K^{-1}$)	Temperature distribution (K)				
	A	B	C	D	E
50	306.64	308.53	309.12	309.73	309.77
70	306.80	308.70	309.28	309.83	309.87
90	306.89	308.80	309.37	309.88	309.91
110	306.96	308.87	309.43	309.91	309.94
120	306.99	308.90	309.45	309.92	309.95

Chapter 4

Development of Piecewise Linear Gradient Smoothing Method (PL-GSM) in Fluid Dynamics

4.1 Introduction

Chapters 2 and 3 presented the research efforts related to the use of gradient smoothing operations for weak-form governing equations. In such applications, the gradient smoothing operation is only adopted as an auxiliary component in the development of various meshfree methods. Recently, a piecewise constant gradient smoothing method (PC-GSM) for strong-form equations has been developed [24], in which the gradient smoothing operation is used to approximate the first and second derivatives at different locations and the resultant instantaneous equations are solved subsequently. Various discretization schemes for approximating spatial derivatives are devised and some efficient and accurate schemes are selected. These schemes for the PC-GSM have been successfully formulated and applied for simulating compressible flows and heat conduction problems [24]. The previous works have demonstrated that the proposed PC-GSM is conservative, conformal, efficient, robust and accurate.

In this Chapter, a novel piecewise-linear gradient smoothing method (PL-GSM) based on the strong form formulation is presented as an alternative to the generalized finite difference method for solving fluid problems. Compared with PC-GSM, the

PL-GSM adopts the linearly-weighted smoothing function in the gradient smoothing domain instead of the piecewise constant smoothing function. In the PL-GSM， all the unknowns are also stored at the nodes and their derivatives at various locations are consistently and directly approximated. A Linearly-weighted gradient smoothing technique is utilized to determine the first and second order derivative approximations by systematically computing weights for a set of nodal points surrounding an interest node. The flexibility of the PL-GSM makes use of existing meshes that have originally been created for finite difference or finite element methods.

4.2 Concept of piecewise linear gradient smoothing method (PL-GSM)

4.2.1 Gradient smoothing operation

Consider a two dimensional problem to illustrate the gradient smoothing operation. The gradients of a field variable U at a point of interest at $\mathbf{x}_i$ in domain Ω_i can be approximated in the form of [18, 107]

$$\nabla U_i \equiv \nabla U(\mathbf{x}_i) \approx \int_{\Omega_i} \nabla U(\mathbf{x}) \hat{w}(\mathbf{x}-\mathbf{x}_i) d\Omega \tag{4.1}$$

Integrating Eq. (4.1) by parts or using divergence theorem gives

$$\nabla U_i \approx \oint_{\partial\Omega_i} U(\mathbf{x}) \hat{w}(\mathbf{x}-\mathbf{x}_i) \mathbf{n} ds - \int_{\Omega_i} U(\mathbf{x}) \nabla \hat{w}(\mathbf{x}-\mathbf{x}_i) dV \tag{4.2}$$

where ∇ is gradient operator, and $\hat{w}$ is a smoothing function that can be chosen based on the required accuracy of the approximation [24]. $\partial\Omega_i$ represents the external boundary of the gradient smoothing domain, and $\mathbf{n}$ denotes the unit normal vector on $\partial\Omega_i$, as shown in Fig. 4.1.

In this work, around a node of interest, *i*, the following piecewise linear smoothing function is adopted:

$$\widehat{w}(\mathbf{x}-\mathbf{x}_i)=\begin{cases}\mathbf{a}_0+\mathbf{a}_1(\mathbf{x}-\mathbf{x}_\mathbf{i}), & \mathbf{x}\in\Omega_i\\ 0, & \mathbf{x}\notin\Omega_i\end{cases} \tag{4.3}$$

where $\mathbf{a_0}$ and $\mathbf{a_1}$ are matrices of coefficients that are dependent on the geometry of each sub-triangle within the smoothing domain of interest. With the Eq. (4.3), the first term in the right hand side of Eq. (4.2) vanishes:

$$\nabla U_i \approx -\int_{\Omega_i} U(\mathbf{x})\nabla\widehat{w}(\mathbf{x}-\mathbf{x}_i)\,dV \tag{4.4}$$

Analogously with the gradient smoothing operation the second order of derivative is expressed as follow:

$$\nabla\bullet\nabla U_i \approx -\int_{\Omega_i} \nabla U(\mathbf{x})\bullet\nabla\widehat{w}(\mathbf{x}-\mathbf{x}_i)\,dV \tag{4.5}$$

The piecewise linear smoothing function in the PL-GSM is required to satisfy the weighted partition of unity [108]:

$$\sum_{k=1}^{2n_i}\int_{\Omega_i^{(k)}}\widehat{w}(\mathbf{x}-\mathbf{x}_i)dV=1 \tag{4.6}$$

The second constrain is that the smoothing function must vanish at the boundary of the smoothing domain:

$$\widehat{w}(x-x_i)=0,\qquad \mathbf{x}\in\partial\Omega_i \tag{4.7}$$

The third constrain implies that a constant value of the smoothing function at the node of interest.

$$\widehat{w}(\mathbf{x}_i-\mathbf{x}_i)=a_0,\qquad \mathbf{x}\in\partial\Omega_i \tag{4.8}$$

4.2.2 Types of smoothing domains

In the PL-GSM, the values of field functions are stored at nodes that can be irregularly distributed in space. By connecting nodes, the problem domain is first divided into a set of primitive cells of any shape. Because triangular cells can be automatically generated, they are usually preferred. Based on these cells, a smooth domain for any point of interest can be constructed. We devise different types of smoothing domains for approximating first derivative at different locations. Figure 4.2 shows three types of gradient smoothing domains, over which spatial derivatives are approximated with gradient smoothing operations. The first type of smoothing domain is the node-associated gradient smoothing domain (nGSD) for the approximation of derivatives at a node of interest. It is formed by connecting the centroids of relevant triangles with midpoints of influenced cell-edges. The second is identical to a primitive cell, which is used for approximating derivatives at the centroid of the cell, as in the cell-centered FVM [109]. It is called centroid-associated gradient smoothing domain (cGSD) here. The third is named midpoint-associated gradient smoothing domain (mGSD) used for the calculation of the gradients at the midpoint of a cell-edge of interest. The preferred mGSD is formed by connecting the end-nodes of the cell-edge with the centroids on the both sides of the cell-edge, as shown in Fig. 4.2.

4.2.3 Determination of smoothing function

For a two-dimensional case, the piecewise linear smoothing function can be rewritten as

$$\widehat{w}(\mathbf{x}-\mathbf{x}_i)=\mathbf{a}_i+\mathbf{b}_i(x-x_i)+\mathbf{c}_i(y-y_i) \tag{4.9}$$

The coefficients in matrices **a**, **b** and **c** are dependent on the geometry of each sub-triangle within the smoothing domain of interest. The matrices of coefficients are in the form of

$$\mathbf{a}_i=\begin{bmatrix} a_{i,1} \\ a_{i,2} \\ \vdots \\ a_{i,2N_i-1} \\ a_{i,2N_i} \end{bmatrix},\ \mathbf{b}_i=\begin{bmatrix} b_{i,1} \\ b_{i,2} \\ \vdots \\ b_{i,2N_i-1} \\ b_{i,2N_i} \end{bmatrix},\ \mathbf{c}_i=\begin{bmatrix} c_{i,1} \\ c_{i,2} \\ \vdots \\ c_{i,2N_i-1} \\ c_{i,2N_i} \end{bmatrix}, \tag{4.10}$$

N_i represents the total number of edges connected with the node of interest, i. As shown in Fig. 4.3, there are totally $2N_i$ sub-triangles that form the smoothing domain for an internal node of interest. For a boundary node, there are ($2N_i$ -2) sub-triangles, correspondingly.

Furthermore, Eq. (4.9) gives

$$\frac{\partial\widehat{w}(\mathbf{x}-\mathbf{x}_i)}{\partial x}=\mathbf{b}_i,\qquad \frac{\partial\widehat{w}(\mathbf{x}-\mathbf{x}_i)}{\partial y}=\mathbf{c}_i \tag{4.11}$$

The discretization of equations on an inner node is considered first.

The smoothing function is required to satisfy the weighted partition of unity:

$$\sum_{k=1}^{N_i}\left[\int_{\Omega_i^{(2k-1)}}\widehat{w}\left(\mathbf{x}-\mathbf{x}_i\right)dV+\int_{\Omega_i^{(2k)}}\widehat{w}\left(\mathbf{x}-\mathbf{x}_i\right)dV\right]=1 \tag{4.12}$$

$$\begin{aligned}&\sum_{k=1}^{N_i}\left\{\int_{\Omega_i^{(2k-1)}}\left[a_{i,2k-1}+b_{i,2k-1}(x-x_i)+c_{i,2k-1}(y-y_i)\right]dV+\right.\\&\left.\int_{\Omega_i^{(2k)}}\left[a_{i,2k}+b_{i,2k}(x-x_i)+c_{i,2k}(y-y_i)\right]dV\right\}=1\end{aligned} \tag{4.13}$$

Besides, for a sub-triangle of interest, for instance, the triangle Δim_kc_k, it is further assumed that

$$\widehat{w}_{m_k} = \widehat{w}(\mathbf{x}_{m_k} - \mathbf{x}_i) = 0 \tag{4.14}$$

$$\widehat{w}_{c_k} = \widehat{w}(\mathbf{x}_{c_k} - \mathbf{x}_i) = 0 \tag{4.15}$$

With Eq. (4.13), it is readily obtained that

$$a_{i,2k} = \widehat{w}(\mathbf{x}_i - \mathbf{x}_i) = \frac{3}{V_i} \tag{4.16}$$

where V_i is the total area of the smoothing domain for the node of interest, i. This formulation implies that all coefficients in the matrix $\mathbf{a}_i$ are constant, regardless of sub-triangles involved.

The parameters $b_{i,2k}$ and $c_{i,2k}$ for each sub-triangle can then be obtained as the solutions to Eq. (4.17) and Eq. (4.18), in the form of

$$b_{i,2k} = -a_{i,2k} \frac{y_{c_k} - y_{m_k}}{(x_{m_k} - x_i)(y_{c_k} - y_i) - (x_{c_k} - x_i)(y_{m_k} - y_i)} \tag{4.17}$$

$$c_{i,2k} = a_{i,2k} \frac{x_{c_k} - x_{m_k}}{(x_{m_k} - x_i)(y_{c_k} - y_i) - (x_{c_k} - x_i)(y_{m_k} - y_i)} \tag{4.18}$$

It is also noticed that the denominator in Eq. (4.17) and (4.18) relates to the area of the sub-triangle $\Delta im_k c_k$, which is

$$Area_{i,2k} = \left| (x_{m_k} - x_i)(y_{c_k} - y_i) - (x_{c_k} - x_i)(y_{m_k} - y_i) \right| /2 \tag{4.19}$$

Therefore, the following relations hold:

$$\xi_{i,2k} = b_{i,2k} Area_{i,2k} = \begin{cases} -a_{i,2k}(y_{c_k} - y_{m_k})/2, & \text{if } \chi > 0; \\ a_{i,2k}(y_{c_k} - y_{m_k})/2, & \text{if } \chi < 0; \end{cases} \tag{4.20}$$

and

$$\eta_{i,2k} = c_{i,2k} Area_{i,2k} = \begin{cases} a_{i,2k}(x_{c_k} - x_{m_k})/2, & \text{if } \chi \geq 0; \\ -a_{i,2k}(x_{c_k} - x_{m_k})/2, & \text{if } \chi \leq 0; \end{cases} \tag{4.21}$$

where $\chi = (x_{m_k} - x_i)(y_{c_k} - y_i) - (x_{c_k} - x_i)(y_{m_k} - y_i)$. It is noticed that if the constitutive nodes (*i* -> m_k -> c_k) for the sub-triangle $\Delta im_k c_k$ obey the right-hand rule sequence, χ will take positive value. Otherwise, it will be negative, as in the sub-triangle $\Delta im_k c_{k-1}$. Therefore, as shown in the previous figure, for the triangle $\Delta im_k c_k$, since $\chi > 0$, we have

$$\begin{cases} \xi_{i,2k} = b_{i,2k} Area_{i,2k} = -a_{i,2k}(y_{c_k} - y_{m_k})/2 \\ \eta_{i,2k} = c_{i,2k} Area_{i,2k} = a_{i,2k}(x_{c_k} - x_{m_k})/2 \end{cases} \tag{4.22}$$

Analogously, for the $(2k-1)^{\text{th}}$ sub-triangle, $\Delta im_k c_{k-1}$, the relevant coefficients are

$$\begin{cases} a_{i,2k-1} = \widehat{w}_i = \dfrac{3}{V_i} \\ \xi_{i,2k-1} = b_{i,2k-1} Area_{i,2k-1} = -a_{i,2k-1}(y_{c_{k-1}} - y_{m_k})/2 \\ \eta_{i,2k-1} = c_{i,2k-1} Area_{i,2k-1} = a_{i,2k-1}(x_{c_{k-1}} - x_{m_k})/2 \end{cases} \tag{4.23}$$

where $Area_{i,2k-1} = \left|(x_{m_k} - x_i)(y_{c_{k-1}} - y_i) - (x_{c_{k-1}} - x_i)(y_{m_k} - y_i)\right|$.

4.2.4 Approximation of first order derivatives

Eq. (4.4) can be simplified to

$$\nabla U_i \approx -\int_{\Omega_i} U(\mathbf{x}) \nabla \widehat{w}(\mathbf{x} - \mathbf{x}_i) dV = -\sum_{k=1}^{N_i} \left[\int_{\Delta im_k c_k} U(\mathbf{x}) \nabla \widehat{w}(\mathbf{x} - \mathbf{x}_i) dV + \int_{\Delta im_k c_{k-1}} U(\mathbf{x}) \nabla \widehat{w}(\mathbf{x} - \mathbf{x}_i) dV \right] \tag{4.24}$$

Eq. (4.24) gives the approximation to the gradients as

$$\frac{\partial U_i}{\partial x} \approx -\sum_{k=1}^{N_i} \left[b_{i,2k} \int_{im_k c_k} U(\mathbf{x}) dV + b_{i,2k-1} \int_{im_k c_{k-1}} U(\mathbf{x}) dV \right] \tag{4.25}$$

$$\frac{\partial U_i}{\partial y} = -\sum_{k=1}^{N_i} \left[c_{i,2k} \int_{im_k c_k} U(\mathbf{x}) dV + c_{i,2k-1} \int_{im_k c_{k-1}} U(\mathbf{x}) dV \right] \tag{4.26}$$

The integral for function U(x) over each sub-triangle can be simply approximated:

$$\int_{\Omega_{i,k}} U(\mathbf{x})d \approx \frac{1}{3}\left[U(\mathbf{x}_i)+U(\mathbf{x}_{m_k})+U(\mathbf{x}_{c_k})\right]A_{i,k} \tag{4.27}$$

Substituting Eq. (4.27) into Eq. (4.25) and (4.26) gives,

$$\frac{\partial U_i}{\partial x} \approx -\sum_{k=1}^{N_i}\left\{\frac{1}{3}\left[U(\mathbf{x}_i)+U(\mathbf{x}_{m_k})+U(\mathbf{x}_{c_k})\right]\xi_{i,2k} + \frac{1}{3}\left[U(\mathbf{x}_i)+U(\mathbf{x}_{m_k})+U(\mathbf{x}_{c_{k-1}})\right]\xi_{i,2k-1}\right\} \tag{4.28}$$

$$\frac{\partial U_i}{\partial y} \approx -\sum_{k=1}^{N_i}\left\{\frac{1}{3}\left[U(\mathbf{x}_i)+U(\mathbf{x}_{m_k})+U(\mathbf{x}_{c_k})\right]\eta_{i,2k} + \frac{1}{3}\left[U(\mathbf{x}_i)+U(\mathbf{x}_{m_k})+U(\mathbf{x}_{c_{k-1}})\right]\eta_{i,2k-1}\right\} \tag{4.29}$$

The function values at midpoints of edges and centroids of triangles can be simply approximated with linear interpolation of values at constitutive nodes.

4.2.5 Approximation of second order derivatives

Analogously, with the help of linear interpolation in integral calculation, the 2nd-order derivatives can be approximated as:

$$\frac{\partial^2 U_i}{\partial x^2} \approx -\sum_{k=1}^{N_i}\left\{\frac{1}{3}\left[\frac{\partial U(\mathbf{x}_i)}{\partial x}+\frac{\partial U(\mathbf{x}_{m_k})}{\partial x}+\frac{\partial U(\mathbf{x}_{c_k})}{\partial x}\right]\xi_{i,2k} + \frac{1}{3}\left[\frac{\partial U(\mathbf{x}_i)}{\partial x}+\frac{\partial U(\mathbf{x}_{m_k})}{\partial x}+\frac{\partial U(\mathbf{x}_{c_{k-1}})}{\partial x}\right]\xi_{i,2k-1}\right\} \tag{4.30}$$

$$\frac{\partial^2 U_i}{\partial y^2} \approx -\sum_{k=1}^{N_i}\left\{\frac{1}{3}\left[\frac{\partial U(\mathbf{x}_i)}{\partial y}+\frac{\partial U(\mathbf{x}_{m_k})}{\partial y}+\frac{\partial U(\mathbf{x}_{c_k})}{\partial y}\right]\eta_{i,2k} + \frac{1}{3}\left[\frac{\partial U(\mathbf{x}_i)}{\partial y}+\frac{\partial U(\mathbf{x}_{m_k})}{\partial y}+\frac{\partial U(\mathbf{x}_{c_{k-1}})}{\partial y}\right]\eta_{i,2k-1}\right\} \tag{4.31}$$

In the above equations, the gradients at midpoints of edges and centroids of triangles can be approximated using either linear interpolation or gradient smoothing operation,

as done in PC-GSM with piecewise constant smoothing function. As for the approximation with gradient smoothing operation, both piecewise constant and linear smoothing functions can be used.

4.2.6 Relations between PC-GSM and PL-GSM

As described in previous sections, the PL-GSM adopts the piecewise linear smoothing functions and the PC-GSM uses the piecewise constant smoothing functions [24]. For PC-GSM, the derivatives are approximated based on the integration over the surface of a gradient smoothing domain. On the other hand, they are approximated based on the integration over the bounding edges of the domain for PL-GSM. These variations are summarized in the Table 4.1.

4.2.7 Treatment of boundary nodes between PC-GSM and PL-GSM

The treatment of boundary nodes in the PC-GSM and PL-GSM is quite different. In the PL-GSM, values at boundaries are dealt with in the same manner as those on internal nodes as described above. In other words, the governing equation is still applied onto the boundary nodes for solutions. Therefore, no special treatment on boundary nodes is needed. Fig. 4.4 not only illustrates the difference in gradient smoothing domain for internal and boundary nodes, but also gives the hint to deal with the boundary nodes in the similar way as for internal nodes.

In PL-GSM, as shown in Fig. 4.4(a), only surface integrals will be involved in the approximation of the gradients at boundary nodes, as described above. As dummy nodes overlap with boundary nodes, the area marked in red becomes zero. Therefore,

only the portion of gradient smoothing domain within the computational domain will be used in the approximation. Thus, the boundary nodes will be treated in the same manner as what is done for internal nodes. As a result, a consistent treatment is applied for all nodes throughout the computational domain. However, the boundary nodes and inner nodes must be solved separately in PC-GSM [24]. For example, additional effort to search for boundary node must be done before solving the governing equation in PC-GSM, which increases computational cost.

4.3 Stencil analysis

In this section, analysis of the stencils of supporting nodes for the PL-GSM is carried out. The coefficients of influence for a node of interest where derivatives are approximated are derived using the PL-GSM and analyzed. The purpose for stencil analyses is to verify whether the proposed PL-GSM scheme meets the basic principles of numerical discretization.

4.3.1 Basic principles for stencil assessment

In the stencil analyses, five basic rules are considered to assess the quality of a stencil resulting from a discretization scheme: a) Consistency at each domain face; (b) Positivity of coefficients of influence; (c) Negative-slope linearization of the source term; (d) The compactness of the stencil; (e) Sum of the coefficients of influence. To satisfy condition (a), it requires that the same expression of approximation must be used on the interface of two adjacent smoothing domains. In the PL-GSM, when the gradient smoothing technique is applied to the gradient smoothing domains, condition (a) is

automatically satisfied, meaning that the local conservation of quantities is ensured and also for the global conservation once proper boundary conditions are used. Condition (b) requires that the coefficient for the node of interest and the coefficients of influence must be positive, once the discretization equation is written in the form of $a_{ii}U_i = \sum_{k=1}^{n_i} a_{ij_k} U_{j_k} + b_i$. It is also necessary for a good discretization stencil to satisfy the condition (c) which relates to the treatment of the source terms. As addressed by Patankar [110], it is essential to keep the slope of linearization negative, since a positive slope can lead to computational instabilities and physically unrealistic solutions. Condition (d) concerns numerical accuracy and efficiency, as commented by Barth [48]. The very first layer of nodes surrounding the node of interest should be included in the discretization stencil. Moreover, as the stencil becomes larger, not only will computational cost increase, but accuracy decreases as less relevant data from further away is brought into approximation. Condition (e) further requires that $a_{ii} = \sum_{k=1}^{n_i} a_{ij_k}$. Barth [48] proposed a few lemmas to address the necessity of positivity of coefficients to satisfy a discrete maximum principle that is key to the design and analysis of numerical schemes for non-oscillatory discontinuity (for example, shock). At steady state, non-negativity of the coefficients is sufficient to satisfy a discrete maximum principle that can be applied successively to obtain global maximum principle and stable results. His statements reiterate the importance of condition (b) as mentioned by Patankar [110].

4.3.2 Stencils for approximated gradients

The stencil for gradient approximation using linearly-weighted gradient smoothing method is first analyzed. The coefficients of influence based on cells of square and equilateral triangle shapes with unit length are shown in Fig. 4.5 and Fig. 4.6.

4.3.2.1 Square cells

As shown in Fig. 4.5, it is found that this stencil is identical to that of 6-point based central-differencing scheme in the FDM. That is to say, when uniform Cartesian meshes are used, the PL-GSM is the same as the FDM. However, the PL-GSM still works for cells of irregular shapes very well.

4.3.2.2 Triangular cells

Figure 4.6 presents the stencil based on cells of equilateral triangle shape. It is observed that the stencil is identical to that of interpolation method using six surrounding nodes [63]. However, the interpolation method usually fails for irregular triangular cells as addressed by Liu[63], but the PL-GSM still performs well, as will be demonstrated in the section on numerical examples. This is due to the crucial stability provided by the smoothing operation.

4.3.3 Stencils for approximated Laplace operator

In the PC-GSM, the use of piecewise constant gradient smoothing function has been shown to be robust, accurate and stable [24]. For comparison, the proposed schemes of PC-GSM and PL-GSM for stencils in the Laplace operator are presented in

this section. In order to examine the effects of the piecewise linear gradient smoothing function, the schemes using linear interpolation for the midpoint and central point are also included in Table 4.2. In this section, compact stencils for the approximated Laplace operator $\left(\frac{\partial^2 u_i}{\partial x^2}+\frac{\partial^2 u_i}{\partial y^2}\right)$ for various schemes are carried out.

4.3.3.1 Square cells

The stencils for the approximated Laplace operator with PL-GSM schemes based on cells of square shape are shown in Fig. 4.7. As shown in Fig. 4.7(a), scheme I results in wide stencils with unfavorable weighting coefficients (zero and negative) due to the simple interpolation of gradient at the midpoint and center. Scheme II of PC-GSM and scheme III of PL-GSM result in the same favorable and compact stencils in Fig. 4.7(b). It demonstrates that the use of gradient smoothing operation is a good alternative for approximating the second order derivatives.

4.3.3.2 Triangular cells

The stencils analyses of triangular cells are shown in Fig. 4.8. It is observed that coefficients at the very first layer of neighbouring nodes are negative as seen in Figure 4.8(a) for scheme I, which is against the basic condition (b). Scheme II of PC-GSM and scheme III of PL-GSM use only the first layer of neighboring nodes with positive coefficient as shown in Fig. 4.8(b), which result in the same compact stencil with favorable coefficients. This is also due to the constant employment of gradient smoothing operations.

From the stencil analysis for Laplace operator, it is found that the PC-GSM and PL-GSM are able to produce the same favorable coefficients in the discretization. The linear interpolation at the midpoint and central point with the PL-GSM in the node has the same results. In the following numerical part, comparison of accuracy in the solving the Poisson equation with three different schemes as listed in Table 4.2.

4.4 Numerical example: Poisson equation

In this study, the proposed PL-GSM is first examined through solving a two-dimensional Poisson's equation as

$$\frac{\partial^2 U}{\partial x^2}+\frac{\partial^2 U}{\partial y^2}=f(x,y) \qquad (0\le x\le 1, 0\le y\le 1) \tag{4.34}$$

The source conditions and analytical solution are given as follows:

$$f(x,y)=\sin(\pi x)\sin(\pi y) \qquad (0\le x\le 1, 0\le y\le 1) \tag{4.35}$$

$$\hat{U}(x,y)=-\frac{1}{2\times\pi^2}\sin(\pi x)\sin(\pi y) \qquad (0\le x\le 1, 0\le y\le 1) \tag{4.36}$$

The contour plot of the analytical solution to the above problem is shown in Fig. 4.9. Boundary conditions adopted in simulations are consistent with the corresponding analytical solutions. These analytical solutions are used for the evaluation of numerical errors in the PL-GSM solutions.

The Poisson equation is also solved with Dirichlet and Neumann boundary conditions as shown in Fig. 4.10.

To investigate quantitatively the numerical results, two types of error indicators are defined as follow:

$$error = \sqrt{\frac{\sum_{i=1}^{n_{node}} (U_i - \hat{U}_i)^2}{\sum_{i=1}^{n_{node}} \hat{U}_i^2}} \tag{4.37}$$

where U_i and $\hat{U}_i$ are predicted and analytical solutions at node *i*, respectively. This type of error is used to compare the accuracy among different schemes.

The second type of error is the node-wise relative error, which is estimated in the form of

$$rerror_i = \frac{\left|U_i - \hat{U}_i\right|}{\left|\hat{U}_i\right|} \tag{4.38}$$

The node-wise relative errors distributed over the computational domain are used to identify problematic regions in simulations.

4.4.1 The effect of linear gradient smoothing

Figure 4.11 illustrates the node-wise relative errors in solving the first Poisson problem with schemes I and III respectively. The right triangular mesh with 121 uniformly distributed nodes is used in this example. The simple linear interpolation of gradient at the midpoint and central point has caused saw-smoothed numerical error (well-known as checkboard problem), which is consistent with the finding as shown in stencil analysis. From Fig. 4.11, the relative error using schemes III has reduced significantly. Such an attractive feature can be attributed to the consistent use of smoothing techniques in scheme III, which provides the crucial stability and robustness of PL-GSM.

4.4.2 Convergence study of the PL-GSM

Four sets of right triangular cells as shown in Fig. 4.12 are employed to investigate the accuracy of three schemes in solving the first Poisson equation.

Table 4.3 summarizes the numerical errors for different discretization schemes. It is obviously found that the use of the gradient smoothing function for approximating gradients at non-storage locations always gives more accurate results than the use of linear interpolation. Additionally, scheme III with piecewise linear gradient smoothing function improved the accuracy of numerical solution significantly compared with schemes I and II.

Another four sets of regular mesh as shown in Fig. 4.13 are used to analyze the numerical error against three types of discretization schemes. The numerical errors for three schemes are presented in Table 4.4. Again, scheme III with constant use of piecewise linear gradient smoothing function always gives higher accuracy than the use of linear interpolation in scheme I and piecewise constant gradient smoothing function. The numerical results obtained from the linear interpolation at the midpoint and the central point are very poor compared with the gradient smoothing operation in schemes II and III.

To study the convergence property of PL-GSM, four models with regularly distributed nodes (131, 478, 1887, 7457 nodes) were analyzed. Evolutions of numerical error with averaged nodal spacing for the first Poisson problem are plotted in Fig. 4.14. Note that the errors in these plots are evaluated using Eq. (4.37), and the average nodal spacing, h, is evaluated using the formula given by Liu [63] in the form of

$$h = \frac{V}{\sqrt{n_{node}} - 1} \tag{4.39}$$

where V and n_{node} denote the area of the whole computational domain and the total number of nodes in the domain, respectively. It is apparent that the averaged node spacing decreases as the number of nodes increases. From Fig. 4.14, it can be found that the convergence rate is approximately the same in all schemes, because all schemes are second order accurate in spatial approximation.

4.4.3 Condition number and iteration

The condition number of the global stiffness matrix $cond(K)$ is an important indicator of numerical stability. The number of iterations is proportional to the condition number when the iteration solver is used to solve the algebraic system equation. As shown in Table 4.5, the condition number and number of iterations for three schemes in the numerical solution of the first Poisson equation are presented. Scheme III has the largest condition number and number of iterations compared with the remaining techniques. This is due to the continuous employment of linear gradient smoothing operation in the midpoint and central point.

4.4.4 Effects of nodal irregularity

To evaluate the influence of mesh irregularities on accuracy, a numerical example with regular mesh and irregular mesh will be tested. The irregularly distributed nodes are generated based on the nodal irregularity degree defined in the following expression:

$$\gamma = \frac{\sum_{i=1}^{n_e} \frac{(a_i - b_i)^2 + (b_i - c_i)^2 + (c_i - a_i)^2}{a_i^2 + b_i^2 + c_i^2}}{n_e} \tag{4.40}$$

where a_i, b_i and c_i, respectively, denote the lengths of cell-edges of a triangular cell, and n_e stands for the total number of cells in the overall domain. Eq. (40) is derived from the formula proposed by Stillinger *et al* [109] for a single triangle. Using Eq. (40), the irregularity vanishes for equilateral triangles and positive for all other shapes including isosceles triangles. Fig. 4.15 shows five sets of triangular cells with various irregularities, but the same number of nodes. It is obvious that as the irregularity increases, the mesh is distorted further.

Figure 4.16 presents the numerical error with different schemes against the degree of irregularity for the second Poisson problem. It is easily found that the numerical error obtained from schemes III does not vary too much. However, the numerical error obtained from schemes I and II become worse when the irregular meshes are used. These crucial findings imply that the present PL-GSM works well even with the extremely distorted cells. The interpolation method, however, is known and confirmed here to be sensitive to mesh distortions.

Based on the above analysis, it is concluded the PL-GSM is more accurate than PC-GSM although they are both second order accuracy in spatial approximation. In addition, the PC-GSM is more sensitive to the distortion of element compared with the PL-GSM. Also, the numerical treatment of PL-GSM is easier than the PC-GSM. Therefore, the PL-GSM is an excellent alternative to the PC-GSM.

4.5 Solutions to incompressible flow Navier-Stokes equations

4.5.1 Discretization of governing equations

The Navier–Stokes equations, regarded as the basic governing equations in incompressible flow, describe the motion of fluid substances. The sets of equations are derived from Newton's second law to denote the conservation of mass, momentum and energy. In this thesis, heat transfer is ignored.

$$\frac{\partial u}{\partial x}+\frac{\partial v}{\partial y}=0 \tag{4.41}$$

$$\frac{\partial \rho u}{\partial t}+u\frac{\partial \rho u}{\partial x}+v\frac{\partial \rho u}{\partial y}+\frac{\partial p}{\partial x}=\frac{\partial \tau_{xx}}{\partial x}+\frac{\partial \tau_{xy}}{\partial y} \tag{4.42}$$

$$\frac{\partial \rho v}{\partial t}+u\frac{\partial \rho v}{\partial x}+v\frac{\partial \rho v}{\partial y}+\frac{\partial p}{\partial y}=\frac{\partial \tau_{xy}}{\partial x}+\frac{\partial \tau_{yy}}{\partial y} \tag{4.43}$$

Written in the conservative form:

$$\frac{\partial \rho u}{\partial x}+\frac{\partial \rho v}{\partial y}=0 \tag{4.44}$$

$$\frac{\partial \rho u}{\partial t}+\frac{\partial \left(\rho u^2+p\right)}{\partial x}+\frac{\partial \rho uv}{\partial y}=\frac{\partial \tau_{xx}}{\partial x}+\frac{\partial \tau_{xy}}{\partial y} \tag{4.45}$$

$$\frac{\partial \rho v}{\partial t}+\frac{\partial \left(\rho v^2+p\right)}{\partial y}+\frac{\partial \rho uv}{\partial x}=\frac{\partial \tau_{yy}}{\partial y}+\frac{\partial \tau_{xy}}{\partial x} \tag{4.46}$$

where

$$\tau_{xy}=\tau_{yx}=\mu\left(\frac{\partial u}{\partial y}+\frac{\partial v}{\partial x}\right),\ \tau_{xx}=2\mu\frac{\partial u}{\partial x},\ \tau_{yy}=2\mu\frac{\partial v}{\partial y} \tag{4.47}$$

There is no temporal term in the continuity equation, which violates the hyperbolic properties of the whole systems. Thus, it requires additional requirements in numerical procedure. In order to maintain hyperbolic behaviors, temporal terms with respect to

pseudo-time are added into the set of the governing equations, together with artificial compressibility.

$$\frac{1}{\beta}\frac{\partial p}{\partial \tau}+\frac{\partial \rho u}{\partial x}+\frac{\partial \rho v}{\partial y}=0 \tag{4.48}$$

$$\frac{\partial \rho u}{\partial \tau}+\frac{\partial \rho u}{\partial t}+\frac{\partial\left(\rho u^2+p\right)}{\partial x}+\frac{\partial \rho uv}{\partial y}=\frac{\partial \tau_{xx}}{\partial x}+\frac{\partial \tau_{xy}}{\partial y} \tag{4.49}$$

$$\frac{\partial \rho v}{\partial \tau}+\frac{\partial \rho v}{\partial t}+\frac{\partial\left(\rho v^2+p\right)}{\partial y}+\frac{\partial \rho uv}{\partial x}=\frac{\partial \tau_{yy}}{\partial y}+\frac{\partial \tau_{xy}}{\partial x} \tag{4.50}$$

Eq. (4.48), (4.49) and (4.50) can be rewritten in the following generic vector form:

$$\frac{\partial \mathbf{Q}}{\partial \tau}+\frac{\partial \mathbf{W}}{\partial t}+\nabla\bullet\left(\mathbf{F}_c-\mathbf{F}_v\right)=0 \tag{4.51}$$

The relevant variables are defined as:

$$\mathbf{Q}=\begin{bmatrix} p \\ \rho u \\ \rho v \end{bmatrix} \quad \mathbf{W}=\begin{bmatrix} 1 \\ \rho u \\ \rho v \end{bmatrix} \quad \mathbf{F}_c=\begin{bmatrix} \beta\rho V \\ \rho uV+n_x p \\ \rho vV+n_y p \end{bmatrix} \quad \mathbf{F}_v=\begin{bmatrix} 0 \\ n_x\tau_{xx}+n_y\tau_{xy} \\ n_x\tau_{xy}+n_y\tau_{yy} \end{bmatrix} \tag{4.52}$$

where $V=\mathbf{v}\bullet\mathbf{n}=un_x+vn_y$, n_x and n_y are the components of the unit outward normal vectors in x- and y-directions.

4.5.2 Convective fluxes, Fc

The convective effect plays an important role in the momentum of fluid dynamics and also causes some difficulty in the spatial discretisation due to the upwinding effect. It is quite straightforward to approximate the convective fluxes at the midpoint of the cell-edge of interest with the average values at the two constitutive node *i* and j_k. This method is easily formulated and works well for low Reynolds number. However, this treatment fails if the Reynolds number increases a certain value. In order to overcome

this problem, the 2nd-order ROE flux differencing splitting upwinding scheme [111] is introduced in the simulation. The convective flux with the use of ROE is expressed as follows:

$$(\mathbf{F}_c)_{ij_k} = \frac{1}{2}\left[\mathbf{F}_c(\mathbf{Q}_{ij_k}^R) + \mathbf{F}_c(\mathbf{Q}_{ij_k}^L)\right] + \bar{\mathbf{A}}_{ROE}^{-}(\mathbf{Q}_{ij_k}^R, \mathbf{Q}_{ij_k}^L)(\mathbf{Q}_{ij_k}^R - \mathbf{Q}_{ij_k}^L) \tag{4.53}$$

In Eq. (4.53), $\mathbf{Q}_{ij_k}^R$ and $\mathbf{Q}_{ij_k}^L$ represent the left and right states. The ROE matrix $\bar{\mathbf{A}}_{ROE}^{-}$ only corresponds to non-positive eigenvalues of the convective flux Jacobian matrix **K**. The convective flux Jacobian matrix **K** with respect to conservative variables is written as follows:

$$\mathbf{K} = \frac{\partial \mathbf{F}_c}{\partial \mathbf{Q}} = \begin{bmatrix} 0 & \beta n_x & \beta n_y \\ n_x & V + n_x u & n_y u \\ n_y & n_x v & V + n_y v \end{bmatrix} \tag{4.54}$$

The right eigenvectors **r**, eigenvalues **Λ** and left eigenvectors $\mathbf{r}^{-1}$ of the **K** matrix are derived:

$$\mathbf{r} = \begin{bmatrix} 0 & c & -c \\ -n_y & u\lambda_2/\beta + n_x & u\lambda_3/\beta + n_x \\ n_x & v\lambda_2/\beta + n_y & u\lambda_3/\beta + n_x \end{bmatrix}$$

$$\mathbf{\Lambda} = \begin{bmatrix} \lambda_1 & 0 & 0 \\ 0 & \lambda_2 & 0 \\ 0 & 0 & \lambda_3 \end{bmatrix} = \begin{bmatrix} V & 0 & 0 \\ 0 & V + c & 0 \\ 0 & 0 & V - c \end{bmatrix} \tag{4.55}$$

$$\mathbf{r}^{-1} = \frac{\beta}{2c^2}\begin{bmatrix} 2(un_y - vn_x)/\beta & -2(vV/\beta + n_y) & 2(uV/\beta + n_x) \\ -\lambda_3/\beta & n_x & n_y \\ -\lambda_2/\beta & n_x & n_y \end{bmatrix}$$

The speed of pressure wave is expressed as: $c = \sqrt{V^2 + \beta}$.

The product of the ROE matrix ($\bar{\mathbf{A}}_{ROE} = \mathbf{r}\mathbf{\Lambda}\mathbf{r}^{-1}$) and the difference between the right and left states can be rewritten as

$$\begin{aligned}\bar{\mathbf{A}}_{ROE}(\mathbf{Q}_{ij_k}^{R}-\mathbf{Q}_{ij_k}^{L}) &= \lambda_1(l_{11}\Delta p+l_{12}\Delta\rho u+l_{13}\Delta\rho v)\begin{bmatrix} r_{11}\\ r_{21}\\ r_{31}\end{bmatrix}\\ &+\lambda_2(l_{21}\Delta p+l_{22}\Delta\rho u+l_{23}\Delta\rho v)\begin{bmatrix} r_{12}\\ r_{22}\\ r_{32}\end{bmatrix}\\ &+\lambda_3(l_{31}\Delta p+l_{32}\Delta\rho u+l_{33}\Delta\rho v)\begin{bmatrix} r_{13}\\ r_{23}\\ r_{33}\end{bmatrix}\end{aligned} \qquad 4.56$$

l_{ij} and r_{ij} (i =1, 3, j =1, 3) are the terms related to the left and right matrices as described previously.

The left and right differences are denoted by:

$$\Delta p = p_{ij_k}^{R}-p_{ij_k}^{L},\ \Delta\rho u=(\rho u)_{ij_k}^{R}-(\rho u)_{ij_k}^{L},\ \text{and}\ \ \Delta\rho v=(\rho v)_{ij_k}^{R}-(\rho v)_{ij_k}^{L} \qquad 4.57$$

In the formulation of second-order ROE upwinding scheme, only negative eigenvalues in the matrix $\mathbf{\Lambda}$ are calculated. Thus, λ_2 in Eq. (4.56) are eliminated because it is a positive value. However, λ_3 are always required in the computation, because it is less than zero. Due to the uncertainty of the λ_1, the terms related to λ_1 are considered in the computation if $\lambda_1 < 0$. Therefore, Eq. (4.56) can be simplified in the process of convective flux.

The key concept of the ROE method is that all variables occurring in the above matrices are based on the averaged values of left and right states at the midpoint of interest, ij_k. The $\mathbf{Q}_{ij_k}^{L}$ and $\mathbf{Q}_{ij_k}^{R}$ represented by the left and right state in the ROE scheme are calculated by the Barth and Jesperson scheme [112]:

$$\begin{aligned}\mathbf{Q}_{ij_k}^{L} &= \mathbf{Q}_i+\frac{1}{2}\nabla\mathbf{Q}_i\cdot\mathbf{r}_{ij_k}\\ \mathbf{Q}_{ij_k}^{R} &= \mathbf{Q}_{j_k}-\frac{1}{2}\nabla\mathbf{Q}_{j_k}\cdot\mathbf{r}_{ij_k}\end{aligned} \qquad 4.58$$

where $\mathbf{r}_{ij_k}$ is the vector from the node i to j_k.

The ROE scheme in detail for 2D and 3D case can be found in Whitfield and Taylor [113] Shin [114] respectively. Compared with the REO scheme in the compressible flow, the limiter function is no longer required in the incompressible flow solver.

4.5.3 Time Integration

4.5.3.1 Point implicit multi-stage RK method

The integration of the temporal terms uses the dual time stepping approach. In the dual time stepping approach, the computational process proceeds along a given physical time step (Δt). At the same time, the physical time (t) does not move to the next step until the steady-state solutions with respect to pseudo time is pursued, as pseudo time is marched by ($\Delta \tau$).Compared to the single global time stepping method, the main advantage of dual time stepping approach is to allow larger physical time step (Δt). Further, the dual time stepping approach can lead to faster convergence rate and high stability in solution.

Eq. (4.51) can be rewritten in the residual form with respect to pseudo time as

$$\frac{\partial \mathbf{Q}}{\partial \tau} = -\mathbf{R}^* \tag{4.59}$$

where $\mathbf{R}^* = \frac{\partial \mathbf{W}}{\partial t} + \mathbf{R}$ and $\mathbf{R} = \nabla \bullet (\mathbf{F}_c^n - \mathbf{F}_v^n)$.

The temporal term with respect to physical time is discretized with 2nd-order backward differencing scheme in the form of

$$\frac{\partial \mathbf{W}}{\partial t} \approx \frac{3\mathbf{W}^{n+1} - 2\mathbf{W}^n + \mathbf{W}^{n-1}}{2\Delta t} \tag{4.60}$$

This scheme is stable, which allows large physical time-step to be used in our simulation.

The temporal terms are related to pseudo-time using the explicit multistage Runge-Kutta scheme. They are performed as follows:

$$\mathbf{Q}^0 = \mathbf{W}^m$$

DO n = 0, *nmax*

$$\mathbf{Q}^{(0)} = \mathbf{Q}^n$$

$$\left\{\begin{array}{c} \text{DO } k = 1, p \\ \left(\mathbf{R}^*\right)^{(k-1)} = \left(\mathbf{R}^*\right)^{(k-1)}\left(\mathbf{Q}^{(k-1)}, \mathbf{W}^m, \mathbf{W}^{m-1}\right) \\ \mathbf{Q}^{(k)} = \mathbf{Q}^{(0)} - \alpha_k \Delta\tau \left(\mathbf{R}^*\right)^{(k-1)} \\ \text{ENDDO} \end{array}\right\} \text{Five stage Runge-kutta method}$$

$$\mathbf{Q}^{n+1} = \mathbf{Q}^{(p)}$$

ENDDO

$$\mathbf{W}_i^{m+1} = \mathbf{Q}_i^{n+1}$$

The five stage Runge-kutta method is expressed as follow:

$$\left.\begin{array}{ll} \mathbf{Q}^{(1)} = \mathbf{Q}^{(0)} - \alpha_1 \Delta\tau \left(\mathbf{R}^*\right)^{(0)} & \mathbf{Q}^{(2)} = \mathbf{Q}^{(0)} - \alpha_2 \Delta\tau \left(\mathbf{R}^*\right)^{(1)} \\ \mathbf{Q}^{(3)} = \mathbf{Q}^{(0)} - \alpha_3 \Delta\tau \left(\mathbf{R}^*\right)^{(2)} & \mathbf{Q}^{(4)} = \mathbf{Q}^{(0)} - \alpha_4 \Delta\tau \left(\mathbf{R}^*\right)^{(3)} \\ \multicolumn{2}{c}{\mathbf{Q}^{(5)} = \mathbf{Q}^{(0)} - \alpha_5 \Delta\tau \left(\mathbf{R}^*\right)^{(4)}} \end{array}\right| \begin{array}{l} \alpha_1 = 0.0695 \\ \alpha_2 = 0.1602 \\ \alpha_3 = 0.2898 \\ \alpha_4 = 0.5060 \\ \alpha_5 = 1.0000 \end{array} \qquad 4.61$$

The main drawback of explicit scheme is that the physical time step Δt is severely restricted by the characteristics of the governing equations and the grid geometry. In addition, as observed by Arnone *et al.* [115], such an explicit RK scheme becomes unstable for small physical time step. Melson *et al.* [116] modified the explicit scheme to get rid of the instability by implicitly treating the term $\frac{3\mathbf{W}^{n+1}}{2\Delta t}$ appearing in the 3-point backward differencing scheme. As a result, the stability region will grow as Δt

decreases. Such a justification results in the following point-implicit multistage Runge-Kutta scheme:

$$\mathbf{Q}^0 = \mathbf{W}^m$$

DO n = 0, $nmax$

$$\mathbf{Q}^{(0)} = \mathbf{Q}^n$$

$$\left\{ \begin{array}{c} \text{DO } k = 1, p \\ \left(\mathbf{R}^*\right)^{(k-1)} = \left(\mathbf{R}^*\right)^{(k-1)}\left(\mathbf{Q}^{(k-1)}, \mathbf{W}^{m-1}, \mathbf{W}^m\right) \\ \mathbf{Q}^{(k)} = \dfrac{1}{1+\dfrac{3}{2}\dfrac{\Delta\tau}{\Delta t}\alpha_k}\left[\mathbf{Q}^{(0)} - \alpha_k \Delta\tau \left(\mathbf{R}^*\right)^{(k-1)} + \alpha_k \dfrac{3}{2}\dfrac{\Delta\tau}{\Delta t}\mathbf{Q}^{(k-1)}\right] \\ \text{ENDDO} \end{array} \right\} \text{Five stage Runge Kutta Method}$$

$$\mathbf{Q}^{n+1} = \mathbf{Q}^{(p)}$$

ENDDO

$$\mathbf{W}^{m+1} = \mathbf{Q}^{n+1}$$

4.5.3.2 Local time stepping

The local time stepping for various time steps are adopted in the approximation of pseudo-time terms. Compared to the global time step, the local time step allows larger physical time step and leads to faster convergence. At any pseudo time (τ), the local time steps, which are varied with local domain volume and local flow characteristics, are first evaluated at each node-associated gradient smoothing domain. Then, they are used in the proposed multi-stage Runge-Kutta iterative process. The local time step at a node, i, of interest is approximated as follows:

$$\Delta\tau_i = \sigma \frac{V_i}{(\Lambda_x + \Lambda_y + D)_i} \qquad 4.62$$

where $(\Lambda_x)_i = \left[(|u| + c_x)S_x\right]_i$, $(\Lambda_y)_i = \left[(|v| + c_y)S_y\right]_i$ and $(D)_i = \frac{2}{\mathrm{Re}} \frac{A_i}{(S_x + S_y)_i}$. The constant σ takes the value of 4 in the current study.

The artificial speeds of sound in each dimension are given by

$$\begin{aligned} (c_x)_i &= \sqrt{u_i^2 + \beta} \\ (c_y)_i &= \sqrt{v_i^2 + \beta} \end{aligned} \qquad 4.63$$

The β is artificial compressibility which is somewhat problem dependent. Kwak *et al*. [117] proposed optimal value for β in the range of 0.1 – 10.0 for most of problems. In this thesis, $\beta = 2.0$ is used.

The projected areas of the smoothing domain are calculated as

$$\begin{aligned} (S_x)_i &= \frac{1}{2}\sum_{k=1}^{n_i} \left|\Delta S_{ij_k}^x\right| \\ (S_y)_i &= \frac{1}{2}\sum_{k=1}^{n_i} \left|\Delta S_{ij_k}^y\right| \end{aligned} \qquad 4.64$$

4.5.4 Steady-state lid-driven cavity flow

The lid-driven cavity flow is classical benchmark testing case designed to evaluate the behavior of algorithms that deal with incompressible viscous flows. In this test, incompressible viscous fluid is confined within a square cavity in which only the upper edge is allowed to tangentially slide at a prescribed velocity (u = 1.0 in the current study). Meanwhile, non-slip conditions ($u = v = 0$) are imposed at the rest of the walls. Reference pressure is prescribed to be zero at the bottom left corner. Relevant boundary conditions used in the test are sketched in Fig. 4.17. The convergence tolerance in this example is that the variation of pressure in the two time steps is less than 0.001.

Figure 4.18 illustrates the streamfunctions for various Reynolds numbers (Re=100 and 1000). The transmission of momentum by means of viscosity produces a large-scale vortex occurring in the centre, and small vortices at the corners. The details about the vertical structures depend highly on Reynolds number. For cases Re = 100, the flow is almost symmetric with respect to the central vertical line, as shown in Figure 4.18(a). As the Reynolds number increases to 1000, the bottom right and left vortices begin to develop at low Reynolds numbers. All the above mentioned phenomena captured with the proposed PL-GSM solver agrees very well with experimental results done by Ghia [118].

Figures 4.19 and 4.20 present the profiles of *u*-component along the vertical line and v-component along a horizontal line through the centre of the cavity for Re=100 and 1000 respectively. It is clearly shown the solutions obtained from PL-GSM have an excellent agreement with referenced data from Ghia *et al.* [118]. The important finding implies that the PL-GSM can be used to analyze fluid problems with very accurate solutions.

4.6 Application: Blood Flow through the Abdominal Aortic Aneurysm (AAA)

An aneurysm found in a brain capillary, epicardial artery, and the abdominal aorta below the rental arteries refers to an abnormal irreversible outward bulging of an artery. There are many possible reasons related to this disease: hypertension, cystic medial degeneration, mycotic infections, life style, genetic disorder, and atherosclerosis. An

abnormal aortic aneurysm (AAA) developed over decades unnoticed is an enlargement in the lining of the abdominal aorta. The risk for AAA patient is the rupture of aorta at the aneurism, and the possibility of rupture of aorta increases with the size of aneurysm. Obviously, aneurysm has to be repaired because of high death rate for AAA patients. In general, 5% of men over the age of 60 develop an aneurysm, and only 10% of AAA patients have symptoms such as back pain, fainting. Therefore, early detection of AAA is very important to save the patients. From the perspective of fluid dynamics, the large expansion of the vessel causes the unusual flow characteristics. Thus, we compare the flow characteristics between the Abdominal Aortic Aneurysm and normal aorta as illustrated in Fig. 4.21, which can help us reveal some important physical phenomenon.

The inlet boundary condition is prescribed as pulsatile flow with sine wave as shown in Eq. 4.65. The pulse period is chosen 1s.

$$u = 3700(abs(y) - 0.009)^2 abs\left(\sin\left(3.14t\right)\right), \qquad v = 0, \tag{4.65}$$

The initial condition is $u = 0.05m/s, v = 0$. We assume the flow is developed flow in the Abdominal Aortic Aneurysm and normal aorta. Fig. 4.22 and 4.23 illustrate the velocity contour at time $t = 0.25,\ 0.5,\ 0.75,\ 1s$ representing early systolic acceleration, late systolic acceleration, systolic deceleration, and diastole period respectively in one complete pulsatile cycle using PL-GSM. The flow characteristic between the Abdominal Aortic Aneurysm and normal aorta is quite similar, except the domain of aneurism. In the early systolic acceleration, the flow begins to accelerate. During the stage of late systolic acceleration，the maximum velocity occurs at the inlet. For $t \in [0.5, 0.75]$, the flow begins to decelerate temporally. During late diastole, the

inlet velocity decreases to zero to complete one cycle. It is noticed that the velocity decreases sharply in the domain of aneurysm due to the sudden increase of flow area, and there is a flow separation and stagnation of flow.

It is well known that the shear stress is the best indicator of AAA rupture. The shear stress along the wall for both Abdominal Aortic Aneurysm and normal aorta at time $t = 0.25,\ 0.5,\ 0.75,\ 1s$ is presented in Fig. 4.24, 4.25, 4.26 and 4.27. As seen from these Figures, the shear stresses are much higher at carotid branch than in the common, external and internal for both normal aorta and Abdominal Aortic Aneurysm. Also, the shear stresses are much higher during systole than during diastole. One important phenomenon is that the maximum shear stress occurring at the branch point during different time stage in the normal aorta is higher than Abdominal Aortic Aneurysm. This is because there is a sudden increase of flow area to reduce the velocity gradient at the branch point in the Abdominal Aortic Aneurysm. However, there is a sharp gradient of the shear stress at proximal and dismal aneurism zones in Abdominal Aortic Aneurysm, which increases the risk of rupture of blood vessel significantly.

4.7 Remarks

In the current study, a conservative and efficient gradient smoothing method formulated for the strong form of governing equations is developed. The PL-GSM is valid for both regular and irregular cells so that it can be readily applied for fluid flow problems with arbitrary geometry. It is found that

- The PL-GSM using triangular elements in two-dimensional space is very simple;

no additional parameters or degrees of freedoms are needed, the system matrices have the same dimension with the FDM model of same mesh and the method can be implemented in a straightforward way with little change to the FDM code

- The accuracy has improved significantly with the application of linearly-weighted smoothing operation instead of linear interpolation.
- The PL-GSM is not sensitive to distortion of element compared with the PC-GSM.
- The current PL-GSM is more accurate than the PC-GSM.

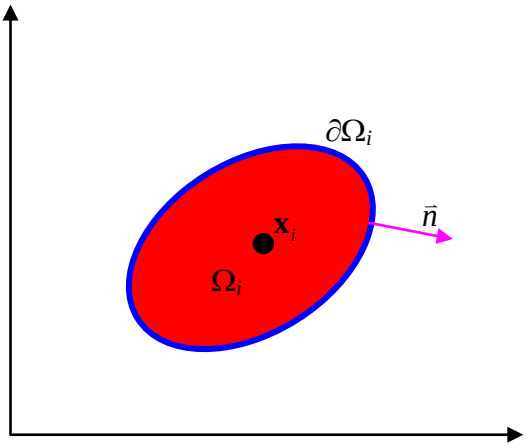

Figure 4.1: Gradient smoothing domain

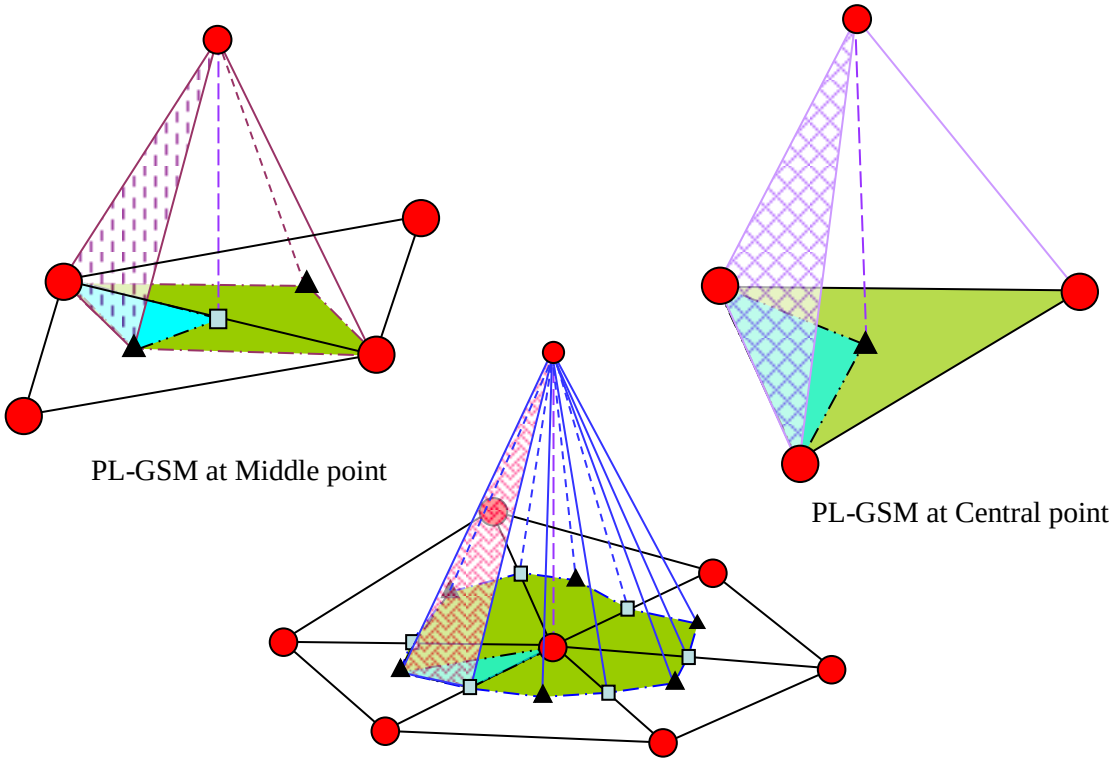

Figure 4.2: Piecewise linear gradient smoothing functions for different types of gradient smoothing domains

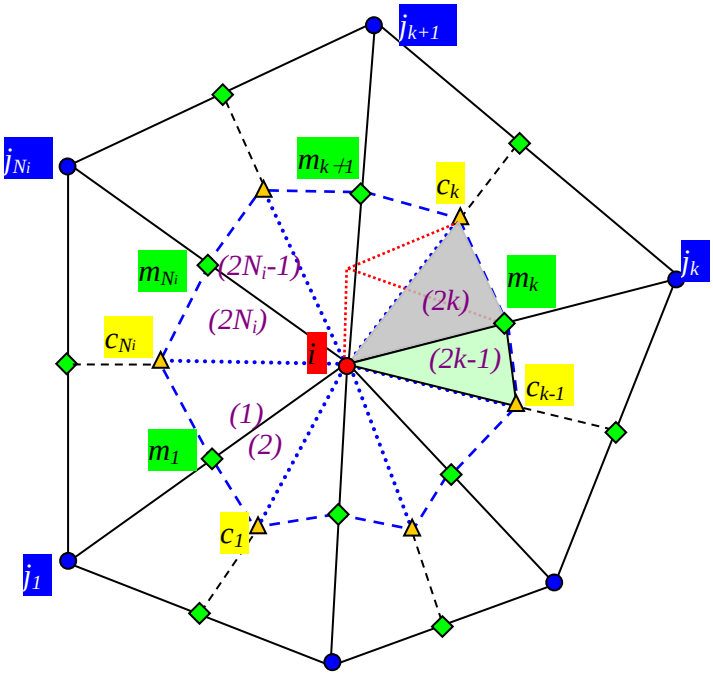

Figure 4.3: Adopted notations and sub-triangulation in the node of *i* interest

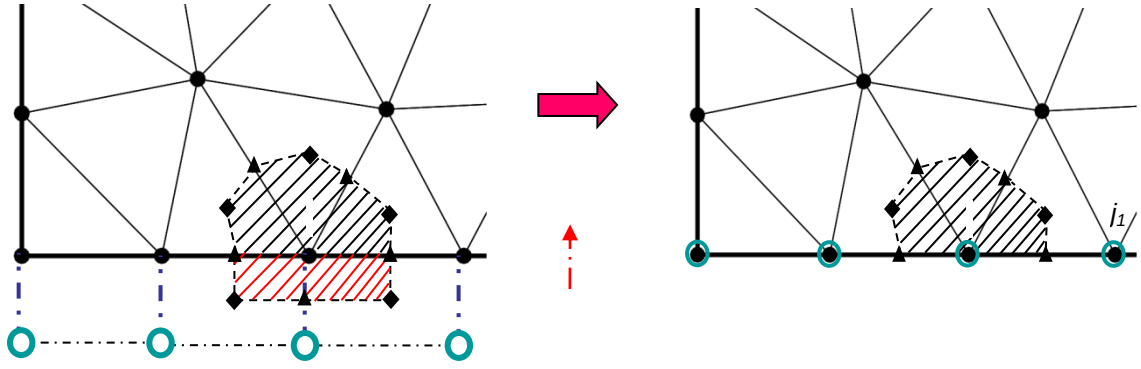

(a) with dummy nodes (b) without dummy nodes

Figure 4. 4: Treatment at boundary nodes

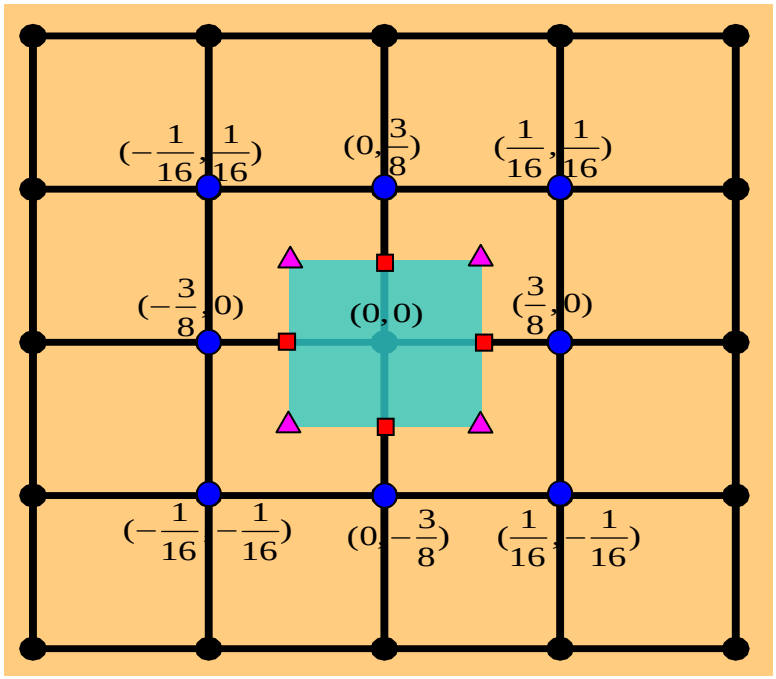

Figure 4.5: Stencils for approximated gradients $(\frac{\partial U_i}{\partial x},\frac{\partial U_i}{\partial y})$ based on cells in square shape

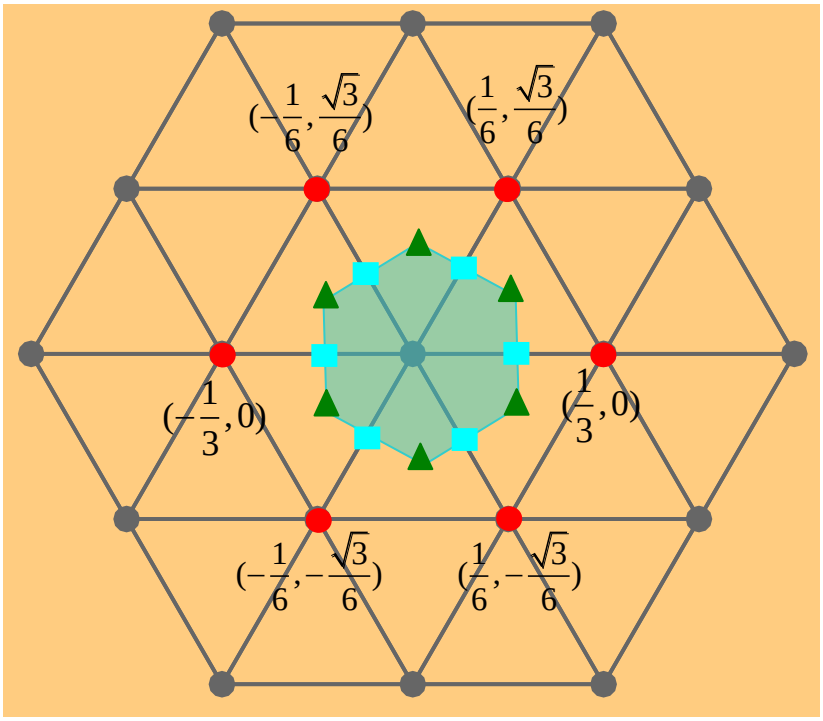

Figure 4.6: The stencil for approximated gradients $(\frac{\partial U_i}{\partial x},\frac{\partial U_i}{\partial y})$ based on cells in equilateral triangle shape

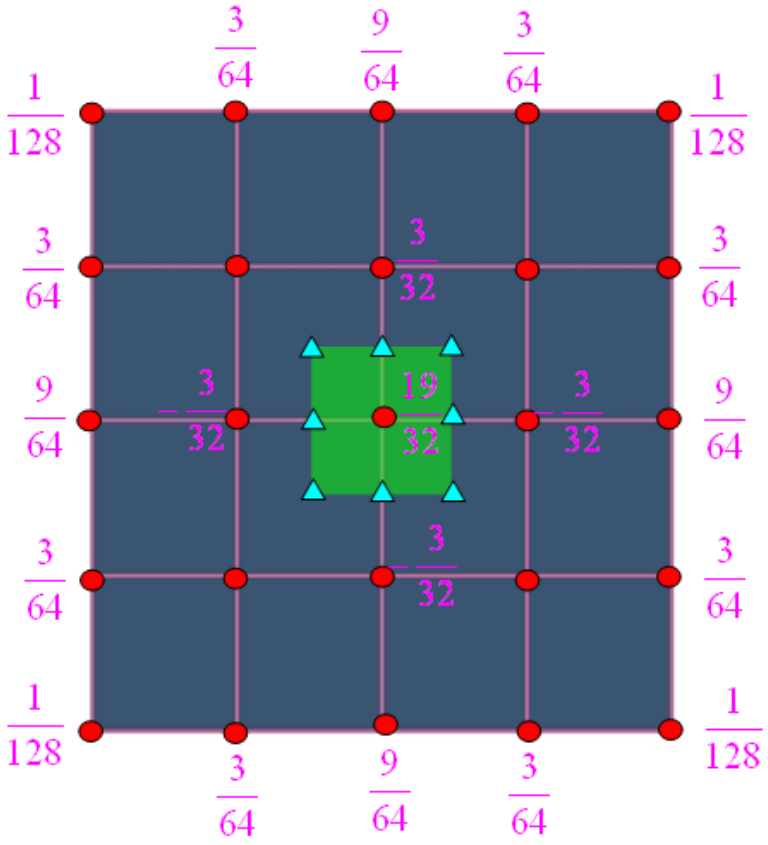

a) Scheme I

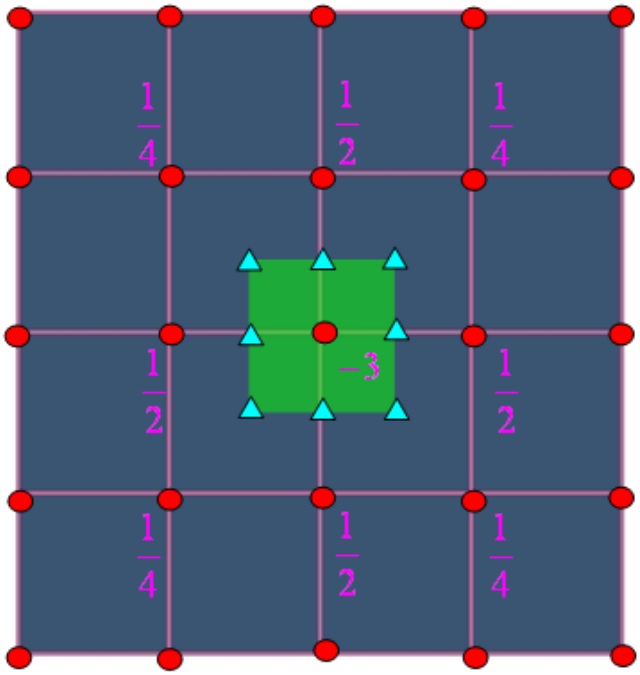

b) Schemes II and III

Figure 4.7: Stencils for the approximation Laplace operator on the cells in square shape

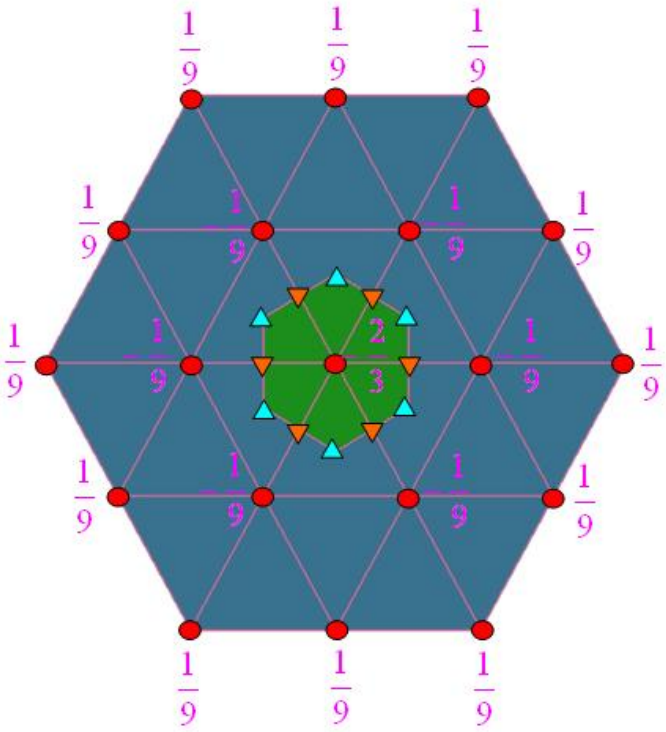

a) Schemes I

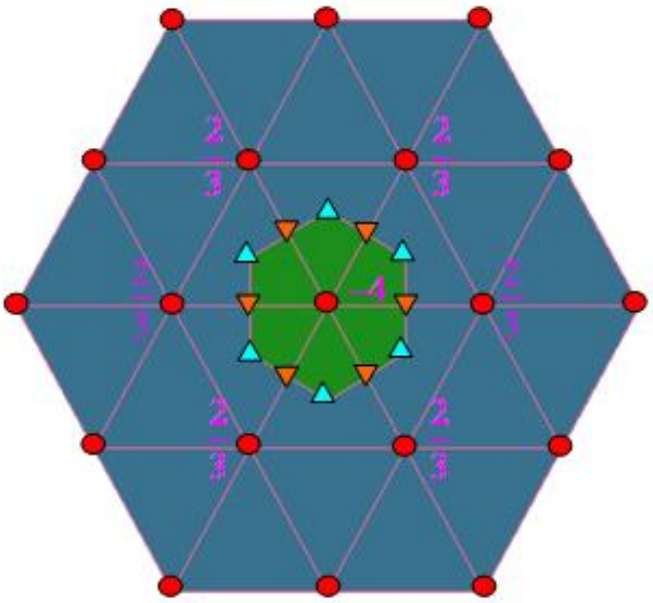

b) Schemes II and III

Figure 4.8: Stencils for the approximated Laplace operator on the cells in equilateral triangular

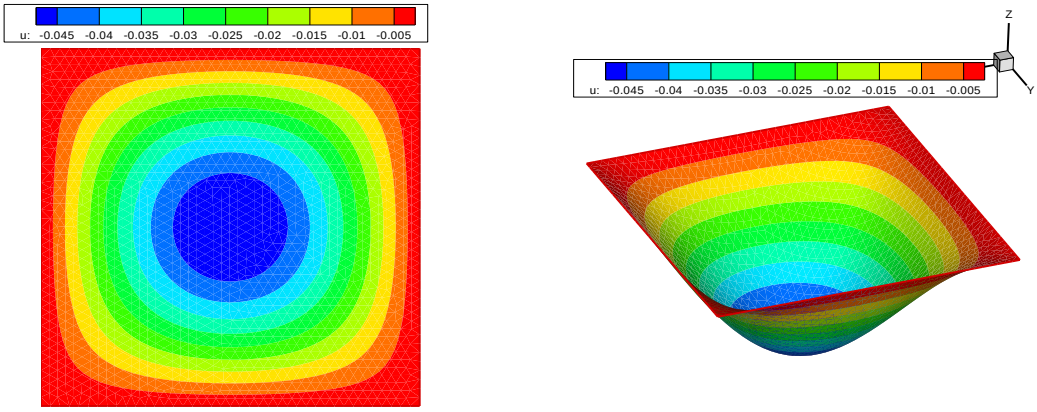

(a) 2D view (b) 3D view

Figure 4.9: Contour plots of exact solutions to the first Poisson problem

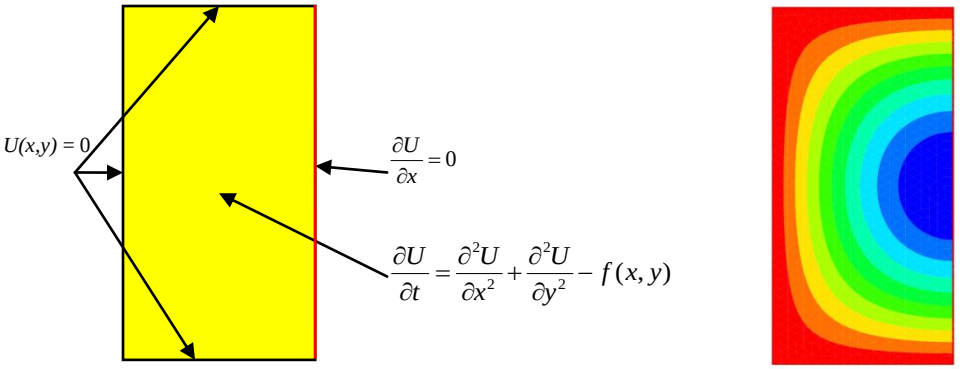

(a) Computational domain (b) Contour plot

Figure 4.10: Second Poisson equation in study

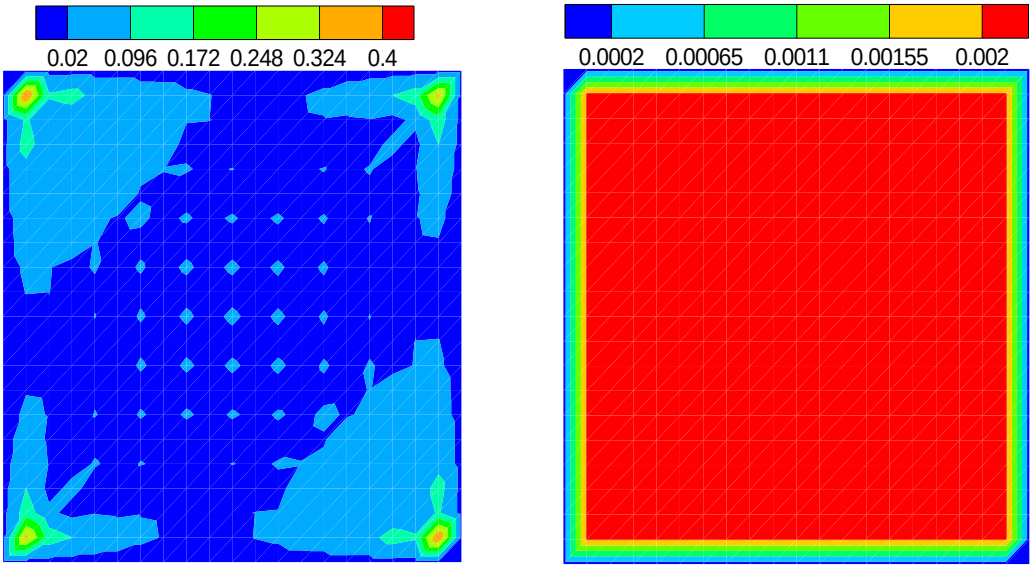

Scheme I Scheme VIII

Figure 4.11: Contour plots of relative errors on cells

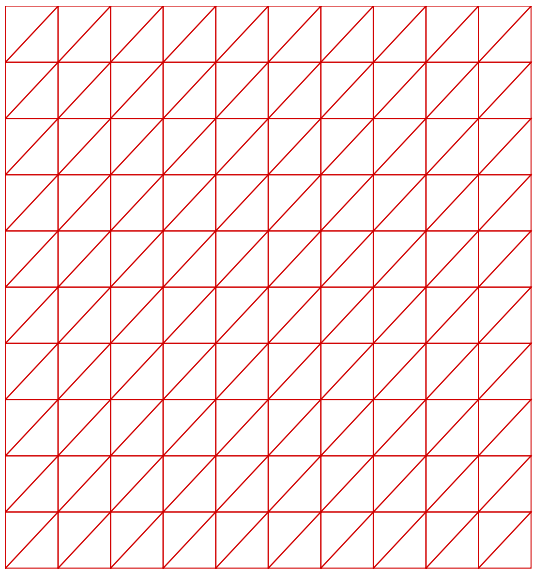

a) 11x11 nodes

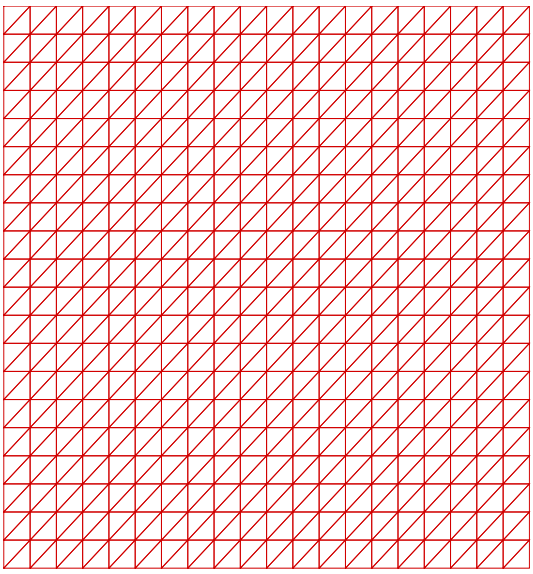

b) 21x21 nodes

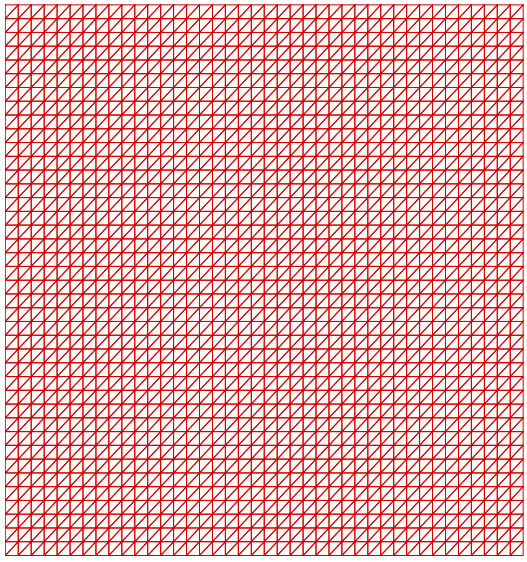

c) 41x41 nodes

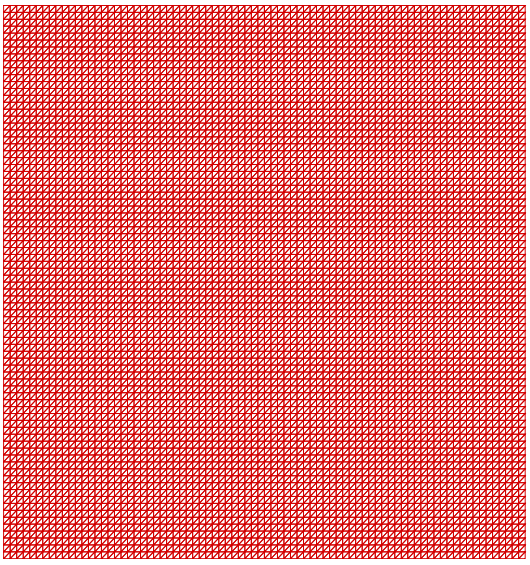

d) 81x81 nodes

Figure 4.12: Right triangle element distribution of Poisson's equation

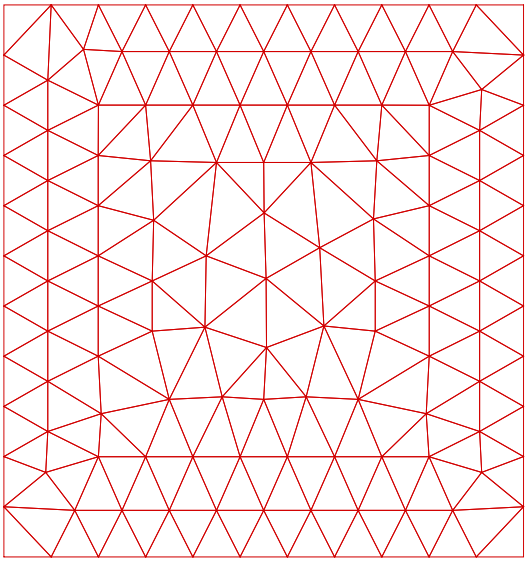

a) 131 nodes

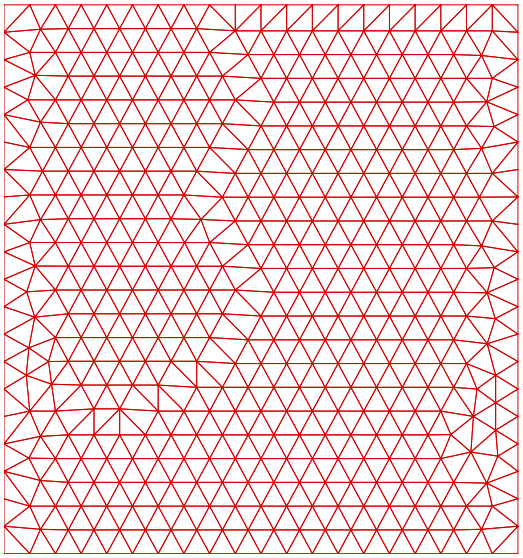

b) 478 nodes

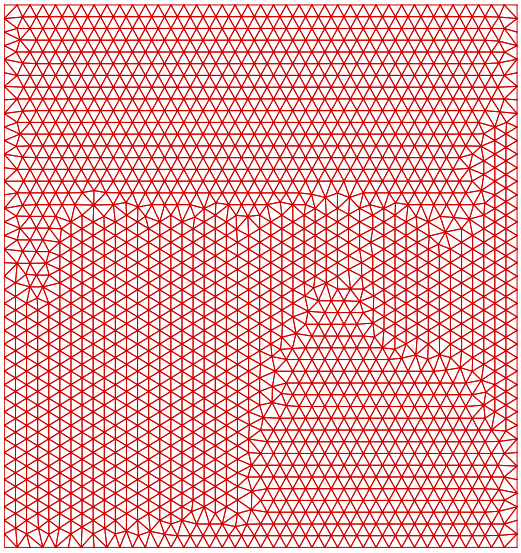

c) 1887 nodes

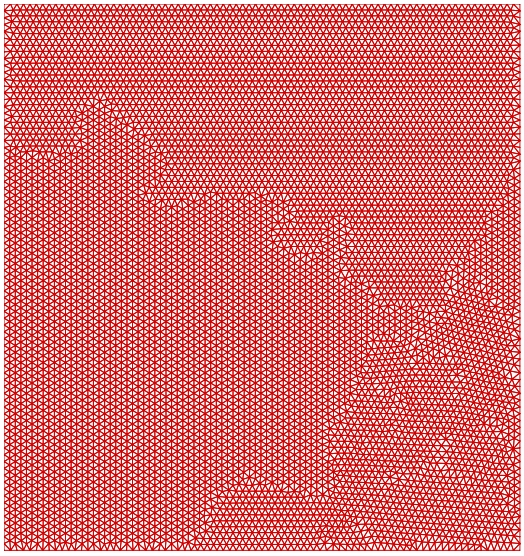

d) 7457 nodes

Figure 4.13: Regular element distribution of Poisson's equation

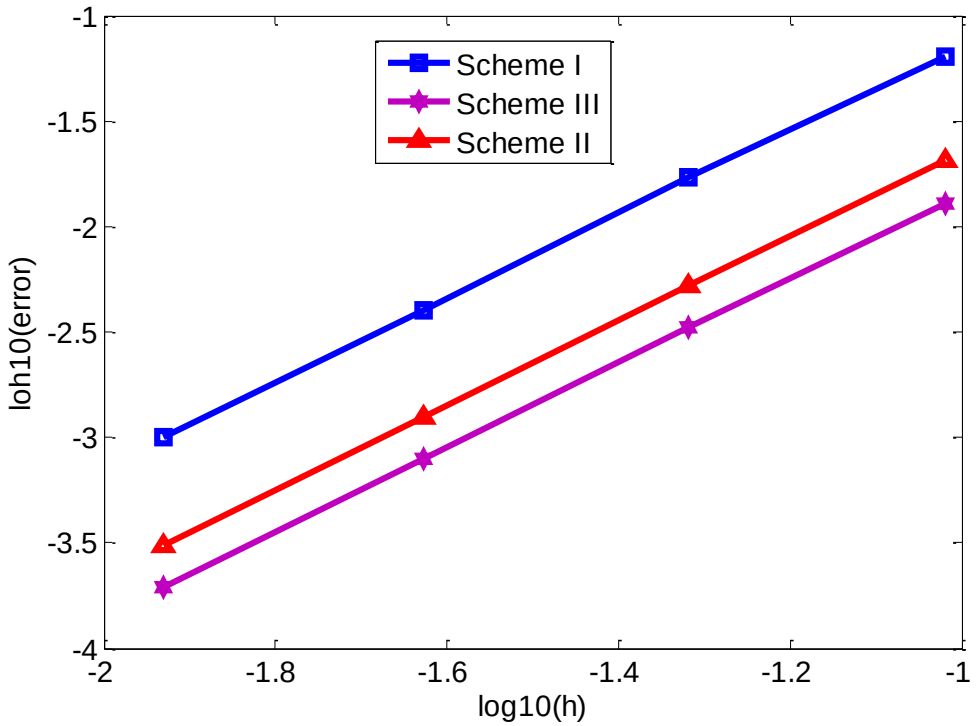

Figure 4.14: Convergence property of all schemes

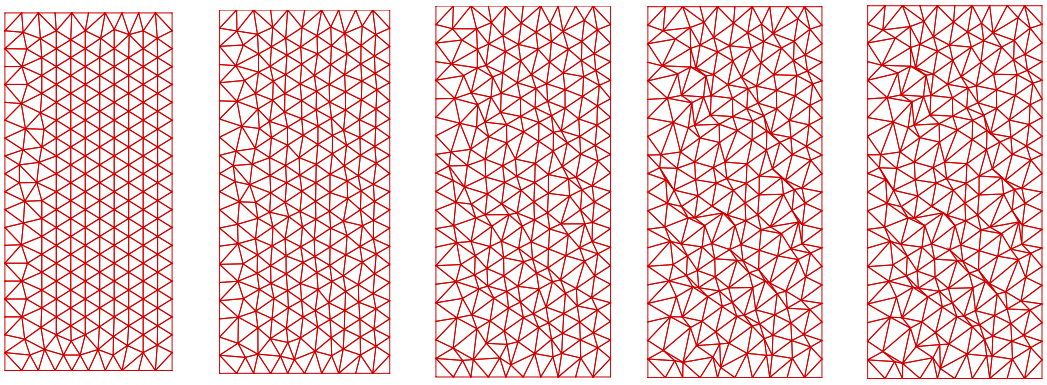

$\gamma = 0.05$ $\gamma = 0.1$ $\gamma = 0.2$ $\gamma = 0.3$ $\gamma = 0.31$

Figure 4.15: Triangular cells with various irregularities

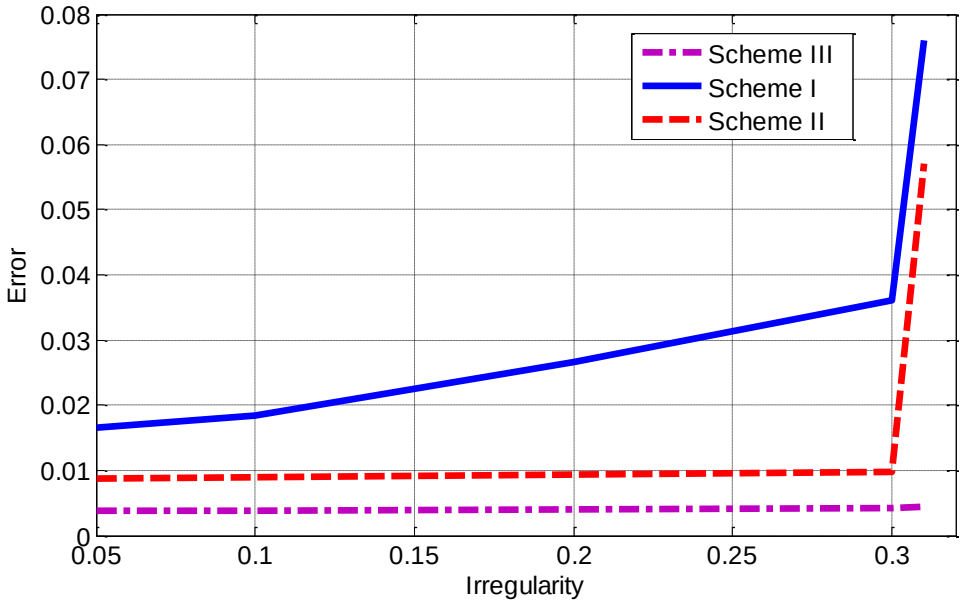

Figure 4.16: Numerical errors in solution (schemes I, II and III) to the second Poisson Problem

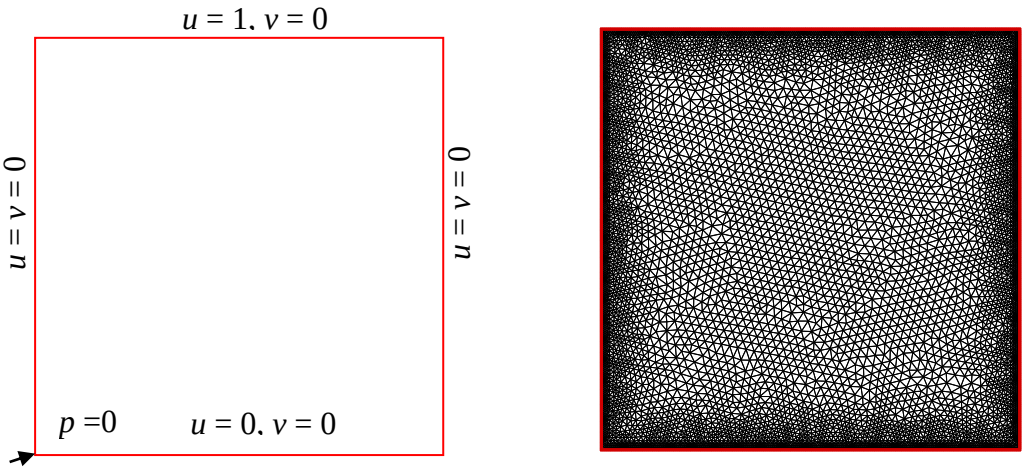

(a) Boundary condition (b) Mesh information (8321 nodes)

Figure 4.17: Boundary conditions and grids studied in the lid-driven cavity flow problem

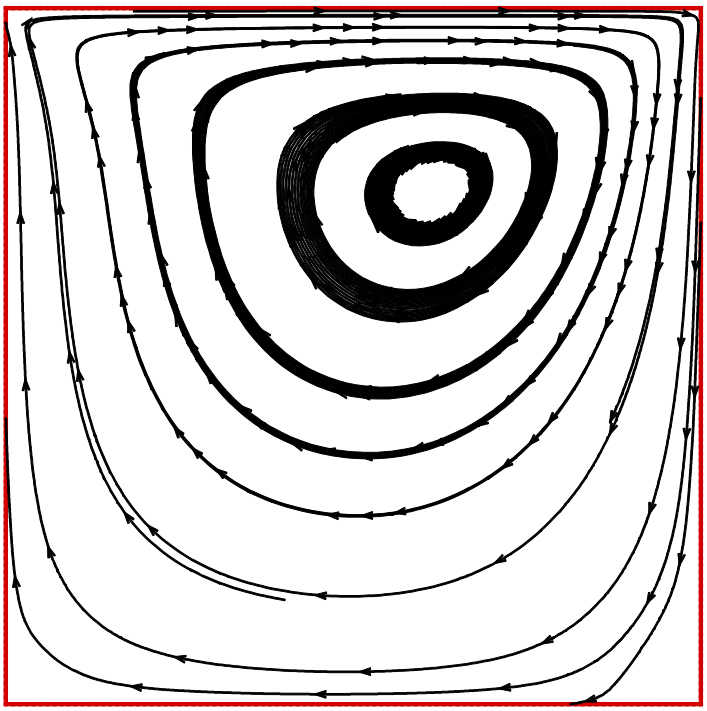

Re=100

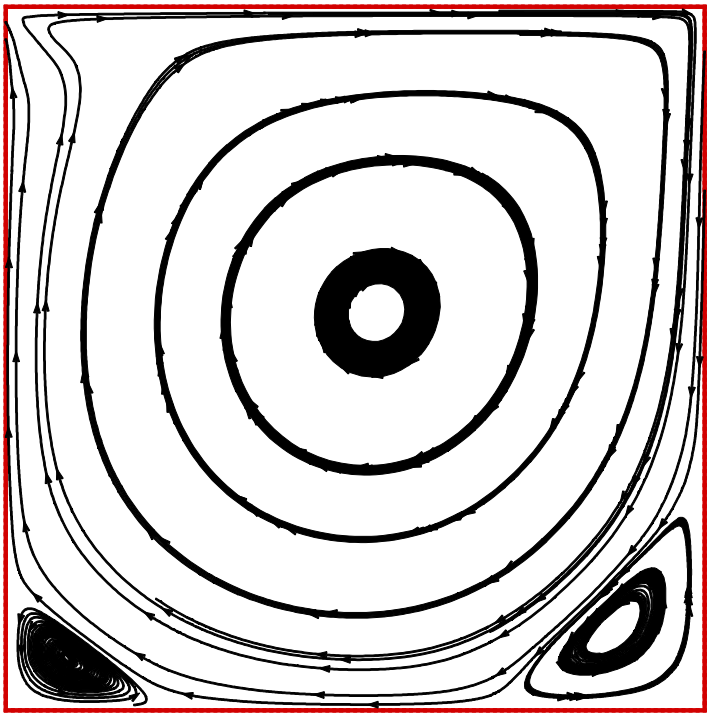

Re=1000

Figure 4.18: Plots of streamlines for various Reynolds number

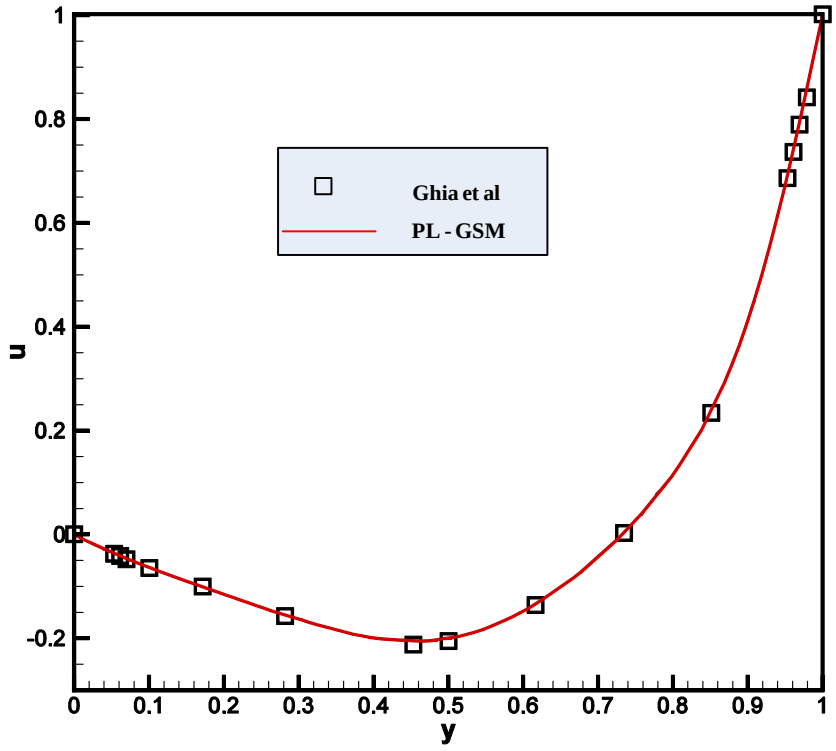

Re=100

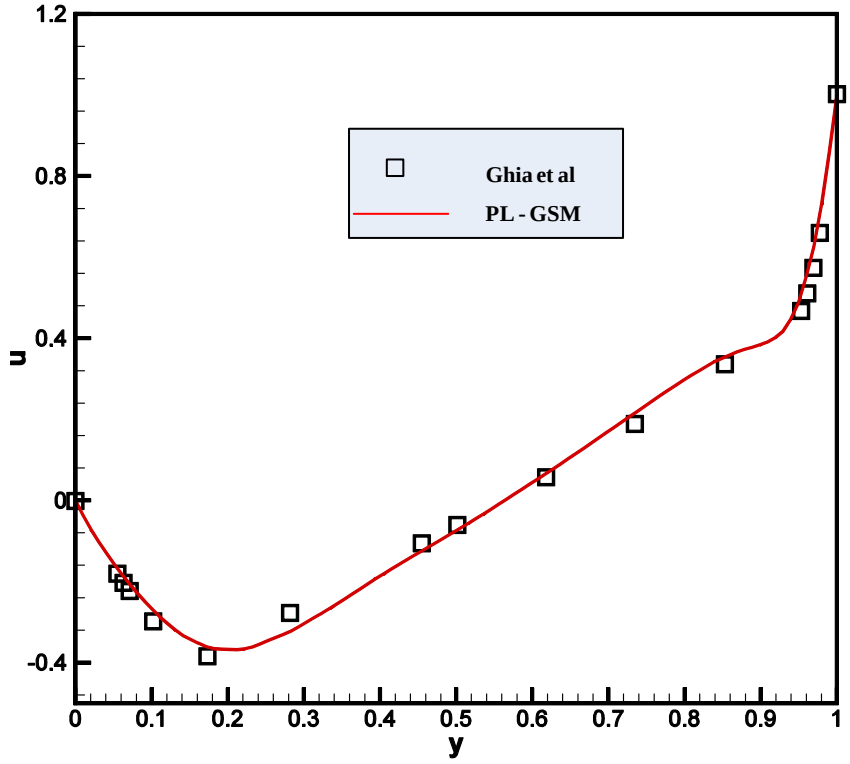

Re=1000

Figure 4.19: Profiles of u velocity along the vertical line x = 0.5 for various Reynolds number

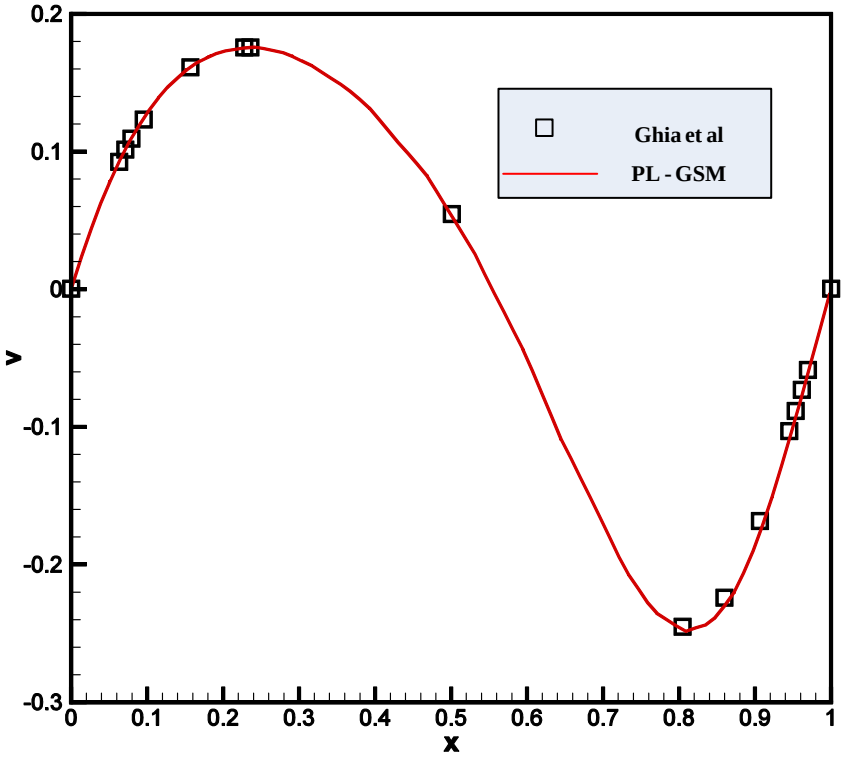

Re = 100

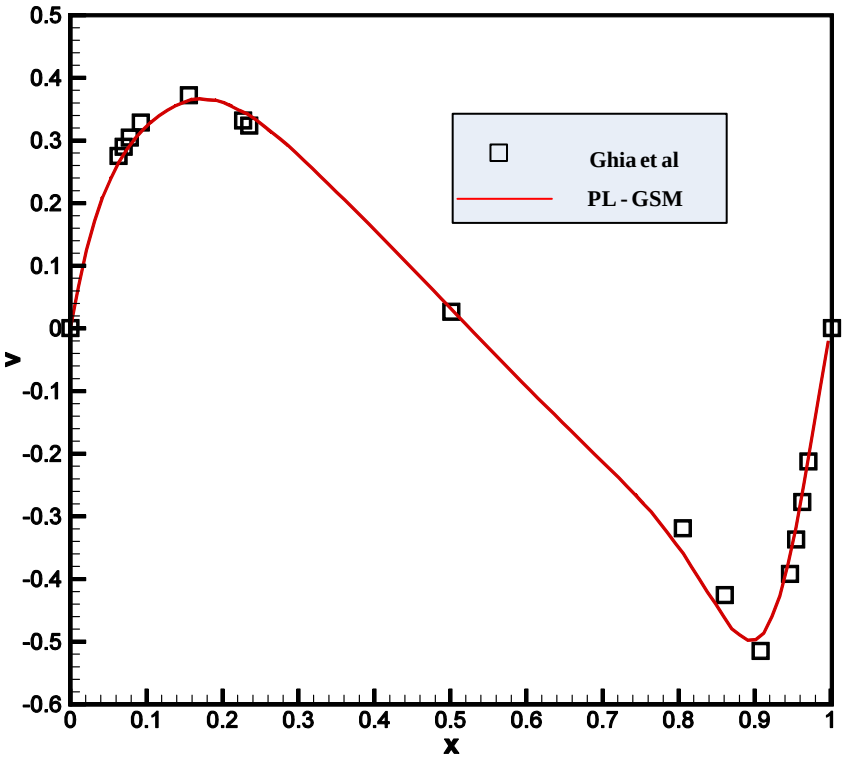

Re = 1000

Figure 4.20: Profiles of v velocity along the vertical line x = 0.5 for various Reynolds number

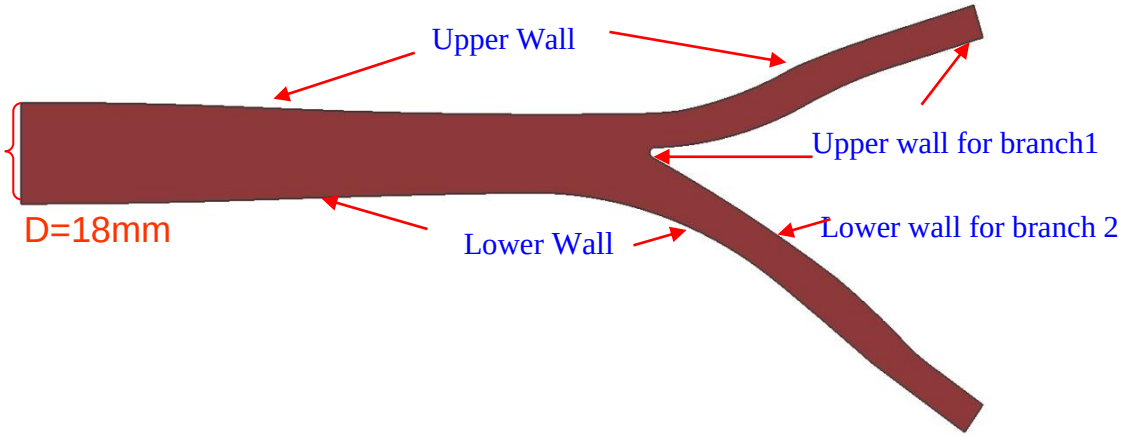

a) Normal aorta

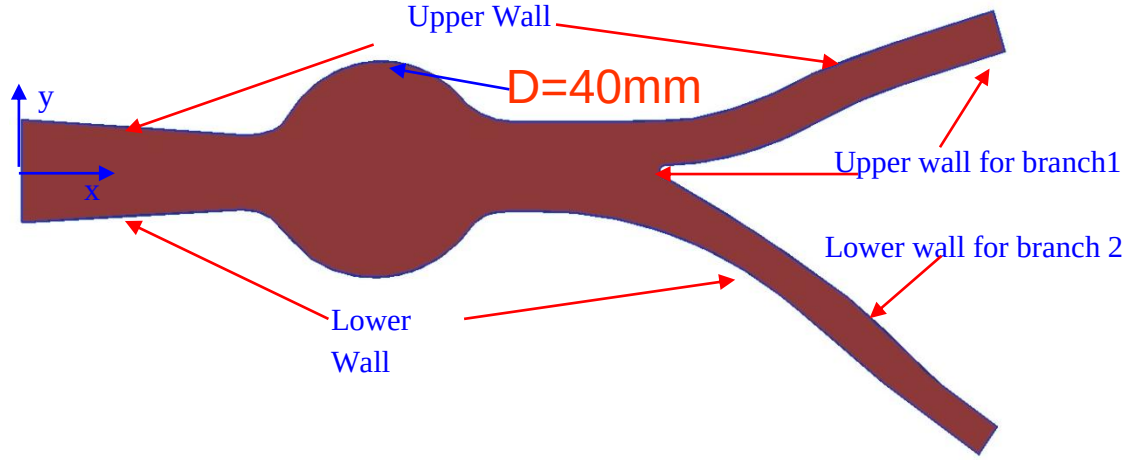

b) Abdominal aortic aneurysm

Figure 4.21: Geometrical parameters for normal aorta and abdominal aortic aneurysm

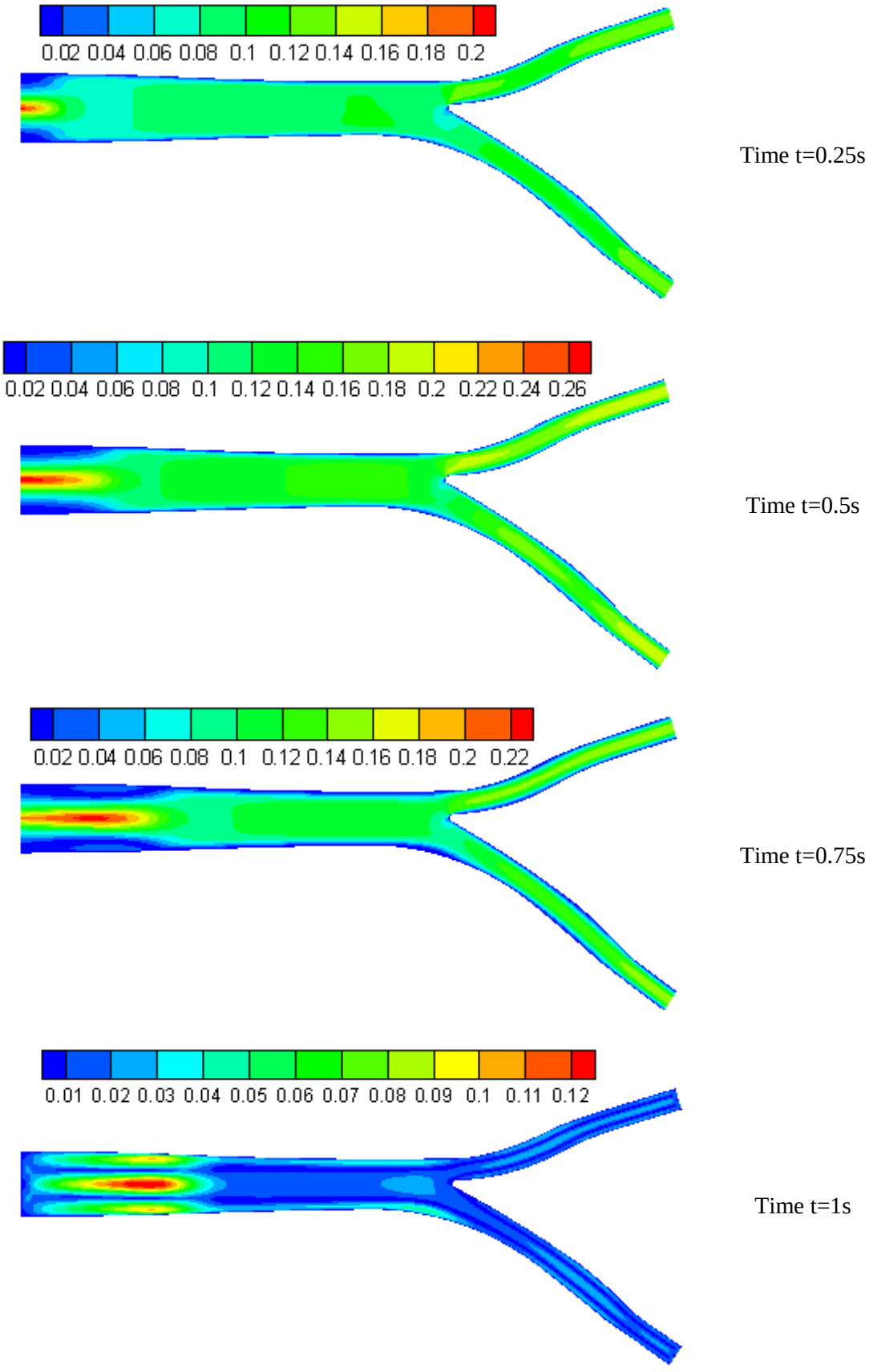

Figure 4.22: Velocity contour ad different stage for normal aorta

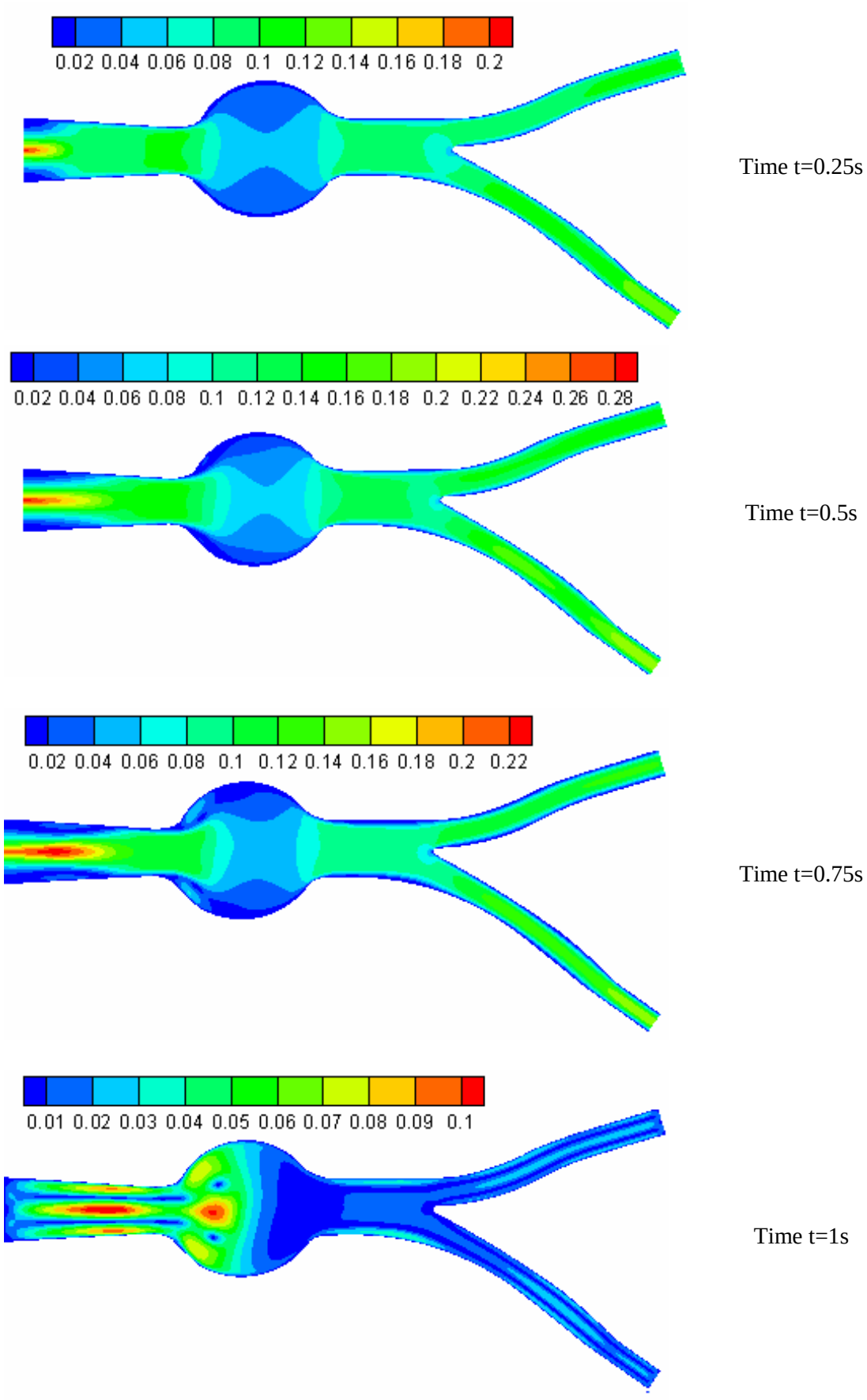

Figure 4.23: Velocity contour at different time stage for Abdominal Aortic Aneurysm

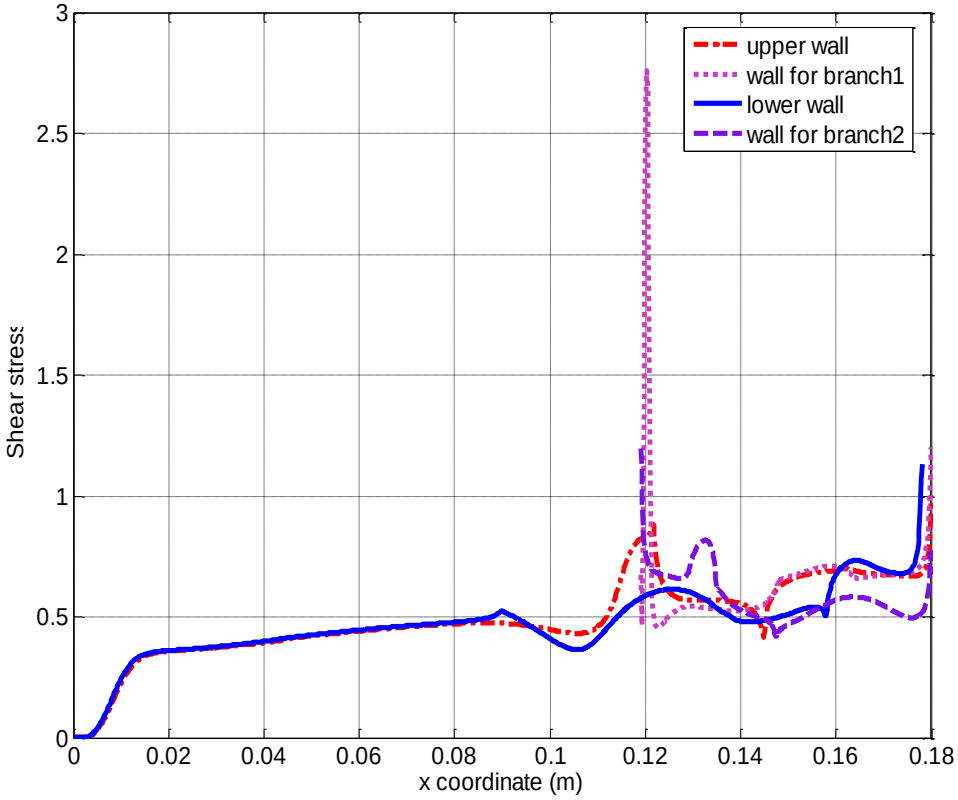

Shear stress for normal aorta

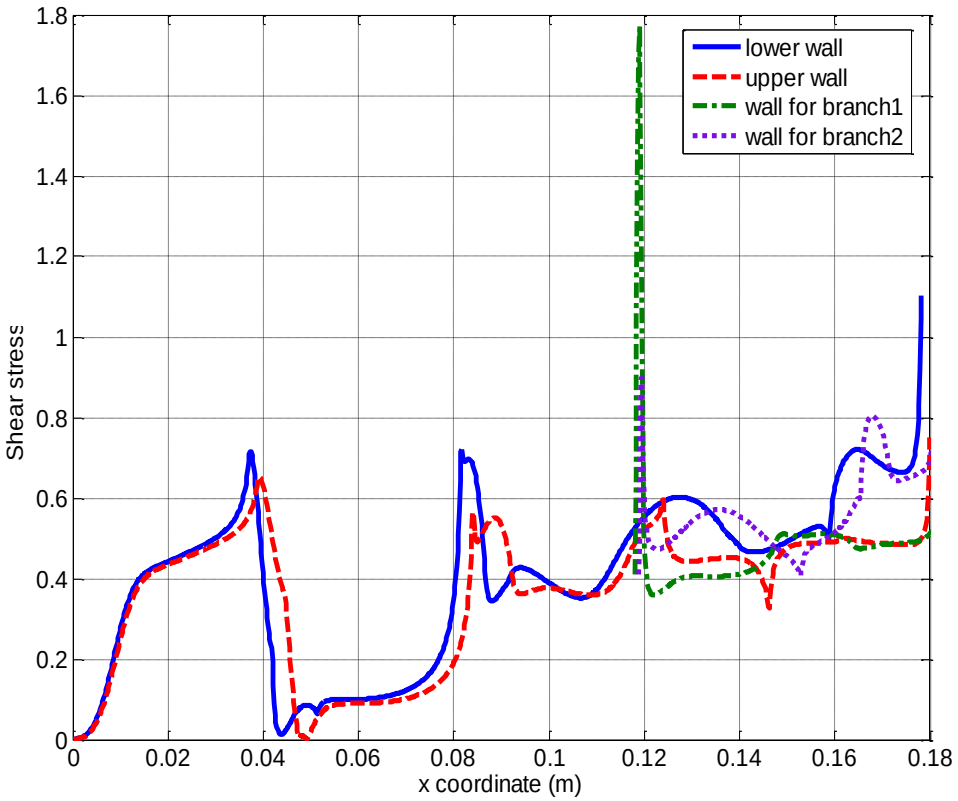

Shear stress for abdominal aortic aneurysms

Figure 4.24: Comparison of shear stress at time t=0.25s

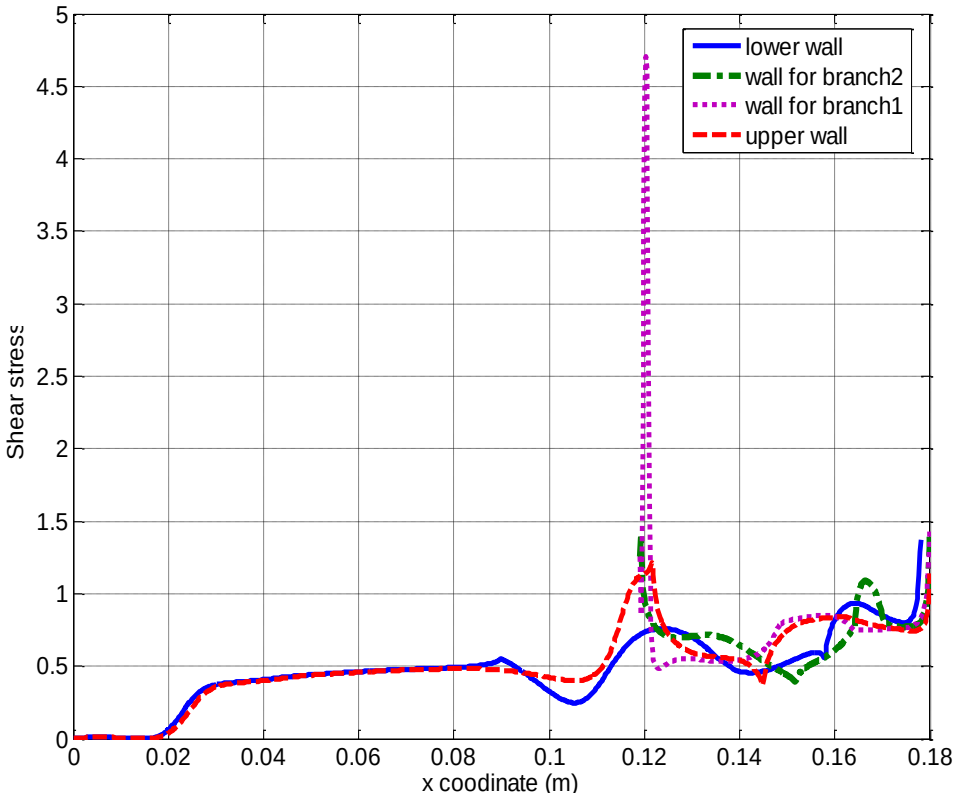

Shear stress for normal aorta

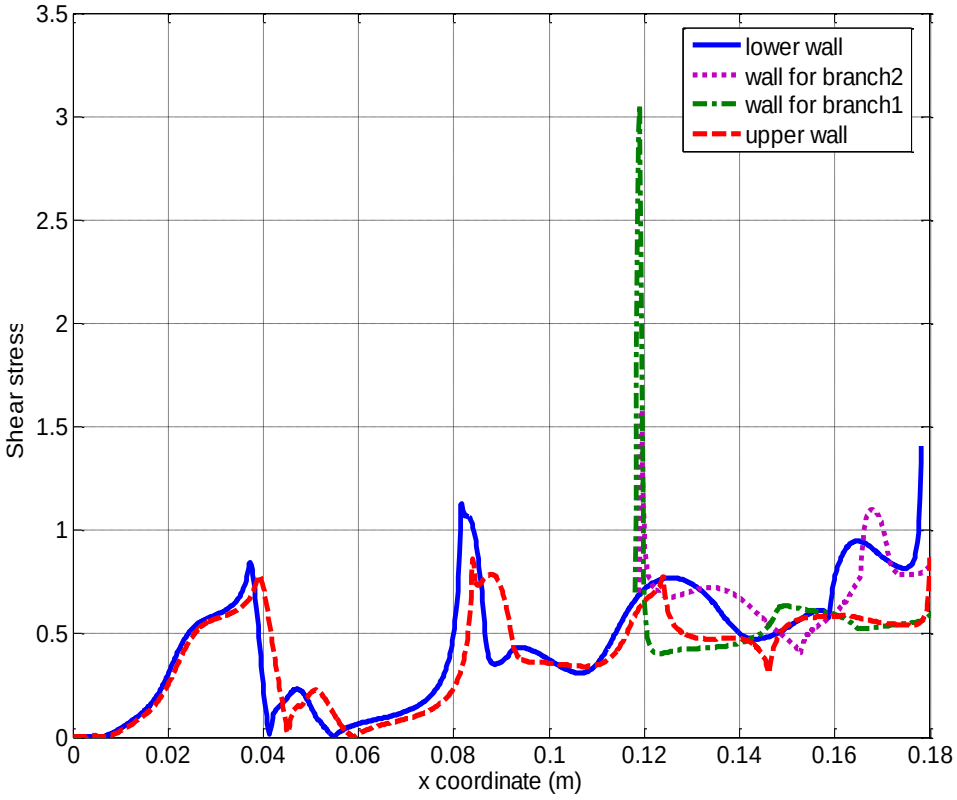

Shear stress for abdominal aortic aneurysms

Figure 4.25: Comparison of shear stress at time t=0.5s

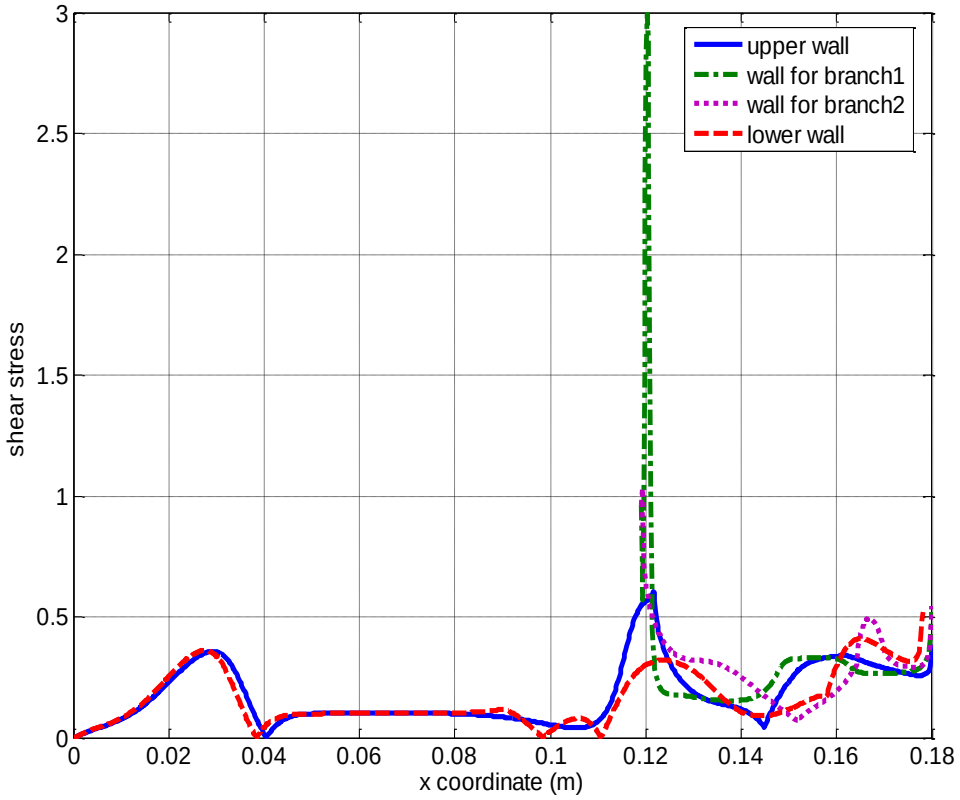

Shear stress for normal aorta

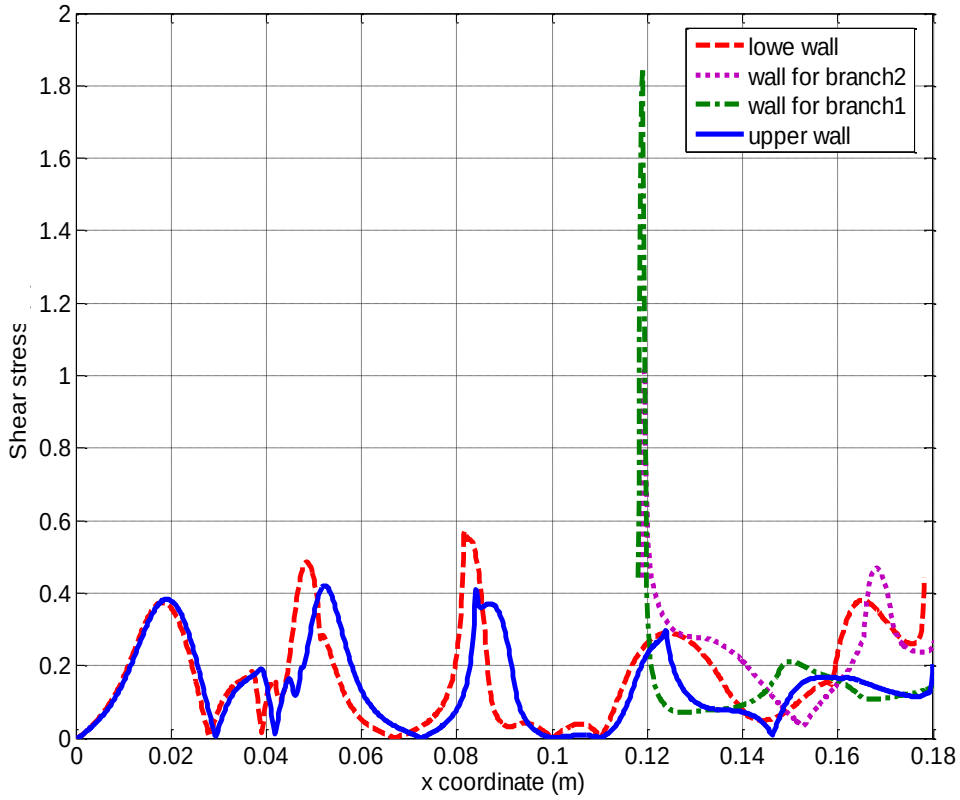

Shear stress for abdominal aortic aneurysms

Figure 4.26: Comparison of shear stress at time t=0.75s

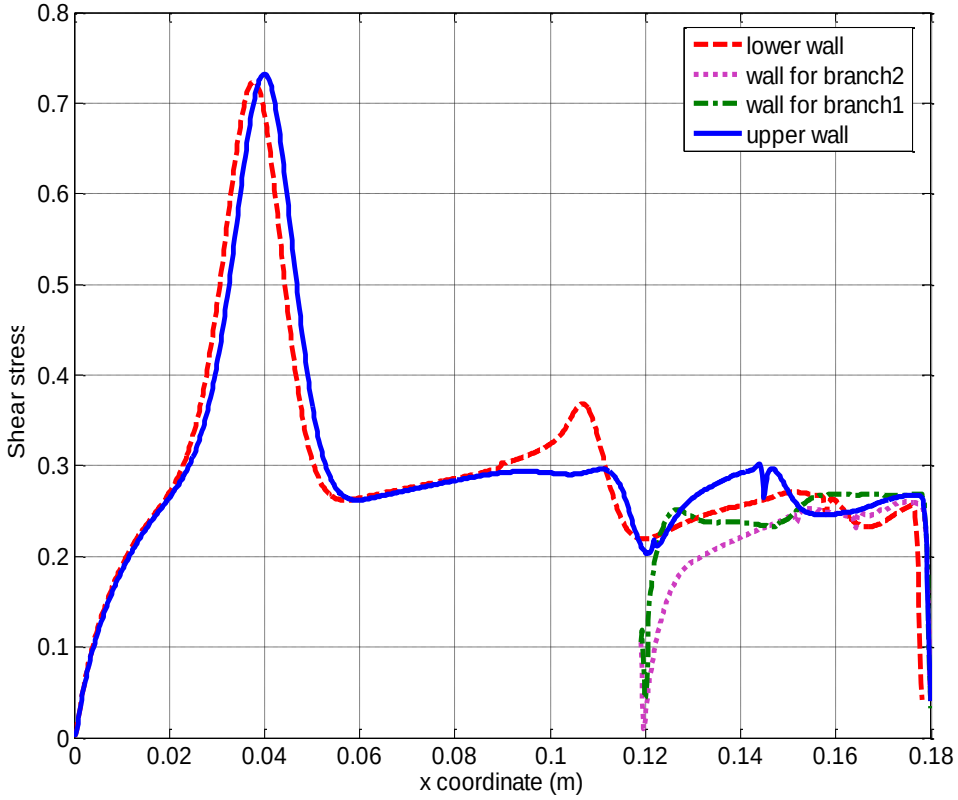

Shear stress for normal aorta

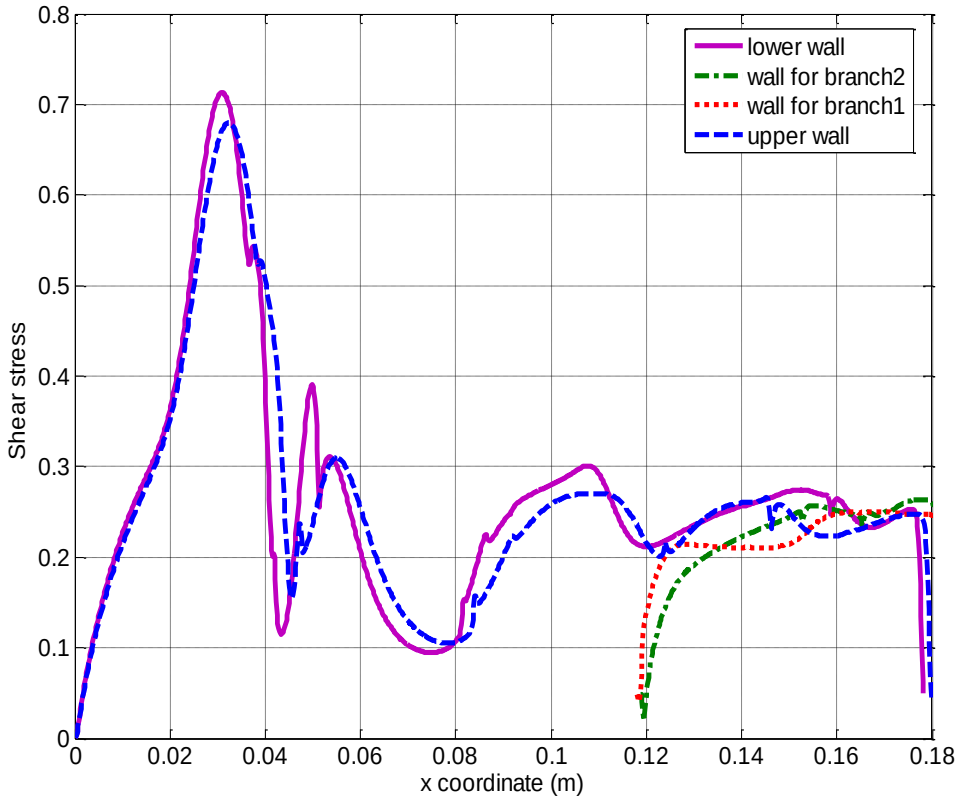

Shear stress for abdominal aortic aneurysms

Figure 4.27: Shear stress for abdominal aortic aneurysms

Table 4.1: Differences between the PC-GSM and the PL-GSM

	PC-GSM	PL-GSM
Smoothing domain	Connection between midpoints and centroids	Connection between midpoints and centroids
Smoothing functions	$\widehat{w}=\begin{cases}1/V_i & \mathbf{x}\in\Omega_i\\ 0 & \mathbf{x}\notin\Omega_i\end{cases}$	$\widehat{w}=\begin{cases}\mathbf{a}_i+\mathbf{b}_i(x-x_i)+\mathbf{c}_i(y-y_i), & \mathbf{x}\in\Omega_i\\ 0, & \mathbf{x}\notin\Omega_i\end{cases}$
Approximation of derivatives	$\nabla U_i \approx \frac{1}{V_i}\oint_{\partial\Omega_i} U(\mathbf{x})\vec{n}d\Gamma$	$\nabla U_i \approx -\int_{\Omega_i} U(\mathbf{x})\nabla\widehat{w}(\mathbf{x}-\mathbf{x}_i)dV$
	$\nabla\bullet(\nabla U_i) \approx \frac{1}{V_i}\oint_{\partial\Omega_i} \vec{n}\bullet\nabla U(\mathbf{x})d\Gamma$	$\nabla\bullet(\nabla U_i) \approx -\int_{\Omega_i} \nabla U(\mathbf{x})\bullet\nabla\widehat{w}(\mathbf{x}-\mathbf{x}_i)dV$

Table 4.2: Spatial discretization schemes for the approximation of derivatives

Scheme	**Type of GSD**	**Approximation of gradients at nodes**	**Approximation of gradients at midpoints**	**Approximation of gradients at centroids**
I	nGSD	PL-GSM	Interpolation	Interpolation
II	nGSD mGSD	PC-GSM	PC-GSM	Not required
III	nGSD mGSD cGSD	PL-GSM	PL-GSM	PL-GSM

Table 4.3: Comparison of numerical errors with scheme I, II and III for the first Poisson problem

No of field nodes	121	441	1681	6561
e_u				
I	7.304E-002	1.781E-002	4.443 E-003	1.112 E-003
II	1.632 E-002	7.312 E-003	8.338 E-004	3.912 E-004
III	8.265E-003	2.059 E-003	5.142 E-004	1.285 E-004

Table 4.4: Comparison of numerical errors with scheme I, II and III for the first Poisson problem

No of field nodes	131	478	1887	7457
h	0.0957	0.0479	0.0236	0.0117
e_u				
I	6.928E-002	1.581 E-002	3.322 E-003	8.164 E-004
II	2.053 E-002	5.211 E-003	1.251 E-003	3.096 E-004
III	1.288E-002	3.310 E-003	7.900 E-004	1.949 E-004

Table 4.5: Comparison of condition number and iteration

	I		II		III	
No. of nodes	Condition number	Iteration	Condition number	Iteration	Condition number	Iteration
131	2.12E2	93	3.17E2	99	4.56E2	119
478	8.14E2	207	1.16E3	309	1.62E3	403
1887	3.25E3	732	5.87E3	1388	7.78E3	1891
7457	1.21E4	2687	2.13E4	4312	3.88E4	5989

Chapter 5

Development of Alpha Gradient Smoothing Method (αGSM)

5.1 Introduction

In this Chapter, a novel alpha gradient smoothing method (αGSM) based on the strong form of governing equations for fluid problem is presented. The basic principle of αGSM is that the spatial derivatives at a location of interest are also approximated by the gradient smoothing operation. The main difference among the piecewise constant gradient smoothing method (PC-GSM) [24], piecewise linear gradient smoothing method (PL-GSM) [26] and αGSM is the selection of smoothing function. In the αGSM, the α value controls the contribution of PC-GSM and PL-GSM. The αGSM is verified by the solving the Poisson equation first. Then the proposed αGSM was tested with one benchmark example. All the numerical results have demonstrated that the αGSM is accurate, robust and stable, but the computational cost for the αGSM is a big bottleneck. Finally, the αGSM has been applied to analyze the flow characteristic in the diseased artery regarding the stenosis.

5.2 Theory of alpha gradient smoothing method (αGSM)

5.2.1 Brief of piecewise constant gradient smoothing method (PC-GSM)

In the piecewise constant gradient smoothing method(PC-GSM), the smoothing function is derived as follow [24]:

$$\widehat{w} = \begin{cases} 1/V_i & \mathbf{x} \in \Omega_i \\ 0 & \mathbf{x} \notin \Omega_i \end{cases} \tag{5.1}$$

where V_i is the smoothing area of Ω_i.

Recall the gradient smoothing operation for approximating gradients at a node of interest, *i*, in the form of

$$\nabla U_i \approx \int_{\partial\Omega_i} U(\mathbf{x})\widehat{w}(\mathbf{x}-\mathbf{x}_i)\mathbf{n}ds - \int_{\Omega_i} U(\mathbf{x})\nabla\widehat{w}(\mathbf{x}-\mathbf{x}_i)dV \tag{5.2}$$

Using Eq. (5.1), the right-side second term in Eq. (5.2) vanishes and Eq. (5.2) then becomes

$$\nabla U_i \approx \frac{1}{V_i}\oint_{\partial\Omega_i} U\mathbf{n}ds \tag{5.3}$$

Analogously, by successively applying the gradient smoothing technique for 2nd-order derivatives [26-27], the Laplace operator at $\mathbf{x}_i$ can be approximated as

$$\nabla\cdot(\nabla U_i) \approx \frac{1}{V_i}\oint_{\partial\Omega_i} \mathbf{n}\cdot\nabla U ds \tag{5.4}$$

5.2.2 Concept of alpha gradient smoothing method (αGSM)

Similarly, there are three types of smoothing domains used for the spatial discretization: midpoint-associated GSD (mGSD), centroid-associated GSD (cGSD), and node-associated GSD (nGSD) for the approximation of node interest as shown in

Fig. 5.1(a), (b) and (c) respectively. The cGSD connecting relevant centroids of triangles with the midpoints of relevant cell-edges is constructed to determine the gradients at the centroid of the cell, and the mGSD connecting the end-nodes of the cell-edge of interest is used for the calculation of the gradients at the midpoint of a cell-edge of interest.

For a two-dimensional case, the piecewise linear smoothing function is still used in the αGSM:

$$\widehat{w}(\mathbf{x}-\mathbf{x}_i)=\boldsymbol{\lambda}_i+\boldsymbol{\beta}_i(x-x_i)+\boldsymbol{\gamma}_i(y-y_i) \tag{5.5}$$

However, the smoothing function does not vanish at the node

$$\widehat{w}_{m_k}=\widehat{w}(\mathbf{x}_{m_k}-\mathbf{x}_i)=\alpha\frac{1}{V_i}\quad \widehat{w}_{c_k}=\widehat{w}(\mathbf{x}_{c_k}-\mathbf{x}_i)=\alpha\frac{1}{V_i} \tag{5.6}$$

where V_i is the area of smoothing domain for nGSD. The parameter α ranges $\in[0,1]$. Comparatively, in the piecewise linear gradient smoothing method (PL-GSM):

$$\widehat{w}_{m_k}=\widehat{w}(\mathbf{x}_{m_k}-\mathbf{x}_i)=0\quad \widehat{w}_{c_k}=\widehat{w}(\mathbf{x}_{c_k}-\mathbf{x}_i)=0 \tag{5.7}$$

The smoothing function is also required to satisfy the weighted partition of unity:

$$\sum_{k=1}^{N_i}\left[\int_{\Omega_i^{(2k-1)}}\widehat{w}\left(\mathbf{x}-\mathbf{x}_i\right)dV+\int_{\Omega_i^{(2k)}}\widehat{w}\left(\mathbf{x}-\mathbf{x}_i\right)dV\right]=1 \tag{5.8}$$

And the smoothing function must be equal to a constant value at the node of interest:

$$\widehat{w}(\mathbf{x}_i-\mathbf{x}_i)=\boldsymbol{\lambda}_i \tag{5.9}$$

With Eq. (5.6), (5.8) and (5.9), it is readily obtained that

$$\lambda_{i,2k}=\widehat{w}(\mathbf{x}_i-\mathbf{x}_i)=\frac{3}{V_i}(1-\alpha) \tag{5.10}$$

This formulation implies that all coefficients in the matrix $\boldsymbol{\lambda}_i$ are constant, regardless of sub-triangles involved.

Furthermore, the gradients of the smoothing function can be obtained by simply differentiating Eq. (5.5) as

$$\begin{cases} \dfrac{\partial \widehat{w}\left(x-x_i\right)}{\partial x} = \boldsymbol{\beta}_i \\ \dfrac{\partial \widehat{w}\left(x-x_i\right)}{\partial y} = \boldsymbol{\gamma}_i \end{cases} \tag{5.11}$$

Thus, the parameters $\beta_{i,2k}$ and $\gamma_{i,2k}$ for each sub-triangle $\Delta ic_k m_k$ as shown in Figure 5.2 can then be obtained as the solutions to Eq. (5.11) in the form of

$$\beta_{i,2k} = -\frac{3}{V_i}(1-\alpha)\frac{y_{c_k} - y_{m_k}}{(x_{m_k} - x_i)(y_{c_k} - y_i) - (x_{c_k} - x_i)(y_{m_k} - y_i)} \tag{5.12}$$

$$\gamma_{i,2k} = \frac{3}{V_i}(1-\alpha)\frac{x_{c_k} - x_{m_k}}{(x_{m_k} - x_i)(y_{c_k} - y_i) - (x_{c_k} - x_i)(y_{m_k} - y_i)} \tag{5.13}$$

The parameter $\beta_{i,2k-1}$ and $\gamma_{i,2k-1}$ in the sub-triangle $\Delta im_k c_{k-1}$ can be obtained in the same way.

5.2.3 Approximation of spatial derivatives

5.2.3.1 Approximation of first order derivatives at nodes

Thus, the gradient of filed variable at a point of interest using the αGSM can be formulated as follows:

$$\begin{aligned} \frac{\partial U_i}{\partial x} &\approx \frac{\alpha}{V_i}\oint_{\partial\Omega_i} U\mathbf{n}ds - (1-\alpha)\sum_{k=1}^{N_i}\left[\beta_{i,2k}\int_{\Delta im_k c_k} U(\mathbf{x})dV + \beta_{i,2k-1}\int_{\Delta im_k c_{k-1}} U(\mathbf{x})dV\right] \\ &= \frac{\alpha}{V_i}\sum_{k=1}^{n_i}\left[\left(\Delta L_x\right)_{ij_k} U_{m_k}\right] - (1-\alpha)\left[\sum_{k=1}^{n_i}\beta_{i,2k}\int_{\Delta im_k c_k} U(\mathbf{x})dV + \beta_{i,2k-1}\int_{\Delta im_k c_{k-1}} U(\mathbf{x})dV\right] \end{aligned} \tag{5.14}$$

$$\begin{aligned} \frac{\partial U_i}{\partial y} &\approx \frac{\alpha}{V_i}\oint_{\partial\Omega_i} U\mathbf{n}ds - (1-\alpha)\sum_{k=1}^{N_i}\left[\gamma_{2k}\int_{\Delta im_k c_k} U(\mathbf{x})dV + \gamma_{2k-1}\int_{\Delta im_k c_{k-1}} U(\mathbf{x})dV\right] \\ &= \frac{\alpha}{V_i}\sum_{k=1}^{n_i}\left[\left(\Delta L_y\right)_{ij_k} U_{m_k}\right] - (1-\alpha)\sum_{k=1}^{N_i}\left[\gamma_{2k}\int_{\Delta im_k c_k} U(\mathbf{x})dV + \gamma_{2k-1}\int_{\Delta im_k c_{k-1}} U(\mathbf{x})dV\right] \end{aligned} \tag{5.15}$$

With

$$\left(\Delta L_x\right)_{ij_k} = \left(\Delta L_x\right)_{ij_k}^{(L)} + \left(\Delta L_x\right)_{ij_k}^{(R)} = L_{ij}^{(L)} n_x^{(L)} + L_{ij}^{(R)} n_x^{(R)} \tag{5.16}$$

$$\left(\Delta L_y\right)_{ij_k} = \left(\Delta L_y\right)_{ij_k}^{(L)} + \left(\Delta L_y\right)_{ij_k}^{(R)} = L_{ij}^{(L)} n_y^{(L)} + L_{ij}^{(R)} n_y^{(R)} \tag{5.17}$$

where $n_x^{(L)}$, $n_y^{(L)}$, $n_x^{(R)}$ and $n_y^{(R)}$ are the components of the unit outward normal vectors in *x*- and *y*- directions on the two edges located at the left and right hand sides of the edge $i-j$. The $L_{ij}^{(L)}$ and $L_{ij}^{(R)}$ represent the lengths of two straight edges along the smoothing boundary located at the left and right hand sides of the edges as shown in Fig. 5.2.

The integral of $U(\mathbf{x})$ over sub-triangular can be approximated:

$$\int_{\Delta i m_k c_k} U(\mathbf{x}) dV \approx \frac{1}{3}\left(U_i + U_{m_k} + U_{c_k}\right) A_{i m_k c_k} \tag{5.18}$$

Substitute Eq. (5.18) into Eq. (5.14) and (5.15), the first order of derivative is expressed:

$$\begin{aligned}\frac{\partial U_i}{\partial x} = & \frac{\alpha}{V_i}\sum_{k=1}^{n_i}\left[\left(\Delta L_x\right)_{ij_k} U_{m_k}\right] - \\ & (1-\alpha)\sum_{k=1}^{n_i}\left[\frac{1}{3}\left(U_i + U_{m_k} + U_{c_k}\right) A_{i m_k c_k}\beta_{i,2k} + \frac{1}{3}\left(U_i + U_{m_k} + U_{c_{k-1}}\right) A_{i m_k c_{k-1}}\beta_{i,2k-1}\right]\end{aligned} \tag{5.19}$$

$$\begin{aligned}\frac{\partial U_i}{\partial y} = & \frac{\alpha}{V_i}\sum_{k=1}^{n_i}\left[\left(\Delta L_y\right)_{ij_k} U_{m_k}\right] - \\ & (1-\alpha)\sum_{k=1}^{n_i}\left[\frac{1}{3}\left(U_i + U_{m_k} + U_{c_k}\right) A_{i m_k c_k}\gamma_{i,2k} + \frac{1}{3}\left(U_i + U_{m_k} + U_{c_{k-1}}\right) A_{i m_k c_{k-1}}\gamma_{i,2k-1}\right]\end{aligned} \tag{5.20}$$

5.2.3.2 Approximation of first order derivatives at midpoints and centroids

Similar to the discretization at nodes mentioned previously, the gradients at the midpoint and centroids can also be formulated using the gradient smoothing technique. The smoothing function in the mGSD can be written as follow:

$$\widehat{w}(\mathbf{x}-\mathbf{x}_i) = \mathbf{a}_i + \mathbf{b}_i(x-x_i) + \mathbf{c}_i(y-y_i) \tag{5.21}$$

Based on constrain in Eq. (5.6), (5.8) and (5.9), the coefficient $\mathbf{a}_i$, $\mathbf{b}_i$ and $\mathbf{c}_i$ can be solved:

$$a_{i,k} = \widehat{w}(\mathbf{x}_i - \mathbf{x}_i) = (1-\alpha)\frac{3}{V_m} \tag{5.22}$$

where V_m is the total area of the smoothing domain for the midpoint. The coefficient $\mathbf{b}_i$ and $\mathbf{c}_i$ in the sub-triangle $\Delta_{ic_km_k}$ can be obtained:

$$b_{ic_km_k} = -a_{i,k}\frac{y_i - y_{c_k}}{(x_{m_k}-x_i)(y_{c_k}-y_i)-(x_{c_k}-x_i)(y_{m_k}-y_i)} \tag{5.23}$$

$$c_{ic_km_k} = a_{i,k}\frac{x_i - x_{c_k}}{(x_{m_k}-x_i)(y_{c_k}-y_i)-(x_{c_k}-x_i)(y_{m_k}-y_i)} \tag{5.24}$$

Therefore, the gradient at the nodes is expressed as follows:

$$\begin{aligned}\frac{\partial U_{m_k}}{\partial x} = {} & \alpha\left[\left(\Delta L_m^x\right)_{c_km_k}U_{c_k} + \left(\Delta L_m^x\right)_{c_km_{k-1}}U_{c_{k-1}}\right] \\ & - (1-\alpha)\left\{\frac{1}{3}\left(U_i + U_{c_k} + U_{m_k}\right)A_{ic_km_k}b_{ic_km_k} + \frac{1}{3}\left(U_{j_k} + U_{c_k} + U_{m_k}\right)A_{j_kc_km_k}b_{j_kc_km_k}\right. \\ & \left. + \frac{1}{3}\left(U_i + U_{c_{k-1}} + U_{m_k}\right)A_{ic_{k-1}m_k}b_{ic_{k-1}m_k} + \frac{1}{3}\left(U_{j_k} + U_{c_{k-1}} + U_{m_k}\right)A_{j_kc_{k-1}m_k}b_{j_kc_{k-1}m_k}\right\}\end{aligned} \tag{5.25}$$

$$\begin{aligned}\frac{\partial U_{m_k}}{\partial y} = {} & \alpha\left[\left(\Delta L_m^y\right)_{c_km_k}U_{c_k} + \left(\Delta L_m^y\right)_{c_km_{k-1}}U_{c_{k-1}}\right] \\ & - (1-\alpha)\left\{\frac{1}{3}\left(U_i + U_{c_k} + U_{m_k}\right)A_{ic_km_k}c_{ic_km_k} + \frac{1}{3}\left(U_{j_k} + U_{c_k} + U_{m_k}\right)A_{j_kc_km_k}c_{j_kc_km_k}\right. \\ & \left. + \frac{1}{3}\left(U_i + U_{c_{k-1}} + U_{m_k}\right)A_{ic_{k-1}m_k}c_{ic_{k-1}m_k} + \frac{1}{3}\left(U_{j_k} + U_{c_{k-1}} + U_{m_k}\right)A_{j_kc_{k-1}m_k}c_{j_kc_{k-1}m_k}\right\}\end{aligned} \tag{5.26}$$

where the face vectors of the two respective domain-edges:

$$\left(\Delta L_m^x\right)_{ij_k} = \left(\Delta L_m^x\right)_{ij_k}^{(L)} + \left(\Delta L_m^x\right)_{ij_k}^{(R)} = L_{c_km_k}^{(L)}n_x^{(L)} + L_{c_km_k}^{(R)}n_x^{(R)} \tag{5.27}$$

$$\left(\Delta L_y\right)_{ij_k} = \left(\Delta L_m^x\right)_{ij_k}^{(L)} + \left(\Delta L_m^x\right)_{ij_k}^{(R)} = L_{c_km_k}^{(L)}n_y^{(L)} + L_{c_km_k}^{(R)}n_y^{(R)} \tag{5.28}$$

where $n_x^{(L)}$, $n_y^{(L)}$, $n_x^{(R)}$ and $n_y^{(R)}$ represent the components of the unit outward normal vectors in *x*- and *y*- directions on the two edges located at the left and right hand sides of the edge $c_k - m_k$. The $L_{ij}^{(L)}$ and $L_{ij}^{(R)}$ denote the two components of the lengths of two

straight edges along the smoothing boundary located at the left and right hand sides of the edges as shown in Fig. 5.3.

Similarly, the smoothing function in the cGSD as shown in Fig. 5.4 can be written:

$$\widehat{w}(\mathbf{x}-\mathbf{x}_i)=\mathbf{d}_i+\mathbf{e}_i(x-x_i)+\mathbf{f}_i(y-y_i) \tag{5.29}$$

Similarly, the coefficient $\mathbf{d_i}$, $\mathbf{e_i}$ and $\mathbf{f_i}$ can be obtained:

$$d_{i,k}=\widehat{w}(\mathbf{x}_i-\mathbf{x}_i)=(1-\alpha)\frac{3}{V_c} \tag{5.30}$$

where the V_c is the area for the smoothing domain of centroid.

$$e_{ic_kj_k}=-a_{i,k}\frac{y_{j_k}-y_i}{(x_i-x_{c_k})(y_{j_k}-y_{c_k})-(x_{j_k}-x_{c_k})(y_i-y_{c_k})} \tag{5.31}$$

$$f_{ic_kj_k}=a_{i,k}\frac{x_{j_k}-x_i}{(x_i-x_{c_k})(y_{j_k}-y_{c_k})-(x_{j_k}-x_{c_k})(y_i-y_{c_k})} \tag{5.32}$$

Therefore, the gradient at the centroid is expressed:

$$\begin{aligned}\frac{\partial U_{c_k}}{\partial x}=&\alpha\left[\frac{1}{2}\left(\Delta L_c^x\right)_{ij_k}\left(U_i+U_{j_k}\right)+\frac{1}{2}\left(\Delta L_c^x\right)_{j_kj_{k+1}}\left(U_{j_k}+U_{j_{k+1}}\right)+\frac{1}{2}\left(\Delta L_c^x\right)_{j_{k+1}i}\left(U_{j_{k+1}}+U_i\right)\right]\\&-(1-\alpha)\left\{\left[\frac{1}{3}\left(U_i+U_{c_k}+U_{j_k}\right)A_{ic_kj_k}e_{ic_kj_k}\right]+\left[\frac{1}{3}\left(U_{j_k}+U_{c_k}+U_{j_{k+1}}\right)A_{j_kc_kj_{k+1}}e_{j_kc_kj_{k+1}}\right]\right.\\&\left.+\left[\frac{1}{3}\left(U_i+U_{c_k}+U_{j_{k+1}}\right)A_{ic_kj_{k+1}}e_{ic_kj_{k+1}}\right]\right\}\end{aligned} \tag{5.33}$$

$$\begin{aligned}\frac{\partial U_{c_k}}{\partial y}=&\alpha\left[\frac{1}{2}\left(\Delta L_c^y\right)_{ij_k}\left(U_i+U_{j_k}\right)+\frac{1}{2}\left(\Delta L_c^y\right)_{j_kj_{k+1}}\left(U_{j_k}+U_{j_{k+1}}\right)+\frac{1}{2}\left(\Delta L_c^y\right)_{j_{k+1}i}\left(U_{j_{k+1}}+U_i\right)\right]\\&-(1-\alpha)\left\{\left[\frac{1}{3}\left(U_i+U_{c_k}+U_{j_k}\right)A_{ic_kj_k}f_{ic_kj_k}\right]+\left[\frac{1}{3}\left(U_{j_k}+U_{c_k}+U_{j_{k+1}}\right)A_{j_kc_kj_{k+1}}f_{j_kc_kj_{k+1}}\right]\right.\\&\left.+\left[\frac{1}{3}\left(U_i+U_{c_k}+U_{j_{k+1}}\right)A_{ic_kj_{k+1}}f_{ic_kj_{k+1}}\right]\right\}\end{aligned} \tag{5.34}$$

where ΔL_c^x and ΔL_c^y are the two components of a respective face vector for a cGSD on interest as shown in Fig. 5.4.

5.2.3.3 Approximation of second order derivatives

Analogously, using linear interpolation in integral calculation, the second order derivatives in the node can be approximated:

$$\frac{\partial^2 U_i}{\partial x^2} \approx \alpha \frac{1}{\Omega_i} \sum_{k=1}^{n_i} \frac{\partial U_{m_k}}{\partial x} \left(\Delta L_x\right)_{ij_k} - (1-\alpha) \sum_{k=1}^{N_i} \left\{ \frac{1}{3} \left[\frac{\partial U(\mathbf{x}_i)}{\partial x} + \frac{\partial U(\mathbf{x}_{m_k})}{\partial x} + \frac{\partial U(\mathbf{x}_{c_k})}{\partial x} \right] \beta_{i,2k} \right. \tag{5.35}$$
$$\left. \frac{1}{3} \left[\frac{\partial U(\mathbf{x}_i)}{\partial x} + \frac{\partial U(\mathbf{x}_{m_k})}{\partial x} + \frac{\partial U(\mathbf{x}_{c_k})}{\partial x} \right] \beta_{i,2k-1} \right\}$$

$$\frac{\partial^2 U_i}{\partial y^2} \approx \alpha \frac{1}{\Omega_i} \sum_{k=1}^{n_i} \frac{\partial U_{m_k}}{\partial y} \left(\Delta L_y\right)_{ij_k} - (1-\alpha) \sum_{k=1}^{N_i} \left\{ \frac{1}{3} \left[\frac{\partial U(\mathbf{x}_i)}{\partial y} + \frac{\partial U(\mathbf{x}_{m_k})}{\partial y} + \frac{\partial U(\mathbf{x}_{c_k})}{\partial y} \right] \gamma_{i,2k} \right. \tag{5.36}$$
$$\left. \frac{1}{3} \left[\frac{\partial U(\mathbf{x}_i)}{\partial y} + \frac{\partial U(\mathbf{x}_{m_k})}{\partial y} + \frac{\partial U(\mathbf{x}_{c_{k-1}})}{\partial y} \right] \gamma_{i,2k-1} \right\}$$

In the Eq. (5.35) and (5.36), the gradient at the node, midpoint and centroid can be obtained from section 5.2.3.2.

5.2.4 Relations between PC-GSM, PL-GSM and αGSM

As described in previous sections, the αGSM also adopts the piecewise linear smoothing functions. However, the contribution at the node in the whole smoothing domain is $\alpha \frac{1}{V_i}$ instead of zero as shown in Fig.5.5. In the PL-GSM, although the linearly smoothing function is also used to discrtize the spatial derivative, the contribution from node is zero. In the PC-GSM, the weight function is constant in the whole smoothing domain. As a result, the α value acts as a knob which control the contribution of PC-GSM and PL-GSM. When the α=1, the smoothing function is constant in the αGSM, thus the αGSM becomes PC-GSM. When the α=0, the αGSM is the exactly same as PL-GSM. Those difference and similarity are summarized in Table 5.1.

Thus, it is seen that the PC-GSM and PL-GSM are special formulations of αGSM respectively. The main difference for these three methods is the selection of smoothing function. Obviously, the computational cost for the αGSM is higher compared with the PC-GSM and PL-GSM; however, the αGSM can obtain better accuracy compared with the PC-GSM and PL-GSM. The main challenge of the αGSM is to determine the α value. Based on our research experience, the $\alpha \in [0.1, 0.3]$ usually achieves the better results. In this thesis, α=0.2 is adopted in the simulation.

5.3 Numerical example

5.3.1 Solution of Poisson equation

In this section, Poisson equation is solved with our αGSM, PC-GSM and PL-GSM code. The following Poisson equation is considered:

$$\frac{\partial^2 U}{\partial x^2} + \frac{\partial^2 U}{\partial y^2} = f(x, y) \qquad (0 \le x \le 0.5, 0 \le y \le 1) \tag{5.37}$$

$$U = e^{-x+y} \qquad f(x, y) = 2e^{-x+y} \tag{5.38}$$

The four sets of mesh as shown in Fig.5.6 are used to examine the accuracy of αGSM. The numerical error defined in this Chapter is the same as Eq. (4. 37) in Chapter 4. This type of error is used to compare the accuracy among different schemes.

Table 5.2 summarizes the errors with the number of nodes adopted to discretize the problem field. It is clear to show that errors obtained from all schemes reduce as the number of nodes increases. The use of combination of piecewise constant and linear smoothing function gives the highest accuracy. However, the computational cost for the αGSM is also higher compared with the PC-GSM and PL-GSM.

The convergence rate for these three schemes is plotted in Fig. 5.7. As shown in Figure 5.7, it is obviously found that the convergence rate is approximately the same in all schemes, because all schemes are second order accuracy in spatial approximation.

5.3.2 Solutions to incompressible Navier-Stokes equations

In this section, the steady-state flow over a sudden backstep is presented. It is assumed that a fully developed laminar flow velocity profile is imposed at the flow entrance with a parabolic distribution function. The fluid flows through the channel bounded by the top and bottom walls and exists at the other end. The boundary conditions adopted in this case are schematically illustrated in Fig.5.8.

For this benchmark problem, several cases with different Reynolds numbers from 100 to 800 have been studied. Because of the sudden change of the cross section, a re-circulation zone will be formed right behind the backward facing step. The main flow will reattach to the wall on the step side at certain distance down stream the step. As the Reynolds number increases, the re-circulation zone enlarges. Meanwhile, on the wall opposite side to the step and further down stream, a low pressure region is gradually forming with the increasing of the Reynolds number. As shown Fig.5.9, The streamline obtained by the αGSM solver captures such change very well. In addition, a secondary vortex attached to the top wall occurs in the downstream region if the Reynolds number becomes 800, as illustrated in Fig.5.9(c). If Reynolds number is greater than 800, no steady-state solutions can be found in current practice becasue of the oscillation of induced vortices.

The major criterion to compare with experimental data is the size of the re-circulation region (characterized by the re-attachment length) as a function of flow Reynolds number based on the inlet bulk velocity. Figure 5.10 compares the attained reattachment lengths of the recirculating zone right behind the backstep with experimental data from Armaly *et al*. [119], the least-squares finite element results from Jiang [120], a meshfree smoothed least-square solutions from Song *et al.* [121], PL-GSM solution and αGSM solutions. Among all schemes, the αGSM solver gives the most accurate prediction amongst different methods considered here, and agrees well with the experimental data.

The computational efficiency is a hindrance for the αGSM. In this example, the numerical results obtained from the αGSM have not been improved significantly in comparison with the PL-GSM, but the overall computational time for the GSM is almost twice than PL-GSM.

5.3.3 Application of αGSM for solution of pulsatile blood flow in diseased artery

In this section, a two dimensional of wall shear stress for blood flow in the normal aorta and abnormal aorta with stenosis vessel using the αGSM is presented. The partial occlusion is a very common anomaly in blood circulation due to stnotic obstruction. The vessel with stenosis is an abnormal narrowing. Stenosis blocks and prevents the supply of nutrition and oxygen to the tissue and organs. An important quantity to be analyzed in hemodynamic is the wall shear stress, a difficultly measurable variable in vivo because of the arising with the moving wall. Many authors mentioned that the

high shear stress is one of factors in the development of atherosclerotic lesions and endothelial damage [122], and play an important role in the natural history of the disease as well. In the presence of a narrowing, the flow exhibits a resistance and hence an increasing of the shear stress.

A fully developed flow is assumed at the inflow. The tangential and normal stresses are zero (stress free condition). The entering flow is pulsatile with a typical sine wave as shown in Fig. 5.11. The period for one cycle is 1 second. The blood density and viscosity is 1050 kg/m^3, 0.0033uN/m respectively. The 2D geometries for normal aorta and abnormal aorta with the stenosis vessel are shown in Fig.5.12 [123].

Figure 5.13, 5.14 and 5.15 depict the shear stress along the upper and lower wall located at the region $(23 < x < 106mm)$ shown in Fig. 5.12 at early systolic acceleration t= $\frac{1}{4}$T , systolic acceleration t= $\frac{1}{2}$T and systolic deceleration t= $\frac{3}{4}$T . From Figure 5.13, 5.14 and 5.15, it is easily observed that the shear stress in the abnormal aorta surrounding the stenosis is much higher in comparison with the normal aorta at all stages, which increases the possibility of rupture of vessel significantly. In addition, it is noticed that the shear stress increases very fast when approaching the stenosis throat, corresponding to the high value of the velocity gradient, and the shear stress gradually decreases beyond the stenosed vessel region. The maximum shear stress occurs in the stenosis throat, which is consistent with observations of maximum velocity in this region. As expected, the shear stress near the stenosis throat is the largest during the systolic peak flow at t= $\frac{1}{2}$T , corresponding to the maximum inlet velocity.

5.4 Remarks

The proposed αGSM based on the combination of the PC-GSM and PL-GSM has resulted in a new form in approximating the spatial derivatives. Although the αGSM can improve the accuracy of PC-GSM and PL-GSM, the computational cost for the αGSM is very high. If the precision requirement in the engineering problem is not so strict, the αGSM is not preferable compared with the PC-GSM and PL-GSM. In addition, the selection of α value still remains an open question. How to build the relationship between the numerical accuracy and the α value is a challenging task, which could be another interesting topic in the future research. Therefore, it is concluded that the proposed αGSM does not show outstanding advantages than the PC-GSM and PL-GSM. As a whole, the PL-GSM is still the most preferable scheme in terms of computational cost and accuracy.

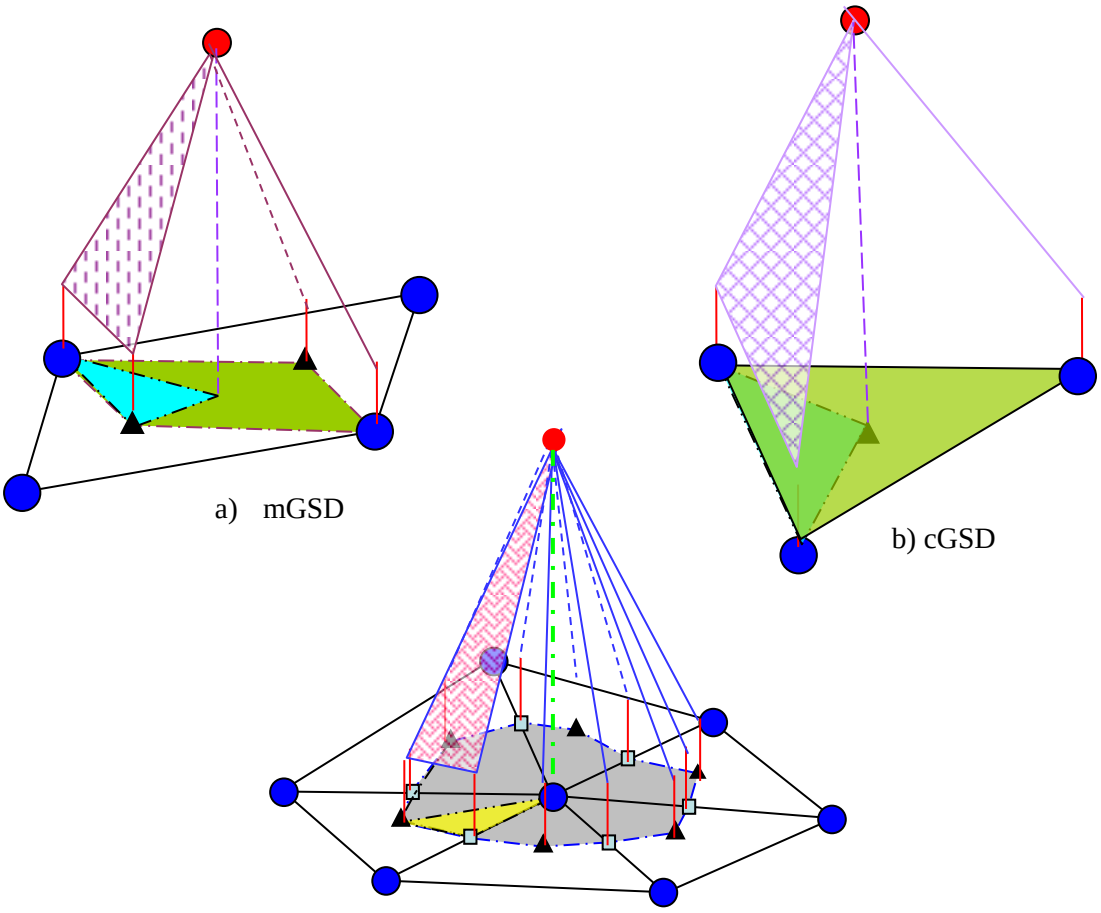

Figure 5.1: Smoothing function for different types of gradient smoothing domains

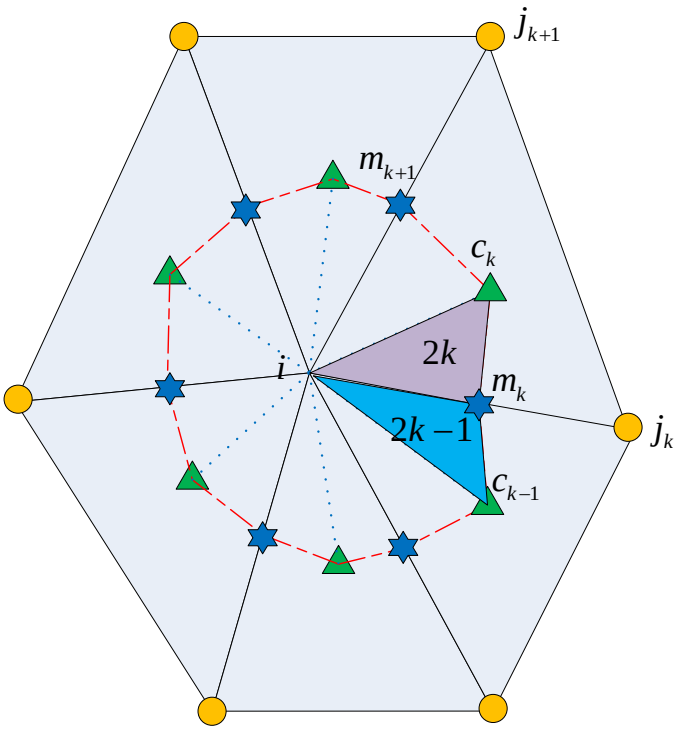

Figure 5.2: Adopted notations and sub-triangulation in the nGSD of αGSM

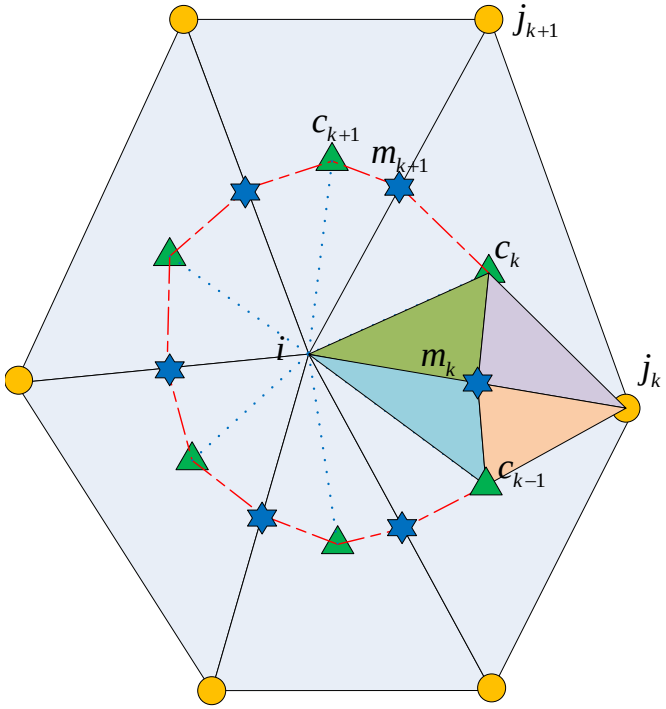

Figure 5.3: Adopted notations and sub-triangulation in the mGSD of αGSM

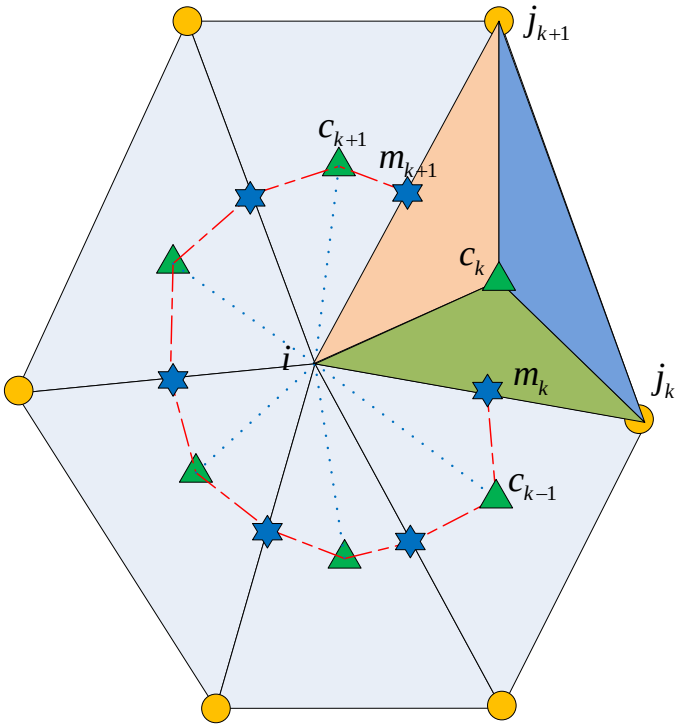

Figure 5.4: Adopted notations and sub-triangulation in the cGSD of αGSM

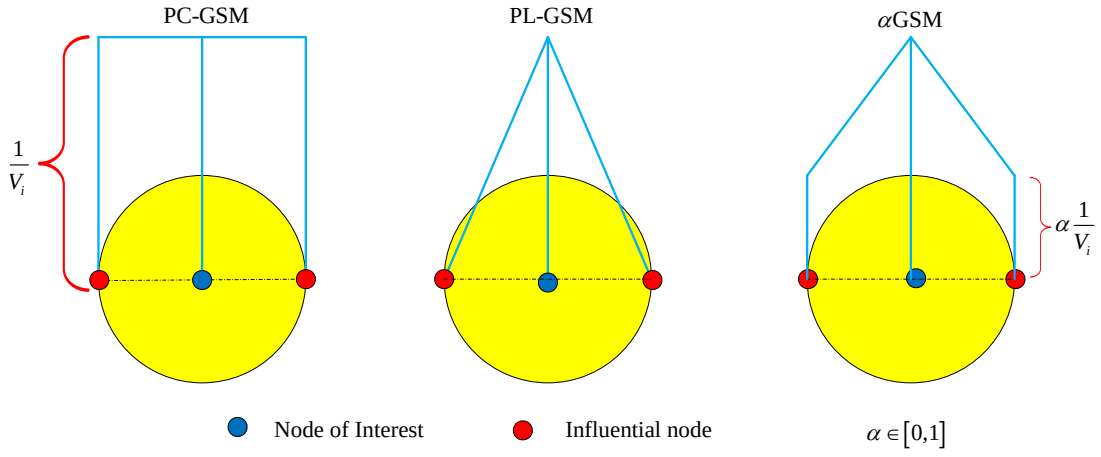

Figure 5.5: Illustration of smoothing function in the PC-GSM, PL-GSM and αGSM

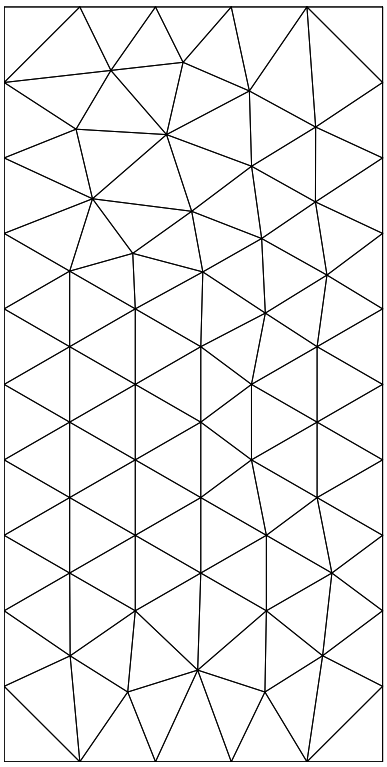

a) 72 nodes

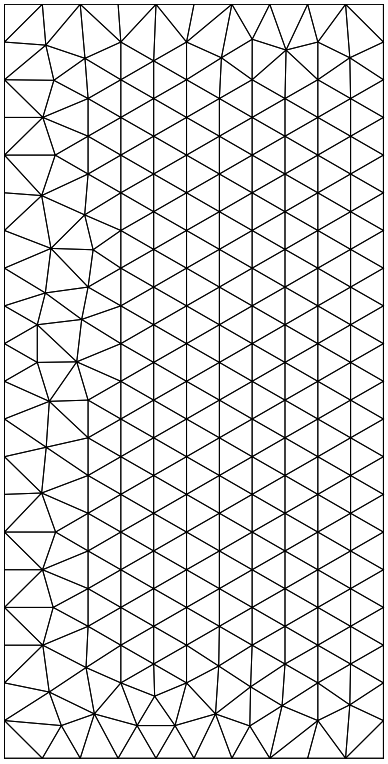

b) 244 nodes

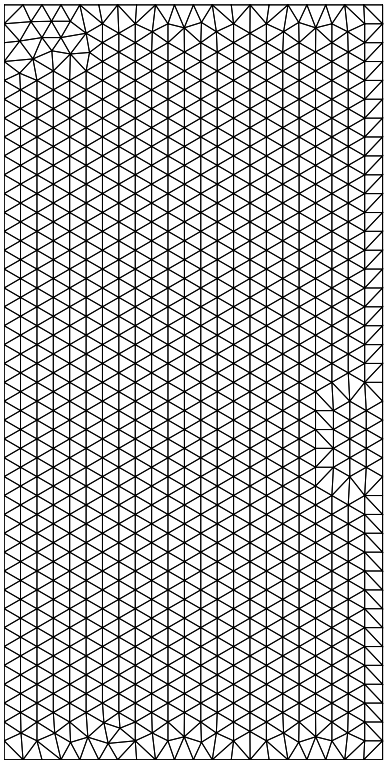

c) 963 nodes

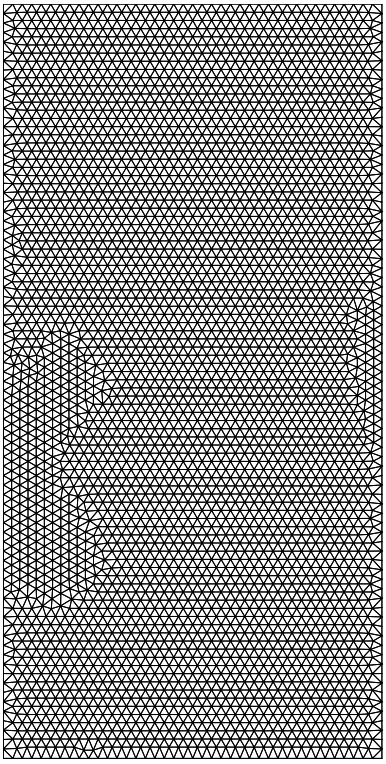

d) 3741 nodes

Figure 5.6: Element distribution of Poisson's equation

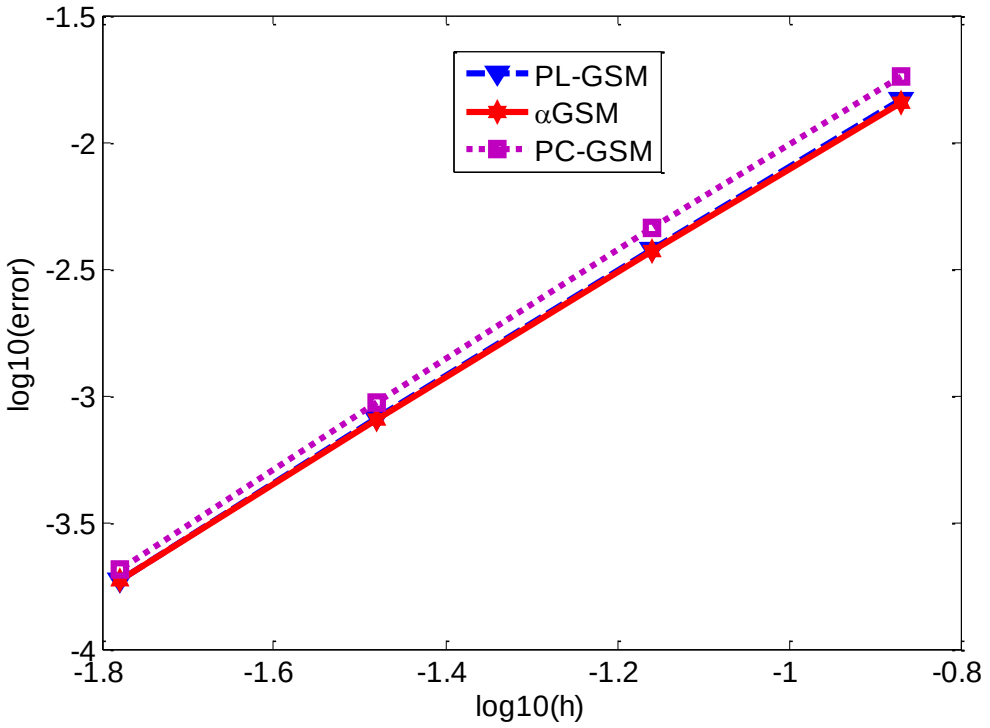

Figure 5.7: Convergence rate

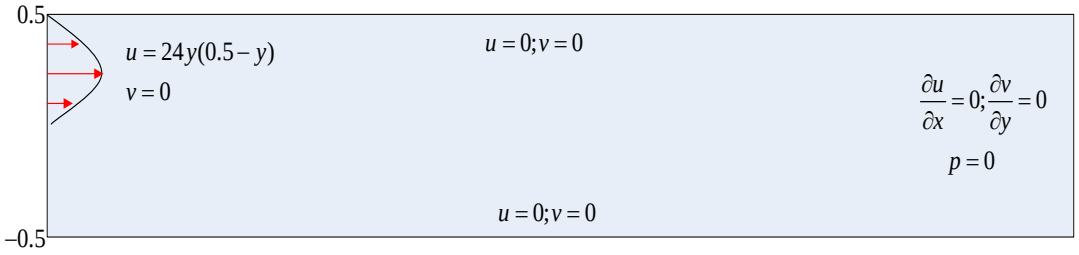

Figure 5.8: Geometrical and boundary conditions for the flow problem over a sudden backstep

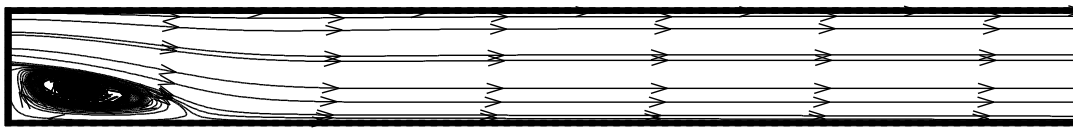

Re = 100

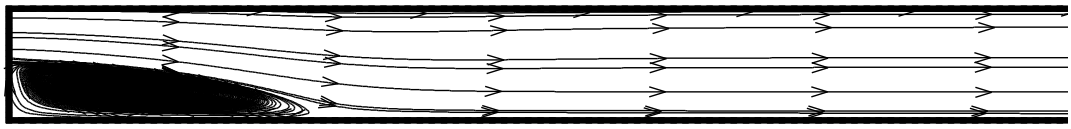

Re = 200

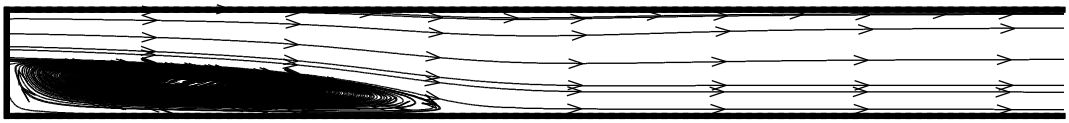

Re = 400

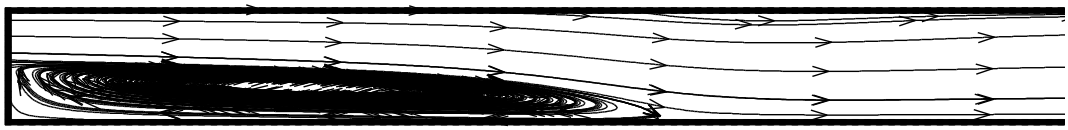

Re = 600

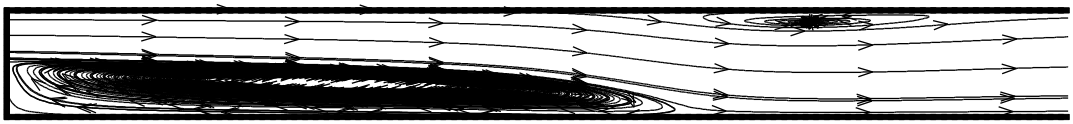

Re = 800

Figure 5.9: Plots of streamlines for various Reynolds number

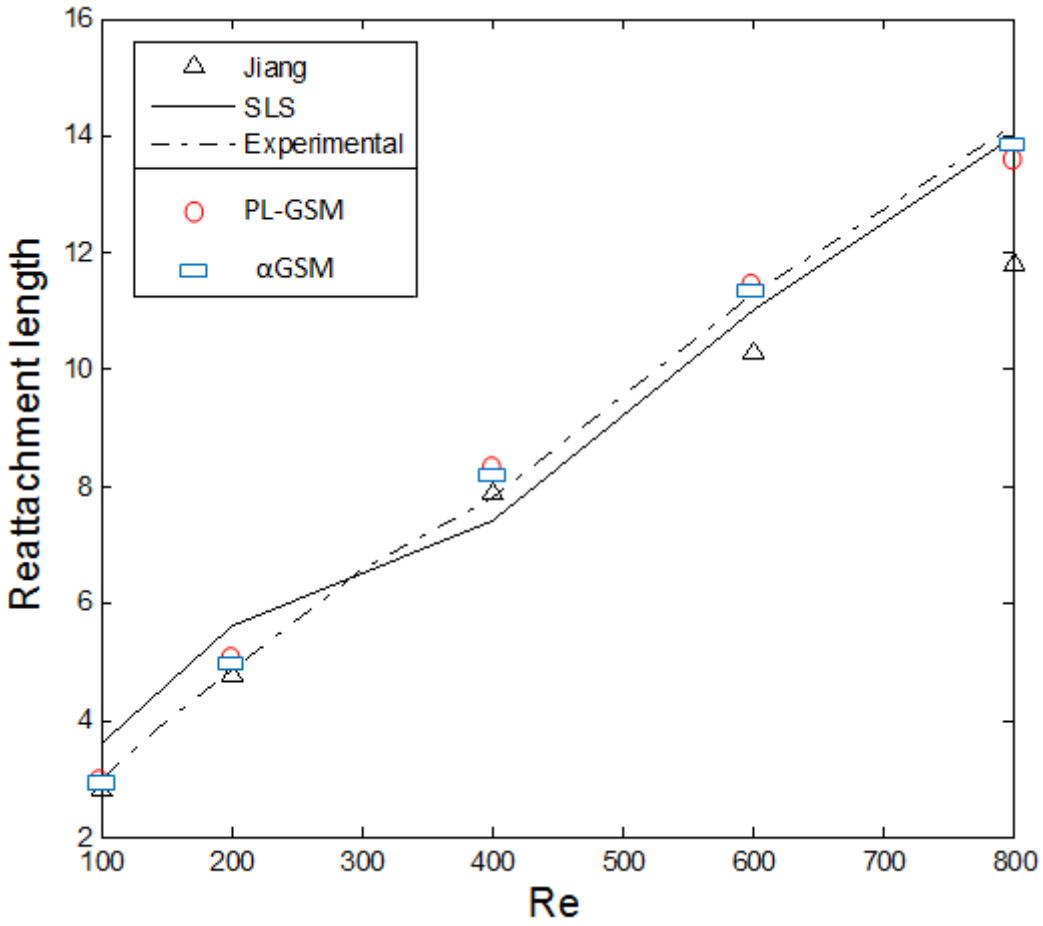

Figure 5.10: Predicted reattachment length ratios varied with Reynolds number

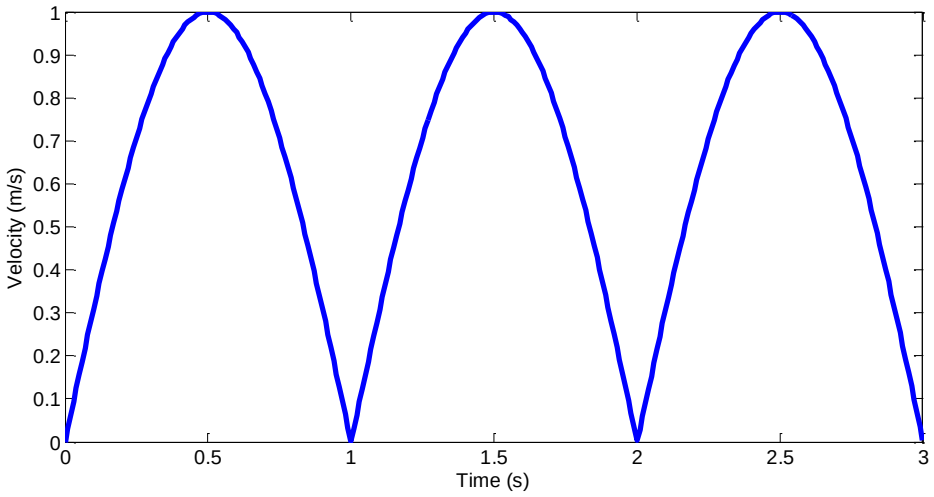

Figure 5.11: Input velocity Profile

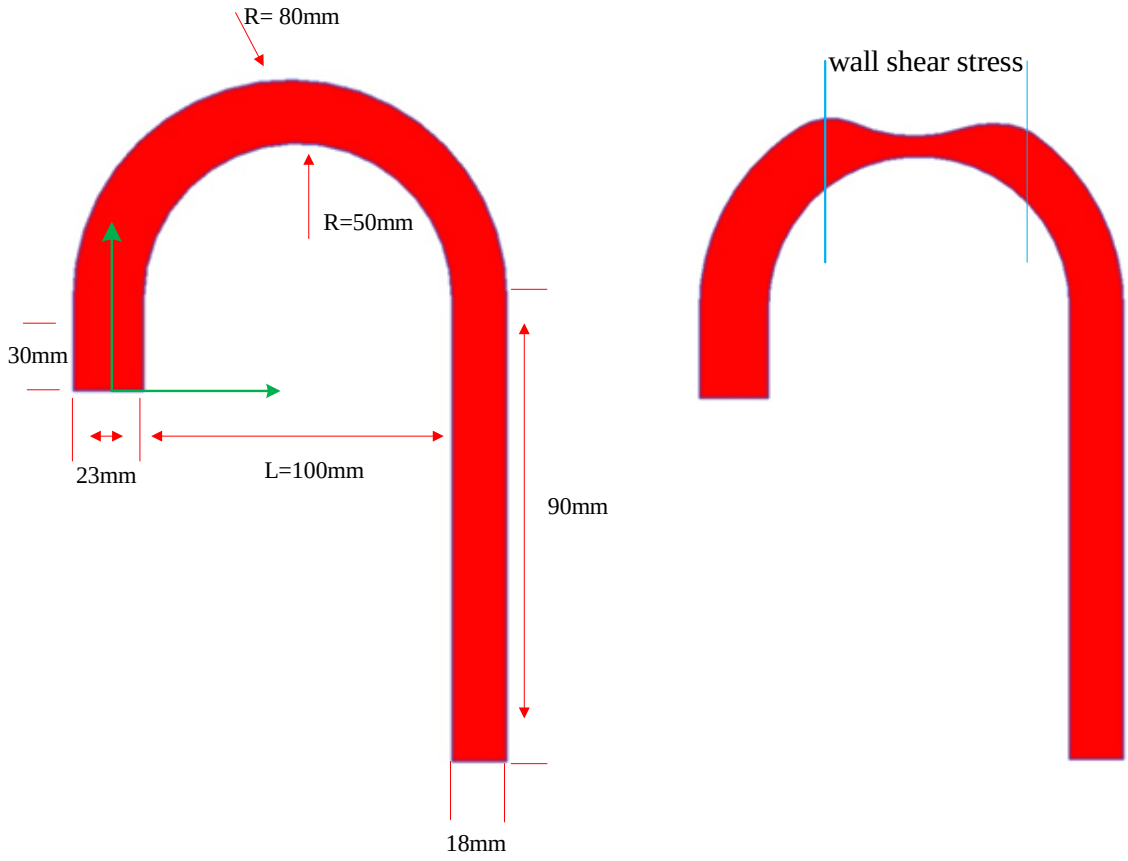

(a) Normal (b) Abnormal

Figure 5.12: Normal and abnormal ascending aorta [123]

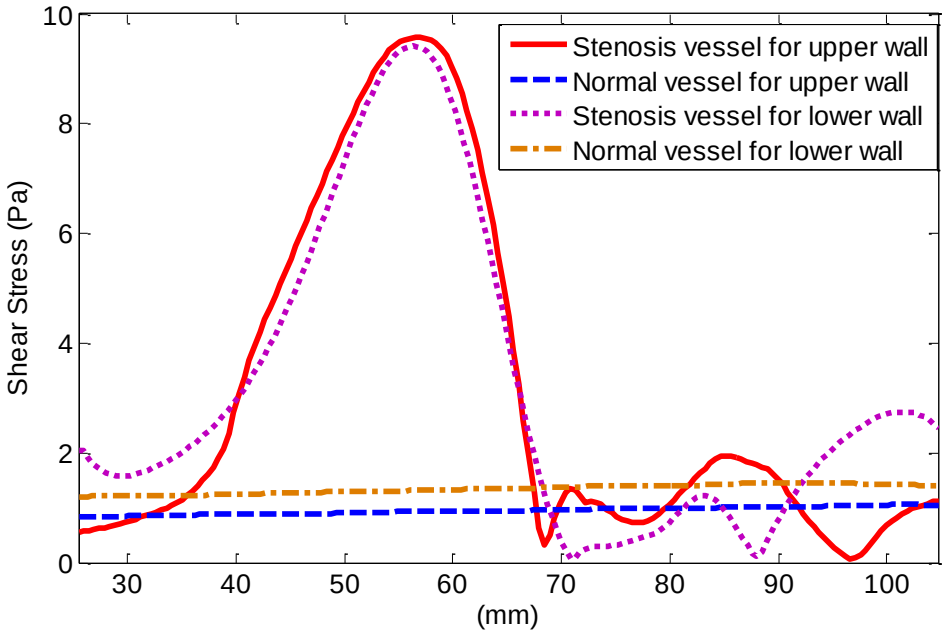

Figure 5.13: Wall shear stress at time t=$\frac{1}{4}$T

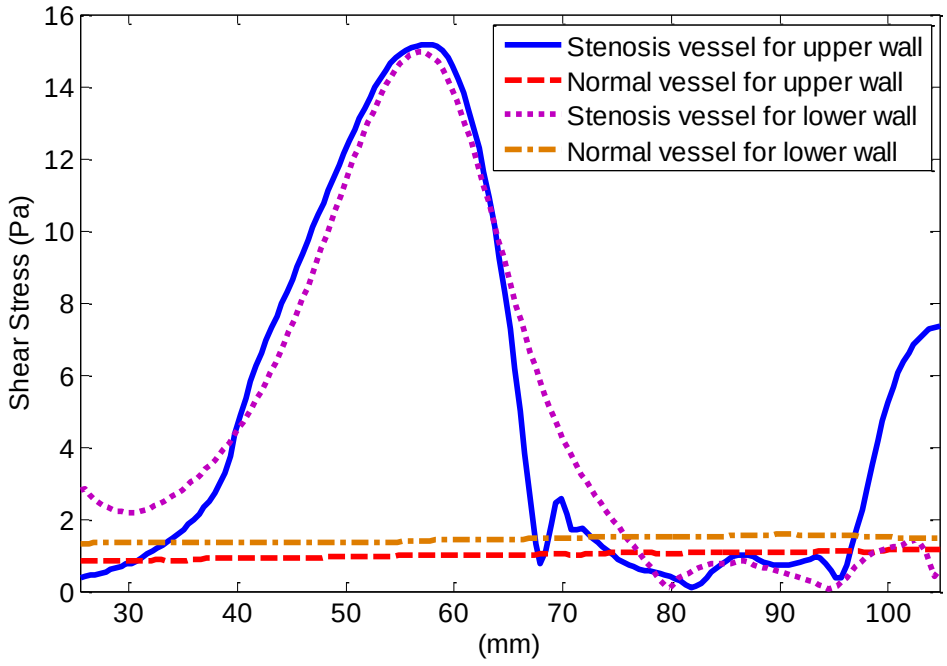

Figure 5.14: Wall shear stress at time t=$\frac{1}{2}$T

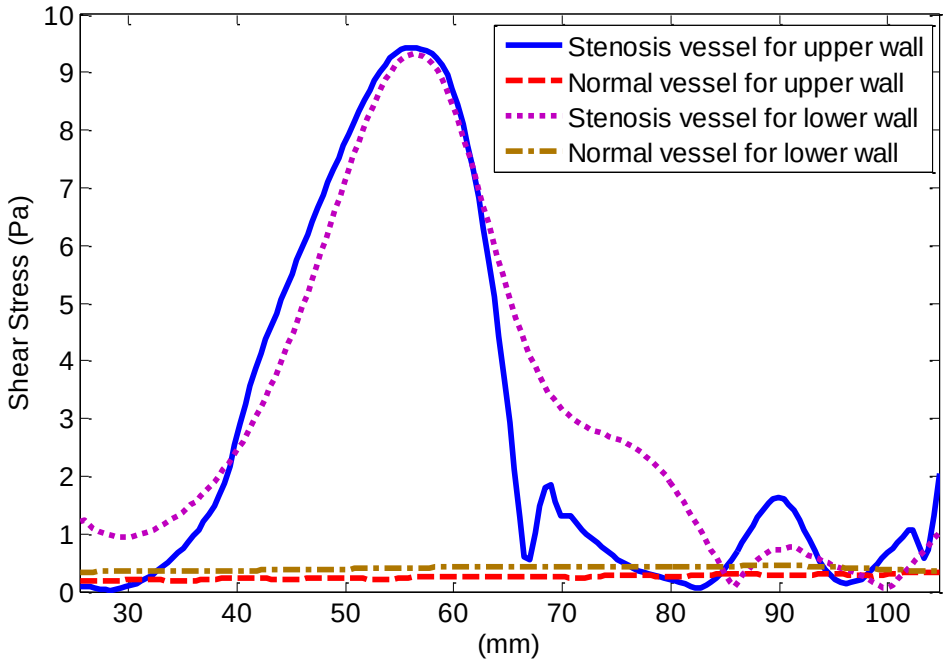

Figure 5.15: Wall shear stress at time t=$\frac{3}{4}$T

Table 5.1: Comparison of the PC-GSM, PL-GSM and αGSM

	Smoothing domain	Smoothing function
PC-GSM	nGSD, mGSD,	$w=\begin{cases}\dfrac{1}{V_i} & x\in\Omega_i \\ 0 & x\notin\Omega_i\end{cases}$
PL-GSM	nGSD, mGSD,	$w=\begin{cases}\mathbf{a}_0+\mathbf{a}_1\left(\mathbf{x}-\mathbf{x}_i\right) & x\in\Omega_i \\ 0 & x\notin\Omega_i\end{cases}$
	cGSD	$w\left(\mathbf{x}_{m_k}-\mathbf{x}_i\right)=0 \qquad w\left(\mathbf{x}_{c_k}-\mathbf{x}_i\right)=0$
αGSM	nGSD, mGSD,	$w=\begin{cases}\mathbf{a}_0+\mathbf{a}_1\left(\mathbf{x}-\mathbf{x}_i\right) & x\in\Omega_i \\ 0 & x\notin\Omega_i\end{cases}$
	cGSD	$w\left(\mathbf{x}_{m_k}-\mathbf{x}_i\right)=\alpha\dfrac{1}{V_i} \qquad w\left(\mathbf{x}_{c_k}-\mathbf{x}_i\right)=\alpha\dfrac{1}{V_i}$

Table 5.2: Errors and time consumed in different schemes

	Errors/Time Consumed		
No. of nodes	PC-GSM	PL-GSM	αGSM
72	1.83E-2/1.23s	1.47E-2/1.56sec	1.43E-2/2.96sec
244	4.59E-3/2.10s	3.76E-3/2.44sec	3.73E-3/4.78sec
963	9.44E-4/3.10sec	8.12E-4/3.76sec	8.10E-4/6.56sec
3741	2.07E-4/20.15sec	1.88E-4/28.33sec	1.87E-4/50.23sec

Chapter 6

Development of Immersed Gradient Smoothing Method (IGSM)

6.1 Introduction

Immersed finite element method (IFEM) [36-38] is a landmark in the development of numerical method to address the fluid-structure interaction problem. In the IFEM, both fluid and solid domains are modeled with the finite element methods (FEM), and the interaction force is distributed through the interpolation process. Because the computational cost for the finite element method (FEM) in the fluid is very high, the piecewise linear gradient smoothing method (PL-GSM) [26]developed in the Chapter 4 is applied to discretize the fluid domain in order to increase the computational efficiency. Furthermore, the accuracy of IFEM model is lost in the large deformation of solid once the element is distorted. Thus, the edge-based smoothed finite element method (ES-FEM) [11, 12]developed in the Chapter 2 is adopted to solve the solid domain. The immersed gradient smoothing method (IGSM) which has combined the gradient smoothing operation in the weak and strong form has the similar algorithm in the numerical procedure with the immersed finite element method (IFEM) as illustrated in the following section.

6.2 Brief of immersed finite element method for fluid-structure interaction

Consider a two dimensional deformable structure completely immersed in a fluid domain as shown in Fig. 6.1. It is assumed that the fluid exists everywhere in the whole domain Ω. Hence, an Eulerian fluid mesh Ω^f is adopted in the computation because the fluid spans over the entire domain Ω; whereas a Lagrangian mesh is constructed for solid domain Ω^s.

$$\Omega^s \cup \Omega^f = \Omega \tag{6.1}$$

$$\Omega^s \cap \Omega^f = \varnothing \tag{6.2}$$

The sub-domain overlapped by the solid domain Ω^s and fluid domain Ω^f is denoted as $\varnothing$ with a closed fluid-structure interface. In the construction of mesh for both fluid and solid domain, the two sets of mesh are not required being coincided as illustrated in Fig. 6.2. This is because the two sets of mesh are independent.

In the fluid domain, the velocity **v** and pressure *p* are the unknown variable, whereas in the solid domain, the nodal displacement is defined as $\mathbf{u}^s = \mathbf{x}^s - \mathbf{X}^s$. In a continuum, the inertial force of a particle is balanced with the derivative of the Cauchy stress and the external force on the continuum:

$$\rho_s \ddot{u} = \sigma_{s_{ij,j}} + f_i^{ext,s} \tag{6.3}$$

where ρ_s, $\sigma_{s_{ij,j}}$ and $f_i^{ext,s}$ are the density for solid, stress related to the internal stress and external force applied respectively.

The virtual work in the solid domain done by the solid is derived by a test function δv_i^s:

$$\int_{\Omega_s} \delta v_i^s \left[\rho_s \ddot{u} - \sigma_{s_{ij,j}} - f_i^{ext,s} \right] d\Omega = 0 \tag{6.4}$$

Add the artificial fluids to the Eq. (6.4) without destroying of system equation.

$$\int_{\Omega_s} \delta v_i^s \left[\left(\rho_s - \rho_f \right) \ddot{u} + \rho_f \ddot{u} - \left(\sigma_{s_{ij,j}} - \sigma_{f_{ij,j}} \right) - \sigma_{f_{ij,j}} - f_i^{ext,s} \right] d\Omega = 0 \tag{6.5}$$

where ρ_f and $\sigma_{f_{ij,j}}$ are the density for the fluid and the Cauchy stress in the fluid domain:

$$\sigma_{f_{ij,j}} = -p_i + \mu \left(v_{i,jj} + v_{j,ij} \right) \tag{6.6}$$

Rearrange the Eq. (6.5) to obtain the following expression:

$$\int_{\Omega_s} \delta v_i^s \left[\left(\rho_s - \rho_f \right) \ddot{u} - \left(\sigma_{s_{ij,j}} - \sigma_{f_{ij,j}} \right) - f_i^{ext,s} \right] d\Omega + \int_{\Omega_s} \delta v_i^s \left(\rho_f \ddot{u} - \sigma_{f_{ij,j}} \right) d\Omega = 0 \tag{6.7}$$

The first term in the Eq. (6.7) is the work done by the solid domain minus the work done by the artificial fluid. The second term denotes the work done by the artificial fluid in the overlapping domain.

The interaction force is defined:

$$f_i^{FSI} = \rho_f \ddot{u} - \sigma_{f_{ij,j}} \tag{6.8}$$

The weak formulation is:

$$\int_{\Omega_s} \delta v_i^s \left(\rho_f \ddot{u} - \sigma_{f_{ij,j}} - f_i^{FSI} \right) d\Omega = 0 \tag{6.9}$$

Substitute Eq. (6.9) into Eq. (6.7), the following weak form for the solid is obtained as follow:

$$\int_{\Omega_s} \delta v_i^s \left[\left(\rho_s - \rho \right) \ddot{u} - \left(\sigma_{s_{ij,j}} - \sigma_{f_{ij,j}} \right) - f_i^{ext,s} \right] d\Omega = -\int_{\Omega_s} \delta v_i^s \, f_i^{FSI,s} \tag{6.10}$$

The $f_i^{FSI,s}$ is the interaction force applied to the solid.

The external force applied to the solid in the solid domain:

$$f_i^{ext,s} = \left(\rho_s - \rho_f \right) g \tag{6.11}$$

Therefore, the fluid-structure interaction force within the solid domain is defined:

$$f_i^{FSI,s} = -\left(\rho_s - \rho_f\right)\ddot{u} + \sigma_{s_{ij,j}} - \sigma_{f_{ij,j}} + \left(\rho_s - \rho_f\right)g \tag{6.12}$$

Hence, the governing equation for the solid domain can be derived:

$$\left(\rho_s - \rho_f\right)\ddot{u} - \left(\sigma_{s_{ij,j}} - \sigma_{f_{ij,j}}\right) + \left(\rho_s - \rho_f\right)g - f_i^{FSI,s} = 0 \tag{6.13}$$

In the fluid domain, the virtual work for the fluid domain is expressed as follow:

$$\int_{\Omega_f} \delta v_i^f \left[\rho_f \left(v_{i,t} + v_j v_{i,j}\right) - \sigma_{f_{ij,j}}\right] d\Omega = 0 \tag{6.14}$$

Add the work done by the artificial fluid to the Eq. (6.14)

$$\int_{\Omega_f} \delta v_i^f \left[\rho_f \left(v_{i,t} + v_j v_{i,j}\right) - \sigma_{f_{ij,j}}\right] d\Omega + \int_{\Omega_s} \delta v_i^f \left[\rho_f \left(v_{i,t} + v_j v_{i,j}\right) - \sigma_{f_{ij,j}} - f_i^{FSI,f}\right] d\Omega = 0 \tag{6.15}$$

Combine the two integral into the whole domain:

$$\int_{\Omega} \delta v_i^f \left[\rho_f \left(v_{i,t} + v_j v_{i,j}\right) - \sigma_{f_{ij,j}} - f_i^{FSI,f}\right] d\Omega = 0 \tag{6.16}$$

Hence, the governing equation for the fluid domain can be derived as follow:

$$v_{i,i} = 0 \tag{6.17}$$

$$\rho_f \left(v_{i,t} + v_j v_{i,j}\right) - \sigma_{f_{ij,j}} - f_i^{FSI,f} = 0 \tag{6.18}$$

From the above equation, it is obviously noticed that the only difference between the standard Navier-Strokes equation and the Eq. (6.18) is the additional term f_i^{FSI}. This force is equivalent to the external force imposed to the fluid domain. The detail concept of the immersed finite element method is available [36]. In the following section, the piecewise linear gradient smoothing method (PL-GSM) for fluid domain and edge-based smoothed finite element method (ES-FEM) for solid part are briefed.

6.3 Piecewise linear gradient smoothing method (PL-GSM) for incompressible flow

6.3.1 Brief of governing equation

As derived above, the governing equations of incompressible viscous fluid flow can be expressed in the conventional Navier-Stokes equation with the additional interaction force. The Eq. (6.17) and (6.18) can be rewritten as the following vector-form:

$$\frac{\partial \mathbf{T}}{\partial t}+\nabla\cdot\left(\mathbf{F}_c-\mathbf{F}_v\right)+\mathbf{F}^{FSI,f}=0 \tag{6.19}$$

The relevant quantities are:

$$\mathbf{T}=\begin{bmatrix}1\\ \rho_f u^*\\ \rho_f v\end{bmatrix}\qquad \mathbf{F}_c=\begin{bmatrix}\rho_f V\\ \rho_f u^* V+n_x p\\ \rho_f v V+n_y p\end{bmatrix}\qquad \mathbf{F}_v=\begin{bmatrix}0\\ n_x\tau_{xx}+n_y\tau_{xy}\\ n_x\tau_{xy}+n_y\tau_{yy}\end{bmatrix}\qquad \mathbf{F}^{FSI,f}=\begin{bmatrix}0\\ \mathbf{F}_x^{FSI,f}\\ \mathbf{F}_y^{FSI,f}\end{bmatrix} \tag{6.20}$$

where

$$\tau_{xy}=\tau_{yx}=\mu\left(\frac{\partial u^*}{\partial y}+\frac{\partial v}{\partial x}\right),\tau_{xx}=2\mu\frac{\partial u^*}{\partial x},\tau_{yy}=2\mu\frac{\partial v}{\partial y} \tag{6.21}$$

$$V=\mathbf{v}\cdot\mathbf{n}=u^* n_x+v n_y \tag{6.22}$$

The velocity u in the fluid domain is marked u^* in order to differentiate the displacement u in the solid domain.

Because there is no temporal form in the continuity equation which violates the hyperbolic properties of the system, temporal terms are added into the Eq. (6.19) with the artificial compressibility [124].

$$\frac{\partial \mathbf{Z}}{\partial \tau}+\frac{\partial \mathbf{T}}{\partial t}+\nabla\cdot\left(\mathbf{F}_c-\mathbf{F}_v\right)+\mathbf{F}^{FSI,f}=0 \tag{6.23}$$

The relevant components are

$$\mathbf{Z}=\begin{bmatrix} p \\ \rho_f u^* \\ \rho_f v \end{bmatrix}, \mathbf{T}=\begin{bmatrix} 1 \\ \rho_f u^* \\ \rho_f v \end{bmatrix}, \mathbf{F}_c=\begin{bmatrix} \beta\rho_f V \\ \rho_f u^* V + n_x p \\ \rho_f v V + n_y p \end{bmatrix}, \mathbf{F}_v=\begin{bmatrix} 0 \\ n_x\tau_{xx} + n_y\tau_{xy} \\ n_x\tau_{xy} + n_y\tau_{yy} \end{bmatrix}, \mathbf{F}^{FSI,f}=\begin{bmatrix} 0 \\ f_x^{FSI,f} \\ f_y^{FSI,f} \end{bmatrix} \quad 6.24$$

Here τ is pseudo time step, t is physical time step.

In the time integration, the governing equation can be written in the following residual form with respect to the pseudo time τ

$$\frac{\partial \mathbf{Z}}{\partial \tau} = -\mathbf{R}^* = -\left(\frac{\partial \mathbf{T}}{\partial t} + \mathbf{R}\right) \quad 6.25$$

where

$$\mathbf{R} = \nabla \cdot (\mathbf{F}_c - \mathbf{F}_v) + \mathbf{F}^{FSI,f} \quad 6.26$$

In the pseudo time step, explicit multi-stage Runge-Kutta (RK5) method [48, 125] is used. The second order of three level backward differencing technique is applied to approximate the physical time step [125].

$$\frac{\partial \mathbf{T}^n}{\partial t} \approx \frac{3\mathbf{T}^{n+1} - 2\mathbf{T}^n + \mathbf{T}^{n-1}}{2\Delta t} \quad 6.27$$

6.3.2 Spatial approximation using PL-GSM

In the PL-GSM, the convective and viscid flux can be approximated with the piecewise linear gradient smoothing operation. Based on the gradient smoothing operation in the strong form, the first and second order derivatives of unknown variable v in the Eq. (6.24) is expressed [26]:

$$\nabla v_i \approx -\int_{\Omega_i} v(x) \nabla w(\mathbf{x} - \mathbf{x}_i)\, dV \quad 6.28$$

$$\nabla \cdot \nabla v_i \approx -\int_{\Omega_i} \nabla v(x) \nabla w(\mathbf{x} - \mathbf{x}_i)\, dV \quad 6.29$$

The linear smoothing function *w*

$$w(\mathbf{x}-\mathbf{x}_i)=\begin{cases}\mathbf{a}_0+\mathbf{a}_1(\mathbf{x}-\mathbf{x}_i), & \mathrm{x}\in\Omega_i\\ 0 & \mathrm{x}\notin\Omega_i\end{cases} \tag{6.30}$$

For brevity, the detail derivation of first and second order derivative [26] is ignored in this section. As shown in Fig. 6.3, the node *i*, the 1st-order derivatives of the field variable *v* are given by:

$$\frac{\partial v_i}{\partial x}\approx-\sum_{k=1}^{N_i}\left\{\frac{1}{3}\left[v(\mathbf{x}_i)+v(\mathbf{x}_{m_k})+v(\mathbf{x}_{c_k})\right]\delta_{i,2k}+\frac{1}{3}\left[v(\mathbf{x}_i)+v(\mathbf{x}_{m_k})+v(\mathbf{x}_{c_{k-1}})\right]\delta_{i,2k-1}\right\} \tag{6.31}$$

$$\frac{\partial v_i}{\partial y}\approx-\sum_{k=1}^{N_i}\left\{\frac{1}{3}\left[v(\mathbf{x}_i)+v(\mathbf{x}_{m_k})+v(\mathbf{x}_{c_k})\right]\gamma_{i,2k}+\frac{1}{3}\left[v(\mathbf{x}_i)+v(\mathbf{x}_{m_k})+v(\mathbf{x}_{c_{k-1}})\right]\gamma_{i,2k-1}\right\} \tag{6.32}$$

The 2nd-order derivatives are obtained with linear gradient smoothing operation and given in the following form

$$\frac{\partial^2 v_i}{\partial x^2}\approx-\sum_{k=1}^{N_i}\left\{\frac{1}{3}\left[\frac{\partial v(\mathbf{x}_i)}{\partial x}+\frac{\partial v(\mathbf{x}_{m_k})}{\partial x}+\frac{\partial v(\mathbf{x}_{c_k})}{\partial x}\right]\delta_{i,2k}+\frac{1}{3}\left[\frac{\partial v(\mathbf{x}_i)}{\partial x}+\frac{\partial v(\mathbf{x}_{m_k})}{\partial x}+\frac{\partial v(\mathbf{x}_{c_{k-1}})}{\partial x}\right]\delta_{i,2k-1}\right\} \tag{6.33}$$

$$\frac{\partial^2 v_i}{\partial y^2}\approx-\sum_{k=1}^{N_i}\frac{1}{3}\left[\frac{\partial v(\mathbf{x}_i)}{\partial y}+\frac{\partial v(\mathbf{x}_{m_k})}{\partial y}+\frac{\partial v(\mathbf{x}_{c_k})}{\partial y}\right]\gamma_{i,2k}\frac{1}{3}\left[\frac{\partial v(\mathbf{x}_i)}{\partial y}+\frac{\partial v(\mathbf{x}_{m_k})}{\partial y}+\frac{\partial v(\mathbf{x}_{c_{k-1}})}{\partial y}\right]\gamma_{i,2k-1}\Bigg\} \tag{6.34}$$

And

$$\delta_{i,2k}=\begin{cases}-\frac{3}{V_i}(y_{c_k}-y_{m_k})/2, & \text{if } \theta>0;\\ \frac{3}{V_i}(y_{c_k}-y_{m_k})/2, & \text{if } \theta<0;\end{cases}\qquad \gamma_{i,2k}=\begin{cases}\frac{3}{V_i}(x_{c_k}-x_{m_k})/2, & \text{if } \theta\geq 0;\\ -\frac{3}{V_i}(x_{c_k}-x_{m_k})/2, & \text{if } \theta\leq 0;\end{cases} \tag{6.35}$$

$$\theta=(x_{m_k}-x_i)(y_{c_k}-y_i)-(x_{c_k}-x_i)(y_{m_k}-y_i)$$

where i denotes the node of interest and j_k is the other end-node of the cell-edge linked to node i (See Fig. 6.3). m_k denotes the midpoint of the cell-edge of interest, and c_k represents the centroids of triangular element. v_n, v_m and v_c denote values of the field variable at nodes, midpoints of cell-edges and centroids of triangular cells, respectively. The parameters $\delta_{i,2k-1}$ and $\gamma_{i,2k-1}$ can be obtained in the similar way .

In virtue of the above analysis, the flow chart to analyze the incompressible flow is summarized as follow:

1. Set initial condition of the fluid
2. Distribute the fluid structure interaction force from solid to the fluid
3. Set the artificial time τ and physical time step t
4. Iterate all the unknown variables within one physical time. If the process converges, the change in the unknown between two successive iterations should be smaller than a given tolerance
5. Update the fluid variables
6. Interpolate the velocity from fluid domain to solid domain and go to step 2 to proceed to next physical time step

6.4 Formulation of Edge-based smoothed finite element (ES-FEM) in the large deformation of structure mechanics

6.4.1 Discrete governing equation

In the present ES-FEM, discretized system equation is formulated based on the smoothed Galerkin weak form that can be derived as follows. The devolved weak form is first obtained by multiplying Eq. (6.13) with a test function w in the solid domain:

$$\int_{\Omega_s} w\left[\left(\rho_s-\rho_f\right)\ddot{u}_i-\frac{\partial\sigma_{ij}^s}{\partial x_j}-\left(\rho_s-\rho_f\right)g+f_i^{FSI,s}\right]d\Omega=0 \tag{6.36}$$

The integration domain is changed from current configuration Ω_s to initial configuration Ω_{s0} in the total Lagrangian formulation. Because the fluid and the solid are incompressible, the Jacobian determinant is 1. Hence, the weak form of the total Lagrangian is expressed:

$$\int_{\Omega_{s_0}} w\left[\left(\rho_s-\rho_f\right)\ddot{u}_i-\frac{\partial P_{ij}^s}{\partial x_j}-\left(\rho_s-\rho_f\right)g+f_i^{FSI,s}\right]d\Omega=0 \tag{6.37}$$

where the first Piola-Kirchhoff stress:

$$P_{ij}=JF_{ik}^{-1}\sigma_{kj}^s \tag{6.38}$$

Integration by part of Eq. (6.37):

$$\begin{aligned}\int_{\Omega_{s_0}} w\left(\rho_s-\rho_f\right)\ddot{u}_i d\Omega+\int_{\Omega_{s_0}} wP_{ij}d\Omega-\int_{\Omega_{s_0}} w\left(\rho_s-\rho_f\right)gd\Omega \\ +\int_{\Omega_{s_0}} wf_i^{FSI,s}d\Omega=0\end{aligned} \tag{6.39}$$

In the above weighted residual form, the field variable displacement can be expressed in the approximate form:

$$u=\sum_{i=1}^{m}\mathbf{N}_i u_i=\mathbf{Nu} \tag{6.40}$$

In the standard Galerkin weak form, the shape function **N** is also used as the weight function *w* and the weak form for solid can be obtained as:

$$\begin{aligned}\int_{\Omega_{s_0}}\mathbf{N}\left(\rho_s-\rho_f\right)\mathbf{N}\ddot{\mathbf{u}}d\Omega+\int_{\Omega_{s_0}}\mathbf{NP}d\Omega-\int_{\Omega_{s_0}}\mathbf{N}\left(\rho_s-\rho_f\right)gd\Omega+ \\ \int_{\Omega_{s_0}}\mathbf{N}\mathbf{f}_i^{FSI,s}d\Omega=0\end{aligned} \tag{6.41}$$

The force is balanced by the inertial force, internal force, external force and interaction force.

$$\mathbf{M}\ddot{\mathbf{u}}+\mathbf{f}_{in}+\mathbf{f}_{ex}=\mathbf{f}^{s,FSI} \tag{6.42}$$

where

$$\mathbf{f}_{in}=\int_{\Omega_{s_0}}\mathbf{N}\mathbf{P}d\Omega \quad \text{The internal force matrix} \tag{6.43}$$

$$\mathbf{M}=\left(\rho_s-\rho_f\right)\int_{\Omega_{s_0}}\mathbf{N}^{\mathrm{T}}\cdot\mathbf{N}\mathrm{d}\Omega \quad \text{The mass force matrix} \tag{6.44}$$

$$\mathbf{f}_{ex}=-\int_{\Omega_{s_0}}\mathbf{N}_i\left(\rho_s-\rho_f\right)gd\Omega \quad \text{The external force matrix} \tag{6.45}$$

$$\mathbf{f}_i^{FSI,s}=-\int_{\Omega_{s_0}}\mathbf{N}\mathbf{f}_i^{FSI,s}d\Omega \quad \text{The interaction force matrix} \tag{6.46}$$

It is noted the formulation for external force vector $\mathbf{f}_{in}$ and mass matrix $\mathbf{M}$ in the ES-FEM are exactly the same as the FEM. Many existing methods can be used to solve the second order time dependent problems, such as the Newmark method, the Crank-Nicholson method, and so on. In this thesis, central difference time step is used: Velocity at time step *n*:

$$\dot{\mathbf{u}}=\frac{1}{2\Delta t}\left(\mathbf{u}_{i+1}-\mathbf{u}_i\right) \tag{6.47}$$

Acceleration a time step *n*:

$$\ddot{\mathbf{u}}=\frac{1}{\Delta t}\left(\dot{\mathbf{u}}_{i+0.5}-\dot{\mathbf{u}}_{i-0.5}\right) \tag{6.48}$$

where the two velocity terms in Eq. (6.48) can be written similarly (half-step forward and backward) in terms of $\mathbf{u}_{i-1}$, $\mathbf{u}_i$ and $\mathbf{u}_{i+1}$. Hence, it can be shown that:

$$\ddot{\mathbf{u}}=\frac{1}{2\Delta t}\left(\mathbf{u}_{i+1}-2\mathbf{u}_i+\mathbf{u}_{i-1}\right) \tag{6.49}$$

Substitute the Eq. (6.49) into (6.42),

$$\mathbf{M}\frac{1}{2\Delta t}\left(\mathbf{u}_{i+1}-2\mathbf{u}_i+\mathbf{u}_{i-1}\right)+\mathbf{f}_{in}+\mathbf{f}_{ex}=\mathbf{f}^{FSI,s} \tag{6.50}$$

6.4.2 Evaluation of internal nodal force using ES-FEM

The isotropic hyperelastic Neo-Hookean material is employed. The hyperelastic materials are characterized by the existence of a stored energy function:

$$\psi\left(\mathbf{C}\left(\mathbf{X}\right),\mathbf{X}\right)=\psi\left(I_1,I_2,I_3,\mathbf{X}\right) \tag{6.51}$$

where the invariants of $\mathbf{C}$:

$$I_1=\mathrm{tr}\mathbf{C}=\mathbf{I}:\mathbf{C}=C_{11}+C_{22}+C_{33} \tag{6.52}$$

$$I_2=\mathrm{tr}\mathbf{C}\mathbf{C}=\mathbf{C}:\mathbf{C} \tag{6.53}$$

$$I_3=\det\mathbf{C}=J^2 \tag{6.54}$$

And

$$E_{ij}=\frac{1}{2}\left(C_{ij}-\delta_{ij}\right) \tag{6.55}$$

For isotropic cases, the second Piola-Kirchhoff stress tensor can be written as:

$$S_{ij}=\frac{\partial\psi}{\partial E_{ij}}=2\frac{\partial\psi}{\partial\mathbf{C}}=2\frac{\partial\psi}{\partial I_1}\frac{\partial I_1}{\partial\mathbf{C}}+2\frac{\partial\psi}{\partial I_2}\frac{\partial I_2}{\partial\mathbf{C}}+2\frac{\partial\psi}{\partial I_3}\frac{\partial I_3}{\partial\mathbf{C}} \tag{6.56}$$

Introducing the following derivatives:

$$\frac{\partial I_1}{\partial\mathbf{C}}=\mathbf{I},\qquad\frac{\partial I_2}{\partial\mathbf{C}}=2\mathbf{C},\qquad\frac{\partial I_3}{\partial\mathbf{C}}=J^2\,\mathbf{C}^{-1} \tag{6.57}$$

Therefore, the second Piola-Kirchhoff stress can be written:

$$S=2\Phi_{,1}\mathbf{I}+4\Phi_{,2}\mathbf{C}+2J^2\Phi_{,3}\mathbf{C}^{-1} \tag{6.58}$$

where

$$\Phi_{,i}=\frac{\partial\psi}{\partial I_i},i=1,2,3 \tag{6.59}$$

In this thesis, the stored energy function in the ES-FEM model is expressed as follow:

$$\psi\left(\overline{\mathbf{C}}\right)=\frac{1}{2}\lambda_0\left(In\overline{J}\right)^2-\mu_0\left(In\overline{J}\right)+\frac{1}{2}\mu_0\left(trace(\overline{\mathbf{C}})-3\right) \tag{6.60}$$

where $\overline{J}$ and $\overline{\mathbf{C}}$ are the determinant of the smoothed deformation gradient and the smoothed deformation gradient respectively, λ_0 and μ_0 are the Lame constants in the linearized theory.

$$\overline{\mathbf{J}}=\det\left(\overline{\mathbf{F}}\right) \tag{6.61}$$

The second smoothed Piola-Kirchhoff stress $\overline{\mathbf{S}}$ can be evaluated in the following way:

$$\overline{\mathbf{S}}=\lambda_0 In\overline{J}\overline{\mathbf{C}}^{-1}+\mu_0\left(\mathbf{I}-\overline{\mathbf{C}}^{-1}\right) \tag{6.62}$$

where the first smoothed Piola-Kirchhoff stress $\overline{\mathbf{P}}$ can be evaluated through the relationship between the first and second Piola-Kirchhof stress:

$$\overline{\mathbf{P}}=\overline{\mathbf{S}}\overline{\mathbf{F}} \tag{6.63}$$

In the ES-FEM, the smoothed deformation gradient associated with edge *k* based on the smoothed domain can be defined as:

$$\overline{\mathbf{F}}=\int_{\Omega^{(k)}}\mathbf{F}(X)\boldsymbol{\varphi}_k(X)d\Omega=\frac{1}{A_k^s}\int_{\Omega^{(k)}}\mathbf{F}(X)d\Omega=\frac{1}{A_k^s}\int_{\Omega^{(k)}}\nabla\mathbf{u}d\Omega+\mathbf{I} \tag{6.64}$$

The smoothing domain Ω_k^s associated with the element edge *k* can be created by connecting two endpoints of the edge to centroids of adjacent elements as shown in Figure 6.4.

$\boldsymbol{\varphi}_k(\mathbf{x})$ is a given smoothing function that satisfies the following requirements:

$$\int_{\Omega_k^s}\boldsymbol{\varphi}_k(\mathbf{x})d\Omega=1 \tag{6.65}$$

$$\boldsymbol{\varphi}_k(\mathbf{x})=\begin{cases}1/A_k^s, x\in\Omega_k^s\\ 0, \quad x\notin\Omega_k^s\end{cases} \tag{6.66}$$

where A_k^s is the area of the smoothing domain Ω_k^s and is calculated by

$$A_k^s = \int_{\Omega_k^s} d\Omega = \frac{1}{3}\sum_{i=1}^{n_{sd}} A_i^e \tag{6.67}$$

where n_{sd} is the number of elements surrounding the edge *k* and A_k^s is the area of the j^{th} element around the edge *k*. It can be observed from Fig. 6.4, that $n_{sd}=1$ when edge *k* is the boundary edge and $n_{sd}=2$ when edge *k* is the inside edge.

In the dynamic analysis, the consistent matrix is used.

$$\mathbf{M} = \frac{\rho_s t_s A_i^e}{3}\mathbf{I} = \frac{\rho_s t_s A_i^e}{3}\begin{bmatrix} 1 & 0 & 0 & 0 & 0 & 0 \\ 0 & 1 & 0 & 0 & 0 & 0 \\ 0 & 0 & 1 & 0 & 0 & 0 \\ 0 & 0 & 0 & 1 & 0 & 0 \\ 0 & 0 & 0 & 0 & 1 & 0 \\ 0 & 0 & 0 & 0 & 0 & 1 \end{bmatrix} \tag{6.68}$$

A_i^e is the area of element; ρ_s and t_s are the mass density and the thickness of the element respectively. The diagonal form of the lumped mass matrix in solving transient dynamics problems results the superiority in terms of efficiency compared with the consistent mass matrix. The use of lumped mass matrix provides a softer model meaning the eigenvalues obtained will be smaller than those obtained using the consistent mass matrix for the same model [126].

The numerical procedure to obtain the interaction force using the ES-FEM is briefly given as follows:

1. Divide the domain into a set of elements and obtain information regarding node coordinates and element connectivity.
2. Search the adjacent elements and the smoothing domain *k* associated with each edge *k*.
3. Loop over all the elements and evaluate the external force vector of the element by

Eq. (6.43) and inertial force by Eq. (6.45), and assemble force vector into the global force vector.

4. Loop over all the edges:

(a) Compute the smoothed deformation gradient $\bar{\mathbf{F}}$ using Eq. (6.64).

(b) Evaluate the second smoothed Piola-Kirchhoff stress using Eq. (6.62)

(c) Calculate the first smoothed Piola-Kirchhoff stress through the Eq. (6.63).

5. Implement essential boundary conditions.

6. Solve the system equations to obtain the interaction force based on Eq. (6.42).

6.5 Construction of Finite Element Interpolation

The fluid structure interaction (FSI) force plays an important role in the momentum of fluid domains. In this chapter, procedure in the distribution of interaction force to the fluid is presented. As shown in Fig. 6.5 (a), the initial configuration for the fluid and solid is given; the solid is completely immersed in the fluid. The solid and fluid domains are represented by two independent elements, which are not required to be coincident. After that, solve the fluid –structure interaction (FSI) force for the solid using the Eq. (6.42) as shown in Fig. 6.5 (b) independently. The interaction force from the solid domain can be distributed to its surrounding fluid in the following way as outlined in Fig. 6.5 (c):

$$\mathbf{f}^{FSI,f} = \int_{\Omega^s} \mathbf{f}^{FSI,s} \zeta\left(\mathbf{x}-\mathbf{x}^s\right) d\Omega \tag{6.69}$$

where $\zeta\left(\mathbf{x}-\mathbf{x}^s\right)$ is the interpolation function, which is related to the distance between the fluid and solid nodes. Several constrains must be imposed on the interpolation

function. First, the continuity of velocity and force in the interface of fluid-solid must be satisfied; second, the interpolation function must be completed and reproducible [127]:

$$\int_{-\infty}^{+\infty} \zeta(x-y)dy = 1 \tag{6.70}$$

And the reproduced function is:

$$\int_{-\infty}^{+\infty} u(y)\zeta(x-y)dy = u(x) \tag{6.71}$$

where x and y are the solid and fluid domain respectively.

Based on the above requirements, there are many ways to generate the interpolation:

1) Reproducing Kernel function

2) Discretized Dirac delta function

3) Finite Element interpolation

The most frequent method in the interpolation function is a discretized Dirac delta function in the original immersed boundary method developed by [32-34]. However, this technique is difficult to apply in the infinitesimally small grids because it numerically thickens the fluid-structure interface and reduce the accuracy in the interpolation process. Alternatively, Liu and Zhang [36-38] proposed the reproducing kernel function to deal with the nonuniform meshes in order to enhance interfacial solutions. In the reproducing kernel function, additional parameter is introduced to control the support size of solid and fluid interface. However, at least four layers in the support domain are needed to induce a smoothed or smeared velocity at the interface, which is not desirable if more accurate interfacial solution is required. Recently, Wang and Zhang [127] developed the FEM interpolation to map the

velocity and interaction force from fluid domain to solid domain or from solid domain to fluid domain. The FEM interpolation can overcome some problems of the discrete Dirac delta function and reproducing kernel function, such as thickening the fluid-structure interface, difficulties when solid is close to fluid boundary, requiring explicitly imposing solution jumps at the interface and so on. The FEM interpolation is capable to produce a sharper interface because it only needs one element layer. Thus, the FEM interpolation is used in this thesis.

In order to map the interaction force from the solid to the fluid nodes, a searching algorithm is required to carry out to identify the corresponding fluid element which a solid node resides in at the configuration of time step *n+1* . During the searching process, there are three cases needed to identify as outlined in Fig. 6.6.

The criteria to judge different cases is illustrated as follow: Assume there is an arbitrary solid point $\mathbf{x}_s$ with a coordinate (x_s, y_s) and a triangular element consisting of three nodes in the fluid domain $\mathbf{x}_1$, $\mathbf{x}_2$ and $\mathbf{x}_3$ with area Δ_{123}. The coordinate for these three nodes is labeled as: (x_1, y_1), (x_2, y_2) and (x_3, y_3). Three triangular areas constructed by $\mathbf{x}_s\mathbf{x}_1\mathbf{x}_2, \mathbf{x}_s\mathbf{x}_1\mathbf{x}_3, \mathbf{x}_s\mathbf{x}_2\mathbf{x}_3$ are denoted by $\sum_{i=1}^{3}\Delta$. In the case 1: $\Delta_{123} = \sum_{i=1}^{3}\Delta$ and all $\sum_{i=1}^{3}\Delta \neq 0$, which implies $\mathbf{x}_s$ is inside of the fluid triangular element. In the case 2: $\Delta_{123} = \sum_{i=1}^{3}\Delta$ and any $\sum_{i=1}^{3}\Delta = 0$, which indicates that $\mathbf{x}_s$ is on the edge of fluid element; In the case 3: $\Delta_{123} < \sum_{i=1}^{3}\Delta$, which proves that $\mathbf{x}_s$ is outside of the element. In the interpolation process, only the first and second cases

are required to consider. Due to the motion of the solid, this searching procedure has to be carried out at every time step.

The interpolation must meet the reproducing conditions:

$$\sum_{n=1}^{3} N_n^e = 1 \tag{6.72}$$

$$\sum_{n=1}^{3} N_n^e x_n^e = x^s \quad \sum_{n=1}^{3} N_n^e y_n^e = y^s \tag{6.73}$$

Therefore:

$$\mathbf{NQ} = \mathbf{K} \tag{6.74}$$

where

$$\mathbf{K}\left(x^s, y^s\right) = \begin{pmatrix} 1 & x^s & y^s \end{pmatrix} \tag{6.75}$$

$$\mathbf{Q} = \begin{bmatrix} 1 & x_1 & y_1 \\ 1 & x_2 & y_2 \\ 1 & x_3 & y_3 \end{bmatrix} \tag{6.76}$$

And

$$\mathbf{N}\left(x^s, y^s\right) = \mathbf{K}\left(x^s, y^s\right)\left(\mathbf{Q}\right)^{-1} \tag{6.77}$$

So the interactions force for the fluid:

$$\mathbf{f}_{i+1}^{FSI,f} = N_n \mathbf{f}_{i+1}^{FSI,s} \tag{6.78}$$

After v_{n+1}^f at time step $n+1$ for the fluid is obtained, the velocity for the solid can be achieved using finite element interpolation again:

$$\mathbf{v}_{n+1}^s = \sum_K N_n \mathbf{v}_K^f \qquad \mathbf{x}_K \in \Omega_{fs} \tag{6.79}$$

The detail procedure in the finite element interpolation can be found [127].

In summary, the whole procedure for the solution of Immersed Gradient Smoothed Method is illustrated as Fig. 6.7:

6.6 Numerical Example

6.6.1 Soft Disk falling in a viscous fluid

In this section, a soft disk falling in a viscous fluid under the gravity as shown in Figure 6.8 is examined using the Immerse Gradient Smoothing Method (IGSM). The density for the fluid and solid is 1kg/ m^3 and 3kg/m^3 respectively. The Young Modulus for the solid is1.2×10^4 N/m^2 , and the Poisson ratio is 0.3. Two sets of viscosity for the fluid are examined. The material properties and size of channel are summarized in Table 6.1. Zero initial conditions are assumed. The acceleration of gravity g=9.8 is applied in the y direction. Non-slip conditions are assumed on the left, right and bottom boundaries of the fluid domain. On the top boundary the velocity is free and the pressure is set to be zero.

Due to the gravity effect acting on the solid, the soft disk accelerates and moves downward. Because the length of fluid channel is much bigger than the size of wall disk, the wall effect is ignored. The drag force increases if the velocity of disk is faster. Once the gravity force is equivalent to the dragging force, the disk arrives at a constant value.

In order to investigate the accuracy of the immersed gradient smoothing method (IGSM), the constant velocity for the rigid disk in the viscous fluid obtained from Clift [128] is presented for comparison. The empirical terminal velocity for the rigid under the gravity is expressed as follow:

$$v=\frac{\left(\rho_s-\rho_f\right)gR^2}{4\mu}\left[\ln\left(\frac{W}{2R}\right)-0.9157+1.7244\left(\frac{2R}{W}\right)^2-1.7302\left(\frac{2R}{W}\right)^4\right] \qquad 6.80$$

Two types of mesh are used: one is coarse mesh (259 nodes for solid, 8326 nodes for fluid); another is fine mesh (802 nodes for solid, 26832 nodes for fluid). Figure 6.9 illustrates the vertical velocity for different meshes at μ=0.4. It is obviously noticed that the numerical solutions obtained from the IGSM using the coarse mesh agree very well with the results from the IFEM using the fine mesh. Furthermore, more fine mesh leads to the solution approaching the reference solution. However, the result from IFEM model using coarse mesh has a large deviation with the reference solution, which verifies the validity and accuracy of the proposed IGSM. Fig. 6.10 shows the contours of the pressure and vertical velocity at the steady state. This obviously shows that the pressure and velocity are symmetrical with the midplane.

Figure 6.11 presents the history of vertical velocity at μ=0.5. Once again, the numerical results obtained from the IGSM using the coarse mesh is very close to the reference solution and results obtained from the IFEM using very fine mesh. Once the fluid viscosity increases, the drag force acting on the disk increases. Hence, the steady velocity decreases compared with μ=0.4 as shown in Fig. 6.9. The contours of the pressure and vertical velocity at the steady state are presented in Fig. 6.12. Again, the pressure and velocity are also symmetrical with the midplane.

6.6.2 Aortic Valve Driven by a Sinusoidal Blood Flow

This example is to analyze the motion, time-dependent deflection of a thin flexible body in a pulsatile blood flow [129]. This type of problem is very important to study the opening and closing behavior of aortic heart valves in reality, which exist complicated

interactions between heart valve leaflets, aorta and blood flow [130]. A two dimensional representation of the aortic valve is presented in Fig. 6.13. The valve is able to rotate around its point of attachment. A cylindrical cavity is present behind the disc, which is modeled version of the physiological sinus of Valsalva. The membranous hinge connects the valve and the rigid channel together. The bending moment in the direction of closed position is caused by the hinge. The material properties and parameters are summarized in Table 6.2. Initially, the blood and leaflet is at rest. A sinusoidal input velocity with amplitude of 0.1 m/s, consistent with parabolic distribution function, is applied at the inlet as shown in Fig. 6.14. No slip condition is applied on the top and bottom channel. The fluid is assumed to be Newtonian, incompressible and laminate. The free outlet conditions for the fluid are applied.

The motion of leaflet in the numerical model using the IGSM is presented in Figure 6.15. The leaflet is pushed upward when the inlet velocity increases gradually. Once the inlet velocity decreases, the leaflet is pushed downward. This motion of the leaflet repeats itself for every cycle. The sequence of movements obtained from the IGSM follows the same motion as the one obtained from [131]. Therefore, the capabilities of the IGSM to solve the fluid-structure interaction are demonstrated by this example again.

The proposed IGSM has captured the motion and deformation of simple two dimensional heart valve model successfully with ultra-accuracy. In real case, the natural valve consists of three flexible leaflets, which are constituted within the

expandable aortic root [132]. Although the two dimensional model is not sufficient to analyze the realistic case, the model can be used to test the current method in predicting the interaction behavior of such systems as a first step towards full three dimensional numerical models in heart valves. The present IGSM can straightforward be extended to three dimensional models.

6.7 Remarks

In this chapter, a two dimensional immersed gradient smoothing method (IGSM) is developed to solve the fluid structure interaction problems. Basically, the procedure of IGSM includes three parts: edge-based smoothed finite element method (ES-FEM) solves the non-linear solid, piecewise linear gradient smoothing method (PL-GSM) is applied to analyze the fluid domain, and distributing the interaction force through the finite element interpolation. Two numerical examples are used to verify the validity of IGSM. Based on the numerical solutions from IGSM, the following remarks can be derived as:

a) The ES-FEM model with triangular elements in structural mechanics is softer than the traditional FEM model. The employment of ES-FEM can provide more accurate solutions without additional parameters or degrees of freedoms than the standard FEM. This is due to the edge-based gradient smoothing operation applied in the ES-FEM producing close-to-exact stiffness in the model.

b) The employment of PL-GSM in the fluid domain is able to provide second

order accuracy in spatial approximation [25]. Furthermore, the implementation of PL-GSM is quite straightforward and easier than the FEM. Hence, the efficiency of PL-GSM is higher than the FEM.

c) The combination of gradient smoothing operation in weak and strong form with distinct feature has successfully solved the complicated fluid structure interaction problem. The comprehensive tests repeatedly prove that the proposed IGSM are remarkably accurate, robust, flexible, efficient, and stable.

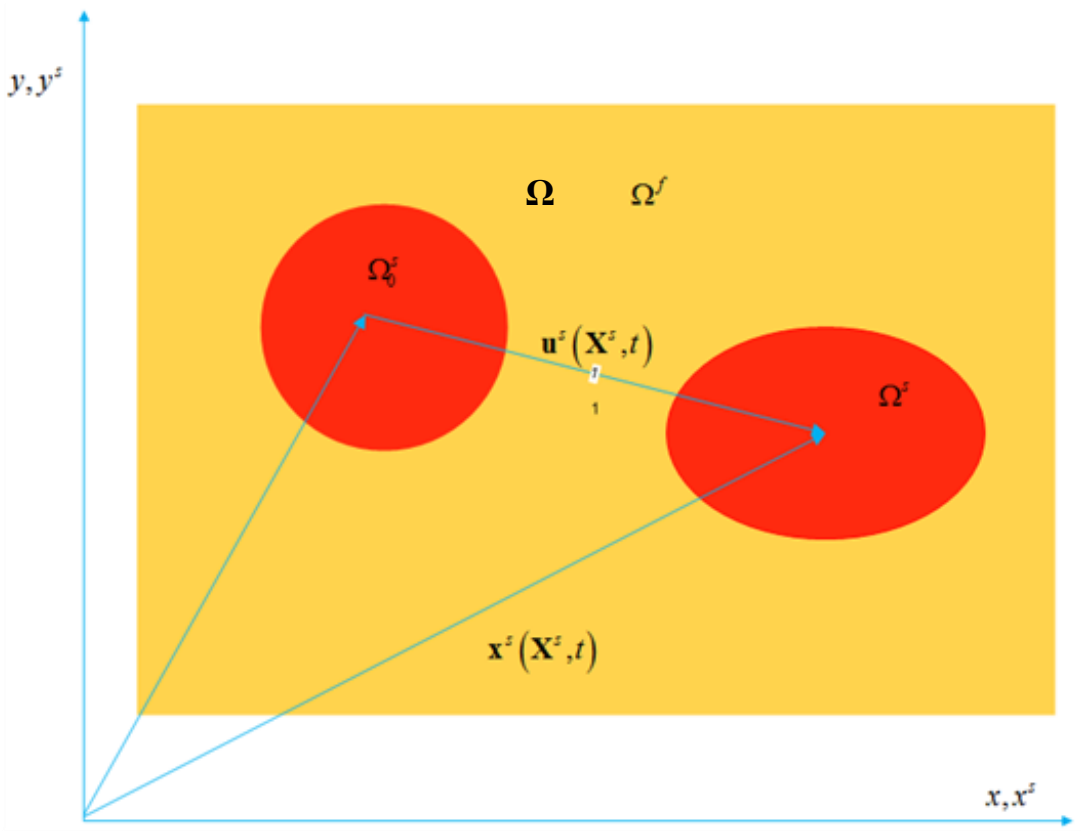

Figure 6.1: The Eulerian coordinates in the computational domain

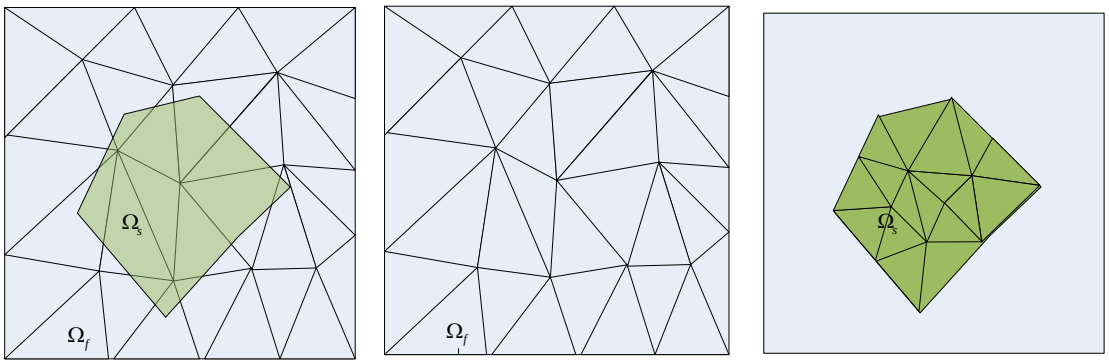

(a) Overlap domain (b) Fluid mesh (c) Solid mesh

Figure 6.2: Illustration of independent mesh for fluid and solid

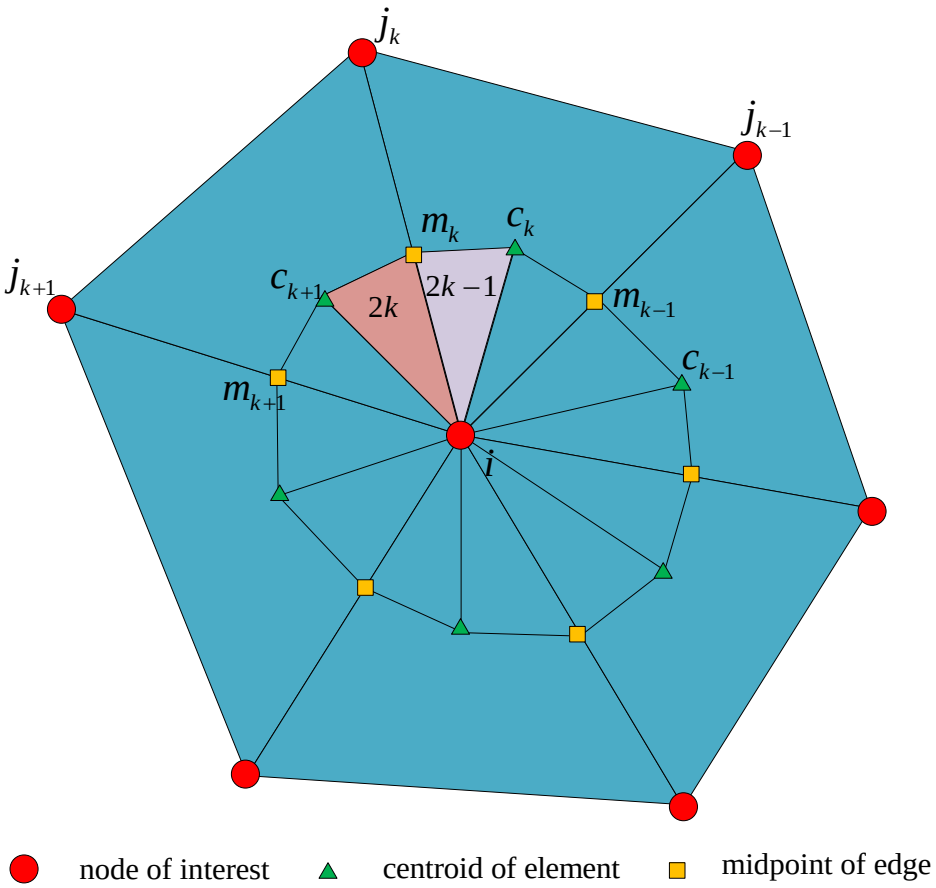

Figure 6.3: Illustration of gradient smoothing domain

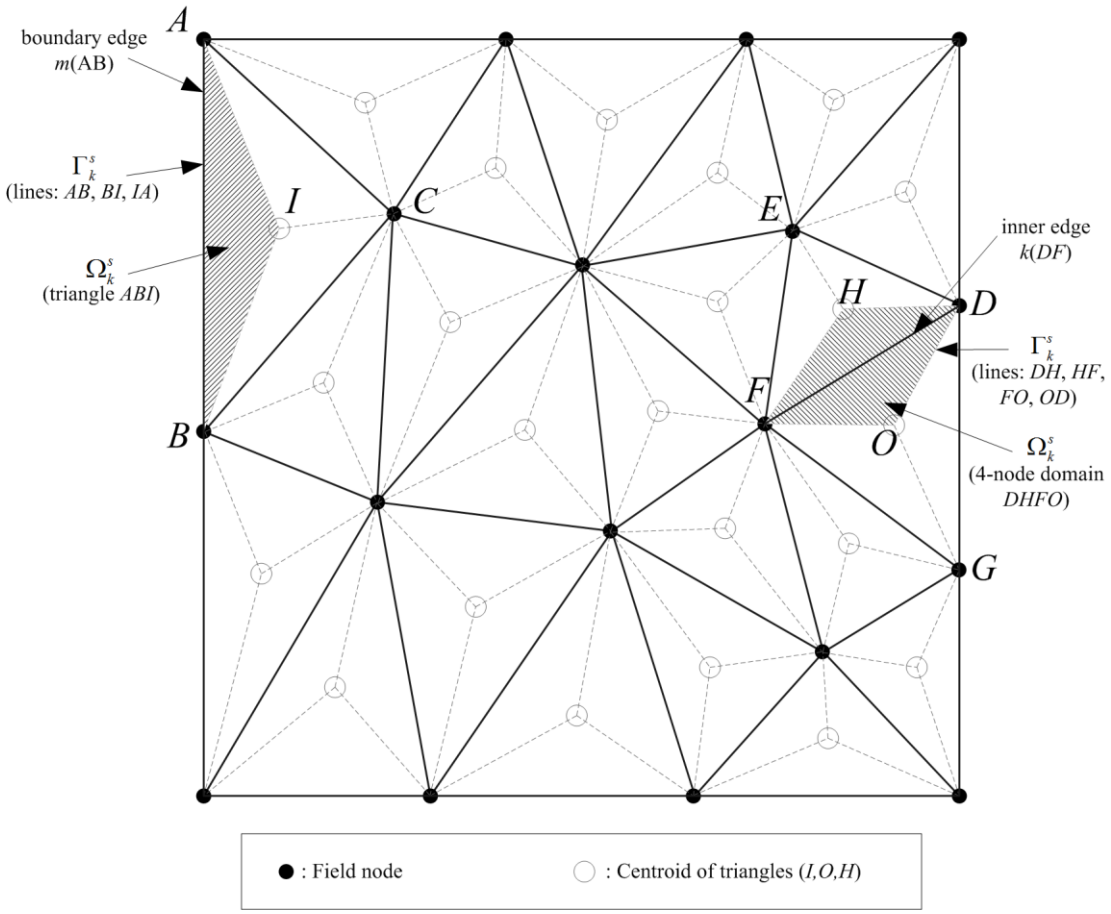

Figure 6.4: Triangular elements and the smoothing domains (shaded areas) associated with edges in ES-FEM

a) Initial status for the fluid and solid

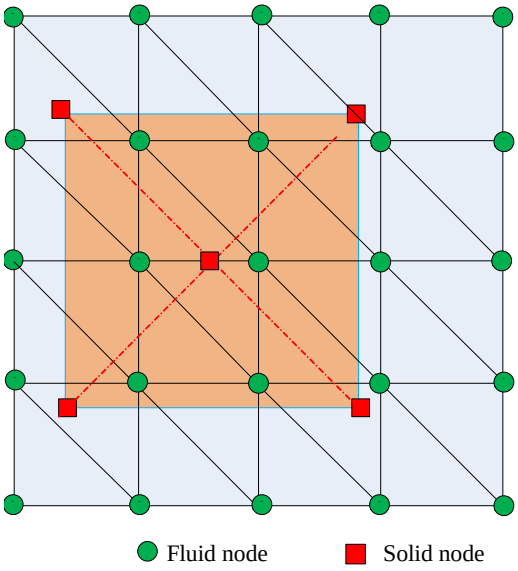

b) Solve interaction force for the solid

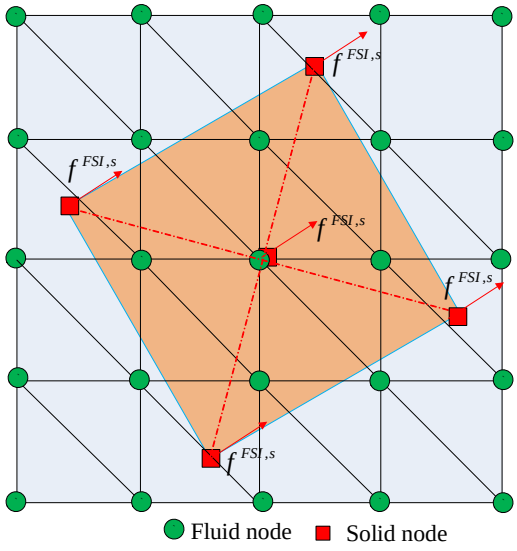

c) Distribute the interaction force to the fluid

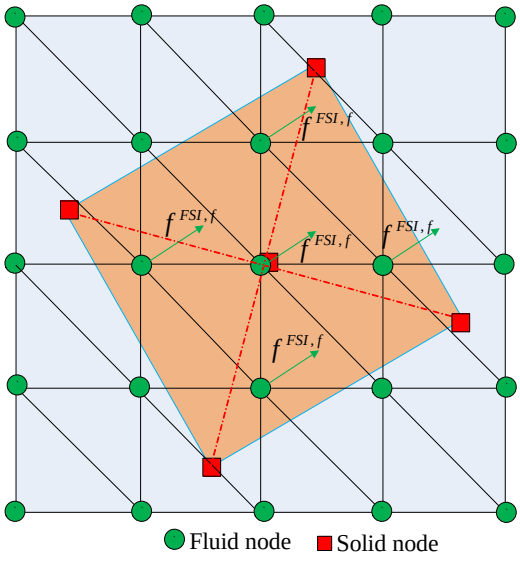

Figure 6.5: Procedure to distribute the interaction force to the fluid domain

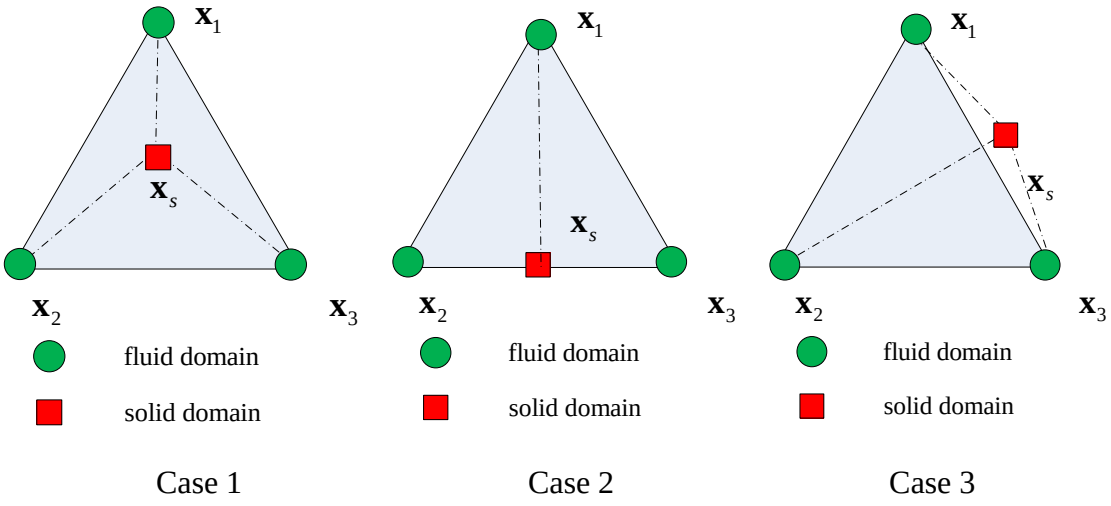

Figure 6.6: Three cases in the searching process

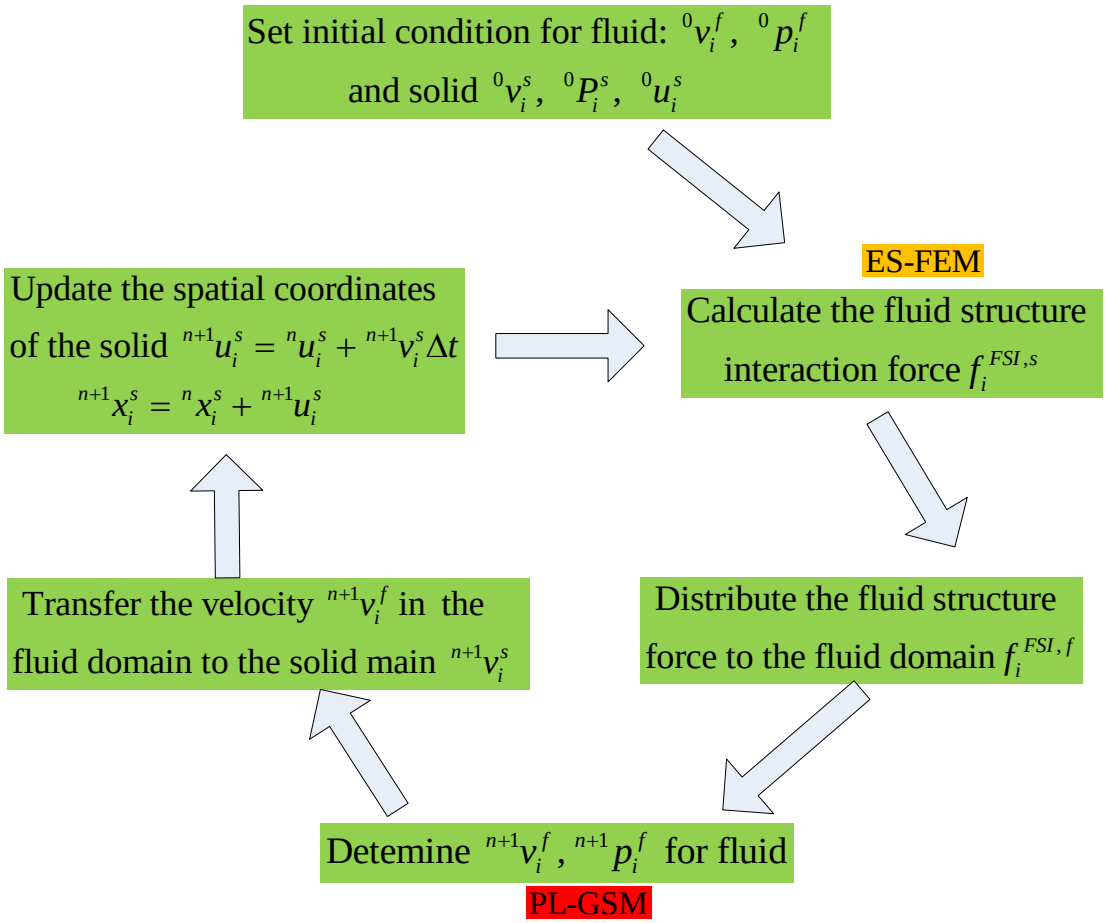

Figure 6.7：Flow chart in the Immersed Gradient Smoothing Method

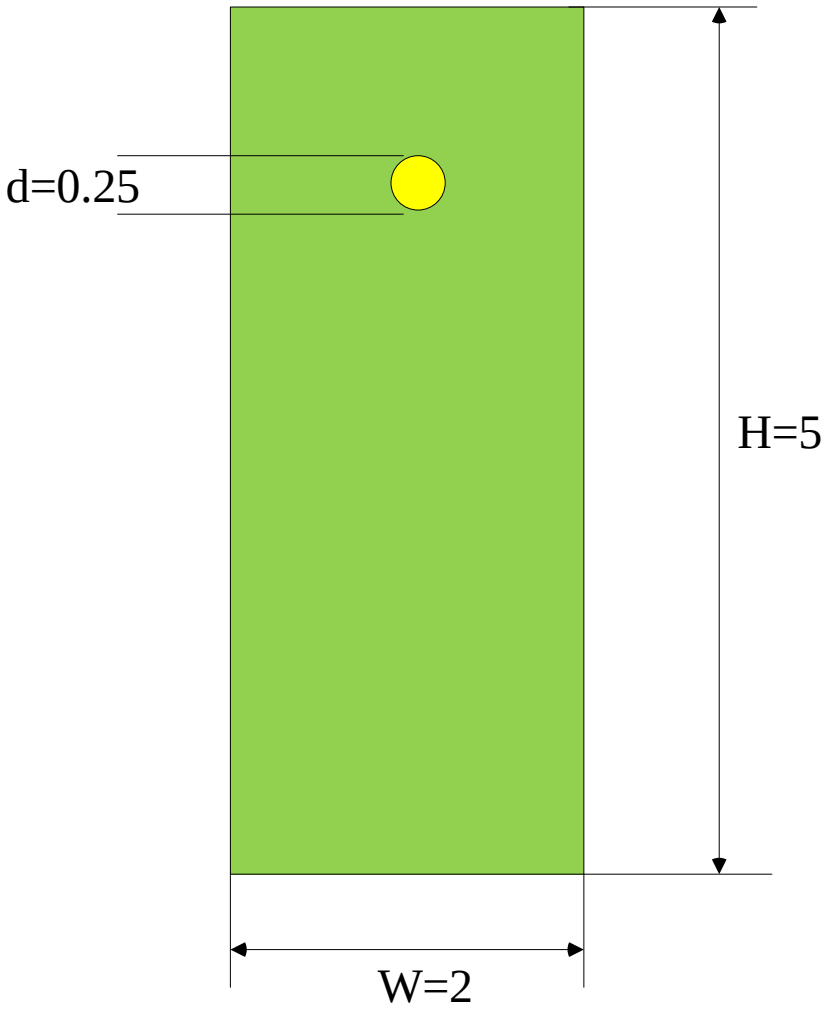

Figure 6.8: A soft disk falling in a viscous fluid (not to scale)

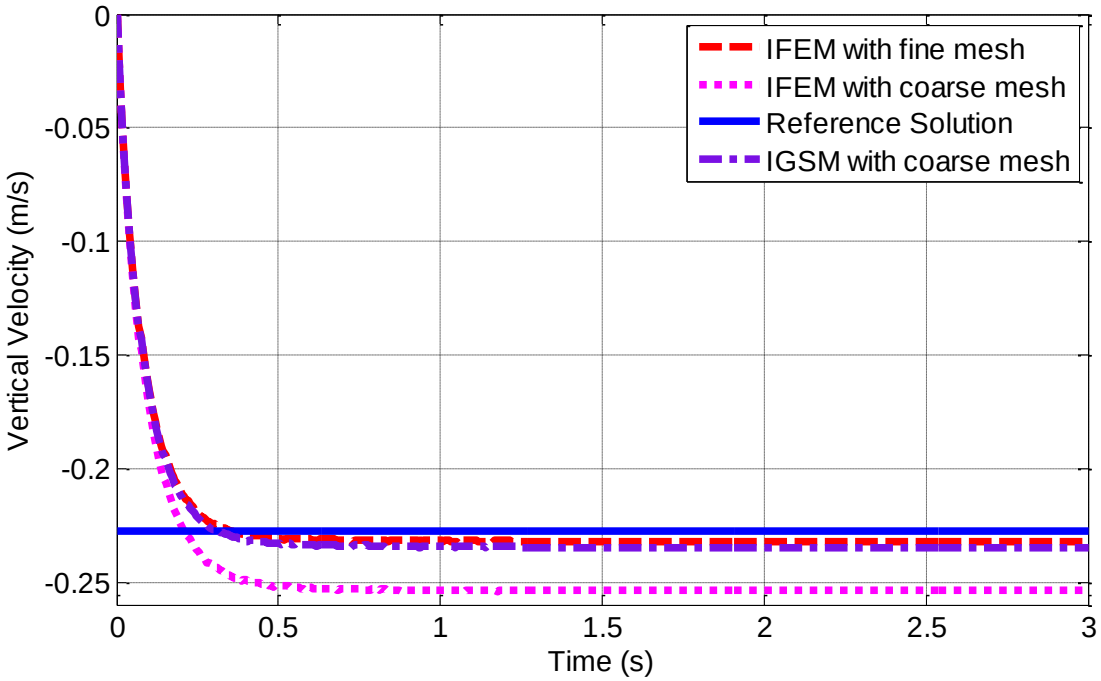

Figure 6.9: Velocity history at μ=0.4

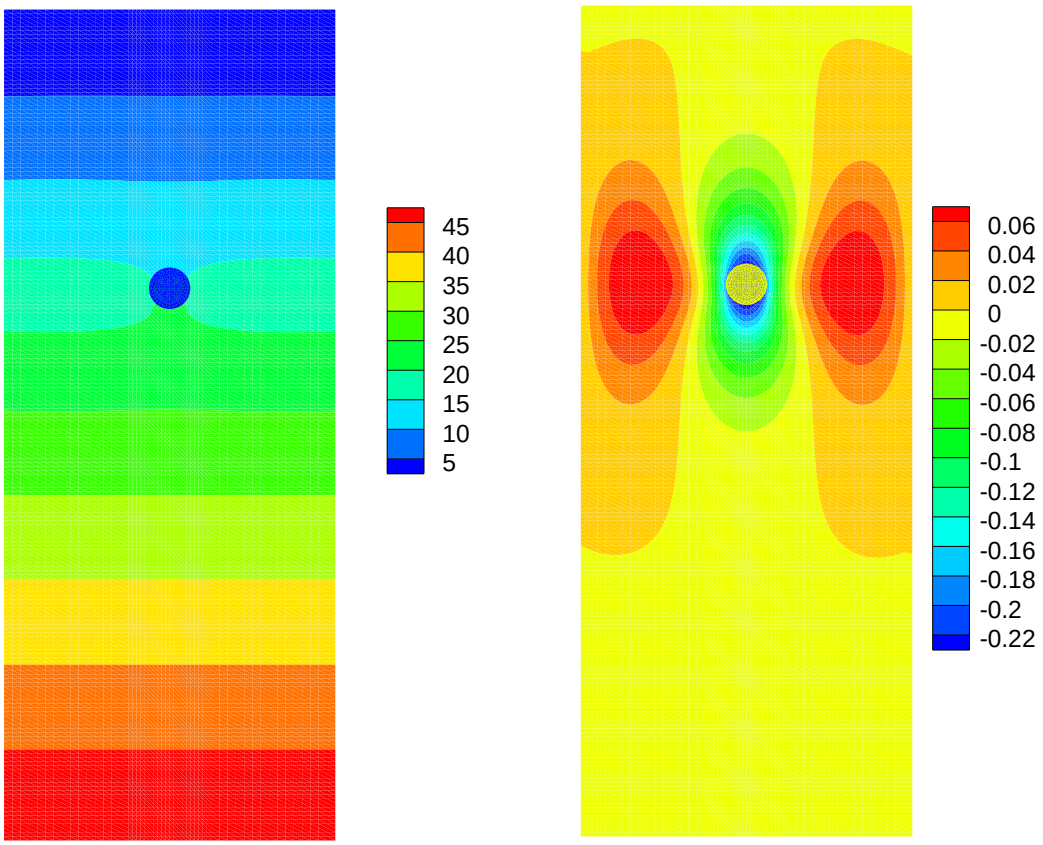

(a) Pressure (b) Vertical Velocity

Figure 6.10: Pressure and vertical velocity contours at the steady state (μ=0.4)

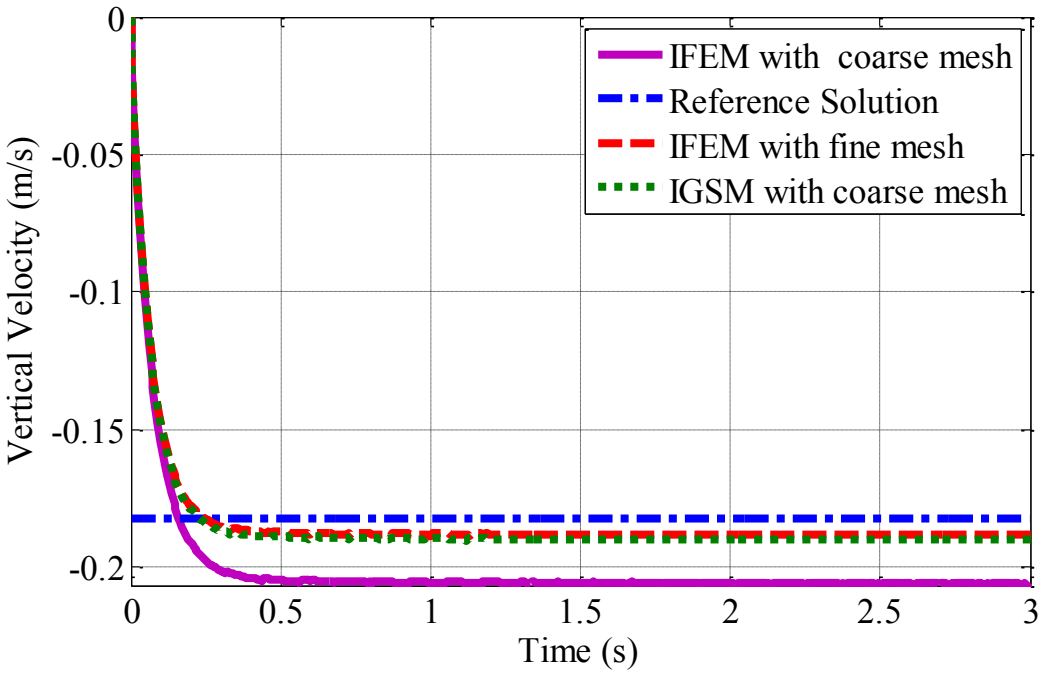

Figure 6.11: Velocity history at μ=0.5

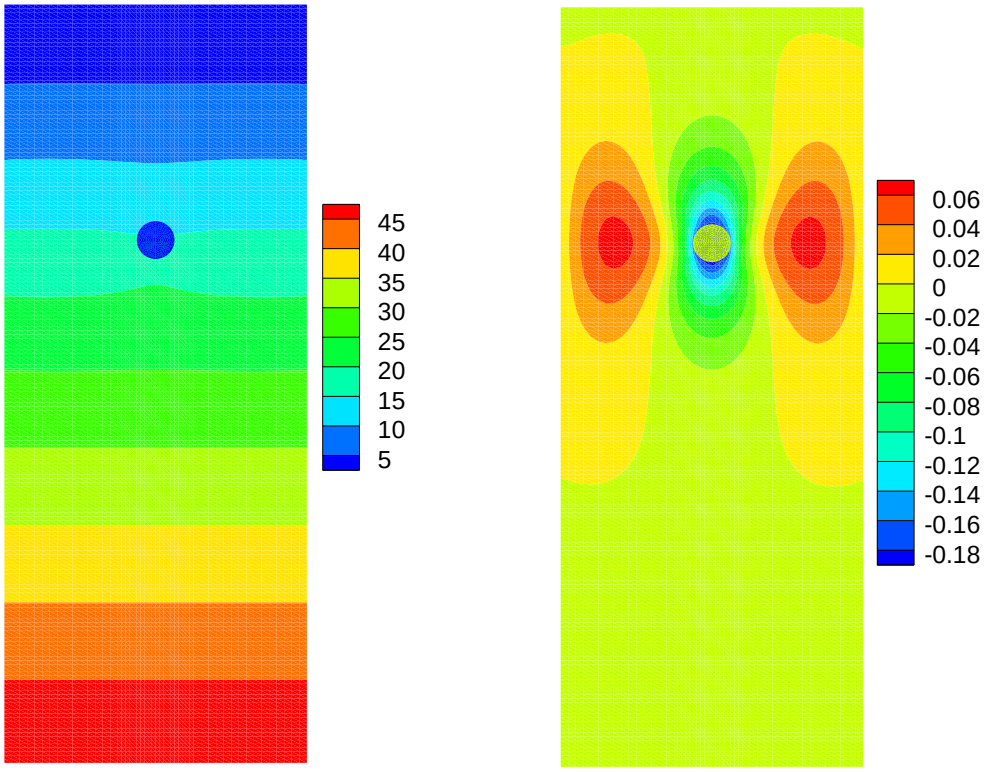

(a) Pressure (b) Vertical Velocity

Figure 6.12: Pressure and vertical velocity contours at the steady state (μ=0.5)

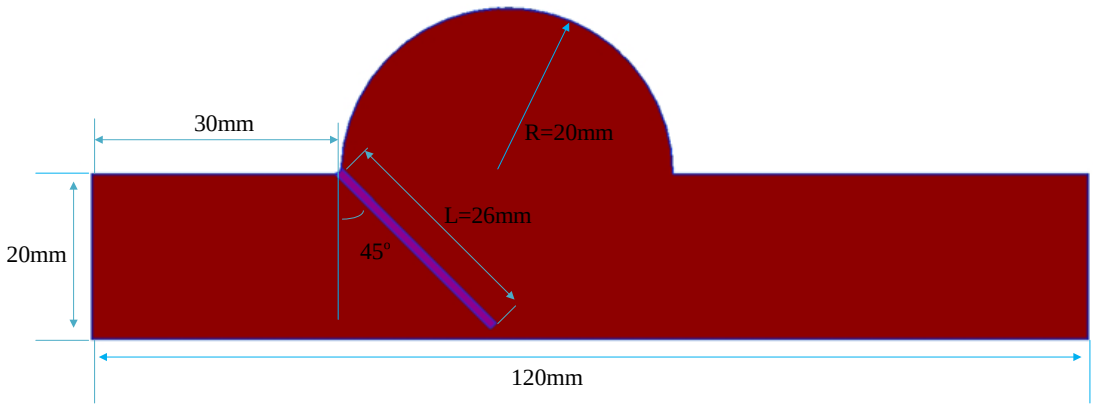

Figure 6.13: Two-dimensional model of aortic valve [130]

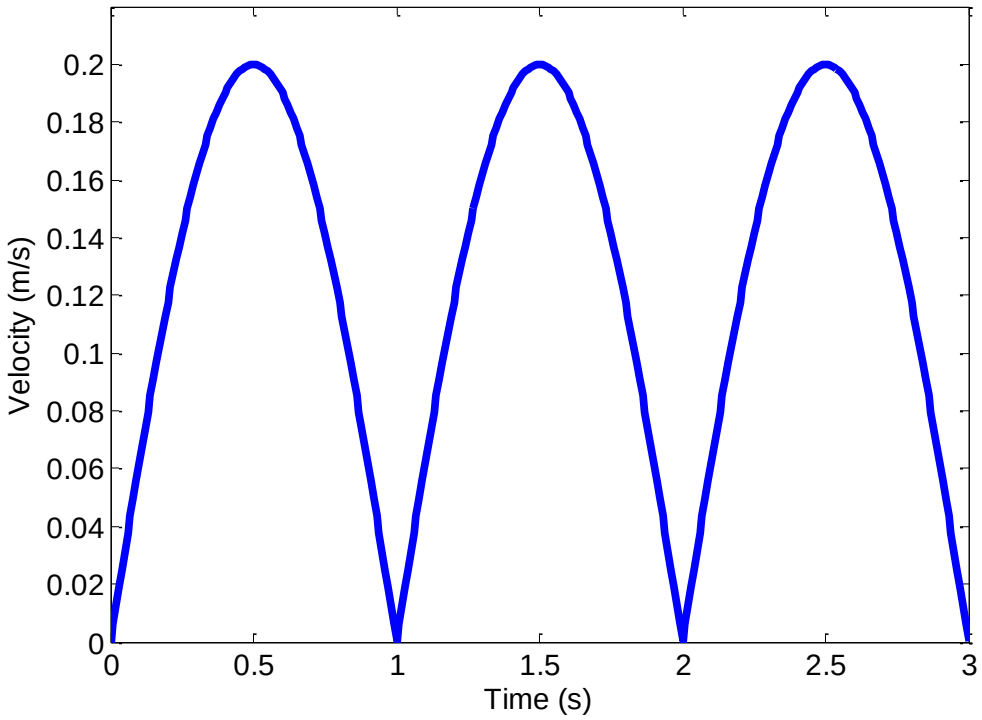

Figure 6.14: Inlet velocity profile

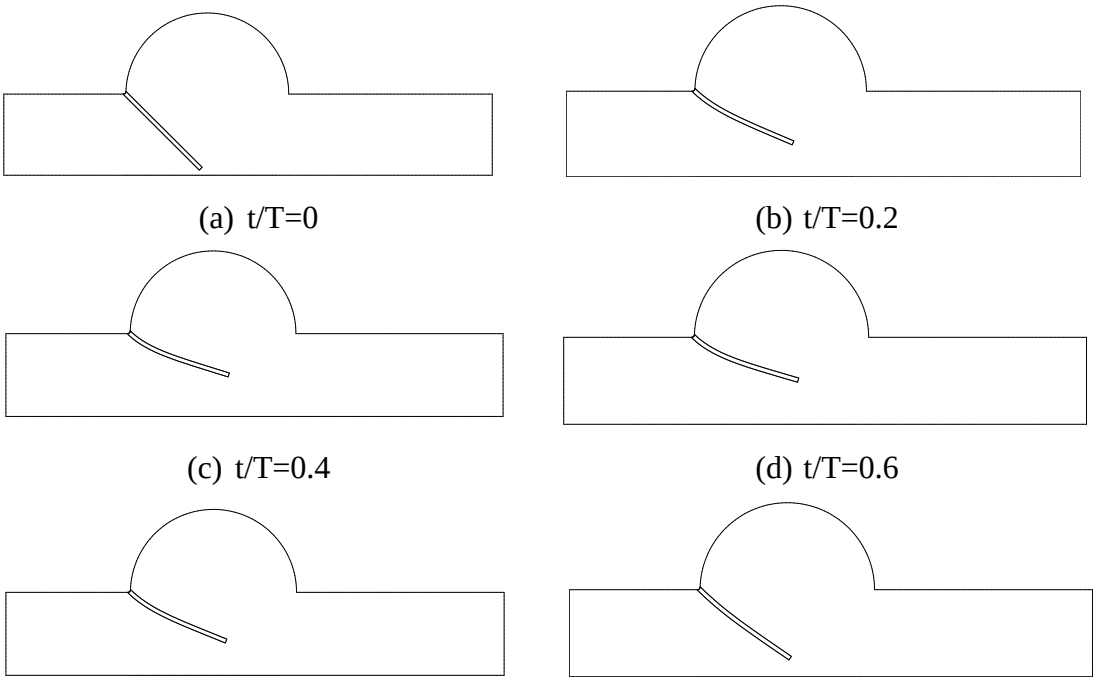

(a) t/T=0 (b) t/T=0.2

(c) t/T=0.4 (d) t/T=0.6

(e) t/T=0.8 (f) t/T=1

Figure 6.15: Leaflet motion and fluid velocity profile

Table 6.1: Fluid and soft disk properties

Fluid Domain	Soft Disk
W=2m, H=5m, R=0.125m	Young Modulus $E = 1.2\times10^4$ N/m^2
Density $\rho_f = 1$ kg/m^3	Density $\rho_s = 3$ kg/m^3
Viscosity μ=0.4 Pa$\cdot$s or μ=0.5 Pa$\cdot$s	Poisson ration $\upsilon = 0.25$

Table 6.2: Material properties

Blood Domain	Leaflet Domain
W=20mm, L=120mm	Poisson Ration $\upsilon = 0.3$
Density ρ_f =1050kg/m^3	Density ρ_s =890kg/m^3
Viscosity μ =0.0033 Pa$\cdot$s	Young Modulus $E = 1.2\times10^4$ N/m^2

Chapter 7

Conclusions and recommendations

7.1 Conclusion remarks

In this thesis, gradient smoothing operations in the weak and strong form have been developed. Some bioengineering models including bioheat transfer in the human eye, hyperthermia treatment in the human breast, phase change in the liver cryosurgery, diseased artery, and heart valve have been established based on the newly developed methods mentioned in this thesis. Through the studies, the following conclusions are drawn:

1) The αFEM is equipped with a scaling factor α that controls the contribution of NS-FEM and FEM. The selection of a good approximation α is still an open topic. Generally, $\alpha \in [0.45{:}0.65]$ for 2D and $\alpha \in [0.60{:}0.80]$ are recommended based on the research experience without mathematical proof. In liver cryosurgery, the αFEM formulation in the fixed grid method captured the interface of solid and liquid more accurately than the standard FEM. The numerical results obtained from FEM using triangular element are poor, especially in the high temperature gradient. Furthermore, the application of αFEM achieves very accurate results compared to the FEM with the same number of degree of freedom in the bioheat transfer in the human eye with very

complicated structure. Additionally, the αFEM model provides a fast, accurate and safe way to detect fever and dry eyes, which can help the doctor to improve the diagnosis and treatment

2) The ES-FEM using the triangular elements in 2D and FS-FEM using tetrahedral elements in 3D are quite stable and accurate in thermal-mechanics models of hyperthermia treatment of human breast compared with the standard FEM. The edge-based smoothed in 2D and face-based in 3D soften the model to achieve 'close to exact' stiffness. Compared with FEM, there are no additional parameters in ES-FEM and FS-FEM. Hence, this method can be implanted in a straightforward way. Thus, the model created by the ES-FEM and FS-FEM is good option to predict the temperature distribution and mechanical response in the hyperthermia treatment of human breast.

3) The PL-GSM using triangular elements in two-dimensional space is very simple; no additional parameters or degrees of freedoms are needed, the system matrices have the same dimensions as the FDM model of same mesh and the method can be implemented in a straightforward way with little change to the FDM code. Compared with the piecewise constant gradient smoothing method (PC-GSM), the PL-GSM is more accurate, stable and not sensitive to distortion of element.

4) The proposed αGSM is a generalized formulation of PL-GSM and PC-GSM. When the $\alpha=0$, the αGSM becomes PL-GSM, when the $\alpha=1$, the GSM is the same as PL-GSM. Although the GSM can achieve more accurate result, the computational time is too high compared with the PC-GSM and PL-GSM.

Hence, the αGSM does not exhibit any outstanding advantages than the PC-GSM and PL-GSM in terms of computational efficiency.

5) The combination of gradient smoothing operations in weak and strong form gave rise to the immersed gradient smoothing method (IGSM) with distinct feature to solve the complicated fluid structure interaction problem successfully. The employment of ES-FEM in the solid model is a good alternative in the large deformation. The PL-GSM applied in the fluid model has reduced the computational cost without losing the computational accuracy. The comprehensive tests repeatedly prove that the proposed IGSM is remarkably accurate, robust, flexible, efficient, and stable.

7.2 Recommendations for future work

Based on the work presented in the thesis, the following aspects are recommended for future research:

(1) Further study is performed to improve the gradient smoothing operation in the weak and strong form. For instance, selection of α in the αFEM is a challenge task through the mathematical theory. Currently, α is just based on research experience and lack of mathematical proof. Furthermore, high-order smoothing functions could be used in the strong form to create more accurate model in the fluid dynamics.

(2) The gradient smoothing operations in the weak and strong form have formulated ES-FEM, αFEM, PL-GSM, αGSM and IGSM. Such methods have

successfully solved the model in the biological systems. It should be extended to the application in more sophisticated bioengineering systems. In addition, development of robust commercial software based on the gradient smoothing operations in the weak and strong form to treat special problems is also an imminent task for research.

(3) It is necessary to develop the IGSM to solve the fluid-structure interaction (FSI) problem in three dimensional domain. Therefore, it is more realistic to apply the IGSM to analyze the interaction behavior in the three dimensional heart valve model. It should be straightforward to extend the 2D IGSM to 3D IGSM.

Bibliography

1. Liu GR, *Meshfree methods: moving beyond the finite element method, 2nd edition*: CRC Press. 2009
2. Zienkiewicz OC and Taylor RL, *The finite element method (5th edition)*: Butterworth Heinemann, Oxford, UK. 2000
3. Pian THH and Wu CC, *Hybrid and Incompatible Finite Element Methods*: CRC Press: Boca Raton. 2006
4. Quarteroni A and Valli A, *Numerical Approximation of Partial Differential Equations*: Springer: Berlin. 1994
5. Chen JS, Wu CT, Yoon S, and You Y, A stabilized conforming nodal integration for Galerkin meshfree method. *International Journal for Numerical Methods in Engineering* **50**: p. 435-466. 2000
6. Yoo JW, Moran B, and Chen JS, Stabilized conforming nodal integration in the natural-element method. *International Journal for Numerical Methods in Engineering*(60): p. 861-890. 2004
7. Liu GR, Nguyen TT, Nguyen XH, and Lam KY, A node-based smoothed finite element method (NS-FEM) for upper bound solutions to solid mechanics problems. *Computers and Structures*. **87**: p. 14-26. 2009
8. Liu GR, Nguyen TT, and Lam KY, A novel alpha finite element method (alpha FEM) for exact solution to mechanics problems using triangular and tetrahedral elements. *Computer Methods in Applied Mechanics and Engineering*. **197**: p. 3883-3897. 2008

9. Eric Li, Liu GR, Vincent Tan, and He ZC, Modeling and simulation of bioheat transfer in the human eye using the 3D alpha finite element method (αFEM). *Intentional Journal for Numerical Methods in Biomedical Engineering*. **26**: p. 955–976. 2010

10. Eric Li, Liu GR, Vincent Tan, and He ZC, An efficient algorithm for phase change problem in tumor treatment using αFEM. *International Journal of Thermal Sciences*. **49**(10): p. 1954-1967. 2010

11. Liu GR, Nguyen TT, and Lam KY, An edge-based smoothed finite element method (E-SFEM) for static and dynamic problems of solid mechanics. *Journal of Sound and Vibration*. **320**: p. 1100–1130. 2009

12. Eric Li, Liu GR, Vincent Tan, and He ZC, Simulation of Hyperthermia Treatment Using the Edge-Based Smoothed Finite-Element Method. *Numerical Heat Transfer, Part A: Applications*. **57**(11): p. 822 -847. 2010

13. Nguyen TT, Liu GR, Lam KY, and Zhang GY, A face-based smoothed finite element method (FS-FEM) for 3D linear and nonlinear solid mechanics problems using 4-node tetrahedral elements. *International Journal for Numerical Methods in Engineering*. **78**: p. 324-353. 2009

14. Trannehill JC, Anderson DA, and Pletcher RH, *Computational Fluid Mechanics and Heat Transfer*: Taylors & Francis, 2nd edition. 1997

15. Thompson JF, Soni BK, and Weatherill NP, *Handbook of grid Generation*: CRC Press. 1999

16. Ferziger JH and Peric M, *Computational Methods for Fluid Dynamics, 3rd edition*: Springer. 2002

17. Hoffmann KA and Chiang ST, *Computational Fluid Dynamics for Engineers, volume I and II*: Engineering Education System: Austin, Texus. 1993

18. Lucy LB, A numerical approach to testing of the fission hypothesis. *The Astronomical Journal*. **8**(12): p. 1013-1024. 1977

19. Gingold RA and Moraghan JJ, Smooth particle hydronamics: theory and applications to non-spherical stars. *Royal Astronomical Society, Monthly Notices*. **181**: p. 375-389. 1977

20. Zhang X, Song KZ, Lu MW, and Liu X, Meshless methods based on collocation with radial basis functions. *Computational Mechanics*. **26**(4): p. 333-343. 2000

21. Kee BBT, Liu GR, and Lu C, A stabilized least-squares radial point collocation method (LS-RPCM) for adaptive analysis. *Engineering Analysis with Boundary Elements*. **32**: p. 440–460. 2008

22. Liu GR and Gu YT, *An introduction to Mesh free Methods and their Porgramming*: Springer, Dordrecht, the Netherlands. 2005

23. Kee BBT, Liu GR, and Lu C, A generalized least-squares radial point collocation method (RLS-RPCM) for adaptive analysis. *Computational mechanics*. **40**: p. 837-853. 2007

24. Liu GR and Xu XG, A gradient smoothing method (GSM) for fluid dynamics problems. *International Journal for Numerical Methods in Fluids*. **58**: p. 1101–1133. 2008

25. Fletcher CAJ, *Computational Techniques for Fluid Dynamics, volume I and II, 2nd edition*: Springer-Verlag. 1991

26. Eric Li, Vincent Tan, Xu XGG, Liu GR, and He ZC, A novel linearly-weighted gradient smoothing method (LWGSM) in the simulation of fluid dynamics problem. *Computers and Fluids* **50**: p. 104-119

27. Eric Li, Vincent Tan, Xu XGG, Liu GR, and He ZC, A novel alpha gradient smoothing method (αGSM) for fluid problems. Submiited to Numerical Heat Transfer, Part A Application (Accepted)

28. Xu GX, Liu GR, and Tani A, An adaptive gradient smoothing method (GSM) for fluid dynamics problems. *International Journal for Numerical Methods in Fluids*. **62**: p. 499-529. 2010

29. Liu WK, *Development of finite-element procedures for fluid-structure interaction*: Pasadena, California. PhD. Thesis. 1981

30. Liu WK and Ma DC, Computer implementation aspects for fluid-structure interaction problems. *Computer Methods in Applied Mechanics and Engineering* **31**: p. 129-148. 1982

31. Huertra A and Liu WK, Viscous flow with large free surface motion. *Computer Methods in Applied Mechanics and Engineering* **69**: p. 277-324. 1988

32. Peskin CS, Numerical-Analysis of Blood-Flow in Heart. *Journal of Computational Physics* **25**: p. 220-252. 1977

33. Perskin CS, Flow patterns around heart valves: a numerical method. *Journal of Computational Physics* **10**: p. 252-270. 1972

34. Peskin CS, The immersed boundary method. *Acta Numerica*. **11**: p. 479-517. 2002

35. Mohd YJ, *Combined Immersed-Boundary/B-Spline Methods for Simulations of Flow in Complex Geometries*: Ctr Annual Research Briefs,NASA Ames Research Center/Stanford Univ. Center for Turbulence Research, Stanford, CA. 1997

36. Zhang L and Gay M, Immersed finite element method for fluid-structure interaction. *Journal of Fluids and Structures* **23**: p. 839-857. 2007

37. Liu WK, Immersed Finite Element Method and Its Applications to Biological Systems. *Computer Methods in Applied Mechanics and Engineering* **195**: p. 1722-1749. 2006

38. Zhang L, Gerstenberger A, Wang X, and Liu WK, Immersed Finite Element Method. *Computer Methods in Applied Mechanics and Engineering* **193**: p. 2051-2067. 2004

39. Wang X and Liu WK, Extended immersed boundary method using FEM and RKPM. *Computer Methods in Applied Mechanics and Engineering* **193**: p. 1305-1321. 2004

40. Eric Li, Vincent Tan, Xu XGG, Liu GR, and He ZC, Immerse Gradient Smoothing Method for Fluid-Structure Interaction Problems. Submitted to Journal of Fluids Engineering

41. Hughes TJR, Franca LP, and Balestra M, A new finite element formulation for computational fluid dynamics: V. Circumventing the babuška-brezzi condition: a stable Petrov-Galerkin formulation of the stokes problem accommodating equal-order interpolations. *Computer Methods in Applied Mechanics and Engineering* **59**: p. 85-99. 1986

42. Tezduyar TE, Behr M, Mittal S, and Liou J, A New Strategy for Finite-Element Computations Involving Moving Boundaries and Interfaces - the Deforming-Spatial-Domain Space-Time Procedure .1. The Concept and the Preliminary Numerical Tests. *Computer Methods in Applied Mechanics and Engineering* **94**: p. 339-351. 1992

43. Brooks AN and Hughes TJR, Streamline Upwind Petrov-Galerkin Formulations for Convection Dominated Flows with Particular Emphasis on the Incompressible Navier-Stokes Equations. *Computer Methods in Applied Mechanics and Engineering* **32**: p. 199-259. 1982

44. Tezduyar TE, Mittal S, Ray SE, and Shih R, Incompressible-Flow Computations with Stabilized Bilinear and Linear Equal-Order-Interpolation Velocity-Pressure Elements. *Computer Methods in Applied Mechanics and Engineering* **95**: p. 221-242. 1992

45. Baiocchi C, Brezzi F, and Franca L, Virtual bubbles and the Galerkin/least-squares method. *Compueter Methods in Applied Mechanics and Engineering*. **105**(1): p. 125-141. 1993

46. Zienkiewicz OC, Nithiarasu P, Codina R, M. V, and Ortiz P, The Characteristic-Based-Split Procedure: An Efficient and Accurate Algorithm for Fluid Problems. *International Journal for Numerical Methods in Fluids* **31**: p. 359-392. 1999

47. Blzaek J, *Computational Fluid Dynamics: Principles and Application*: ELSE-VIER Press, Oxford, first edition. 2001

48. Barth TJ, *Numerical Methods for Conservation Laws on Structured and Unstructured Grids*: VKI Lecture Series in CFD course 2003, Von Karman Institute. 2003

49. Stauffer PR and Goldberg SN, Introduction: Thermal ablation therapy. *International Journal of Hyperthermia*. **20**: p. 671-677. 2004

50. Tang X, Dai W, Nassar R, and Bejan A, Optimal Temperature Distribution in a Three-Dimensional Triple-Layered Skin Structure Embedded with Artery and Vein Vasculature. *Numerical Heat Transfer: Part A Applications* **50**: p. 809-834. 2006

51. He Y, Shirazaki M, Liu H, Himeno R, and Sun ZA, A Numerical Coupling Model to analyze the Blood Flow, Temperature, and oxygen Transport in Human Breast Tumor under Laser Irradiation. *Computers in Biology and Medicine*. **36**: p. 1336-1350. 2006

52. Arora D, Skliar M, and Roemer RB, model-predictive control of hyperthermia treatments. *IEEE Transactions on Biomedical Engineering*. **49**: p. 629-639. 2002

53. Field SB and Hand JW, *An introduction to the practical Aspects of Hyperthermia*: New York: Taylor & Francis. 1990

54. Diederich CJ, Thermal ablation and high-temperature thermal therapy: Overiew of technology and clinical implementation. *International Journal of Hyperthermia*. **21**: p. 745-753. 2005

55. Shih TC, Yuan P, Lin WL, and Kou HS, Analytical analysis of the Pennes bioheat transfer equation with sinusoidal heat flux condition on skin surface. *Medical Engineering & Physics* **27**: p. 946-953. 2007

56. Shen WS, Zhang J, and Yang FQ, *Modeling and numerical simulation of bioheat transfer and biomechanics in soft tissue*: Technical Report No. 391-04, Department of Computer Science, University of Kentucky, Lexington, KY. 2004

57. Dai W, Yu H, and Nassar R, A fourth-order compact finite-difference scheme for solving a 1-D Pennes' bioheat transfer equation in a triple-layered skin structure. *Numerical Heat Transfer, Part B Fundamentals*. **46**(5): p. 447-461. 2004

58. Zhao JJ, J. Z, Kang N, and Yang FQ, A two level finite difference scheme for one dimensional Pennes's bioheat equation. *Applied Mathematics and Computation* **171**: p. 320-331. 2005

59. Torvi DA and Dale JD, A Finite Element Model of Skin Subjected to a Flash Fire. *Journal of Biomechanical Engineering*. **116**: p. 250-255. 1994

60. Haghighi MRG, Eghtesad M, and Malekzadeh P, A couple differential quadrature and finite element method for 3-D transient heat transfer analysis of functionally graded thick plates. *Numerical Heat Transfer, Part B Fundamentals*. **53**(4): p. 358-373. 2008

61. Dai W and Nassar R, A hybrid finite element-finite difference method for solving three-dimensional heat transport equations in a double-layered thin film with microscale thickness. *Numerical Heat Transfer, Part A Applications*. **38**(6): p. 573-588. 2000

62. Ruan LM, An W, Tan HP, and Qi H, Least-squares finite-element method of multidimensional radiative heat transfer in absorbing and scattering media. *Numerical Heat Transfer, Part A Applications*. **51**(7): p. 657-677. 2007

63. Liu GR, *Mesh Free Methods: Moving beyond the Finite Element Method*: CRC Press. 2002

64. Wissler EH, Pennes' 1948 paper revisited. *Journal of Applied Physiology*. **85**: p. 35-41. 1998

65. Liu GR, A generalized gradient smoothing technique and the smoothed bilinear form for Galerkin formulation of a wide class of computational methods. *International journal for numerical methods in engineering*. **5**: p. 199-236. 2008

66. Osman MM and Afify EM, Thermal Modeling of the Normal Woman's Breast. *Journal of Biomechanics* **106**: p. 123-130. 1984

67. Osman MM and Afify EM, Thermal Modeling of Malignant Woman's Breast. *Journal of Biomechanics* **110**: p. 269-276. 1988

68. Kumaradas JC and Sherar MD, Edge-element based finite element analysis of microwave hyperthermia treatments for superficial tumors on the chest wall. *International Journal of Hyperthermia*. **19**(4): p. 414-430. 2003

69. Karaa S, Zhang J, and Yang FQ, A numerical study of a 3D bioheat transfer problem with different spatial heating. *Applied Mathematics and Computation* **68**: p. 375–388. 2005

70. Lewis RW, Morgan K, Thomas HR, and Seetharamu KN, *The Finite Element Method in Heat Transfer Analysis*: WILEY. 1996

71. Chua KJ, Chou SK, and Ho JC, An analytical study on the thermal effects of cryosurgery on selective cell destruction. *Journal of Biomechanics* **40**: p. 100-116. 2007

72. Stanczyk M and Telega JJ, Thermal problems in biomechanics-a review. Part III. Cryosurgery, cryopreservation and cryosurgery. *Acta of Bioengineering and biomechanics*. **5**. 2003

73. Bischof JC, Micro and nanoscale phenomenon in bioheat transfer. *International Journal of Heat and Mass Transfer* **42**: p. 955-966. 2006

74. Andrew AG and John B, REVIEW Mechanism of Tissue Injury in Cryosurgery. *Cryobiology*. **37**: p. 171-186. 1998

75. Cooper IS, Cryosurgery as viewed by the surgeon. *Cryobiology*. **1**: p. 44-54. 1964

76. Gill W and Long W, A critical look at cryosurgery. *International Surgery* **56**: p. 344-351. 1971

77. Chandler J, Cryosurgery for recurrent carcinoma of the oral cavity. *Arch Otolaryngol*. **97**: p. 319-321. 1973

78. Minkowycz WJ and Sparrow EM, *Advanced in numerical heat transfer. Volume III*: Taylor & Francis Group. 2009

79. Deng ZS LJ, Numerical simulation of 3-D freezing and heating problems for combined cryosurgery and hyperthermia therapy. *Numerical heat transfer, Part A: Applications*. **46**(6): p. 587-611. 2004

80. Kumar S and Katiyar VK, Numerical study on phase change heat transfer during combined hyperthermia and cryosurgical treatment of lung cancer. *International Journal of Applied Mathematics and Mechanics*. **3**(3): p. 1-17. 2007

81. Zhang YT and Liu J, Numerical study in three-region thawing problem during cryosurgical re-warming. *Medical Engineering & Physics* **24**: p. 265-277. 2002

82. Sergio RI and Mario A, Numerical methods in phase change problems. *Archives of Computational Methods in Engineering*. **1**: p. 49-74. 1994

83. Dalhuijsen AJ and A S, Comparison of finite element techniques for solidification problems. *International Journal for Numerical Methods in Engineering*. **23**: p. 1807-1829. 1986

84. Clavier L, Arquis E, and Caltagirone JP, A fixed grid method for the numerical solution of phase change problems. *International Journal for Numerical Methods in Engineering* **37**: p. 4247-4261. 1994

85. Lewis RW and Roberts PM, Finite element simulation of solidification problems. *Applied Scientific Research*. **44**: p. 61-92. 1987

86. Zienkiewicz OC, Parekh CJ, and Wills AJ, The application of finite elements to heat conduction problems involving latent heat. *Rock Mechanics*. **5**: p. 65-76. 1973

87. Crivelli LA and Idelsohn SR, A temperature-based finite element solution for phase change problems. *International Journal for Numerical Methods in Engineering*. **23**: p. 99-119. 1986

88. Krabbenhoft K, Damkide L, and Nazem M, An implicit mixted enthalpy-temperature method for phase change problems. *International Journal of Heat and Mass Transfer* **43**: p. 233-241. 2007

89. Voller VR, Swaminathan CR, and Thomas BG, Fixed grid techniques for phase change problems: A Review. *International Journal for Numerical Methods in Engineering*. **30**: p. 875-898. 1990

90. Zhao P, Heinrich JC, and Poirier DR, Fixed mesh front-tracking methodology for finite element simulations. *International Journal for Numerical Methods in Engineering*. **61**: p. 928-948. 2004

91. Belytschko T, Lu YY, and Gu L, Element-free Galerkin method. *International journal for numerical methods in engineering*. **37**(2): p. 229-256. 1994

92. Atluri SN and Shen SP, *The meshless local Petrov-Galerkin (MLPG) Method*: Tech Science Press, Balboa Blvd, USA. 2002

93. Liu WK, Jun S, and Zhang YF, Reproducing kernel particle methods. *International Journal for Numerical Methods in Fluids* **20**(8-9): p. 1081-1106. 1995

94. Arkin H, Xu LX, and Holmes KR, Recent developments in modeling heat transfer in blood perfused tissues. *IEEE Transactions on Biomedical Engineering*. **41**: p. 97-100. 1994

95. Necati OM, *Heat conduction*: John Wiley & Sons. 1993

96. Banaszek J, comparison of control volume and Galerkin finite element methods for diffusion-type problems. *Numerical Heat Transfer, Part B: Fundamentals*. **16**: p. 59-78. 1989

97. Rank E, Katz C, and Werner H, On the importance of the discrete maximum principle in transient analysis using finite element methods. *International Journal for Numerical Methods in Engineering*. **19**: p. 1771-1782. 1983

98. Macqueene JW, Akau RL, Krutz GW, and Schoenhals RJ, Numerical mcthods and measurements related to weldingprocesses, in R. W. Lewis, K. Morgan

and B. A. Schrefkr (eds), Numerical Methods in Thermal Problems (Proc.Conf.), Venice, July 1981, Pineridge Press. Swansea. p. 153-167. 1981

99. Giudice SD, Comini G, and Lewis RWFesofpis, Finite element simulation of freezing process in soils. *International Journal for Numerical and Analytical Methods in Geomechanics*. **2**: p. 223-235. 1978

100. Lees M, A linear three-level difference scheme for quasi-linear parabolic equation. *Mathematics of Computation*. **20**: p. 516-522. 1966

101. Thomas BG, Samarasekera IV, and Brimacombe JK, Comparison of numerical modeling techniques for complex two-dimensional, transient heat-conduction problems. *Metallurgical and Materials Transactions B* **15**: p. 307-318. 1984

102. Ng EYK and Ooi EH, FEM simulation of the eye structure with bioheat analysis. *Computer Methods and Programs in Biomedicine* **82**: p. 268-276. 2006

103. Tharp HS and Roemer RB, Optimal power deposition with finite-sized, planar hyperthermia applicator arrays. *IEEE Transactions on Biomedical Engineering*. **39**: p. 569-579. 1992

104. Kowalski ME and Jin JM, Model-order reduction of nonlinear models of electromagnetic phased-array hyperthermia. *IEEE Transactions on Biomedical Engineering*. **50**: p. 1243-1254. 2003

105. Scott JA, A finite element model of heat transport in the human eye. *Physics in Medicine and Biology*. **33**(2): p. 227-241. 1988

106. Rimantas B, Antanas G, Tomas V, and Giedrius B, Finite element modeling of cooled-tip probe radiofrequency ablation processes in liver tissue. *Computers in Biology and Medicine*. **38**: p. 694-708. 2008

107. Liu GR and Liu MB, *Smoothed Particle Hydrodynamics-A Meshfree Particle Method*: World Scientific: Singapore. 2003

108. Chen JS YS, Wu CT, Non-linear version of stabilized conforming nodal integration for galekin mesh-free methods. *International Journal for Numerical Methods in Engineering* **53**: p. 2587-2615. 2002

109. Stillinger DK, Stillinger FH, Torquato S, Truskett TM, and Debenedetti PG, Triangle distribution and equation of state for classical rigid disks. *Journal of Statistical Physics*. **100**(1–2): p. 49–71. 2000

110. Patankar SV, *Numerical Heat Transfer and Fluid Flow*: McGraw-Hill: New York. 1980

111. Roe PL, Approximate Riemann solvers, parameter vectors, and difference schemes. *Journal of Computational Physics* **43**: p. 357-382. 1981

112. Barth TJ and Jespersen DC, The design and application of upwind schemes on unstructured grids. *AIAA paper* **89**(89-0366): p. 1-12. 1989

113. Whitfield DL and Taylor LK, *Numerical Solution of the Two-Dimensional Time-Dependent Incompressible Euler Equations*: NASA-CR-195775. 1994

114. Shin S, *Reynolds-Averaged Navier-Stokes Computation of Tip Clearance Flow in a compressor Cascade using an unstructured Grid*: PhD Thesis, Virginia Polytechnic Institute and State University. 2001

115. Arnone A, Liou MS, and Provinelli LA, Multigrid time-accurate integration of Navier-Stokes equations. *AIAA Paper 93-3361CP*. 1993

116. Melson ND, Sanetrik MD, and Atkins HL, Time-accurate Navier-Stokes calculations with multigrid acceleration. *6th Copper Mountain Conf. on Multigrid Methods*: p. 423-439. 1993

117. Kwak D, Chang JLC, Shanks SP, and Chakravarthy SK, A three-dimensional incompressible Navier-Stokes solver using primitive variables. *AIAA Journal*. **24**: p. 390-396. 1986

118. Ghia U, Ghia KN, and Shin CT, Journal of Computational Physics *High-Re solutions for incompressible flow using the Navier-Stokes equations and a multigrid method*. **3**: p. 217-231. 1982

119. Armaly BF, Durst F, Pereira JCF, and Schonung B, Experimental and theoretical investigation of backward-facing step flow. *The Journal of Fluid Mechanics*. **127**: p. 473-496. 1982

120. B.N. J, A least-squares finite element method for incompressible Navier Stokes problems. *International Journal for Numerical Methods in Fluids*. **14**: p. 843-859. 1992

121. Song CX, Liu GR, Li H, and Xu GX, A Meshfree smoothed least-squares (SLS) method for simulating steady incompressible viscous flows. *International Journal for Numerical Methods in Fluids (submitted)*.

122. Zhao SZ, Xu XY, and Collins MW, The numerical analysis of fluid-solid interactions for blood flow in arterial structures, Part 1: a review of models for

arterial wall behavior. *Proceedings of the Institution of Mechanical Engineers - Part H: Journal of Engineering in Medicine*. **212**: p. 39-59. 1998

123. Milos K, Nenad F, Boban S, and Nikola K, *Computer Modeling in bioengineering, Theoretical background, examples and Software*: Willey:England. 2008

124. Chorin AJ, A numerical method for solving incompressible viscous flow problem. *Journal of Computational Physics* **2**: p. 203-223. 1997

125. Venkatakrishnan V, Convergence to steady-state solutions of the euler equations on unstructured grids with limiters. *Journal of Computational Physics* **118**: p. 120-130. 1995

126. Zhang ZQ and Liu GR, Temporal stabilization of the node-based smoothed finite element (NS-FEM) and solution bound of linear elasto-statics and vibration problems. *Computational Mechanics* **46**(2): p. 229-246. 2009

127. Wang XS and Zhang LT, Computational Mechanics *Interplotation functions in the immersed boundary and finite element methods*. **45**: p. 321-334. 2010

128. Clift R, Grace JR, and Weber ME, *Bubbles, Drops, and Particles*: New York: Academic Press. 1978

129. Hart JD, Cacciola G, Schreurs PJG, and Peters GWM, Journal of Biomechanics *A three-dimensional analysis of a fibre-reinfored aortic valve prothesis*. **31**(7): p. 629-638. 1998

130. Hart JD, Peters GWM, Schreurs PJG, and Baaijens FPT, A two-dimensional fluid-structure interaction model of the aortic value. *Journal of Biomechanics* **33**: p. 1079-1088. 2002

131. Loon VR, Anderson PD, and Vosse VDFN, A fluid interaction method with solid-rigid contact for heart valve dynamics. *Journal of Computational Physics* **217**: p. 806-823. 2006

132. Thubrikar M, *The Aortic valve*: CRC Press, Boca Raton, FL. 1990

Appendix A

Relevant Publication

A.1 Journal papers

1. Eric Li, G. R. Liu, Vincent Tan, and Z. C. He. Modeling and simulation of bioheat transfer in the human eye using the 3D alpha finite element method (αFEM). Intentional Journal for Numerical Methods in Biomedical Engineering. 2010; 26:955–976
2. Eric Li, G. R. Liu, Vincent Tan. Simulation of Hyperthermia Treatment Using the Edge-Based Smoothed Finite-Element Method. Numerical Heat Transfer, Part A: Applications. 2010; 57: 11, 822 -847
3. Eric Li, G.R. Liu, Vincent Tan, Z.C. He. An efficient algorithm for phase change problem in tumor treatment using αFEM. International Journal of Thermal Sciences. 2010; 49: 10, 1954-1967.
4. George X. Xu, Eric Li (corresponding author), Vincent Tan, G.R. Liu. Simulation of steady and unsteady incompressible flow using gradient smoothing method (GSM). Computers and Structures. doi:10.1016/j.compstruc.2011.10.001.
5. Eric Li, G.R. Liu, George X. Xu, Vincent, Tan, Z. C. He. Numerical modeling and simulation of pulsatile blood flow in rigid vessel using gradient smoothing method.

Engineering Analysis with Boundary Elements. doi:10.1016/j.enganabound. 2011.09.003.

6. Eric Li, Vincent Tan, George X. Xu, G.R. Liu, Z. C. He. A novel linearly-weighted gradient smoothing method (LWGSM) in the simulation of fluid dynamics problem Computers and Fluids. doi:10.1016/j.compfluid.2011.06.016.
7. Eric Li, Zhang ZQ, Vincent Tan, George X. Xu, G.R. Liu, Z. C. He. Immerse Gradient smoothing Method for Fluid-Structure Interaction Problems. Submitted to Journal of Fluids Engineering.
8. Eric Li, Vincent Tan, George X. Xu, G.R. Liu, Z. C. He. A novel alpha gradient smoothing method (αGSM) for fluid problems. Submitted to Numerical Heat Transfer, Part A: Applications (Accepted).

A.2 Book contribution

1. Eric Li, G. R. Liu, Vincent Tan, and Z. C. He. Modeling and Simulation of bioheat transfer in the human eye using the ES-FEM, in MULTI-MODALITY TATE-OF-THE-ART: HUMAN EYE IMAGING AND MODELING, CRC Press, Singapore, 2011. Editors: EYK Ng, Rajendra Acharya U, JH Tan and Jasjit S. Suri.